University of Oxford

Department of Materials

Carrier Dynamics within Semiconductor Nanocrystals

by

Simon Michael Fairclough

Mansfield College

A thesis submitted for the degree of

Doctor of Philosophy

Abstract

This thesis explores how the carrier dynamics within semiconductor nanocrystals can be directly engineered through specific core-shell design. Emphasis is placed on how material characteristics, such as strain or alloying at a core-shell interface, can influence the exciton energies and the recombination dynamics within semiconductor nanocrystals.

This study synthesises type-II heterojunction ZnTe/ZnSe core-shell nanocrystals via a diethyl zinc-free synthesis method, producing small size distributions and quantum yields as high as 12%. It was found that the 7% lattice mismatch between the core and shell materials places limitations on the range of structures in which coherent growth is achieved.

By developing compositional and strained atomistic core-shell models a variety of physical and optical properties could be simulated and has led to a clear picture of the core-shell architecture to be built. This characterisation provides evidence that the low bulk modulus ZnTe cores are compressed by the higher modulus ZnSe shells. Further studies show how strain is manifested in structures with 'sharp' core-shell interfaces and how intentional alloying the interface can influence the growth and exciton energies. A (2-6)-band effective mass model was able to distinguish between the as-grown 'sharp' and 'alloyed' interfaces which indicated that strain accentuates the redshift of the excitonic state whilst reduced strain within an alloyed interface sees a reduced redshift.

Single nanocrystal spectroscopy investigations of brightly emitting single graded alloyed nanocrystals and of a size series of commercially available CdSe/ZnS nanocrystals showed almost no fluorescence intermittency (nearly 'non-blinking'). These investigations also identified trion recombination as the main mechanism within the blinking 'off' state.

Ultimately this thesis adds to the growing understanding of how specific core-shell architectures manipulate the electronic structure and develops techniques to identify specific material characteristics and how these characteristics influence the physical and optical properties within semiconductor nanocrystals.

Dedicated to my parents and family

"To learn to succeed, you must first learn to fail."

Michael Jordan

"The pleasure of finding things out."

Richard Feynman

Acknowledgements

I am very grateful to Dr Jason Smith for all his supervision and guidance through out this thesis and in particular for providing the environment and support to pursue my own ideas and experiments and always having a door open to discuss problems or brainstorm new ideas. For this I will always be grateful.

I am very grateful to Dr Andrew Watt for allowing me to use his lab, in which many of these experiments were conducted, and the support given to me throughout this thesis.

I would like to thank Dr Ian Sellers whose initial idea sparked this whole project.

I would like to thank my collaborators from the University of Oxford; Mr Edward Tyrrell for all his effective mass calculations. Mr Johnny Fill and Miss Charlotte Lynch who conducted some of the single nanocrystal spectroscopy experiments with me. Dr Neil Young and Dr Sarah Haigh for all our attempts at abberation corrected TEM and discussions on TEM. Dr Susie Speller for all our discussions on XRD. Professor Steve Roberts for our discussion over critical radius calculations.

I would like to thank my collaborators from the University of Manchester; Mr Musa Cadirci, Dr Stuart Stubbs and Dr David Binks for their transient absorption experiments of my ZnTe/ZnSe material. Dr Darren Graeme, Professor Wendy Flavell and the people at MAXLAB Sweden who conducted synchrotron XPS on my ZnTe/ZnSe material under the European Community's Seventh Framework Programme grant no. 226716. Dr Katayune Presland and Professor Paul O'Brien for their discussions and knowledge in making alloyed nanocrystals.

I would like to thank Dr Travis Jenkins at eBioscience Inc. for providing the eFluor® material and all our discussions on the nanocrystal field.

I would like to thank my fellow co-workers and fellow students in the lab; Dr Johnny Moghal, Dr Benny Sher, Dr Alexandros Stavrinadis, Dr Brian Patton, Dr Ziyun Di, Dr Fabio Grazioso, Dr Shawn Willis, Dr Petos Kovacik, Dr Elva Zou, Mr Cheng Cheng, Mr Chris Cattley, Mr Matthew Wincote, Mr Sam Johnson, Mr Alex Buccheri, Mr Alex Powell, Miss Jenna Holder, Mr Edward Tyrrell, Mr Johnny Fill and most notably to Dr Laura Drössler and Dr Philip Dolan. To quote Alexandros Stavrinadis "We have shared many instruments, discussed a lot of science and had a decent number of pints too".

I would like to acknowledge the Department of Materials and its staff in giving me the opportunity and equipment to conduct this work and the UK Engineering and Physical Sciences Research Council for providing the funding. I would also like to thank staff and

students of Mansfield College for providing such a friendly community environment for me to work and play.

I am grateful of my friends Michael Brown, Dennis Marcus, Graeme Johnstone, Susanne Pfeifer, Ricardo Engel, Katie Moore, Simon Picot and Julia Shanks, and to Mr Terry Greenwood who have kept my spirits high when times were low and shared all the successes and failures with me.

Finally I would like to acknowledge my parents, Joan and Bill, and my brothers and sister David, Peter and Sandie for their love, support and affection for which I will always be grateful.

Contents

Abstract i

Acknowledgements iv

List of Figures xi

List of Tables xvi

0.1 General abbreviations . . . xvii
0.2 Chemicals and synthesis abbreviation . . . xvii
0.2.1 Elements and semiconductor abbreviations . . . xvii
0.2.2 Chemical compounds abbreviations . . . xvii
0.2.3 Chemical techniques abbreviations . . . xviii

1 Thesis outline 1
1.1 Goals of this thesis . . . 1
1.2 Structure of the thesis . . . 2

2 Introduction 4
2.1 Background . . . 4
2.2 Colloidal nanocrystals . . . 5
2.2.1 Specific architectures within binary structures . . . 6
2.2.2 Material choice for exciton engineering . . . 7
2.3 Nanocrystal synthesis and shelling . . . 11
2.3.1 Nucleation and growth . . . 11
2.3.2 Synthesis of core-only structures . . . 14
2.3.3 Synthesis of core-shell structures . . . 16
2.3.3.1 Dropwise addition . . . 16
2.3.3.2 Successive Ion Layer Adsorption and Reaction (SILAR) . . . 17
2.3.3.3 Single-source precursors . . . 18
2.3.4 Binary systems in literature . . . 19
2.3.4.1 Type-I nanocrystals . . . 19
2.3.4.2 Type-II nanocrystals . . . 20
2.3.4.3 Strain tuned heterojunctions . . . 22
2.3.5 Notable core-shell-shell structures . . . 25
2.3.6 Notable alloyed structures . . . 25

2.3.7 Anisotropic growth: From nanodot to nanorods and tetrapod formation . . . 28
2.4 Optical properties of nanocrystals . . . 30
2.4.1 Quantum confinement . . . 30
2.4.2 Extension in to the type-II regime . . . 33
2.5 The importance of understanding exciton dynamics . . . 36
2.5.1 Auger recombination . . . 36
2.5.2 Blinking . . . 37
2.5.2.1 Alloyed interfaces . . . 39
2.5.2.2 Type-II structures . . . 40
2.5.2.3 'Giant' nanocrystals . . . 41
2.5.2.4 Three types of blinking . . . 42

3 The theory and development of techniques used to investigate strain within the physical and optical properties of nanocrystals 46
3.1 Continuum elasticity model . . . 47
3.1.1 Application of the continuum elasticity model . . . 50
3.2 Introduction to the atomistic models developed for transmission electron microscopy (TEM) and powder X-ray diffraction (XRD) simulation . . . 52
3.2.1 Pseudo code . . . 53
3.2.2 Building a unit cell: The incorporation of radial and tangential strain . . . 55
3.2.3 Growth schemes . . . 58
3.3 Introduction to TEM simulation . . . 60
3.4 Introduction to XRD simulation . . . 62
3.5 Introduction to critical radius calculations . . . 65
3.6 Introduction to effect mass modeling . . . 69

4 Experimental methods 72
4.1 Synthetic methods to ZnTe/ZnSe nanocrystals . . . 72
4.1.1 Chemicals . . . 72
4.1.2 Preparation of precursors . . . 73
4.1.2.1 General precursors . . . 73
4.1.2.2 Zinc precursor preparation . . . 73
4.1.3 Synthesis of ZnTe cores . . . 74
4.1.3.1 Optimised Zhang method . . . 74
4.1.3.2 Xie method . . . 75
4.1.3.3 Jiang method . . . 75
4.1.4 ZnSe shell growth using SILAR . . . 75
4.1.5 Variations of the standard ZnSe shell protocol . . . 76
4.1.5.1 Successive Ion Layer Adsorption and Reaction — Thermal cycling (SILAR-TC) method . . . 77
4.1.5.2 Zinc oleate with oleylamine method . . . 77
4.1.5.3 Zinc acetate/TOP and Se-TOP method . . . 78
4.1.5.4 Diethyl zinc and Se-TOP method . . . 78
4.1.5.5 Zinc stearate and Se-TOP method . . . 78
4.1.5.6 Diethyl zinc core method with zinc oleate Se-TOP shell method . . . 79

4.1.5.7 Growth of alloyed nanocrystals . . . 79
4.2 The synthetic method to graded alloyed CdZnSeS nanocrystals . . . 80
4.3 Physical characterisation . . . 81
4.3.1 TEM, electron dispersive X-ray spectroscopy (EDX), Selected area electron diffraction patterns (SAED) and XRD characterisation . . . 81
4.3.2 X-ray photoelectron spectroscopy (XPS) characterisation . . . 81
4.4 Optical characterisation . . . 82
4.4.1 Ensemble absorption, photoluminescence (PL), photoluminescence excitation (PLE), quantum yield (QY) and lifetime measurements 82
4.4.2 Single nanocrystal spectroscopy . . . 83
4.4.2.1 Sample preparation . . . 83
4.4.2.2 Experimental setup and processing . . . 83

5 Synthesis of type-II ZnTe/ZnSe nanocrystals 86
5.1 Introduction & motivation . . . 87
5.2 Development of synthetic techniques to ZnTe core nanocrystals . . . 88
5.2.1 Previous related syntheses . . . 88
5.2.2 Results and discussion . . . 91
5.3 Development of synthesis procedures towards ZnTe/ZnSe nanocrystals . . . 95
5.4 Physical characterisation of ZnTe/ZnSe nanocrystals . . . 99
5.4.1 TEM characterisation . . . 99
5.4.2 High resolution TEM (HRTEM) characterisation . . . 105
5.4.3 Simulation of HRTEM data . . . 108
5.4.4 XRD characterisation . . . 116
5.4.5 XRD simulation . . . 122
5.4.6 XPS characterisation . . . 134
5.4.7 Critical radius calculations . . . 138
5.5 Optical characterisation . . . 141
5.5.1 General optical characterisation . . . 141
5.5.2 Exciton dynamics . . . 147
5.5.3 PL stability . . . 150
5.5.4 (2-6)-band effective mass simulation . . . 152
5.5.5 Single nanocrystal spectroscopy of ZnTe/ZnSe nanocrystals . . . 157
5.6 Conclusion . . . 159

6 Single-nanocrystal optical investigations of highly luminescent alloyed and commercially-available type-I nanocrystals 162
6.1 Introduction . . . 162
6.2 A facile synthetic method to highly-luminescent graded alloyed nanocrystals:
From synthesis to single nanocrystal investigations . . . 165
6.2.1 Introduction and motivation . . . 165
6.2.2 Results . . . 166
6.2.2.1 Physical characterisation . . . 166
6.2.2.2 Ensemble optical properties . . . 169
6.2.2.3 Single nanocrystal spectroscopy . . . 172
6.2.3 Summary . . . 181
6.3 eBioscience eFluor® nanocrystals . . . 182

6.3.1 Introduction and motivation . . . 182
6.3.2 Stated properties and composition . . . 182
6.3.3 Results . . . 184
6.3.3.1 Ensemble lifetimes . . . 184
6.3.3.2 TEM images of eFluor® nanocrystals . . . 186
6.3.4 Single nanocrystal spectroscopy . . . 190
6.3.4.1 eBioscience eFluor® 605 nm nanocrystals . . . 190
6.3.4.2 eBioscience eFluor® 625 nm nanocrystals . . . 195
6.3.4.3 eBioscience eFluor® 640 nm nanocrystals . . . 200
6.3.4.4 eBioscience eFluor® 650 nm nanocrystals . . . 206
6.3.5 Summary . . . 212
6.4 Discussion . . . 213
6.4.1 Reserved analysis: Further discussion on Auger lifetimes through knowledge of the composition . . . 216
6.4.2 Reserved analysis: Critical radius calculations . . . 219
6.5 Conclusion . . . 221

7 Conclusion and future work 223
7.1 Conclusion . . . 223
7.2 Future work . . . 226
7.2.1 Further synthesis of ZnTe/ZnSe nanocrystals . . . 226
7.2.2 Interatomic diffusion of Te in ZnTe/ZnSe nanocrystals . . . 226
7.2.3 Development of type-II structures . . . 227
7.2.4 Further work on strain modeling . . . 227
7.2.5 Further work on single nanocrystal spectroscopy . . . 228

Appendix 229

A 230
A.1 Derivation of the critical radius calculations . . . 230
A.2 Critical radius calculations for CdSe/ZnS nanocrystals . . . 233

B 235
B.1 Materials parameters for all strain model simulations and critical radius calculations . . . 235

C 237
C.1 (2-6)-band effective mass model. . . . 237
C.1.1 General effective mass model . . . 237
C.1.2 Strained effective mass model . . . 239

D 244
D.1 Additional information for the ZnTe/ZnSe nanocrystals . . . 244
D.1.1 EDX spectrum of ZnTe core-only nanocrystals . . . 244
D.1.2 Vegard's Law . . . 245
D.1.3 XRD concentration values . . . 245
D.1.4 Scherrer equation . . . 246

D.1.5 Additional ZnTe/ZnSe absorption data 248
D.1.6 Full 2nd derivatives of the ZnTe/ZnSe absorption spectra 249
D.1.7 Additional lifetime information for ZnTe/ZnSe nanocrystals 250
D.1.8 Disassociation constants and dynamic equilibrium 251

E **252**
E.1 Further strain analysis through TEM simulation 252
E.1.1 The strained and unstrained atomistic models for 3.2 nm diameter ZnTe core and 4 ML shell 252
E.1.2 Further characterisation through aberration corrected microscopy simulation 253
E.1.3 Further characterisation through geometric phase analysis simulation 255

F **262**
F.1 Additional ensemble lifetime information for the CdZnSeS nanocrystals . 262

G **263**
G.1 eFluor®605 nm nanocrystals under electric fields 263
G.2 eFluor®650 nm nanocrystals agglomeration at 4°C 265

References **266**

List of Figures

2.1 A schematic of a nano-island self-assembled quantum dot and a colloidal semiconductor nanocrystal (NC). . . . 4
2.2 A schematic representation of the bandgap alignments in a type-I, type-II, inverted type-II, and inverted type-I heterojunction core-shell NC. . . . 7
2.3 The bulk relative electron affinities, ionisation potentials and bandgaps for the II-VI, III-V semiconductors. . . . 8
2.4 a) A schematic showing the free energy profile as function of radius highlighting the critical radius for nucleation. b) A schematic showing size focusing and size broadening regimes as function of critical radius. . . . 12
2.5 A schematic representation of the SILAR technique. . . . 17
2.6 a) A schematic showing the crystal structure and bandgap alignments of an unstrained CdTe/ZnSe NC showing a type-I heterojunction and a strained CdTe/ZnSe NC with a compressed core showing a type-II heterojunction; b) a ternary CdSe/ZnSe/ZnS NC with a ZnSe layer mitigating strain. . . . 24
2.7 A schematic showing the first three allowed eigenstates and the associated energies for a particle in an infinite potential well. . . . 31
2.8 A schematic showing the density of states for a bulk, 1-D, 2-D, and 3-D quantum confined object. . . . 32
2.9 The absorption spectrum of a 4.1 nm diameter CdSe NC with the indexed exciton transitions. . . . 33
2.10 A schematic showing the energy potential, energy levels and wavefunctions for a a) type-I b) quasi type-II and c) type-II NC. . . . 34
2.11 An example of an intensity-time trajectory for a single NC showing distinct 'on' and 'off' periods known as 'blinking'. . . . 37
2.12 a) Photoluminescence (PL) spectra of several alloyed CdZnSe/ZnSe NC showing three-peak emission b) The proposed recombination mechanism to produce three-peak emission. . . . 40
2.13 A schematic showing the intensity-time trajectories, lifetime-time trajectories and the associated recombination pathways for type-A type-B and type-C blinking. . . . 44
2.14 A schematic 'fluorescence lifetime intensity distribution' (FLID) for type-A, type-B and type-C blinking . . . 45

3.1 A schematic defining the core radius and shell thickness used for the continuum elasticity model. . . . 48
3.2 The theoretical interface pressure, strain and lattice constants of ZnTe/ZnSe NC as a result of 7% lattice mismatch calculated using the continuum elasticity model. . . . 51

3.3 A schematic representation of the pseudo code used to build the atomistic strained NC. . . . 54
3.4 A schematic highlighting the rotation of the strain tensor on the surface of a sphere. . . . 55
3.5 A schematic comparing the two growth schemes used to build the atomistic models. . . . 59
3.6 A comparison of a variety of protocols used to simulate XRD patterns. . . . 63
3.7 A schematic of a Frank partial and Shockley partial dislocation. . . . 67
3.8 A schematic showing the energy level considerations of a simple effective mass approximation and (2-6)-band effective mass approximation showing the lowest $1S^{(e)}1S^{(h)}$ and $1S^{(e)}_{1/2}1S^{(h)}_{3/2}$ transitions respectively 69
3.9 A plot of the conduction and valence band profiles calculated with and without strain for a 2.4 nm diameter ZnTe core NC with 4 ML ZnSe shell. 70

4.1 A schematic of the home built epi-fluorescence setup used for single NC spectroscopy. . . . 84

5.1 The evolution of the first excitonic absorption feature and the corresponding second derivative of ZnTe NC using variety of synthetic methods. A comparison is made to the size distributions as determined by TEM. . . . 92
5.2 Room temperature absorption spectra showing the evolution of the first excitonic feature with time using the SILAR growth method. . . . 97
5.3 The evolution of first excitonic feature as determined by *in situ* absorption spectroscopy after each precursor injection and growth 98
5.4 TEM images and size distribution profiles for a size series of ZnTe/ZnSe NC. . . . 100
5.5 TEM images showing anisotropic growth with ∼5 ML of ZnSe using a variety of Zn precursors growth. . . . 102
5.6 TEM images of 4.6 nm diameter ZnTe core NC with a) 5 ML ZnSe b) 5% alloying of the interface c) 10% alloying of the interface. . . . 104
5.7 HRTEM images of a) 2.4 b) 3.6 and c) 4.6 nm ZnTe core diameter NC with 4-5 ML ZnSe shell thickness. . . . 106
5.8 HRTEM images of 3.6 nm ZnTe core diameter NC with 4 ML ZnSe growth showing quasi-tetrahedral NC with a large amount of twinning stacking faults. . . . 107
5.9 A comparison of the experimental and simulated images and fast Fourier transforms of a 2.4 nm diameter ZnTe core with 4 ML ZnSe shell. . . . 109
5.10 A HRTEM image showing the variation of lattice constant in the radial and tangential directions of a 3.6 nm diameter ZnTe core NC with 4 ML ZnSe shell. A simple model was applied to determine the core and shell thicknesses. . . . 110
5.11 A comparison of the a) experimental, b) strain simulated and c) unstrained simulated HRTEM images for a 3.2 nm diameter ZnTe core NC with 4 ML ZnSe shell. . . . 112
5.12 A comparison of the lattice constant obtained along the radial and tangential components within the experimental, strained simulated and unstrained simulated HRTEM images. A comparison is also made to the tangential and radial component of the continuum elasticity model. . . . 114

5.13 Four proposed stacking faults in a 3.6 nm diameter ZnTe core NC with 4 ML ZnSe shell. . . . 114
5.14 The experimental XRD patterns of a) a core size series and b) a shell size series of ZnTe/ZnSe NC. . . . 116
5.15 The XRD patterns for a 4.6 nm diameter ZnTe core with 5 ML ZnSe NC with a) an as-grown core-shell interface, b) 5% of alloying and c) 10% of alloying over the first 3 ML growth. . . . 120
5.16 The simulated XRD patterns using two unstrained geometries. . . . 123
5.17 A comparison of the experimental XRD patterns, taken from a core size series, with simulated XRD patterns using two unstrained core-shell models. 125
5.18 A comparison of the experimental XRD patterns, taken from a core size series, with simulated XRD patterns using a fully strained and a faceted strained core-shell model. . . . 128
5.19 A comparison of the experimental XRD patterns, taken from a shell size series, with simulated XRD patterns using a fully strained and a faceted strained core-shell model. . . . 129
5.20 A comparison of the experimental XRD patterns, taken from a shell size series, with a best fit simulation . . . 130
5.21 A comparison of the lattice constants, interface pressure and strain between a full strained model and the best fit model. From this an alloying of the interface is deduced. . . . 132
5.22 XPS analysis and compositional simulation of a 2.4 nm diameter ZnTe core with a 4 ML shell. . . . 135
5.23 The full, Frank partial and Shockley partial dislocation critical radii boundaries for ZnTe/ZnSe NC. . . . 140
5.24 The absorption and PL spectra of ZnTe/ZnSe NC with a) 2.4 nm, b) 3.6 nm, and 4.6 nm ZnTe core diameters with increasing shell thickness. . 142
5.25 The Stokes shift for 2.4 nm, 3.6 nm and 4.6 nm diameter ZnTe core NC as a function ZnSe shell thickness. . . . 143
5.26 The absorption and PL spectra of 4.6 nm diameter ZnTe core NC with a) 5% alloying and b) 10% alloying of core-shell interface with increasing shell ZnSe thickness. . . . 145
5.27 A contour plot of the theoretical absorption wavelength of the $1S^{(e)}_{1/2}1S^{(h)}_{3/2}$ transition in the strained regime showing the type-I, type-II and quasi type-II regions. . . . 147
5.28 The PL lifetime decays for a 3.9 nm diameter ZnTe core NC with 3, 4 and 5 ML of ZnSe shell with the corresponding tri-exponential lifetime components. . . . 148
5.29 PL stability of 3.8 nm diameter ZnTe core NC with 1 ML ZnSe shell after 1 methanol/butanol precipitation clean without and with exposure to ambient conditions. . . . 150
5.30 A comparison of the energy deviation of the $1S^{(e)}_{1/2}1S^{(h)}_{3/2}$ exciton energy from the core absorption feature and compared to the predicted energies with a model that incorporates and does not incorporate strain. . . . 152
5.31 The mapped absorption features obtained from the second derivative of the absorption data as a function of shell thickness and compared with the theoretically calculated exciton transitions. . . . 154

5.32 The mapped absorption features obtained from the fourth derivative of the absorption data as a function of shell thickness and compared with the theoretically calculated exciton transitions. 155
5.33 Spectral trajectories and individual spectra of single 3.8 nm diameter ZnTe core NC with 5 ML ZnSe shell showing both single-peak and two-peak emission. 158

6.1 TEM images and the corresponding size distribution histograms for CdZnSeS NC after a) 1 b) 3 and c) 5 minutes growth. 167
6.2 Selected area electron diffraction patterns for CdZnSeS NC after a) 1 minute b) 3 minutes and c) 5 minutes growth. 167
6.3 HRTEM images and corresponding FFT of CdZnSeS NC after a) 3 minute and b) 5 minutes growth. 168
6.4 The ensemble optical properties for the growth series of CdZnSeS NC. a) Ensemble absorption and PLE spectra b) PL spectra excited at 400 nm c) QY and d) a comparison of the ensemble PL with first excitonic feature highlighting the Stokes shift. 170
6.5 The ensemble lifetime measurements for CdZnSeS NC after 1, 3 and 5 minutes growth and corresponding bi- and tri-exponential lifetime components as a function of growth time 170
6.6 Representative spectra of two CdZnSeS 5 minutes NC showing Lorentzian line emission. The corresponding Hanbury Brown Twiss measurement on a NC showing a FWHM of 20 nm 172
6.7 Spectral trajectories of four separate CdZnSeS NC showing NC predominately in the 'on' state with small amount of spectral diffusion and NC showing a large amount of blinking. 173
6.8 Intensity-time and blinking statistics of three CdZnSeS NC investigated over 10 minutes showing nearly non-blinking NC. 174
6.9 Intensity-time, lifetime-time trajectories and FLID analysis for a CdZnSeS NC under pulsed excitation showing minimal blinking. 176
6.10 Intensity-time, lifetime-time trajectories and FLID analysis for a CdZnSeS NC under pulsed excitation showing A-type and B-type blinking. 177
6.11 Intensity-time, lifetime-time trajectories and FLID analysis for a CdZnSeS NC under pulsed excitation showing A-type, B-type and 'grey' state blinking. 179
6.12 Intensity-time, lifetime-time trajectories and FLID analysis for a CdZnSeS NC under pulsed excitation showing A-type and 'grey' state blinking. . . 180
6.13 Extinction coefficient and PL spectra for the eFluor®605 nm, 625 nm and 650 nm NC. 183
6.14 Ensemble lifetime data for eFluor®605 nm, 625 nm, eFluor®640 nm and eFluor®650 nm NC. 184
6.15 TEM images of eFluor®605 nm NC showing limited number of twinning stacking faults. 187
6.16 TEM images of eFluor®625 nm NC showing a mixture of coherent and incoherent crystals structures. 188
6.17 TEM images of eFluor®640 nm NC showing predominently coherent crystals structures. 188
6.18 HRTEM images of eFluor®650 nm NC showing twinning stacking faults. 189

6.19 Representative spectra and spectral trajectories of single eFluor®605 nm NC showing good optical performance with mild blinking and spectral diffusion. 190
6.20 Intensity-time trajectories and blinking statistics of two different eFluor®605 nm NC under continuous wave excitation showing non-blinking and blinking characteristics 191
6.21 Intensity-time, lifetime-time trajectories and FLID analysis for an eFluor®605 nm NC under pulsed excitation showing no blinking. 192
6.22 Intensity-time, lifetime-time trajectories and FLID analysis for an eFluor®605 nm NC under pulsed excitation showing an increase in lifetime. 193
6.23 Representative spectra and spectral trajectories of single eFluor®625 nm NC showing NC with good optical performance, mild blinking and spectral diffusion. 195
6.24 Intensity-time trajectories and blinking statistics of two different eFluor®625 nm NC under continuous wave excitation showing nearly non-blinking and blinking properties. 196
6.25 Intensity-time trajectories and blinking statistics of the same eFluor®625 nm NC under 8 W cm^{-2} pulsed and continuous wave excitation showing nominally the same power law exponent. 196
6.26 Intensity-time, lifetime-time trajectories and FLID analysis for an eFluor®625 nm NC under pulsed excitation showing nearly non-blinking NC. 198
6.27 Intensity-time, lifetime-time trajectories and FLID analysis for an eFluor®625 nm NC under pulsed excitation showing A-type blinking. 199
6.28 Representative spectra and spectral trajectories of single eFluor®640 nm NC, showing NC with good optical performance, limited blinking and spectral diffusion. 200
6.29 Intensity-time trajectories and blinking statistics of two different eFluor®640 nm NC under continuous wave excitation showing nearly non-blinking, blinking and grey state properties. 201
6.30 Intensity-time trajectories and blinking statistics of the same eFluor®640 nm NC under 8 Wcm^{-2} pulsed and continuous wave excitation showing nominally the same power law exponent. 202
6.31 Intensity-time, lifetime-time trajectories and FLID analysis for an eFluor®640 nm NC under pulsed excitation showing a nearly non-blinking NC with A-type blinking. 203
6.32 Intensity-time, lifetime-time trajectories and FLID analysis for an eFluor®640 nm NC under pulsed excitation showing A-, B-type and 'grey' state blinking. 205
6.33 Representative spectra and spectral trajectories of single eFluor®650 nm NC, showing NC with good optical performance, blinking and spectral diffusion. 206
6.34 Intensity-time trajectories and blinking statistics of four different eFluor®650 nm NC under continuous wave excitation showing non-blinking and blinking NC. 207
6.35 Intensity-time, lifetime-time trajectories and FLID analysis for an eFluor®650 nm NC under pulsed excitation showing a non-blinking NC. 209
6.36 Intensity-time, lifetime-time trajectories and FLID analysis for an eFluor®650 nm NC under pulsed excitation showing a A-type blinking NC. 211
6.37 The full, Frank partial and Shockley partial dislocation critical radii for a) CdSe/CdS NC and b) CdS/ZnS NC for $\alpha = 4$. 220

List of Tables

2.1 The physical properties of II-VI, III-V and IV-VI semiconductors under ambient conditions. . . . 9
2.2 The lattice mismatch between the quoted zinc blende lattice constants of the II-VI semiconductors. . . . 9
2.3 Bulk moduli and the conduction and valence band volume deformation potentials for the II-VI semiconductors. . . . 10
2.4 The physical data, synthetic routes, PL redshift and QY for the most notable type-I structures. . . . 21
2.5 The physical data, synthetic routes, PL range and QY for the known type-II structures. . . . 23

4.1 The optimum temperature for each monolayers growth of ZnSe on a ZnTe core. . . . 77

5.1 The experimental lattice constants obtained from XRD patterns compared to the theoretical homogenously alloyed (Vegard's Law) lattice constant when considering the stoichiometry and relative volumes of precursors of the NC. . . . 118
5.2 A table comparing the Scherrer diameter as determined through XRD and to the experimental diameter as determined through TEM. . . . 119
5.3 A table showing the first excitonic features, peak PL, Stokes shift and FWHM for 2.4 nm, 3.6 nm, and 4.6 nm diameter ZnTe cores with various shell thicknesses. . . . 146

6.1 The eFluor®NC samples and quoted optical properties. . . . 182
6.2 The bi- and tri-exponential lifetime components for the lifetime trajectories of the eFluor®605 nm, 625 nm, 640 nm and 650 nm NC. . . . 185

0.1 General abbreviations

CW - Continuous wave
FWHM - Full width at half maximum
HRTEM - High resolution transmission electron microscopy
ML - Monolayer
NC - Colloidal semiconductor nanocrystal
N-IR - Near-infrared
N-UV - Near-ultraviolet
PL - Photoluminescence
PLE - Photoluminescence excitation
QD - Quantum dot
QY - Quantum yield
SAED - Selected area electron diffraction
SNS - Single nanocrystal spectroscopy
TEM - Transmission electron microscopy
UV - Ultraviolet
XPS - X-ray photoelectron spectroscopy
XRD - Powder X-ray diffraction

0.2 Chemicals and synthesis abbreviation

0.2.1 Elements and semiconductor abbreviations

Cd - Cadmium
CdS - Cadmium sulphide
CdSe - Cadmium selenide
CdTe - Cadmium telluride
S - Sulphur
Se - Selenium
Te - Tellurium
X - (Cd, Zn)
Y - (S, Se, Te)
Zn - Zinc
ZnS - Zinc sulphide
ZnSe - Zinc selenide
ZnTe - Zinc telluride

0.2.2 Chemical compounds abbreviations

BTMPPA - bis(2,4,4-trimethyl-pentyl) phosphinic acid
$Cd(Ac)_2$ - Cadmium acetate
$CdCl_2$ - Cadmium chloride
$Cd(Et)_2$ - Diethyl cadmium
CdO - Cadmium oxide

DOA - Dioctylamine
HDA - Hexadecylamine
HPA - Hexylphosphinic acid
LA - Lauric acid
MA- Mysteric acid
OA - Oleic acid
OE - Octyl ether
ODA - Octadecylamine
ODE - Octadecene
OLA - Oleylamine
PMMA - Polymethyl(methyl acrylate)
SA - Stearic acid
TBP - Tributylphosphine
TDPA - Tetradecylphosphonic acid
TOP - Trioctylphosphine
TOPO - Trioctylphosphine oxide
$(TMS)_2S$ - Hexamethyldisilthiane
$Zn(Ac)_2$ - Zinc acetate
$Zn(Et)_2$ - Diethyl zinc
$Zn(Ol)_2$ - Zinc oleate
$Zn(St)_2$ - Zinc stearate
Y -TBP - Y-Tributylphosphine
Y -TDP - Y-Tridecylphosphine
Y -TOP - Y-Trioctylphosphine

0.2.3 Chemical techniques abbreviations

DW - Dropwise addition
HI - Hot-injection technique
HU - Heat-up technique
LA - Long anneal
SILAR - Successive ion layer absorption and reaction
SILAR-TC - Successive ion layer absorption and reaction — thermal cycling
PreC - Pre-clean & purification

Chapter 1

Thesis outline

1.1 Goals of this thesis

This thesis aims to add to the growing knowledge of exciton dynamics within the field of colloidal II-VI 'semiconductor nanocrystals' (NC) through direct engineering of novel NC architectures, and the investigation of the physical and optical properties. Whilst this aim can be conceived to be intrinsically broad, this thesis limits its investigation to three areas which have shown exciting potential within the field;

1. The synthesis of ZnTe/ZnSe NC as a cadmium free alternative towards a type-II heterojunction NC.

2. The role of strain within the material and exciton dynamics of core-shell ZnTe/ZnSe NC.

3. The recombination dynamics and blinking behaviour within highly luminescent type-I heterojunction NC.

1.2 Structure of the thesis

Since there is much overlap between these specific goals the thesis is set out in the following way:

Chapter 2 gives an introduction to the colloidal NC field and the basic principles and advances in synthetic practice. The chapter presents the current state-of-the-art core-shell structures with both type-I and type-II heterostructures. The chapter further presents the current understanding of how excitons can be manipulated through direct control of specific heterostructure and architectures. Finally, this chapter presents the current understanding of exciton processes with specific emphasis on how specific architectures manipulate trion emission, Auger recombination, and fluorescence intermittency known as 'blinking'.

Chapter 3 describes the experimental methods used for chapters 5 & 6.

Chapter 4 presents the continuum elasticity model which is used to model strain throughout this thesis. This chapters also shows the development of models used to simulate the physical and optical properties within strained core-shell NC.

Chapter 5 presents the first attempt to produce type-II heterojunction ZnTe/ZnSe core-shell NC via a diethyl zinc-free synthetic method. Due to the limited synthetic procedures to ZnTe NC, the first part of this chapter explores various ZnTe synthetic procedures as a good seed for epitaxial growth. The second part of the chapter explores the growth dynamics within ZnTe/ZnSe core-shell NC and how strain can influence the growth dynamics within this system. This chapter sets out to investigate the role of

strain in the physical and optical properties through comparisons to transmission electron microscopy (TEM), X-ray diffraction (XRD), X-ray photoelectron spectroscopy (XPS), critical radius and effective mass simulations.

Chapter 6 presents single NC spectroscopy (SNS) investigations of graded alloyed CdZnSeS NC, synthesised via a facile synthetic method, and a size series of commercially available type-I CdSe/ZnS NCs from a commercial collaborator which have all shown high quantum yields (QY).

Chapter 7 gives an over-all conclusion and describes future work.

Chapter 2

Introduction

2.1 Background

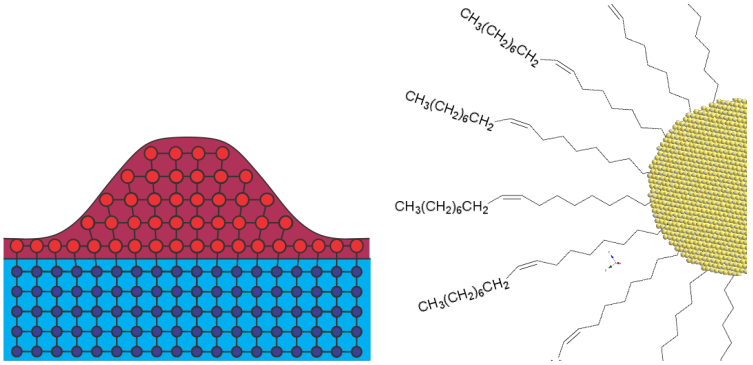

(A) (B)

FIGURE 2.1: A schematic of a) a nano-island self-assembled QD produced using the Stranski-Krastanov growth method. b) a colloidal semiconductor NC with encapsulating ligands.

The discovery that a 0-D quantum confined object, known as a 'quantum dot' (QD), could be made through wet chemical techniques within glass and aqueous matrixes in the 1980's sparked real research interest [1, 2]. However it was the work of Murray *et al.* [3] on the hot injection of organometallic precursors in an organic coordinating solvent which sparked exponential growth within the new field of colloidal QD, which are referred to in this thesis as colloidal 'semiconductor nanocrystal[s]' (NC). An exciting

array of NC geometries can be produced which can be dispersed in a wide variety of solvents. This extra degree of freedom and the ability to change the surface chemistry has enabled direct manipulation and exploitation of the quantum confined excited electron-hole pairs known as 'excitons' for application in photovoltaics [4], biological tagging [5] and optoelectronic devices [6]. Whilst the NC field is not as mature as their self-assembled QD cousins produced through molecular beam epitaxy [MBE] (Figure 2.1a), the pace of NC research has matured past the developing stage. An understanding of synthetic routes to high quality materials has matured and the field is now developing a variety of new designs and architectures, such as type-II heterostructure NC, alloyed NC, strained and strain mitigated NC in an effort to understand the fundamental processes within the NC.

The NC architecture is crucial to the electronic structure and optical properties of the system and thus the architecture and material characteristics engineers the 'carrier dynamics within NC'. The following sections present the basic principles and concepts of NC with specific emphasis on the state-of-the-art methodologies to NC design and exciton manipulation. The section ultimately describes the latest understanding of the carrier dynamics within NC to understand the phenomenon of fluorescence intermittency known as 'blinking'.

2.2 Colloidal nanocrystals

Colloidal NC are principally described as a nanocrystal with an organic terminated surface, commonly known as 'ligands' (Figure 2.1b). This organic layer chemically and electrically passivates the NC surface whilst also giving the ability to be dispersed in a variety of solutions, and prevents agglomeration. The layer is such, that it can promote

exciton radiative recombination, increasing fluorescence quantum yield (QY), by occupying surface trap sites which can allow for non-radiative recombination of the exciton. Whilst these ligands are good passivators of dangling bonds, the dynamic state of a ligand on the surface means that these NC can degrade physically and optically over time.

The first NC were made from a single material, the majority of NC are now binary structures [7–10]. These binary NC comprise of a semiconductor 'core' encased within a semiconductor 'shell' structure. This shell physically passivates the electronically active core surface by binding a subsequent covalently bonded layer and thus gives added protection to the core.

2.2.1 Specific architectures within binary structures

The electronic properties of these binary (core-shell) and ternary structures (core-shell-shell) are very dependent on the constituent materials. Two of the most significant contributions come from the relative bandgap alignments/specific heterojunction and the crystal structure of the materials. The relative bandgap alignments can be categorised as type-I, type-II and type-III heterojunctions. The most extensively studied are binary NC which have bandgap alignments in the type-I heterostructure configuration (Figure 2.2a). This describes a NC with small bandgap material core which is encased within a larger bandgap material. Since charge relaxes to the lowest energy level, the wider bandgap material will act as potential barrier, spatially confining the exciton within the core. This maintains the quantum confinement effects and the general optical characteristics of the core structure. Type-II heterojunction NC are described by a staggered band alignment (Figure 2.2b). In this scenario the charge carriers of the exciton tend to the lowest energy states, localising within either the core or the shell respectively, spatially

separating the charge carriers and thus lowering the effective bandgap energy. Type-III heterojunction NC refer to a total misalignment of the relative bandgaps and will not be referred to again in this text. The above regimes are similarly true for the inverted core-sell structures (Figure 2.2c-d). For example in an inverted type-I NC, the band alignment is reversed and the electrons and holes are localised to the shell layer. Further shelling layers have been employed to produce more advanced ternary structures which include type-I-I, type-II-I and type-II cascades NC which will be discussed in later sections.

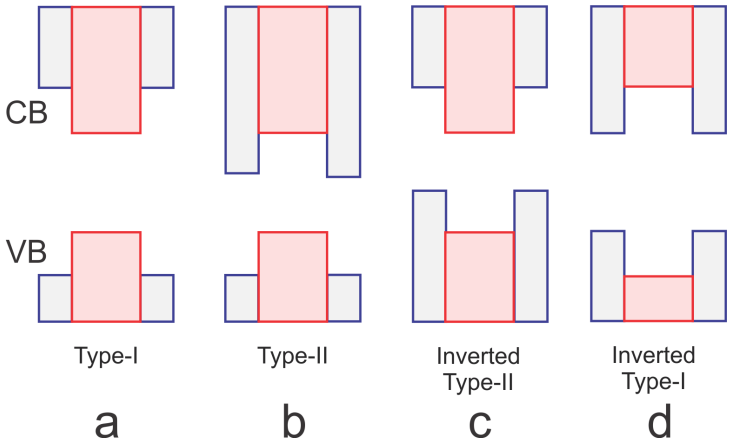

FIGURE 2.2: A schematic representation of the bandgap alignments in a a) type-I b) type-II c) inverted type-II and d) inverted type-I heterojunction core-shell NC. The conduction band (CB) and valence band (VB) of the core and shell materials are marked in red and blue respectively.

2.2.2 Material choice for exciton engineering

As can be seen by figure 2.3 most of the II-VI and III-V material combinations produce either a type-I or type-II heterojunction structure, indeed out of the 30 combinations of XY (X= Cd,Zn) (Y=S,Se,Te) materials which this thesis focuses on, there are fourteen type-I, twelve type-II and four quasi type-II heterojunction combinations. The specific properties of these structures will be discussed in further sections. Whilst these combinations can be in theory be produced, other parameters such as crystal structure and lattice mismatch must all so be considered. As can be seen from table 2.1 the material

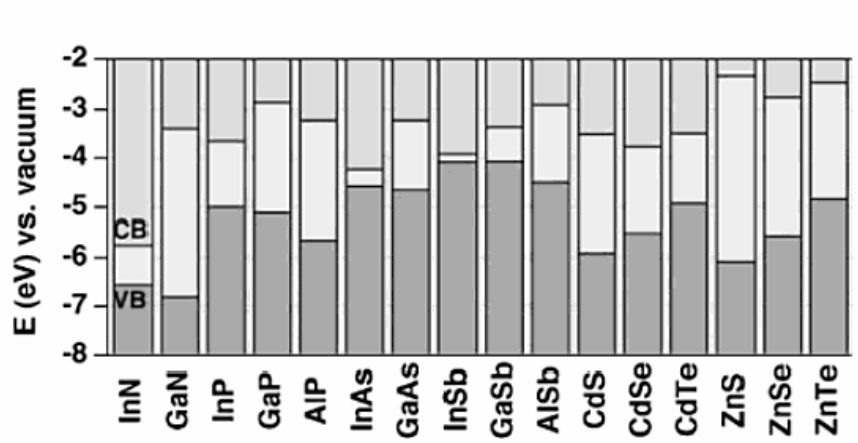

FIGURE 2.3: The bulk relative electron affinities and ionisation potentials showing energy bandgap (Light grey), the conduction (CB) and valence band (VB) alignments for the II-VI, III-V semiconductors. Reproduced from [11] awaiting permission.

crystal structure and lattice constant under ambient conditions can vary considerably. It is well known from thin film deposition that having common crystal structure and lattice constant can improve epitaxial growth and reduces defects. From table 2.2 it can be seen that the lattice mismatch within the II-VI semiconductors can be as high as 19.8% for CdTe/ZnS and low as 0.4% for ZnTe/CdSe.

Whilst the strain associated with a large lattice mismatch can potentially induce defects [7, 15], it is known that within colloidal NC [16] and Stranski Krastanov QD in MBE [17] that strain can be more readily absorbed when compared to the same bulk structures. This strain induces a change in the intrinsic inter-atomic distances and thus modifies the energy levels [18]. It has been shown that shifts in the conduction (valence) band energy, $E^{c(v)}$, can be related to the fractional change in volume, $d\ln v$, due to hydrostatic strain by [19]

$$a_v^{c(v)} = \frac{dE^{c(v)}}{d\ln v} \tag{2.1}$$

where $a_v^{c(v)}$ is the conduction (valence) band volume deformation potential. The deformation potential and bulk moduli for each II-VI semiconductor material can be seen in table 2.3 and highlights that the CdTe and ZnTe have the lowest bulk moduli. Whilst

Material	Structure	Type	E_{gap} (eV)	Lattice parameter (Å)
ZnS	Wurtzite	II-VI	3.53 [12]	3.83/6.27 [12]
ZnS	Zinc blende	II-VI	3.61	5.41
ZnSe	Wurtzite	II-VI	2.80 [12]	4.01/6.55 [12]
ZnSe	Zinc blende	II-VI	2.69	5.67
ZnTe	Wurtzite	II-VI	2.42 [12]	4.28/7.01 [12]
ZnTe	Zinc blende	II-VI	2.39	6.10
CdS	Wurtzite	II-VI	2.49	4.14/6.71
CdS	Zinc blende	II-VI	2.5 [13]	5.82 [14]
CdSe	Wurtzite	II-VI	1.75	4.3/7.01
CdSe	Zinc blende	II-VI	1.87 [13]	6.08 [14]
CdTe	Wurtzite	II-VI	2.0 [12]	4.58/7.48 [12]
CdTe	Zinc blende	II-VI	1.43	6.48
GaN	Wurtzite	III-V	3.44	3.188/5.18
GaP	Zinc blende	III-V	2.27 i	5.45
GaAs	Zinc blende	III-V	1.42	5.65
GaSb	Zinc blende	III-V	0.75	6.10
InN	Zinc blende	III-V	0.8	3.54/5.70
InP	Zinc blende	III-V	1.35	5.87
InAs	Zinc blende	III-V	0.35	6.06
InSb	Zinc blende	III-V	0.23	6.48
PbS	Rocksalt	IV-VI	0.41	5.94
PbSe	Rocksalt	IV-VI	0.28	6.12
PbTe	Rocksalt	IV-VI	0.31	6.46

TABLE 2.1: The physical properties of II-VI, III-V and IV-VI semiconductors under ambient conditions. Unless specified the stated values are from reference [11].

Material	CdS	CdSe	CdTe	ZnS	ZnSe	ZnTe
CdS	-	4.3%	10.2%	-7.6%	-2.6%	4.6%
CdSe	-4.5%	-	6.2%	-12.4%	-7.2%	0.3%
CdTe	-11.3%	-6.6%	-	-19.8%	-14.3%	-6.2%
ZnS	7.0%	11.0%	16.5%	-	4.6%	11.3%
ZnSe	2.6%	6.7%	12.5%	-4.8%	-	7.0%
ZnTe	-4.8%	-0.3%	5.9%	-12.8%	-7.6%	-

TABLE 2.2: The lattice mismatch between the quoted zinc blende lattice constants of the II-VI semiconductors. As calculated from lattice constants in table 2.1.

this highlights that CdTe and ZnTe can be easily compressed, the change in volume also leads to the largest change in the conduction and valence band energy of the II-VI semiconductors due the high deformation potential. Smith *et al.* [20] used this concept to great effect with CdTe core NC with a large lattice mismatched shell, modifying the relative band alignments from a type-I system to a type-II and *vice versa*.

Material	Bulk modulus (GPa) [18]	Volume deformation potential	
		Valence band a_v^v (eV) [21]	Conduction band a_v^c (eV) [21]
ZnS	77.1	-1.74	-6.02
ZnSe	62.4	-1.97	-5.93
ZnTe	50.5	-2.28	-6.95
CdS	60	-1.51	-3.59
CdSe	53.1	-1.81	-3.77
CdTe	42.4	-2.14	-5.09

TABLE 2.3: Bulk moduli and the conduction and valence band volume deformation potentials for the II-VI semiconductors.

2.3 Nanocrystal synthesis and shelling

The synthetic routes to NC is an ever growing topic which includes a variety of exciting techniques and methodologies which are extensively reviewed in the following articles [10, 22, 23]. This section highlights the main principles of core synthesis and the progression to state-of-the-art techniques. Focus will then be placed on a literature review of the hot-injection technique and shelling techniques within organic solvents.

2.3.1 Nucleation and growth

The nucleation of NC has been achieved by a variety of different techniques including hot injection [3, 24, 25], microwave heating [26, 27] and heat-up technique [28, 29] to name but a few. All the techniques require the same three physical components:

1. Precursors, which provides elemental feedstock for NC growth;
2. A solvent medium;
3. Surfactants or ligands which mediates the growth of the NC, prevents coagulation and can be utilised as a coordinating solvent.

The underlying processes of nucleation within these techniques adhere to the same La Mer theory [29, 30] which defines a three stage process:

1. A decomposition of precursor producing conditions for anion and cation supersaturation;
2. A rapid nucleation step then occurs, consuming the anion and cation monomers until the system falls below the supersaturation point;

3. Growth.

Ideally the nucleation and growth should be two distinct stages, otherwise large size distributions can occur. The energy required to instigate nucleation can be described by the Gibbs free energy. This thermodynamic property considers the energy needed to form spherical crystals with a radius r from a solution with a supersaturation concentration S. The Gibbs free energy, ΔG, in the simplest approximation has two contributing terms; the surface chemical potential, μ_s, and volume chemical potential, μ_v, which can be seen in figure 2.4a and described by

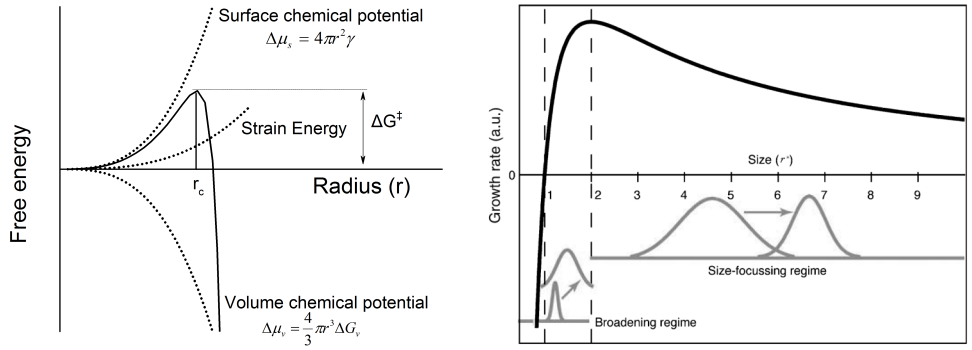

(A) (B)

FIGURE 2.4: a) A schematic showing the free energy profile (Black line) as function of radius highlighting the critical radius for nucleation, r_c. Highlighted are the surface chemical potential, volume chemical potential and strain energy (Dotted lines) which contribute to the free energy profile. Also highlighted is the associated energy barrier $\Delta G^{\ddagger}$ at the critical radius. Adapted with permission from [31]. b) The NC growth rate as a function of the r^* where $r^* = r_c$ at $dr/dt = 0$, demonstrating the size-broadening regime and size-focussing regime. Reproduced from [32] awaiting permission.

$$\Delta G = \mu_s + \mu_v \tag{2.2}$$

$$= 4\pi r^2\gamma + \frac{4}{3}\pi r^3\Delta G_v \tag{2.3}$$

where $\Delta G_v = (-RTlnS)/V_m$ is the free energy change between monomers in the solution and unit volume of bulk crystal, V_m is the molar volume of the of bulk crystal, γ is the surface energy per unit area [29, 30, 33].

The minimum radius and energy at which a NC can be formed is described by the critical radius, r_c, below which no stable NC are formed and NC will self-decompose. From this, it can be further shown that for NC to become stable, the NC must overcome a critical free energy $\Delta G^{\ddagger}$ condition. Both these quantities are described by [29]

$$r_c = \frac{-2\gamma}{\Delta G_v} = -\frac{2\gamma V_m}{RTlnS} \tag{2.4}$$

$$\Delta G^{\ddagger} = \frac{16\pi\gamma^3}{3(\Delta G_v)^2} = \frac{16\pi\gamma^3 V_m^2}{3(RTlnS)^2} \tag{2.5}$$

As seen from equation 2.4 and 2.5, r_c and $\Delta G^{\ddagger}$ are very much dependent on temperature and concentration. Further terms contribute to this, but are not included in the simplest model, such as the steric hindrance from ligands and strain which will be discussed in the next sections [31].

The third process is the continued growth of the particle by the consumption of the anion and cation reagent in the solution. In this growth regime there are two competing processes: the dissociation and addition of monomers. Peng *et al.* showed the growth rate dr/dt within NC is inversely proportional to the radius of the NC r and the critical radius r_c by [34]

$$\frac{dr}{dt} \propto \left(\frac{1}{r_c} - \frac{1}{r}\right) \tag{2.6}$$

Figure 2.4b plots this relation and defines several growth regimes, where $r^* = r_c$ at $dr/dt = 0$ [29]. Peng *et al.* showed that r^* is dependent on the monomer concentration and NC concentration. If the monomer concentration and reaction conditions produced a situation whereby $r^* \geq 2r_c$, then the growth would produce a 'size focusing' effect. If the monomer concentration and conditions such that $r_c < r^* < 2r_c$, there will be 'size broadening'. The condition where a fraction of the NC size distribution is partly below the r_c sees negative growth and self-decomposition. The decomposition adds to

the monomer concentration which feeds the growth of larger NC growth [35]. This regime is defined as 'Ostwald ripening' and is typically seen at high temperatures [34]. Ostwald ripening is detrimental to the size distribution and to the quality of the core-shell structure when using high temperatures for shell growth. Thus, trends towards low temperature shell growth are used to negate Ostwald ripening.

2.3.2 Synthesis of core-only structures

The most common nucleation and growth technique is by 'hot-injection'. The initial hot-injection was developed by Murray *et al.* and required the co-injection and pyrolysis of diethyl Cd and Y-tri-octylphosphine (TOP) into a tri-octylphosphine oxide (TOPO) coordinating solvent at 300°C [3]. These NC were then grown for 3-10 minutes but required size-selective precipitation to obtain the desired NC size. Further variations of this synthetic method were conducted by Bowen-Katari *et al.* and much later Talapin *et al.* who used diethyl Cd and Se-TBP into TOPO at 350°C and Se-TOP into hexadecylamine (HDA)/TOPO at 250-310°C respectively, which enhanced the size distributions [36, 37]. Trends have moved away from TOPO as a coordinating solvent and have used the non-coordinating solvent of octadecene (ODE). Using ODE has enabled a greater degree of control and flexibility over the reactivity of the precursors and precursor choice. Thus, a greater number of reactions can be conducted at lower growth temperatures [10]. As was reported by Peng and Peng [25], "$Cd(CH_3)_2$[Diethyl Cd] is extremely toxic, pyrolytic, expensive, unstable at room temperature and explosive at elevated temperatures by releasing large amounts of gas". Thus, methodologies were found to minimise the use of these highly volatile organometallic complexes. One of the first was to substitute diethyl Cd with Cd oxide (CdO). This involved dissolving CdO in hexylphosphinic acid (HPA)/tetradecylphosphonic acid (TDPA)/TOPO above 300°C

and the subsequent injection of Se-tributylphosphine (TBP) [38]. Further trends have aimed to limit the use of phosphines and amines within the reactions, with the hope of making all the precursors air stable and reduce the toxicity of the system. One of the trend setters was to dissolve elemental S in ODE and inject this precursor into CdO/oleic acid (OA)/ODE solution. This technique was shown to have equal, if not better, size distributions than the diethyl Cd counterparts and can be nucleated at 300°C [39] or 250°C [40] without a drop in quality. A further trend has been to find phosphine free ligand to dissolve Te and Se. The current state-of-the-art as this thesis is being written is to dissolve Se in ODE which is not used here. The combination of raising Se above its melting point (∼220°C) and the double bond within ODE enables Se to be dissolved in ODE. The combination of these two trends led to the synthesis of CdSe [41] and ZnSe [42], using CdO or Zn oxide (ZnO) dissolved within OA/ODE and the injection of Se-ODE, to be produced with only air-stable reagents. Green Te precursors is still the subject of much work.

Ligands play a large role within NC passivation. Several functional groups have been used including alkyl phosphines, alkyl phosphonic acid, fatty acids, amines and thiols. The fatty acid, OA has become somewhat the ligand of choice as it dissolves X-salts readily, is cheap and ambient stable, whilst under certain conditions it has been shown to provided better protection against oxidation and emission loss than octadecylamine (ODA) and stearic acid (SA) [43]. Although all these ligands have the same length (C_{18}), the oxidation protection is thought to be due to the interwoven amorphous structure which the tail of cis-unsaturated chains can provide. The saturated ligands provide more crystalline ligand structure and thus allow easier diffusion pathways to oxidation. Likewise branched phosphine ligands also provide more protection to the NC [43].

2.3.3 Synthesis of core-shell structures

The first published syntheses of a core-shell NC structures were conducted by Danek *et al.* [44] and Hines *et al.* [8] in which they encapsulated ZnSe and ZnS shelling layers around CdSe cores respectively, however CdSe/ZnSe did not yield particular good QY. The Hines method used a one pot synthesis procedure of Bowen-Katari *et al.* [36] to synthesise the CdSe cores and then subsequent aliquots of diethyl Zn/S-TOP solution were injected in the reaction solution at 300°C. The resulting NC saw a mild redshift in photoluminescence (PL) wavelength, the loss of trap site emission, a marked improvement in QY (50%) and increased photostability ("PL[...]can be seen for months" [8]). TEM and XPS showed that all the core NC had been encapsulated by ZnS. This marked improvement in optical performance heralded great excitement, not only in the NC community but also for subsequent exploitation for biological means [45]. From this paper a variety of techniques have been developed to produce core-shell structures.

2.3.3.1 Dropwise addition

The 'dropwise' technique typically combines the anion and cation precursors and requires slow addition, typically <1-2 mmol hr^{-1} [46]. Though this technique has shown high QY [47, 48], it has typically been applied to TOPO solvents with high temperatures. This can lead to the nucleation of shell precursors and poor epitaxial growth leading to changes in morphology, defects and drops in QY [49]. Specific control of the dropwise addition is typically controlled by syringe pump [50].

2.3.3.2 Successive Ion Layer Adsorption and Reaction (SILAR)

An evolution in growth methods was the introduction of the 'Successive Ion Layer Adsorption and Reaction' (SILAR) technique by Li *et al.* [51]. The principle can be schematically seen in figure 2.5, and adopts similar principles from 'atomic-layer-epitaxy' within MBE [52], which sees the separate injection and growth of the equivalent of a single monolayer[s] (ML) growth of the anion and cation precursors. This has the added advantage that the two precursors do not coexist in the same solution; therefore, the likelihood of separate nucleation of the shell precursors is negligible even at high temperature.

The advantage of this technique is that direct control of the size of the NC can be obtained and can be used to build 'giant' NC with up to 19 ML of shell. These structures have shown some good optical performance and will be discussed again in section 2.5.2.3 [53].

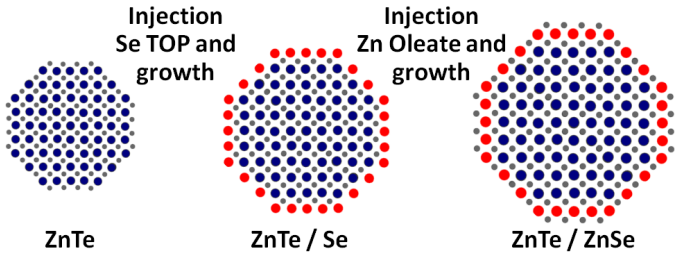

FIGURE 2.5: A schematic representation of the SILAR technique.

A further development of the SILAR technique was presented by Blackman *et al.* [54] in which a thermal cycling step (SILAR-TC) was incorporated within the shell synthesis to create CdSe/CdTe NC, an inverted type-II NC, where the reaction temperature is brought down below the critical growth temperature 190°C and then quickly raised above it 260°C.

Two things of note have come from this paper. Firstly the dramatic rise in QY from 30% to 60% from SILAR to SILAR-TC. Secondly, even though temperature and concentration are known to have a large effect on morphology, specifically at low temperature [55], it was reported that without thermal cycling, peanut-shaped NC were still produced irrespective of temperature and concentration. The injection of precursor below the critical growth condition was argued to allow homogeneous diffusion of the precursor throughout the solution, whilst for peanut NC, the initial injection of precursor could potentially produce a local high concentration of precursor which could preferentially bind to form peanut NC.

2.3.3.3 Single-source precursors

Single-source precursors (SSP) were initially developed for chemical vapour deposition to enable a precursor to have a common evaporation temperature. SSP utilise the fact that the desired molecules are already covalent bonded and are commonly air stable. The two most notable SSP shell synthetic methods have grown ZnS shells on CdS cores. Protière *et al.* grew a ZnS shell using Zn-ethylxanthate with Zn stearate in dioctylamine (DOA), into a solution of oleylamine (OLA) and ODE at 150-230°C [56] whilst Chen *et al.* uses Zn-diethyldithiocarbamate with SILAR-TC technique in ODA/ODE at 120-200°C [40]. This X-ethylxanthate method has been extended to CdS capping within CdSe/CdS and CdSe/CdS/ZnS [57] and is often used in conjunction with amines to help facilitate a low reaction temperature. Selenourea and diseleno-carbamato complexes have been developed for CdSe and ZnSe core-only NC [58, 59], but to the author's knowledge, have not been used for ZnSe nor CdSe for shelling.

2.3.4 Binary systems in literature

This section highlights some of the most notable type-I, type-II and strain heterojunction NC.

2.3.4.1 Type-I nanocrystals

Since the seminal work of Hines *et al.* [8] on CdSe/ZnS, a large amount of work has been conducted on type-I NC. All but a few of the material combinations that give a bulk type-I heterojunction have been produced. A review of the most notable precursors, procedures, optical range and performance for all the type-I NC configurations can be found in table 2.4. All of synthetic methods, with a few exceptions, have seen an improvement in the optical performance of the NC in terms of QY and optical stability. The majority of NC have seen the highest QY within 3 ML of growth and PL range which spans most of the visible spectrum through direct engineering of the core size. The NC show strong exciton absorption features and general redshift from the original core PL wavelength, this is often < 15 nm with a ZnS shell, which can be related to wavefunction leakage into the large bandgap shell [7, 8, 40, 42, 48, 60]. NC like CdSe/CdS show larger redshifts (< 80 nm) due to closer conduction band alignment allowing larger electron wavefunction leakage and reduced confinement [53, 61].

Like the core-only NC, there is a trend to greener techniques which forgo diethyl X compounds and minimise the use of phosphines. These have shown equal or improved optical performance [40, 53]. It is noteworthy to highlight drops in QY for NC with CdTe and ZnTe shells [62–64], which are notoriously oxygen sensitive and require good surface passivation or another physical barrier to prevent oxidation [9, 20, 65].

Interestingly, inverted type-I have not been actively pursued with the notable absence of ZnS/XY structure. The structures that have been produced are ZnSe/CdSe [66–68] and CdS/CdSe [69].

ZnSe/CdSe offers a highly luminescent structure with QY (80%) but also type-II behavior which can be explained by the relative bandgap alignment between the ZnSe/CdSe. Here the difference in valence bands is six times smaller than that of the relative conduction bands [67]. Thus the electron will de-localise away from the core with a smaller increase in shell thickness compared to the hole. Theoretical calculations show the electron localises to the shell after 1.1 nm of shell growth, whilst for the hole to localize to the shell requires a shell thickness 1.6 nm [67].

2.3.4.2 Type-II nanocrystals

Kim *et al.* gave the first demonstration of a type-II NC (CdTe/CdSe) and inverted type-II NC (CdSe/ZnTe) [62]. This seminal work has spurred rigorous investigations into many of the bulk type-II NC. A comprehensive description of synthetic routes to type-II NC and the emission ranges can be seen in table 2.5. All these papers show the defining optical features of type-II NC, in that an increase in shell thickness must be supported by:

- a large redshift in emission wavelength;
- a gradual reduction in the optical absorption features;
- a significant increase in fluorescence lifetimes.

As seen from figure 2.3, the intrinsically high valence band of X-Te, has seen CdTe and ZnTe as the core for many type-II structures [9, 20]. These structures with Cd-Y

Material	Bulk	Lattice Mismatch (%)	Core Synthesis Materials	Technique	Pre-Shell Preparation	Shell Precursors	Technique	Core PL (nm)	Type-I Redshift (nm)	QY (%)	Reference
CdS/CdSe	InType-I	4.3	CdO OA ODE S-ODE	HI	None	CdO-OA-ODE OLA Se-TOP	SILAR	380	280	5	[69]
CdS/ZnS	Type-I	7.6	$Cd(Ac)_2$ OLA TOP BTMPPA	HI	PreC TOPO OLA BTMPPA	$Zn(Et)_2$ $(TMS)_2S$ TOP	DW LA	450-475	∼10	20-30	[60]
			CdO OA ODE S-ODE	HI	In-situe PreC	$Zn(DDTC)_2$	SILAR-TC	375-475	∼10	50	[40]
CdSe/CdS	Type-I/ QType-II	4.5	$Cd(Et)_2$ Se-TBP TOPO	HI	PreC Pyridine	$Cd(Et)_2$ S-TBP	DW	520	<60	50	[61]
			CdO SA ODE ODA TOPO Se-TBP	HI	PreC ODA ODE	CdO-OA-ODE S-ODE	SILAR	585	<40	20-40	[51]
			CdO OA ODE ODA TOPO Se-TOP	HI	PreC DOA ODE	CdO-OA-ODe S-ODE	SILAR	550	<90	80	[53]
CdSe/ZnS	Type-I	12.4	$Cd(Et)_2$ Se-TBP TOPO	HI		$Zn(Et)_2$ $(TMS)_2S$ TOP	DW	530	∼5	50	[8]
			$Cd(Et)_2$ Se-TOP TOPO	HI	PreC TOPO	$Zn(Et)_2$ $(TMS)_2S$ TOP	DW	480-625	∼10	50	[7]
			CdO OA ODE Se-OA-ODE	HI	PreC ODE	ZnO OA ODE S-ODE	SILAR	491-595	N/A	30-60	[70]
CdSe/ZnSe	Type-I/ QType-II	7.2	$Cd(Et)_2$ Se-TOP TOPO TOP	HI	PreC	$Zn(Et)_2$ TOP Se-TOP	DW LA	580	∼ 2	0.4	[44]
			CdO TOPO HDA Se-TOP	HI	PreC HDA TOPO	$Zn(Str)_2$ Toluene Se-TOP	DW LA	∼565	<10	85	[66]
CdTe/ZnTe	Type-II	6.5	CdO Te-TOP HDA TDP ODE	HI	PreC OLA	$Zn(Et)_2$ S-TOP	SILAR	620	Type I 50	60	[20]
ZnS/X			No papers published								
ZnSe/CdTe	Type-I	12.5	No papers published								
ZnSe/ZnS	Type-I	4.8	ZnO LA HDA Se-TOP	HI	PreC LA HDA	ZnO-LA-HDA S-TOP	DW	400-440	∼15	32	[48]
			ZnO OA Paraffin Se-ODE	HI	PreC ODA ODE	ZnO-OA-ODE S-ODE	SILAR	390-450	<10	70	[42]
ZnTe/ZnS	Type-I	12.8	No papers published								

TABLE 2.4: The physical data, synthetic routes, PL redshift and QY for the most notable type-I structures.

Abbreviations can be found in section 0.2.

shells have tuned the effective bandgap over the full visible optical spectrum and into the N-IR with the largest redshifts coming from CdTe/CdSe and ZnTe/CdSe showing emission from 500 nm up to 1000 nm and 800 nm respectively [9, 20], which has great potential for biological tagging [71]. The most studied structure has been CdTe/CdSe which has been produced by various synthesis routes and shown a range of QY(4-82%) where the QY maximum were often in the quasi type-II regime [20, 62, 72, 73]. PL lifetimes typically see a transition from the standard core-only lifetime of ∼10 ns to in excess of 100 ns [73, 74]. As will be shown later, the PL lifetime for the largest shelled NC can be associated with a radiative lifetime of up to 1.5 μs in comparison to non-radiative recombination lifetime of 100 ns [74] and thus has the potential for larger charge extraction within photovoltaic devices [50, 75].

2.3.4.3 Strain tuned heterojunctions

As shown in table 2.3, CdTe offers the lowest bulk modulus and one of the highest volume deformation potentials out of the II-VI semiconductors, thus a shell material with a significant lattice mismatch enables the manipulation of the energy levels. Several core-shell structures were investigated with CdTe core diameters ranging between 1.8-6 nm and using the SILAR technique for shell growth [20]. CdTe/ZnSe is a good demonstration of this concept which shows a 14.4% lattice mismatch. In the bulk regime CdTe/ZnSe forms a type-I heterostructure however with a 1.8 nm core, the structure produces a type-II heterostructure as seen schematically in figure 2.6a. The emission could be tuned from 500 nm for a core structure to 900 nm with increasing shell thickness and showing the classic optical attributes of a type-II structure.

The emission range was shown to be at its most extensive (a range of 400 nm) with a core diameter of 1.8 nm (PL from the core only 480 nm to 6 ML 880 nm). Increasing

Material	Bulk	Lattice Mismatch (%)	Core Synthesis Materials	Technique	Pre-Shell Preparation	Shell Precursors	Technique	Core PL (nm)	Type-II PL range (nm)	QY (%)	Reference
CdS/CdTe	QType-II	10.2	CdO-OA-ODE S-ODE	HI	PreC HDA ODE	CdO-OA-ODE Te-TBP	SILAR-TC	430	700	10	[63]
CdS/ZnSe	InType-II	14.4	CdAc MA S-ODE ODE	HU	PreC ODA ODE	Zn(AcO)2 OA SeTOP	DW LA	426	520-620	45	[46]
CdS/ZnTe	InType-II	4.6	No papers published								
CdSe/CdTe	InType-II	7.1	$Cd(Et)_2$,$(TMS)_2S$, TOPO	HI	PreC TOPO	$Cd(Et)_2$, Te-TOP	DW	620	890	4	[62]
			NN Technology		PreC ODE	CdO, OA, ODE,SE-TBP	SILAR-TC	600	1000	60	[54]
CdSe/ZnTe	InType-II[a]	14	$Cd(Et)_2$ Te-TOP TOPO	HI	PreC TOPO	$Zn(Et)_2$ Te-Top	DW	670	900	3	[62]
CdTe/CdS	QType-II[a]	11.4	CdO Te-TOP HDA TDP ODE	HI	PreC OLA	$Cd(Et)_2$ S-TOP	SILAR	620	760	60	[20]
CdTe/CdSe	Type-II	7.1	$Cd(Et)_2$ Te-TOP TOPO	HI	PreC TOPO	$Cd(Et)_2$ $(TMS)_2Se$	DW	670	1000	4	[62]
			CdO Te-TOP HDA TDP ODE	HU	PreC TOPO HDA	Se-TBP $CdCl_2$-TBP	HU LA	690	1025	3.1	[76]
			CdO Te-TOP TDA HDA TDP ODE	HI	PreC OLA	$Cd(Et)_2$ Se-TOP	SILAR	620	1000	55	[20]
			$Cd(Me)_2$ DDA Te-TOP	HI	PreC TOPO HDA	CdAc-TOP Se-TOP	SILAR	535	789	82	[73]
CdTe/ZnS	Type-I	19.8	CdO Te-TOP HDA TDP ODE	HI	PreC OLA	$Zn(Et)_2$ S-TOP	SILAR	620	750	70	[20]
CdTe/ZnSe	Type-I	14.4	CdO Te-TOP HDA TDP ODE	HI	PreC OLA	$Zn(Et)_2$ Se-TOP	SILAR	620	980	55	[20]
ZnSe/CdS	Type-II	2.6	$Zn(Str)_2$ ODA Se-TOP	HI	PreC ODA ODE	CdO-OA-ODE S-ODE	SILAR	410	590	20	[77]
ZnSe/CdSe	InType-I	6.7	$Zn(Et)_2$ Se-TOP HDA TOP	HI	HDA	$Cd(Et)_2$ Se-TOP TOP	DW LA	320	Type II (480-520)	80	[78]
			$Zn(Et)_2$ Se-TOP ODA TOP	Hi	None ODE OLA	CdO-OA-ODE TOP Se-TOP-ODE	DW	375	Type-II 674	85	[68]
ZnSe/ZnTe	Type-II	7	No papers published								
ZnTe/CdS	Type-II	4.4	$Zn(Et)_2$, Te-TOP ODA ODE	HI	None	CdO OA ODE S-ODE	SILAR	NA	580-660	20-30	[9]
ZnTe/CdSe	Type-II	0.8	$Zn(Et)_2$, Te-TOP ODA ODE	HI	None	CdO OA ODE Se-TOP	SILAR	NA	550-800	20-30	[9]
ZnTe/CdTe	Type-II	6.2	$Zn(Et)_2$, Te-TOP ODA ODE	HI	None	CdO OA ODE Te-ODE	SILAR	NA	550-800	20-30	[9]
ZnTe/ZnSe	Type-II	7.6	$Zn(Et)_2$, Te-TOP ODA ODE	HI	PreC HDA ODE	$Zn(Et)_2$ Se-TOP	DW	NA	510-570	5	[50]

TABLE 2.5: The physical data, synthetic routes, PL range and QY for the known type-II structures.

[a] = same conduction band level in bulk
Abbreviations can be found in section 0.2.

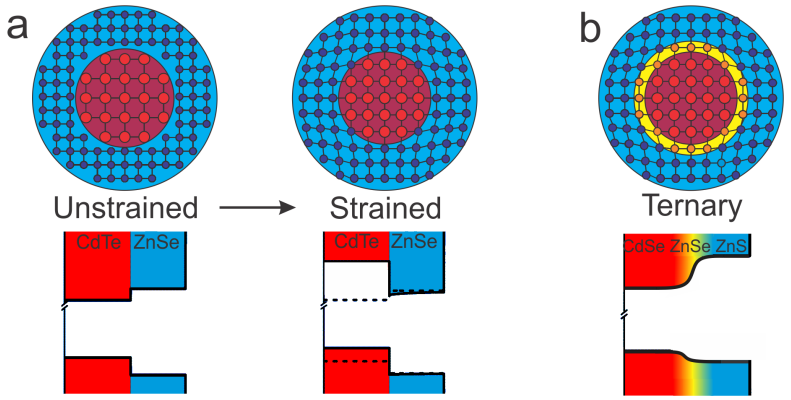

FIGURE 2.6: A schematic showing the crystal structure and bandgap alignments of a) an unstrained CdTe/ZnSe NC showing a type-I heterojunction and a strained CdTe/ZnSe NC with a compressed core showing a type-II heterojunction; b) a ternary CdSe/ZnSe/ZnS NC with a ZnSe intermediary layer mitigating strain.

the core size to 6.2 nm produced a PL range drop to only 30 nm, which shows type-I characteristics (PL range 620 nm to 650 nm). It was argued that for critically large cores full dislocations can take place which release the strain energy thus reducing the strain induced bandgap modification.

Similar strain effects and changes in heterostructures were also demonstrated for CdTe/CdS and CdTe/ZnS NC which have a large lattice mismatch of 11.4% and 19.8% respectively.

Strain induced bandgap manipulation was also demonstrated for CdTe/ZnTe which shows a bulk type-II alignment and type-II characteristics in the inverse ZnTe/CdTe NC structure [9]. Within CdTe/ZnTe NC however shows a type-I characteristic with only a redshift in PL of less than 50 nm [20].

This concept offers the possibility of engineering exciton dynamics further than previously thought and demonstrates that, though the bulk regime can offer a good starting point for engineering core-shell heterojunction configurations, ultimately more factors must be taken into consideration including bulk modulus and lattice mismatch.

2.3.5 Notable core-shell-shell structures

Core-shell-shell structures have had increasing esteem for their ability to mitigate large lattice mismatches between the core and outer shell. This has been used to great effect for CdSe/CdS/ZnS and CdSe/ZnSe/ZnS NC [79, 80]. Here, thin layers of CdS and ZnSe, which have intermediate lattice constants and bandgaps between the core and shell, act as strain mitigators, overcoming the large lattice mismatch. As seen schematically in figure 2.6b, this enables improved coherent epitaxial growth [81] and improved QY of up to 85% [79, 80].

Type-II-I structures have also been demonstrated for CdTe/CdSe/ZnS, CdTe/CdSe/CdS and the inverted CdSe/CdTe/ZnSe NC which show mild redshifts with the final shell but also sees improvement in NC stability and maintains the QY [65, 82, 83]. The type-II cascades of CdSe/CdTe/ZnTe NC has been produced where it was argued that effective bandgap was that of the CdSe/ZnTe transition. Though a low QY of 0.15% was observed, the radiative lifetime was deduced to be as high as 10 ms due to the particularly large spatial separation [64].

2.3.6 Notable alloyed structures

A growing number of synthetic techniques have been developed to produce alloyed structures, giving the ability to tune the effective bandgap over the whole visible spectrum into the N-IR with QY of up to 50-80% [84–89]. The electronic structure is engineered through direct control of the composition and growth dynamics with the resulting NC being categorised as either homogenously alloyed or graded alloyed.

Homogenously alloyed structures have been synthesised for CdZnSe [84], CdZnS [85], CdTeSe [86] and CdSeCdS [87] NC using two different procedures. Firstly, the NC can

be synthesised utilising the natural growth dynamics of the system in which the NC are grown in excess of the anion precursors [86, 87]. Swafford *et al.* argued the growth rates within this system follow first-order kinetics with respect to anion concentration [Y] and the available growth site concentration [AS] such that the relative growth rates could be described as [87]

$$\frac{\frac{d[\text{AS-S}]}{dt}}{\frac{d[\text{AS-Se}]}{dt}} = \frac{k_1[\text{AS}][\text{S}]}{k_2[\text{AS}][\text{Se}]} = \frac{k_1[\text{S}]}{k_2[\text{Se}]} \tag{2.7}$$

where k_1 and k_2 are the growth rate constants for S and Se respectively. For homogenous alloy growth to occur either k_1 and k_2 should be identical or the anion concentration should be almost constant throughout the growth. However, within the CdTeSe and CdSeS NC reported in references [86, 87], [AS] is kept low through a high anion:cation ratio. The result of a low [AS] essentially keeps the anion concentration [Y] constant within equation 2.7 and thus leads to homogenous growth. Secondly, homogenous alloying can been achieved through interatomic diffusion in which a pre-synthesised core-shell NC is annealed at high temperatures. A homogenous alloy can be made within 15/30 minutes at 310/270°C for CdZnSe and CdZnS NC respectively [84, 85] and could be argued to occur at a lower rate at temperatures as low as 190°C within CdZnSe NC [88].

Graded alloyed structures have been made for CdZnSe [84, 88], CdTeSe [86] and CdZnSeS [89] using either seeded growth or utilising the natural growth dynamics within the system.

Seeded growth has been most notably applied to CdZnSe NC where an initial CdSe or ZnSe NC is synthesised and subsequent precursors are added during the growth phase [84, 88]. This techniques has been used to great effect to produce QY as high as 50-70% and can produce 'non-blinking' NC as will be discussed in section 2.5.2 [84, 88].

The reactivity of the precursors can also be used to synthesis a graded NC. Firstly, it was shown within CdTeSe NC that the addition of excess cation increases the [AS] concentration which accentuates the relative growth rates as described in equation 2.7 [86, 87]. Secondly, it was shown by Protière *et al.* that the reactivity of the cation can be used to grade the structure [84]. In which the Zn precursor has a lower reactivity when compared to Cd precursors with the same ligand. This is due to the stronger affinity of the hard Zn^{2+} Lewis acid to the hard Lewis base of the ligand when compared to the softer Cd^{2+} Lewis acid [84]. Thus, the natural reactivity of the precursors will lead to a Cd rich core and Zn rich shell. Using both these growth dynamics has enabled a graded CdZnSeS alloy NC to be synthesised which will be used in chapter 6.

2.3.7 Anisotropic growth: From nanodot to nanorods and tetrapod formation

Whilst in most cases classical diffusion-based growth theory is used to produce spherical NC, this growth mechanism does not take into account the effects such as facet energetics, strain or the steric hinderance of ligands which can alter growth dynamics. The stability and diffusion of these ligands on the NC are dependent on temperature. It must be considered that these ligands not only bind to the surface of the NC but also form complexes with the monomer species. In general, it is accepted that heating disassociates the ligands and assists diffusion based growth, however this may not be at the same point at which the precursor activates. Whilst there is a general methodology towards diffusion based growth, there are intricacies which still need to be explained. One of the most understood mechanisms of anisotropic growth is when the growth rate goes beyond the size-focusing regime. A variety of highly anisotropic shapes are obtained, starting with simple rods and disks, but ultimately including shapes like arrows and tetrapods [90]. The growth mechanism to these particles is kinetically driven and utilises the energetic properties of specific facets and the affinities of the ligand to these facets. Thus, in the presence of high monomer concentration, low ligand affinity facets will preferentially grow [54, 91].

Another mechanism towards anisotropic growth is using a seeded growth mechanism which utilises planer defects at specific facets. Whilst these are typically stress relieving in large lattice mismatched systems [92], these can also be found in lattice-matched systems [93]. The tetrapod structures can also be formed by naturally occurring or pre-synthesised zinc blende cores which then have wurtzite stacking faults [94, 95].

This utilises the polytypic nature of II-VI semiconductors and describes the coexistence

of two crystal phases for the same specific energy. This is especially found in tetrahedrally bound materials in which the crystals structure tends from zinc blende→wurtzite→rock salt [18]. The energy between zinc blende and wurtzite phases is known to be small and are on the order of $\sim$ meV atom^{-1} [96]. Thus with the right reaction conditions specific zinc blende or wurtzite structures can be synthesised [43, 97]. The tetrapods described above typical use a planar stacking fault to initialise arm growth which comes about due to the similarity of a {111} zinc blende facets and the (001) wurtzite facet. This stacking fault acts a preferential growth facet and can initialise either further wurtzite growth or zinc blende growth [5, 94, 95].

2.4 Optical properties of nanocrystals

This section sets out to demonstrate the principles behind the optical properties of NC. It introduces the principles of quantum confinement in the type-I and type-II regimes and then further shows the importance of understanding the exciton dynamics within NC, specifically in terms of Auger recombination and blinking.

2.4.1 Quantum confinement

Spatially confining an electron, hole or exciton within a structure leads to quantum confinement effect which modifies the NC energy levels and optical transitions. In the simplest approximation quantum confinement can be described by a particle-in-a-box problem, as seen in figure 2.7, which describes a particle in an infinite potential well where the potential $U(a)$ is defined as

$$U(a) = \begin{cases} 0 & \text{for } |x| \leq a/2 \\ \infty & \text{for } |x| > a/2 \end{cases} \tag{2.8}$$

By solving the time independent Schrödinger equation

$$-\frac{\hbar^2}{2m}\nabla^2\psi(r) + U(x)\psi(r) = E\psi(r) \tag{2.9}$$

with the following wavefunctions

$$\psi(x)^{(-)} = \sqrt{\frac{2}{a}}\cos\left(\frac{\sqrt{2mE_n}}{\hbar}x\right) \quad \text{for odd n (1,3,5...)} \tag{2.10}$$

$$\psi(x)^{(+)} = \sqrt{\frac{2}{a}}\sin\left(\frac{\sqrt{2mE_n}}{\hbar}x\right) \quad \text{for even n (2,4,6...)} \tag{2.11}$$

where m is the particle mass, $\hbar$ is the reduced Plank's constant and E_n is the energy of the particle. By implementing the boundary conditions $\psi(x) = 0$ for $|x| = a/2$, it can be shown that eigenstates can described as [98]

$$E_n = \frac{\pi^2\hbar^2}{2ma^2}n^2 \quad \text{for n=1,2,3...} \tag{2.12}$$

Whilst it can be seen that the energy levels will rise with increasing confinement, semi-

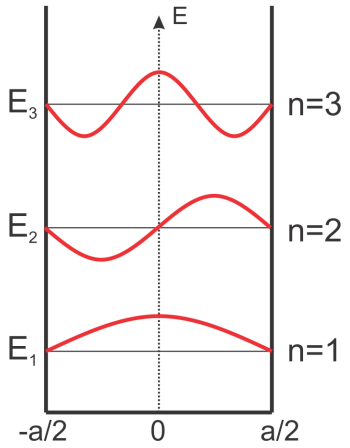

FIGURE 2.7: A schematic showing the first three allowed eigenstates and the associated energies for a particle in an infinite potential well.

conductors have a valence and conduction band which can both be quantum confined. The energy needed to excite an electron from the ground valence band energy level to the first excited conduction band energy level, more generally known as the bandgap energy E_g, can be approximated within the weak confinement regime to

$$E_g = E_g^{bulk} + \frac{\hbar^2\pi^2}{2a^2}\left(\frac{1}{m_e^*} + \frac{1}{m_h^*}\right) - Ry^* \tag{2.13}$$

where E_g^{bulk} describes the bulk bandgap energy of the material, a is the NC radius, m_e^* and m_h^* are the effective masses of the electron and hole respectively in the material and Ry^* is the Rydberg energy which describes the exciton binding energy [98].

The weak confinement regime can be defined when the spatial confinement becomes comparable to the exciton Bohr radius $a_{B_{ex}}$. Where the Bohr radius a_B is defined as [99]

$$a_B = \epsilon \frac{m}{m^*} a_0 \tag{2.14}$$

where ϵ is the dielectric constant of the material, m^* is the effective mass of the particle, m is the rest mass of the particle and a_0 is the bohr radius of a hydrogen atom. In this case, the Ry^* term still dominates over the confinement effects in equation 2.13. However, when $a \ll a_{B_{ex}}$ the spatial confinement (middle term equation 2.13) dominates the Ry^* term and leads to larger shifts in E_g and defines the 'strong confinement regime'. The spatial confinement also influences the density of states ($\rho(E)$), which moves from

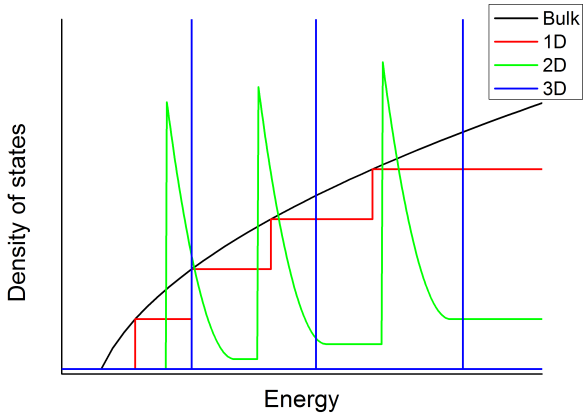

FIGURE 2.8: A schematic showing the density of states for a bulk (Black), 1-D (Red), 2-D (Green) and 3-D (Blue) quantum confined object.

a continuum of allowed energies which follows $\rho(E) \propto E^{1/2}$, to a more discrete density of states with 1,2 and 3-D degrees of confinement (Figure 2.8). 3-D confinement gives discrete density of states which are almost δ-functions, such that their transitions behave akin to "artificial atoms". These discrete states can most notably be seen in the absorption patterns. This can particularly be seen in CdSe NC in which the ensemble size distributions can be below 5% and thus give the ability observe and identify discrete

transitions. The early theoretical work of Ekimov *et al.* [100] identified the bandedge transition to be the $1S_{1/2}^{(e)}1S_{3/2}^{(h)}$ transition and also identified higher-energy transitions as seen in figure 2.9 [101]. The labeling of these transition will be discussed further in chapter 3.6.

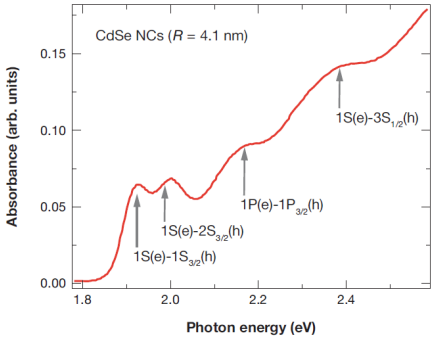

FIGURE 2.9: The absorption spectrum of a 4.1 nm diameter CdSe NC with the indexed exciton transitions. Reproduced with permission from reference [101].

2.4.2 Extension in to the type-II regime

By considering the particle-in-a-box analogy, a type-II system can be described by a perturbation of the potential and defining the core region $0 - a_c$ and shell region $a_c - a_s$ and the potential well as

$$U(a) = \begin{cases} 0 & \text{for } 0 < a \leq a_c \\ U_s(a) & \text{for } a_c < a \leq a_s \\ \infty & \text{for } a_s < a \end{cases} \tag{2.15}$$

a full treatment can be found in reference [46]. By considering a continuous transition of the wavefunction at the interface of the two regions it can be shown that the energy level will increase or decrease dependent on whether $U_s(a)$ is positive or negative. Within a type-II regime, as described in figure 2.10, it can be seen that the conduction band

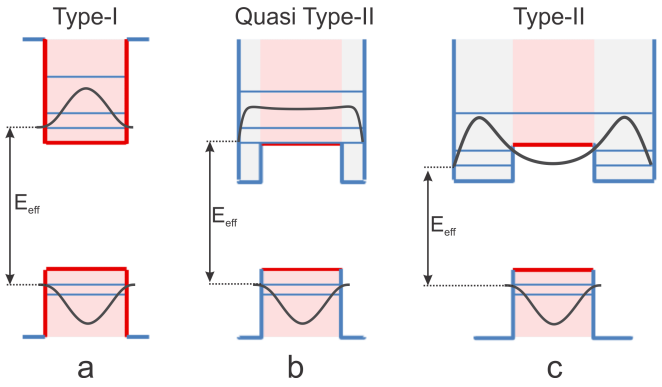

FIGURE 2.10: A schematic showing the energy potential and energy levels within the core (Red) and shell (Blue) for a a) type-I b) quasi type-II and c) type-II NC. Also shown is the effective bandgap energy (E_{eff}) and spatial probability wavefunctions of the electron and hole highlighting the decrease in wavefunction overlap.

energy level decreases with increasing shell thickness, which in turn reduces the effective bandgap energy (E_{eff}).

The increasing type-II nature of the band potential leads to a larger spatial separation between the electron and hole, and a noticeable reduction in the oscillator strength or wavefunction overlap, Θ^2, between the two charge carriers described as

$$\Theta^2 = |\langle \psi_e | \psi_h \rangle|^2 \tag{2.16}$$

where $\psi_{e,h}$ are the electron and hole wavefunctions respectively.

Figure 2.10 shows a schematic representation of the wavefunction overlap within the type-I, quasi type-II and type-II regimes. Where it can be seen that for the type-I regime both the electron and hole wavefunctions are localised to the core which gives near-unity Θ^2. In contrast, the type-II regime electron wavefunction is predominately in the shell and the hole is still localised within the core. A third regime can also be defined; the quasi type-II regime, where one wavefunction is spatial localised (in this case the hole in the core) whilst the other (electron) is localised over the whole NC. Rather surprisingly, the definition for the onset of the type-II region used by many within the

theoretical field [102, 103] uses an energy level argument rather than oscillator strength or peak wavefunction localisation argument [102, 103]. For the example seen in figure 2.10, the type-II region is defined by the point at which the conduction energy level goes below the core conduction band potential. The associated oscillator strength using this definition, can range from 0.5-0.7 [102, 103]. Thus, the quasi type-II is defined by an oscillator strength between unity and the type-II onset.

This decrease wavefunction overlap has noticeable effect on the radiative lifetime, τ_r, as

$$\frac{1}{\tau_r} \propto |\langle \psi_e | V | \psi_h \rangle|^2 \tag{2.17}$$

where $V = e.r$ defines the transition dipole moment. As was described previously, experimental observation of the PL lifetime with increasing shell thickness, shows an increase from 5-20 ns [102] for a core only structure to PL lifetimes in excess of 100 ns with large shell thicknesses [74]. In the simplest case, the PL lifetime, τ, has a radiative lifetime, τ_r, component and a competing non-radiative lifetime τ_{nr} component as below

$$\frac{1}{\tau} = \frac{1}{\tau_r} + \frac{1}{\tau_{nr}} \tag{2.18}$$

which also helps describe QY as

$$\text{QY} = \frac{\tau}{\tau_r} \tag{2.19}$$

Using these equations reports have shown the radiative lifetimes to be as high as 1500 ns [74]. Thus, to maximise the radiative component the system needs to increase the non-radiative lifetime.

2.5 The importance of understanding exciton dynamics

The inherently efficient emissive properties of NC has sparked much research interest due to their potential application as low-threshold lasers [104], biological tags [45] and light emitting diodes (LED) [105], which takes advantage of the size-selective nature of the bandgap, high QY and flexibility for application. One of the major obstacles hindering application is fluorescence intermittency, known as 'blinking' [106, 107], and excessive charging, which quenches PL within LEDs [108] and reduces the optical gain lifetimes [104]. The main mechanism common to all these problems is Auger recombination.

This section initially focuses on the principles of Auger recombination and the theory behind 'blinking'. The section then focuses on state-of-the-art structures and how these structures overcome the hinderance of ultra-fast Auger recombination.

2.5.1 Auger recombination

The ability to excite two excitons to the excited state in one NC has sparked much interest, specifically within the photovoltaics and optical gain fields. Unlike the simple radiative recombination observed which occurs in the single exciton regime, multi-exciton recombination is predominantly governed by the ultra-fast 'Auger recombination' lifetime [101]. Auger recombination requires an exciton in the presence of at least one other charge carrier. These three charge carrier are collectively known as a 'trion'. Here upon the recombination of the exciton, the energy is transferred to the third charge carrier. Depending on the energy of the exciton, the extra charge carrier is either expelled from the NC/placed in a trap state (Auger ionisation) or is excited up the potential well and

then relaxes back down to the band edge through phonon interactions (Auger recombination). This extra charge carrier can act as a further catalyst for further non-radiative recombination until neutralisation of the extra charge carrier which is notoriously slow.

Investigations have shown the Auger recombination lifetime to scale with volume within a type-I NC [102]. It was proposed within the photovoltaic field that by making anisotropic structures, the spatial volume for the charge carrier to exist could be increased whilst keeping the desired quantum confinement effects therefore increasing charge extraction [109]. However as will be discussed later the phenomenon of 'blinking' still persisted [110]. The biggest hinderance of Auger recombination is within optical gain or lasing which requires a bi-exciton for a type-I NC [111]. The Auger recombination competes with radiative recombination and thus increases the optical gain threshold close to the stability limit of type-I NC [104, 112, 113]. It is worth noting that type-II structure NC have recently been able to achieve optical gain within the single exciton due to the positive binding energy and can forgo the Auger recombination, highlighting a potential application of type-II NC [111, 114].

2.5.2 Blinking

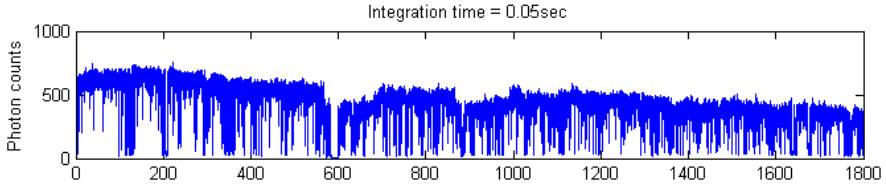

FIGURE 2.11: An example of an intensity-time trajectory for a single NC showing distinct 'on' and 'off' periods known as 'blinking'.

From the pioneering single NC spectroscopy (SNS) studies of Nirmal *et al.* [106], characteristic fluorescence intermittency known as 'blinking' has been observed within NC which described distinct 'on' and 'off' periods in emission (Figure 2.11). The 'on' state

is principally described by the radiative recombination of photoexcited exciton or photoluminescence (PL), and the 'off' state is described by a non-radiative recombination process. It has been shown that these 'on' and 'off' states show a probability duration that follows a power law distribution spanning decades of time (ns-10 s) independent of material and architecture [107, 115].

$$P(\tau) \propto \tau^{-\alpha} \tag{2.20}$$

This 'universal' blinking intermittency was shown to have power law exponent, (α), within a range of between 1.2-1.8 which has been shown to be remarkably insensitive to power and temperature [107, 116], whilst the 'on' exponent varies considerable more than this [117]. Several models can account for a power law probability distribution, a comprehensive review of these models can be found in references [110, 118, 119].

The underlying mechanism that initiates the 'off' state is still in question but many of the initial models predict either a diffusion, tunneling, thermal, or Auger auto-ionisation process that places a charge carrier in to a external trap site leaving a charge carrier in the core. This extra charge carrier enables the non-radiative recombination via a process of Auger recombination to take place. This was supported through observations by Kraus *et al.* who saw photoinduced charging of the NC using electrostatic force microscopy [120]. This technique showed that the NC could hold 1 or 2 extra charge carriers and SNS of the same particles also found evidence that the transition from the 'off' state corresponds to the charging of the NC and subsequent neutralisation. Whilst these initial investigations went some way to describe the mechanism for blinking, the following sections describe the development of non-blinking NC which have given rise to the current understanding of the processes behind blinking. These studies have

developed rapidly in the last two years and give direct experimental evidence for three types of blinking within a NC.

2.5.2.1 Alloyed interfaces

Wang *et al.* were the first to identify that alloying the core-shell interface improved the non-blinking properties of NC [88]. In this pioneering work, CdZnSe/ZnSe NC were produced and it was found that out of the 120 NC observed, 118 showed non-blinking characteristics. An interesting feature of the PL was that the majority showed three-peak emission (Figure 2.12a). The difference in adjacent peak positions were found to be ∼160 meV and were argued not to be due to thermal contributions (∼13 meV). It was proposed, along side theoretical calculations, that the observation could be described by partial radiative recombination of the exciton and the excitation of a hole to a higher energy level (Figure 2.12b). It was theoretically demonstrated in a follow up paper by Cragg *et al.* that Auger recombination requires well defined wavefunctions which an abrupt interface provides [121]. Alloying the interface mitigates this criterion and thus theoretical predictions placed the trion recombination lifetime to be 8-10 ns in close agreement with that observed in fluorescence lifetime observed in experiment (5-10 ns) highlighting that Auger recombination is still the rate limiting step in NC [88, 121]. Whilst there was a high QY of 50% in these non-blinking NC, it is interesting to note that in comparison to the previously best CdSe/ZnSe NC, this is a significant reduction (85-90%) [66, 79].

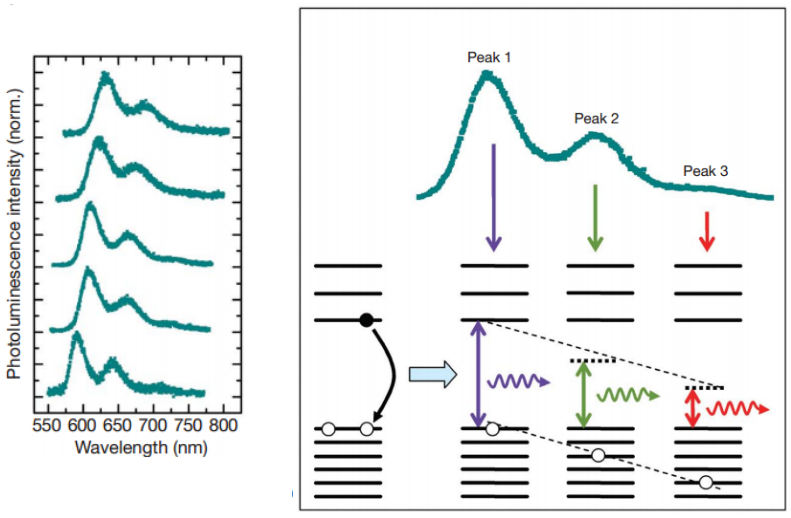

(A) (B)

FIGURE 2.12: a) PL spectra of several alloyed CdZnSe/ZnSe NC showing three-peak emission. b) The proposed scheme for the three-peak PL following a partial radiative contribution and occupancy of the hole in higher energy state. The dotted lines represent the total recombination energy of the exciton. Reprinted with permission from Macmillan Publishers Ltd: Nature, 459, 686, copyright (2009) [88].

2.5.2.2 Type-II structures

A letter by Kloper *et al.* showed the first non-blinking characteristics of CdTe/CdSe which showed 88% QY in the quasi type-II regime [122]. Alongside this remarkable feat, there was the observation of increased Stokes shifts and the observation of bi-, tri- and tetra-exciton emission at 4K [122]. An inspection of multi-exciton dynamics conducted by Oron *et al.* [114] showed that the bi-exciton Auger lifetimes did not scale with volume, as seen in type-I systems, but rather scaled much faster. It was shown that the Auger lifetime scaled with both volume and the exciton PL lifetime, thus, highlighting the importance of wavefunction overlap as well as volume in the Auger recombination lifetime. The increased Auger recombination lifetime makes type-II NC a potential candidate for non-blinking NC.

2.5.2.3 'Giant' nanocrystals

A large amount of research has been conducted on large shelled CdSe/CdS structures since the initial observation by Mahler *et al.* [123], that CdSe with a shell up to 8 ML CdS markedly suppressed blinking. Mahler *et al.* reported that over 95% of the NC investigated showed no distinct 'off' states over the observed time scale, this was in contrast to CdSe/ZnS NC in which 75% showed distinct 'off' states in the same study. It was proposed that the 4% lattice mismatch could enable good epitaxial growth to be realised mitigating the potential for defects, thus, by increasing the shell thickness the potential of charge migrating to the surface could be suppressed and thus inhibit charging of the NC core. Further 'giant' NC, up to 19 ML, were developed and investigated by Klimov group in Los Almos, which saw even better non-blinking performance albeit with a lower but still respectable QY of 40% which is in contrast NC with smaller shells which have a higher 80-90% QY [53, 124].

Whilst full non-blinking NC were observed for large shells, Spinicelli *et al.* [125] were the first to show that moderately large shells (∼10 ML) showed two radiative 'on' states; one much brighter 'bright' state and a lower intensity 'grey' state. This 'grey' state was explained by the trion Auger recombination rate being comparable with the radiative lifetime of the trion thus rendering the trion optically active with a trion radiative QY of 19% [125]. In subsequent papers, García-Santamaría *et al.* saw a marked increase in the Auger bi-exciton lifetime up to ∼10 ns [126]. This is in comparison with a standard CdSe/ZnS NC which shows a bi-exciton lifetime of 200 ps [126] and is comparable to the bi-exciton Auger recombination lifetime thus shows the Auger lifetime to be the rate-limiting step. Using several approximations the bi-exciton Auger recombination lifetime was shown to be 210 ns which is three orders of magnitude longer than in CdSe/ZnS

[126]. The increase in Auger recombination lifetime was utilised to observe emission from multiple higher-order excitons with large excitation intensities [126]. It was theoretically shown that these emission peaks could only be seen if the NC was holding 9-13 excitons in the system thus indicating not only the bi-exciton Auger lifetime increased but higher-order Auger recombination lifetimes increased too. Going to 16 ML of CdS saw the complete suppression of trion Auger recombination and almost unity bi-exciton QY [127, 128]. This highlights that multi-excitonic emission is not just observable, but efficient in these systems. An investigation into the scaling of the Auger recombination lifetimes saw a larger than volume scaling [129]. Whilst initially this could be initial thought to be due to the reduction in wavefunction overlap, due to the ever-increasing quasi type-II nature of the NC, (as seen in type-II NC [114]), it was however theoretically predicted and observed that the greater volume scaling could only be explained by the interdiffusion of the cation and the subsequent alloying of the interface. This alloying was identified at relatively mild temperatures (240°C) and within 0.5 nm of the shell interface [129].

The highlight of this work, in terms of blinking, was shown in the extremely recent papers of Galland *et al.* [130, 131] in which SNS was conducted using moderately blinking quasi-giant NC within an electrochemical cell. This electrochemical cell allowed direct control over the Fermi energy enabling recombination centres to be activated or quenched, or allowing charge injection thus actively charging the core. This enabled the first experimental identification and manipulation of three blinking processes.

2.5.2.4 Three types of blinking

The experimental identification of three types of blinking gives the most up-to-date theory of blinking as this thesis is being written which can be summarised in figure 2.13

and by [130, 131]:

1. Type-A blinking refers to a charging of the NC in such away that a non-radiative trion is formed. This gives an intensity-time trajectory that has distinct 'on' and 'off' states which have individual lifetimes respectively; one for the radiative recombination ('on' state) and the unlikely trion radiative recombination (perceived as an 'off' state). The intensity-time and lifetime-time trajectories give a characteristic fluorescence lifetime-intensity distribution (FLID) from a high-intensity high-lifetime single exciton radiative recombination mode to a low-intensity low-lifetime mode (Figure 2.14a).

2. Type-B blinking sees the activation of a recombination centre which the excited electron preferentially decays down. This non-radiative recombination centre can be activated or quenched by specific engineering of the Fermi energy. When activated, the NC shows an 'off' state but the lifetime in this region still shows single exciton lifetime highlighting the very small probability of an exciton going down the radiative channel. This gives a characteristic FLID from a high-intensity high-lifetime single exciton radiative recombination mode to a low-intensity high-lifetime mode (Figure 2.14b).

3. Type-C blinking describes the most recently discovered 'grey' state which shows an optically active trion. This process closely resembles type-A blinking, however trion emission is a prominent process in the recombination dynamics. The intensity of this trion emission is related to the relative trion Auger recombination lifetime to the radiative lifetime of the trion. A less bright 'grey' state is observed when the non-radiative route still partakes in the recombination process. If the Auger recombination lifetime becomes much larger than the radiative lifetime, the trion

QY increases to such a degree that it is indistinguishable in an intensity-time trajectory to single exciton PL. However, this route can still be observed by a reduction in the lifetime. This gives a characteristic FLID from a high-intensity high-lifetime single exciton radiative recombination mode to a mildly high-intensity mildly high-lifetime mode (Figure 2.14c).

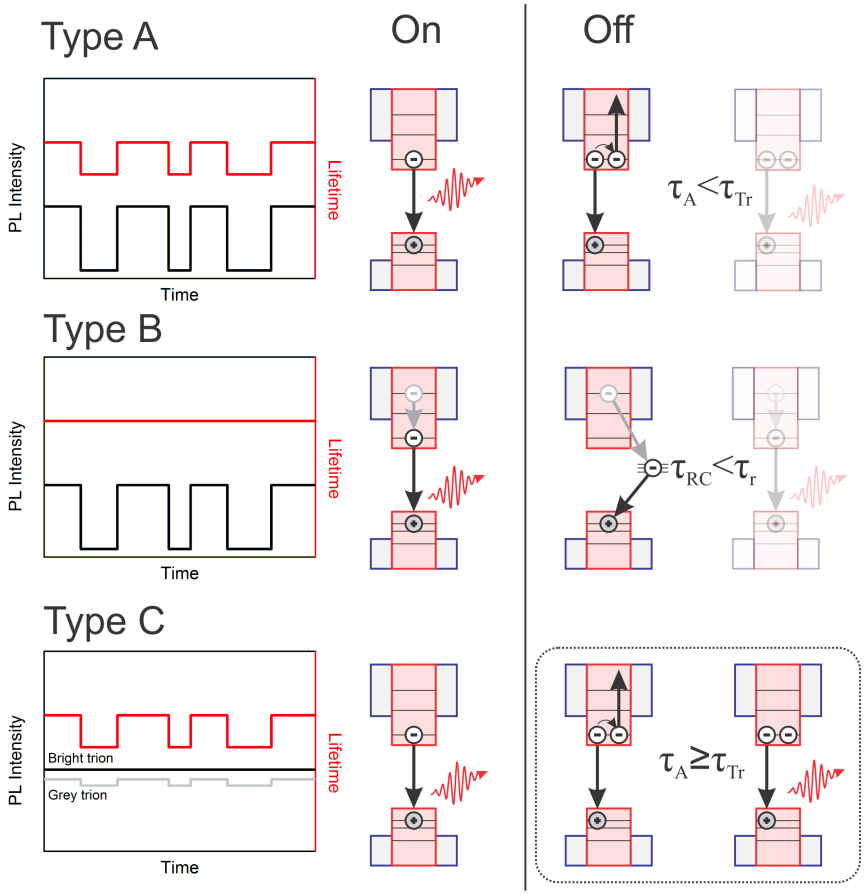

FIGURE 2.13: A schematic showing the intensity-time trajectory (Black) and lifetime-time trajectory (Red) for a NC blinking in the type-A, -B and -C blinking regimes. The associated mechanism for the 'on' and 'off' state is given next to the blinking trajectory. All types of blinking show PL as the mechanism for the 'on' state. Type-A blinking describes the non-radiative recombination of the exciton through ultrafast Auger recombination. Type-B blinking describes a fast recombination centre which makes the exciton bypasses the radiative route. Type-C blinking shows a combination of radiative trion recombination and non-radiative recombination via an Auger mechanism. These have comparable lifetimes and thus give a bright 'dark' state.

In summary blinking events occur due to either the ionisation of the core and the subsequent Auger recombination, or the activation of recombination centre which enables the exciton to recombine by bypassing the normal recombination channels. Though

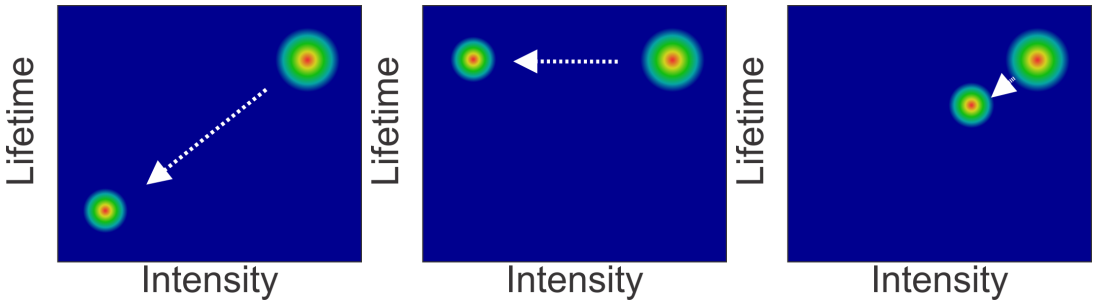

(A) (B) (C)

FIGURE 2.14: A schematic fluorescence lifetime-intensity distribution (FLID) obtained from the intensity-time and lifetime-time trajectories showing the change from a radiative 'on' state mode to the a) type-A, b) type-B and c) type-C blinking mode.

Auger ionisation and charging of the core still happens, the effect on blinking can be mitigated by increasing the Auger recombination lifetime which makes the charged NC optically active. This can be achieved either through direct control through composition (alloying) or heterojunction design (towards type-II NC). Recombination centres can be quenched through defect-free epitaxial growth and good surface passivation.

Chapter 3

The theory and development of techniques used to investigate strain within the physical and optical properties of nanocrystals

Driven by the potential observation of strain within ZnTe/ZnSe NC which will be described in the chapter 5, this chapter seeks to present an introduction to the theoretical and experimental techniques that will be used to investigate the influences of strain within physical and optical properties of a core-shell NC. Building on the continuum elasticity theory of Balasubramanian *et al.* [15], this chapter present the influences of strain within the core-shell system and utilises this theory to build a strained atomistic model of the core-shell NC which will be used to simulate high resolution TEM (HRTEM) and XRD data. Further application of the continuum elasticity theory can be applied to critical radius calculations to determine the onset of dislocation formation

and further applied to effective mass modeling to model the exciton energy within the NC. Thus, this chapter is split into six sections

1. The description of strain with in a core-shell geometry using continuum elasticity theory.
2. The development of the elastically strained core-shell atomistic model.
3. An introduction to HRTEM image simulation.
4. An introduction to XRD pattern simulation.
5. An introduction to the determination of the critical radius within core-shell NC.
6. The development of (2-6)-band effective mass calculations used to model the exciton energies.

3.1 Continuum elasticity model

This section presents the continuum elasticity theory which will be used for modeling strain within all strain simulations but must notably applied within in the (2-6)-band effective mass approximation, HRTEM simulations, XRD simulations and critical radius calculations.

In describing the model, a definition of the core and shell regions is required. As depicted in figure 3.1 the model describes a NC with a core radius a and shell thickness a_s. It must be noted that this model assumes the outer surface to be traction free and that the core is always being compressed. It must also be noted that this model is based on continuum mechanics rather than on discrete particles and therefore the theory is

expected to be less accurate in the vicinity of material interface or for very thin shell layers where comprehensive atomistic models may be required.

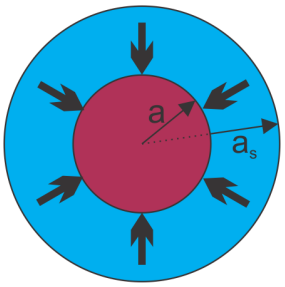

FIGURE 3.1: A schematic defining the core radius a and shell thickness a_s used for the continuum elasticity model.

By assuming the shell encompasses the whole of the core, the stress associated with the lattice mismatch and the accommodation of a smaller lattice constant around the core applies a homogenous hydrostatic pressure, p, on the core. Thus, it can be shown that stress components within the core can be related to the hydrostatic pressure by [15]

$$\sigma_{rr} = \sigma_{\theta\theta} = \sigma_{\phi\phi} = -p \tag{3.1}$$

Using Hooke's law in a spherical coordinate system, stress can be related to strain in elastic as [132]

$$\epsilon_{rr} = \frac{1}{E}(\sigma_{rr} - 2\nu\sigma_{\theta\theta}) \tag{3.2}$$

$$\epsilon_{\theta\theta} = \frac{1}{E}((1-\nu)\sigma_{\theta\theta} - \nu\sigma_{rr}) \tag{3.3}$$

and thus the strain in the core can be written as

$$\epsilon_{rr} = \epsilon_{\theta\theta} = \epsilon_{\phi\phi} = \frac{p}{E_c}(2\nu_c - 1) \tag{3.4}$$

where p in the context of core-shell NC is the interface pressure and defined as

$$p = \frac{\frac{2E_s}{3(1-\nu_s)}\epsilon(1-c)}{1-\frac{2m}{3}(1-c)} \tag{3.5}$$

where $\nu_{c(s)}$ is the poisson ratio of the core(shell), $c = a^3/(a+a_s)^3$ is the volume fraction of the core, K_c is the bulk modulus of the core, μ_s is the shear modulus of the shell, m is the elastic mismatch parameter and ϵ is the constrained strain. The last two quantities are given by [15]

$$m = \frac{E_s}{1-\nu_s}\left(\frac{1-2\nu_s}{E_s} - \frac{1-\nu_c}{E_c}\right), \quad \epsilon = \frac{3K_c(a_{0c}-a_{0s})}{a_{0s}(3K_c+4\mu_s)}. \tag{3.6}$$

where $a_{0c(s)}$ is the equilibrium lattice constant of the core (shell). In the shell it has been shown that the stress can be given by [15]

$$\sigma_{rr} = \frac{cp}{(1-c)}\left(1-\left(\frac{a+a_s}{r}\right)^3\right) \tag{3.7}$$

$$\sigma_{\theta\theta} = \sigma_{\phi\phi} = \frac{cp}{(1-c)}\left(1+\frac{1}{2}\left(\frac{a+a_s}{r}\right)^3\right). \tag{3.8}$$

and thus using equation 3.2, the stress and can be related to strain by

$$\epsilon_{rr} = \frac{cp_i}{E_s(1-c)}\left((1-2\nu_s)-(1+\nu_s)\left(\frac{a+a_s}{r}\right)^3\right) \tag{3.9}$$

$$\epsilon_{\theta\theta} = \frac{cp_i}{E_s(1-c)}\left((1-2\nu_s)+\frac{3}{2}(1-\nu_s)\left(\frac{a+a_s}{r}\right)^3\right). \tag{3.10}$$

The diagonal elements (ϵ_{ii}) of the strain ϵ tensor can be related to the lattice constant (a_{ii}) as

$$a_{ii} = (1+\epsilon_{ii})a_{0_{c(s)}} \tag{3.11}$$

3.1.1 Application of the continuum elasticity model

Using the continuum elasticity theory several factors can be accounted for including; the pressure on the core, the radial and tangential strain components for the core and shell, and, the radial and tangential lattice constants in the core and shell. Figure 3.2 shows these for the case of ZnTe/ZnSe NC. A close inspection of figure 3.2b and 3.2c sees that the core strain and core lattice constant are dependent on shell thickness. The magnitude of strain and compression of the lattice constant saturates after roughly 5 ML of shell growth and is almost independent of core diameter. This strain saturates at -0.013 which shows a compression of the core lattice constant from 6.10 Å to 6.02 Å and relates to an interface pressure of almost 2.2 GPa (Figure 3.2a). Figure 3.2d shows the strain in the shell to be almost 4 times of that of the core (-0.04) and sees both large radial compression and tangential tensile strain at the core-shell interface. Figure 3.2e shows that the resulting lattice constant in the shell varies from 5.4 Å and 5.85 Å at the core-shell interface for the radial and tangential lattice constants respectively and returns to the bulk lattice constant of 5.67 Å at surface of the NC.

It is noteworthy to compare this pressure on the core to the phase change threshold of CdSe which is between 2.13-2.9 GPa [18, 133], however in the case of bulk ZnTe this is much higher 7-9.5 GPa [18] thus a full phase change is not expected in ZnTe/ZnSe NC.

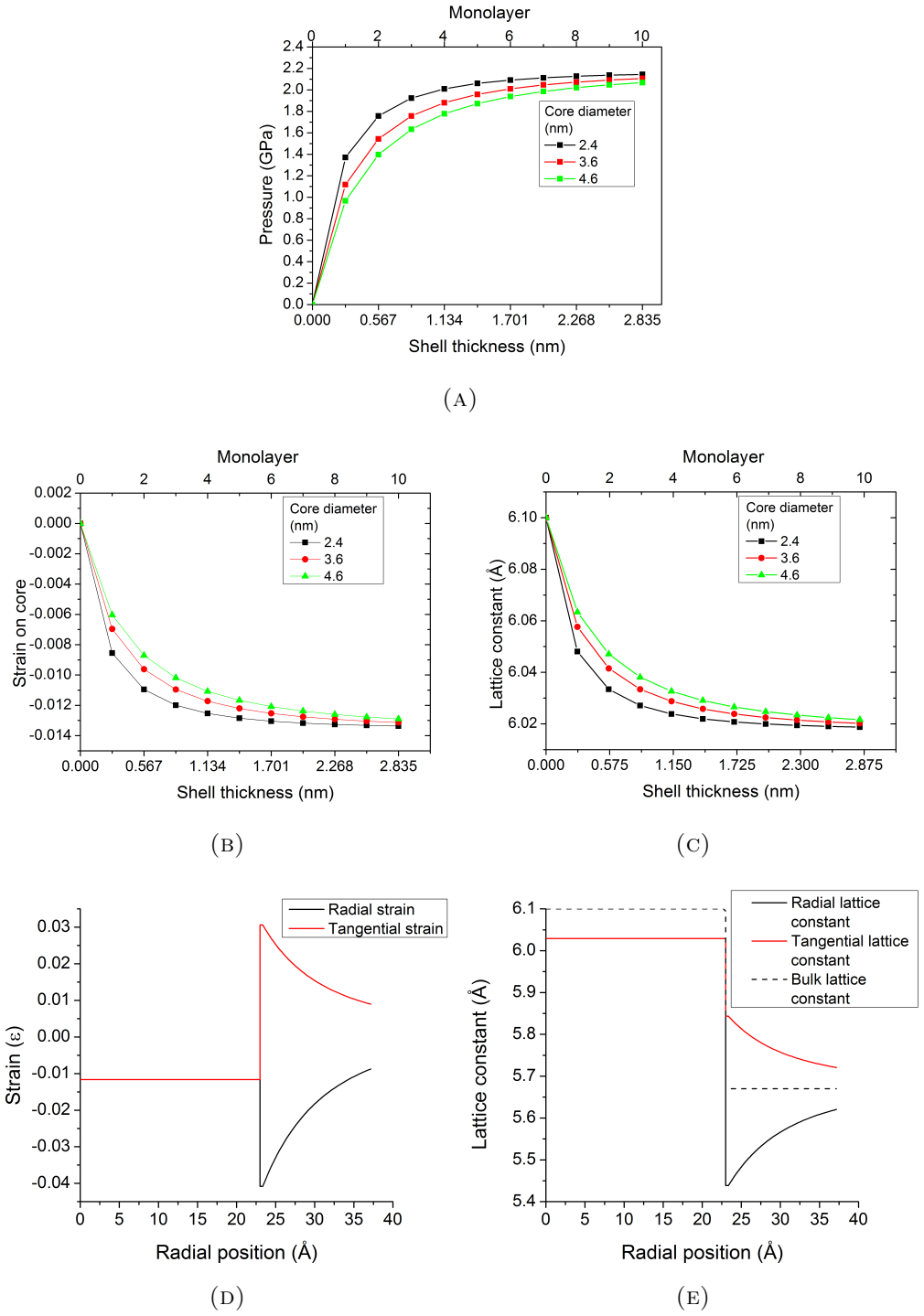

FIGURE 3.2: The theoretical interface pressure, strain and lattice constants of ZnTe/ZnSe NC as a result of 7% lattice mismatch calculated using the continuum elasticity model. a) The interface pressure on various core diameters as function of shell thickness. b) Strain in the core as a function of core diameter and shell thickness. c) Lattice constant of the core as function of shell thickness. d) Strain as a function of radial position in the radial and tangential directions for a 4.6 nm diameter ZnTe core with 5 ML ZnSe shell. e) The radial and tangential lattice constants as a function of radial position for a 4.6 nm diameter ZnTe with 5 ML growth.

3.2 Introduction to the atomistic models developed for transmission electron microscopy (TEM) and powder X-ray diffraction (XRD) simulation

Several atomistic models have been developed to investigate the crystal structure of NC through XRD simulation and TEM simulation [3, 7, 20, 95, 134–137]. These models within XRD have been limited to investigations of polytypism/stacking faults [3, 134] and the pressure effects of ligands [135] within mono material NC systems. Within TEM/Scanning TEM (STEM) these models have been produced to support crystal structure claims in single material NC [95] and compositional information within STEM [136, 137]. More recent XRD simulations within binary core-shell NC have focused on shape effects within CdSe/ZnS NC [7] and stacking faults within CdTe/ZnSe NC [20]. Despite the large lattice mismatches between many of the core-shell materials (CdSe/ZnS 12.2% and CdTe/ZnSe 14.4%), either no consideration of strain effects were included [7] or only global average lattice constants were used [20]. This lack of inclusion of strain into these models and our observation potential lattice bowing from the core to shell within HRTEM as will be shown later, serves as motivation to build an atomistic spherical core-shell NC that incorporates the idea of strain.

3.2.1 Pseudo code

To produce an atomistic model of a strained NC, a MATLAB® script was written and developed using the following the pseudo code (below) which can be visually described in figure 3.3.

Pseudo code

1. Build boundary atoms of octant using strained lattice constants
2. Build zinc blende structure considering the radial position of the atom and the strain model
3. Repeat 1 & 2 for each octant
4. Combine all octants
5. Define each atom
6. Define shape

The zinc blende structure was constructed by considering that each face of FCC structure is a translation of a cubic structure in the positive $\langle 1/2\ 1/2\ 0 \rangle$ directions. A zinc blende structure is the single translation of a FCC structure in the $[1/4\ 1/4\ 1/4]$ direction and each FCC translation represents one type of atom. Whilst for simplicity one can consider just orthogonal unit vectors as shown here, the software can accommodate the various unit vectors and translations that any strain model will require. By building the structure in this way rather than a full unit cell increases the accuracy of the position by up to 0.8% per unit cell for ZnTe/ZnSe.

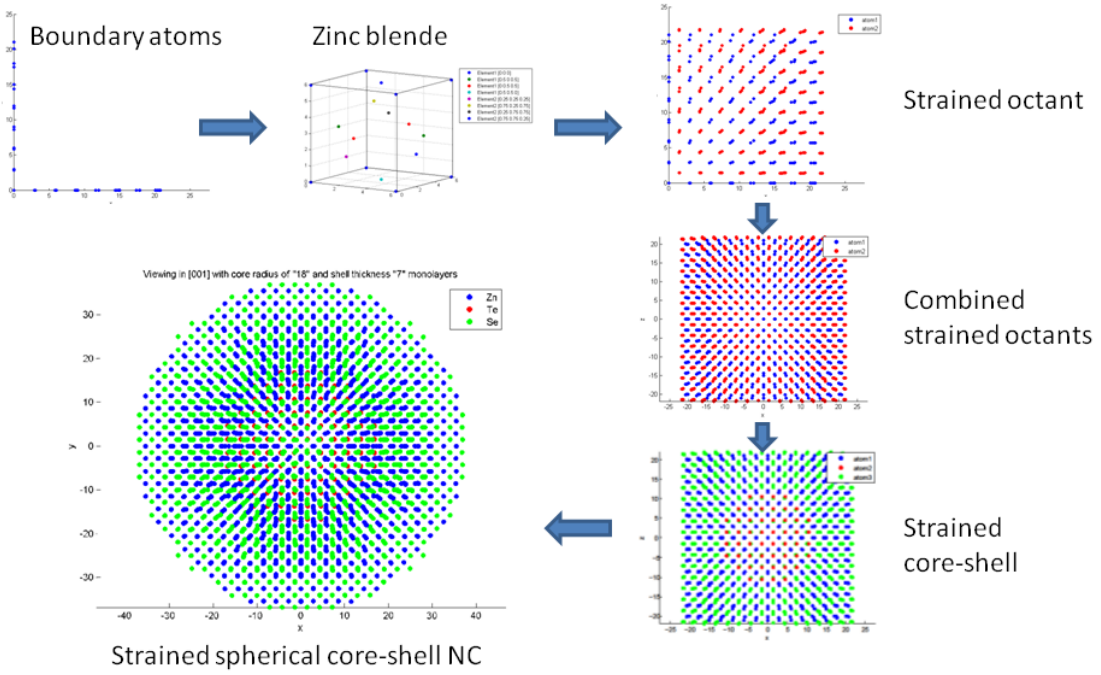

FIGURE 3.3: A schematic representation of the pseudo code used to build a strained NC. The code develops from a face centred cubic structure to a zinc blende structure. An octant is built using the idea of strain and sets up common boundary atoms. All 8 octants are combined and atoms are designated. The NC shape is then defined.

3.2.2 Building a unit cell: The incorporation of radial and tangential strain

This sections sets describe how radial and tangential strain coefficients in a spherical geometry described in section 3.1 can be related to the growth of unit cells in a cubic basis. The radial and tangential strain can be related to lattice constants in to the growth unit vectors in the following way.

Initially the principle strain axis and the cartesian basis are aligned, thus the strain coefficient can be related as below and schematically seen in figure 3.4

$$\epsilon_{rr} = \epsilon_{xx},\ \epsilon_{\theta\theta} = \epsilon_{yy},\ \epsilon_{\phi\phi} = \epsilon_{zz} \tag{3.12}$$

Along this principle axis the lattice constant in the cartesian basis are defined as

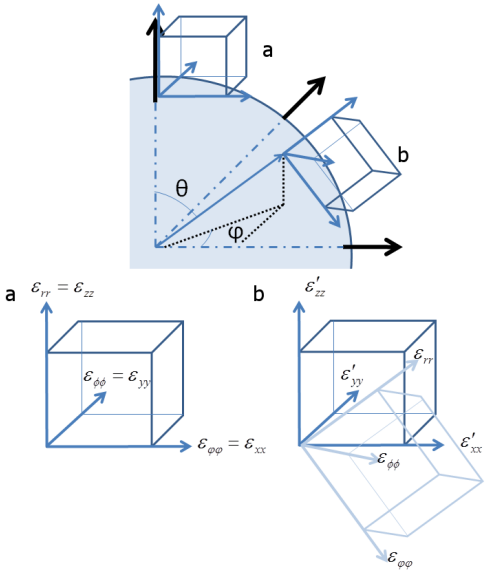

FIGURE 3.4: A schematic highlighting the rotation of the strain tensor on the surface of a sphere. a) The alignment of spherical and cartesian tensor systems along a principle axis. b) The cartesian strain tensor in relation to spherical tensor system off the principle axis.

$$a_{xx} = a_0(1+\epsilon_{rr}) \tag{3.13}$$

$$a_{yy} = a_0(1+\epsilon_{\theta\theta}) \tag{3.14}$$

$$a_{zz} = a_0(1+\epsilon_{\phi\phi}) \tag{3.15}$$

Thus the cartesian strain tensor ϵ'' along the principle axis can be described as

$$\epsilon'' = \begin{bmatrix} \epsilon_{xx} & 0 & 0 \\ 0 & \epsilon_{yy} & 0 \\ 0 & 0 & \epsilon_{zz} \end{bmatrix} = \begin{bmatrix} \epsilon_{rr} & 0 & 0 \\ 0 & \epsilon_{\theta\theta} & 0 \\ 0 & 0 & \epsilon_{\phi\phi} \end{bmatrix} \tag{3.16}$$

To relate both tensors one initially considers the spherical polar strain tensor at any point along the surface of the sphere as the principle cartesian tensor with a rotation about the centre (Figure 3.4). The rotations can be applied by using standard rotation matrices about the z and y axis akin to spherical polar coordinates where

$$\mathbf{A_y} = \begin{bmatrix} cos(\theta) & 0 & sin(\theta) \\ 0 & 1 & 0 \\ -sin(\theta) & 0 & cos(\theta) \end{bmatrix} \tag{3.17}$$

$$\mathbf{A_z} = \begin{bmatrix} cos(\phi) & -sin(\phi) & 0 \\ sin(\phi) & cos(\phi) & 0 \\ 0 & 0 & 1 \end{bmatrix} \tag{3.18}$$

Secondly, utilising the fact that strain tensors are contravariant second order tensors, thus the below transformation can be made to project the rotated strain tensor back in

the original coordinate basis.

$$\epsilon' = \mathbf{A_z}\epsilon''\mathbf{A_z}^{\mathbf{T}} \tag{3.19}$$

$$\epsilon = \mathbf{A_y}\epsilon'\mathbf{A_y}^{\mathbf{T}} \tag{3.20}$$

Thus, to find the projected lattice constant within the cartesian coordinate system, the unit vectors and the magnitude are given as

$$\begin{pmatrix} \mathbf{a_x} \\ \mathbf{a_y} \\ \mathbf{a_z} \end{pmatrix} = a_0 \left(\mathbf{A_z}\mathbf{A_y}\epsilon''{\mathbf{A_y}}^T{\mathbf{A_z}}^T + \begin{pmatrix} 1 & 0 & 0 \\ 0 & 1 & 0 \\ 0 & 0 & 1 \end{pmatrix} \right) \tag{3.21}$$

N.B. These lattice constants are vectors and also takes into consideration shearing effects.

3.2.3 Growth schemes

Using the above vectors the NC can built using two growth schemes

1. Scheme 1: This scheme is referred to as 'quasi-epitaxial' and builds each new atom by the taking into consideration the three adjacent atoms in the x, y, and z directions as shown in figure 3.5a.

2. Scheme 2: This scheme is referred to as 'epitaxial growth' and builds each new atom by the sum of the $\mathbf{a_x}, \mathbf{a_y}, \mathbf{a_z}$ vectors as shown in figure 3.5b. In an unperturbed cubic system this akin to growing in the [111] direction.

As can be seen figure 3.5c, scheme 1 overestimates the shifts in position and thus the scheme will break down for large core NC. As can be seen by figure 3.5d, scheme 2 overcomes the accumulated errors of scheme 1 by considering the growth from one atom and assumes the locality of the surrounding unit cell atoms along the basis directions. This approach gives the best approximation to epitaxial growth and thus, unless stated, scheme 2 is used to model all strained NC. It must be noted that this scheme can not be used for an unstrained system.

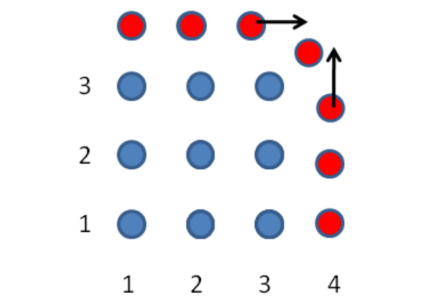

$$p_{mn}(x) = p_{m-1,n}(x) + a_1(x)$$
$$p_{mn}(y) = p_{m,n-1}(y) + a_1(y)$$

(A) Scheme 1

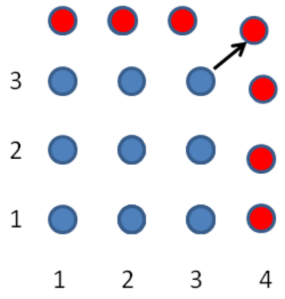

$$p_{mn}(x) = p_{m-1,n-1}(x) + a_1(x)$$
$$p_{mn}(y) = p_{m-1,n-1}(y) + a_1(y)$$

(B) Scheme 2

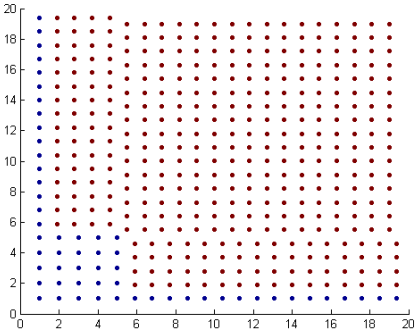

(C) Quasi epitaxial growth

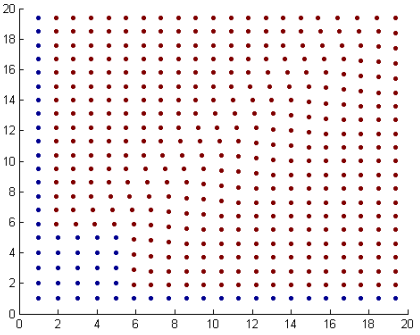

(D) Epitaxial growth

FIGURE 3.5: A 2-D schematic showing: a) Scheme 1 utilising two previous atoms in the x and y direction to converge on the new position; b) Scheme 2 utilising one previous atom to converge on through sum of vectors x and y to converge on the new position. c-d) A 2-D representation of growth mechanism used in c) Scheme 1: 'quasi-epitaxial growth' and d) Scheme 2: 'epitaxial growth' in a cubic system with two different cubic lattice constants for the core and shell.

3.3 Introduction to TEM simulation

HRTEM is very powerful technique in determining crystal structure, shape and defects within materials and has been used to great effect in the identification of defects and phase changes within core-shell NC [20, 138] and tetrapod structures [93]. Further investigation, past this simple bulk analysis, has not been readily utilised within the NC field even within some complex NC structures (core-shell etc.). Since TEM image are 2-D projections of a 3-D objects, TEM simulation can serve to explore subtleties within the image, such as an understanding of moire fringes, defects and other phenomena, and thus lead to a better understanding of the structure. The successful analysis of complex systems have required image simulation to verify the proposed model analysis and have been applied most notably within the STEM investigations of PbSe/CdSe and CdSe/ZnS NC [136, 137]. Little work has been done to explore TEM images of strained core-shell structures and serves as motivation for this analysis [20, 138–140].

Simulation of TEM images are easily produced with modern software and are regularly simulated using '*Java Electron Microscopy Software*' (JEMS) as developed by Pierre Stadelman [141]. This program takes into consideration the complex nature of the electron wavefront and interaction with atoms within the model crystal to produce a TEM image. Further known inputs, such as defocus and instrument characteristics, can also be taken into consideration to increase the accuracy of the simulated image. Here the atomistic models, as described in section 3.2, and the parameters for a JEOL 4000EX HRTEM operating a 400 kV were used to simulate the images. To account for the atom-wavefront interactions, the multi-slice calculations use the Peng-Ren-Dudarev-Whelan (PRDW) atomic form factors. Simulated images only account for defocus, instrument

characteristics and thermal contributions at room temperature. No amorphous carbon support was taken into consideration.

3.4 Introduction to XRD simulation

X-ray diffraction is one of the standard methods to characterise the crystal structure within NC [3]. If the X-ray penetration depth is significantly larger than the material being investigated the XRD pattern can be considered to investigate the whole crystal structure. The penetrating waves scatter when there is a change in the incident wave front due to a discontinuity/plane of atoms in the medium. If the phase between waves scattered by the discontinuity remains constant, the waves combine in a superposition effect to producing constructive or destructive interference, known as diffraction.

In the simplest approximation the angles at which the crystal will give constructive interference is given by Braggs law,

$$2dsin\theta = n\lambda \tag{3.22}$$

which is a function of the distance between planes of atoms (d) and the wavelength of the X-ray (λ). Here the angle θ is only half the angle observed in XRD diffraction pattern (2Θ). The characteristic angle and intensities of the diffraction pattern can be typically assigned to one of the 14 Bravais crystal groups.

One way to model XRD patterns is to use Rietveld refinement [142]. This purely analytical technique assumes homogenous materials (or mixtures of materials) and average strain within the individual systems [143]. Whilst this technique is useful for looking at single or multi-phase homogenous systems, it has the draw back that it is very time consuming to fit and can not give insight in to the atomistic make up of the NC. Thus, this technique will not be discussed further.

Another approach to simulate the diffraction patterns is to use an atomistic model of the particle under investigation. This route is pursued as the atomist model can also be utilised and compared to TEM simulation as described above. The simplest theoretical approach to find the resulting diffraction pattern is to apply a Fourier transform of the atomistic model. This approach serves to model single crystal NC diffraction within TEM and neutron scattering extremely well. The computational cost of this approach can also be thought to be high as the Fourier transform needs to be calculated for all points in the reciprocal space mesh and thus can lead to information being lost if the mesh size is too small as can be seen in figure 3.6 [144].

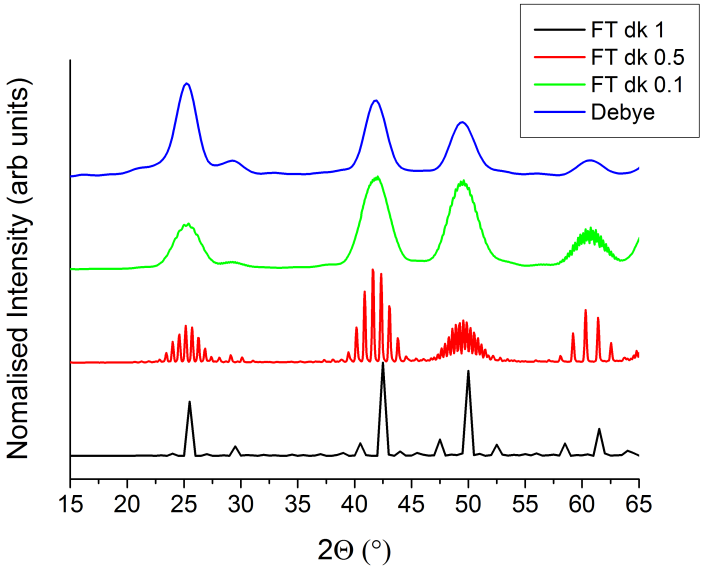

FIGURE 3.6: A comparison of the XRD patterns obtained using Fourier transforms with a mesh interval size of 1, 0.5 and 0.1 times the reciprocal lattice constant (Black, Red and Green respectively) and the Debye equation (Blue) for a 3.6 nm diameter ZnTe NC. The XRD patterns were simulated using a Cu $k\alpha$ X-ray source.

A faster and more reliable way to produce NC powder XRD patterns used by many in the NC field, is to use the Debye equation of kinematic diffraction given by

$$I(h) = \sum_i D f_i^2 + \sum_i \sum_{j,j\neq i} D f_i f_j \frac{\sin(2\pi h r_{ij})}{2\pi h r_{ij}} \tag{3.23}$$

This equation calculates contributions from all atom pairs to give a diffraction intensity [144–146]. The first part of the equation is the sum of all scattering (f_i) from individual atoms (i) and the second term sums the scattering contributions for each atom pair, where f_j describes the scattering from the second atom, $h = 2\sin(\theta)/\lambda$ defines the scattering direction (again where θ is half the scattering angle observed in XRD), D incorporates the Debye-Waller factor and accounts for the thermal dependence on scattering and r is spatial separation between atoms i and j. Using this approach reduces the simulation time to a matter of seconds and accurately models the diffraction pattern of small NC (Figure 3.6 Blue).

3.5 Introduction to critical radius calculations

It has long been known that the growth of lattice mismatched epitaxial layer upon a substrate in a thin film geometry could considerably effect the performance of these binary systems [147, 148]. It was shown that an epitaxial film could be be grown coherently up to a critical thickness h_c, at which point, it is energetically more favourable for dislocations to form and minimise the strain energy within the system [148]. Self-assemble QD use strain from the lattice mismatch to grow specific formations of QD up to a critical thickness [149]. The importance of this critical thickness was shown on the performance of the QD, in which, defects could be shown to reduce performance and produce anisotropic materials [31]. It has long been theorised that a similar effect should occur in NC and qualitative evidence for this has been shown [7], however, quantitative work to calculate this critical radius within a core-shell geometry is hard to come by. The lack of quantitative analysis falls into to two categories;

1. The elastic properties of NC can vary with size [150].

2. The geometry and full growth dynamics on an atomistic scale are not fully understood.

Whilst these problem exist, attempts have been made to calculate the critical radius within core-shell NC. A few papers have approximated this critical radius to the critical height, h_c, of a strain induced misfit dislocation on a planer interface [137, 151]. This is described by Matthews-Blakeslee theory [152]

$$h_c = \frac{|\mathbf{b}|}{8\pi\chi\cos\lambda}\left(\frac{1-\nu\cos^2\beta}{1+\nu}\right)\ln\left(\frac{h_c}{|\mathbf{b}|}\right) \tag{3.24}$$

where $|\mathbf{b}|$ is magnitude of the Burgers vector $\mathbf{b}$, χ is the lattice mismatch as a fraction, ν is the poisson ratio of the shell, β is the angle between misfit dislocation line and the Burgers vector and λ is the angle between Burgers vector and the direction orthogonal to the misfit dislocation line. This is thought, by others, to give a first approximation/an upper bound to the critical radius of the core-shell NC. For ZnTe/ZnSe this critical radius is calculated to be less than 1 nm (∼4 ML) which is exactly comparable to that shown by others for other materials [137, 151].

A more rigourous route to calculate critical thickness in a core-shell geometry was shown by Balasubramanian *et al.* for Si/Ge core-shell NC which has only recently been applied to II-VI semiconductor NC and only in the full dislocation case [15, 20]. All critical thickness/radius calculation serve to calculate the point at the energy of coherent state, $E_{Coherent}$, is lower than energy incoherent state $E_{Incoherent}$(i.e. $0 > \Delta E = E_{Coherent} - E_{Incoherent}$). Taking into consideration the continuum model described in section 3.1 Balasubramanian *et al.* [15] showed that the critical radius for a full dislocation ΔE_F and partial dislocations ΔE_P can be written as (A full derivation is shown in the Appendix A.1)

$$\Delta E_F = 0 = 2\pi r_{loop}\left(\frac{\mu_i|\mathbf{b}|^2}{4\pi(1-\mu_i)}\right)\ln\left(\frac{8\alpha r_{loop}}{|\mathbf{b}|}-1\right) - \pi r_{loop}^2 p(a,a_s)|\mathbf{b}| \quad (3.25)$$

$$\Delta E_P = 0 = 2\pi r_{loop}\left(\frac{\mu_i|\mathbf{b}|^2}{4\pi(1-\mu_i)}\right)\ln\left(\frac{8\alpha r_{loop}}{|\mathbf{b}|}-1\right) - \pi r_{loop}^2 p(a,a_s)|\mathbf{b}| + \pi r_{loop}^2\gamma \quad (3.26)$$

where r_{loop} is radius of the dislocation loop around the core-shell interface, $\mu_i = 2\mu_c\mu_s/(\mu_c+\mu_s)$ is the average shear modulus at the interface using the shear core(shell) $\mu_{c(s)}$ respectively, α is dislocation core parameter, p is the interface pressure describe by equation 3.5 and γ is the stacking fault energy of the shell material.

The critical radius is a function of core radius (a) and shell thickness (a_s) by virtue of the interface pressure, p, at the core-shell interface and r_{loop} which is the core radius a in this case.

To account for a full dislocation within a FCC structure the full dislocation Burgers vector $\mathbf{b_{fd}}$ is described as [153]

$$\mathbf{b_{fd}} = \frac{a_0}{2}\langle 110\rangle \tag{3.27}$$

where a_0 here is the lattice constant in the shell. It was shown by Frank and Shockley that it can be more energetically favourable for a full dislocation to split into partial dislocations [153]. The two types of partial dislocations can be seen in figure 3.7. It can be easily seen that the Frank partial dislocation produces an interstitial defect which would have dangling bonds which could be detrimental to the performance of the material, whereas a Shockley partial produces a stacking fault and still has all the bonds bound.

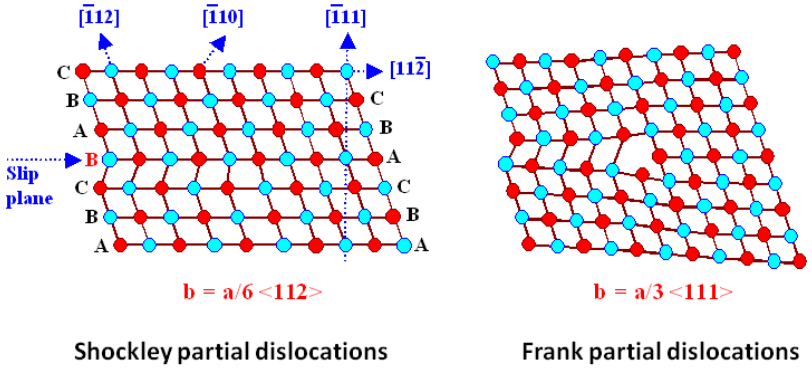

FIGURE 3.7: A schematic of a Frank partial and Shockley partial dislocation. Reproduced with permission from the online lectures by H. Föll, University of Kiel [154] based on images of Hull and Bacon [153].

It was further shown by Ovid'ko *et al.* [155] that within a nano-island self assemble QD that there is preferential formation of single partial dislocation near the edges of the QD

rather than a full or two partial dislocations.

With this in mind, the critical radii for a Frank partial $\mathbf{b_{fp}}$ and Shockley partial $\mathbf{b_{sp}}$ within a FCC structure can be calculated using the below Burgers vectors,

$$\mathbf{b_{fp}} = \frac{a_0}{3}\langle 111\rangle \tag{3.28}$$

$$\mathbf{b_{sp}} = \frac{a_0}{6}\langle 112\rangle \tag{3.29}$$

As this is a relatively new technique to the NC field, section A.2 in the Appendix shows the corresponding full, Frank and Shockley partial dislocations for CdSe/ZnS NC which are then compared to the highest reported QY which show some agreement to a full dislocation and better agreement than Matthews-Blakeslee theory.

3.6 Introduction to effect mass modeling

This section sets out to introduce the (2-6)-band effective mass approximation used to model exciton energies with in ZnTe/ZnSe NC. This work was conducted in conjunction with Edward Tyrrell. Whilst the calculations of the exciton energies were conducted by Edward Tyrrell, the compilation, analysis and interpretation was conducted by myself.

Many theoretical studies have been used to support type-II experimental data [13, 20, 46, 62, 67, 83]. These theoretical studies have primarily focused on single-band effective mass approximations and envelope function approximations to obtain exciton energies, wavefunction overlap and biexciton energies. Our group has recently applied a (2-6) band effective mass approximation to CdTe/CdSe type-II NC [103]. The theory utilises a two-band electron and six-band hole Hamiltonian to take account of the complex nature of the valence band as can be seen in figure 3.8, and takes into consideration the Coulomb interaction between the charge carriers and the dielectric polarization energies. This model was shown to have better agreement to the observed optical transitions when compared to simple effective mass approximation [103].

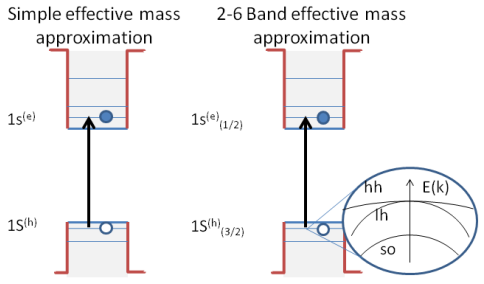

FIGURE 3.8: A schematic showing the energy level considerations of a simple effective mass approximation and (2-6)-band effective mass approximation showing the lowest $1S^{(e)}1S^{(h)}$ and $1S^{(e)}_{1/2}1S^{(h)}_{3/2}$ transitions respectively

To compare the optical absorption features by including strain in the (2-6)-band effective mass calculations. To take the complex nature of the energy level in to consideration the

electron and hole levels are labeled as $nQ_j^{(e)}$ and $nQ_j^{(h)}$ respectively where $Q = S, P, D, ..$ denotes the lowest value of the envelope angular momentum, n is the level number and j is total angular momentum [156]. We therefore describe the lowest exciton transition as $1S_{1/2}^{(e)}1S_{3/2}^{(h)}$.

The model sets to expand on the original model by calculating the stress and strain fields in the heterostructure using the continuum elasticity model as describe earlier, and then applying the model-solid theory of Van de Walle [19] to find the resulting band alignments of the strained structure. A was stated in section 2.2.2, shifts in the conduction (valence) band energy $E^{c(v)}$ are calculated by converting the fractional volume changes of the materials due to hydrostatic strain to perturbation in energy level using equation 2.1. The deformation of the crystal lattice changes the conduction and

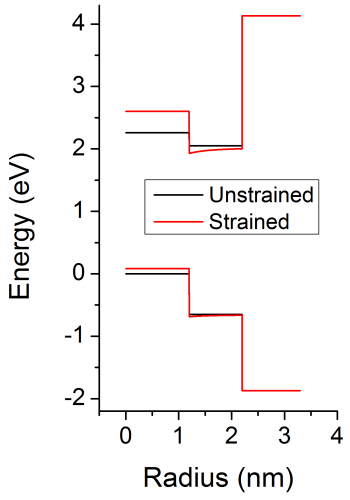

FIGURE 3.9: A plot of the conduction and valence band profiles calculated with (Red) and without strain (Black) for a 2.4 nm diameter ZnTe core with 4 ML ZnSe shell.

valence band edges. As was shown in table 2.3 in section 2.2.2, ZnTe and ZnSe have some of the highest deformation potentials out of the II-VI semiconductor materials, thus, the inclusion of lattice strain in the model gives rise to significant shifts in the conduction band edges of both the core and shell. As seen in figure 3.9, the compressive strain in

the core increases the bandgap confinement potential which increases the conduction band energy, whilst tensile strain in the shell reduces the conduction band energy in this region. This change in the shell band potential is most notably near the core-shell interface where the largest amount strain occurs (Figure 3.2d). For ZnTe/ZnSe NC that will be discussed later, the strain-induced shifts in the conduction band potential can be as high as several hundred meV for the core and are considerably smaller in the shell. The shifts in the valence band are much smaller than the conduction band, typically being less than 100 meV in the core and even less in the shell. These shifts in confinement potential lead to a more pronounced type-II band alignment ('double straining' [20]) which tends to redshift the exciton energy. It must be noted that the size of the shift in the band edge exciton energy with increasing shell thickness is also found to depend on the valence band offset E_v and the bandgap E_{g3} in the external matrix due the large intrinsic bandgap of the core-shell materials. Since these values are not well known for these materials, these are considered fitting parameters when testing the agreement between the strained and unstrained NC models with the experimental data (see Appendix C.1.2). The parameters E_{g3} and E_v that minimise the deviation from experimental data are stated in the Appendix C.1.2 and comparable to values reported in the literature.

For completeness, a full description of the theoretical calculations as used by Edward Tyrrell to calculate the exciton energies is described in the Appendix C.1.

Chapter 4

Experimental methods

4.1 Synthetic methods to ZnTe/ZnSe nanocrystals

4.1.1 Chemicals

All chemicals were purchased from Sigma Aldrich® and used without further purification or modification unless stated: Benzyl ether (BE) 98%, butylamine 98%, diethyl Zn (Zn 52.0 wt.), octyl ether (OE) 99%, OA 99%, ODE 90%, OLA 70%, ODA 97%, Se pellets 99.9%, SA 95%, superhydride in THF (1 M), Te pellets 99.999 % mesh, TOP 90%, TOPO 90%, Zn acetate dihydrate 98% [Acros®], Zn acetate anhydrous 99.99%, and anhydrous butanol, anhydrous chloroform, anhydrous hexane and anhydrous methanol. All reactions and optical characterisations were conducted using standard air-free techniques.

4.1.2 Preparation of precursors

4.1.2.1 General precursors

A 1 M superhydride solution was prepared by solvent exchange with OE. Here equal volumes of OE and superhydride THF were mixed and placed under vacuum. This was then raised slowly to 110°C for 30 minutes until the solution was clear again. 0.8 M Te-TOP, 0.1 M Te-TOP and 0.1 M Se-TOP precursors were prepared by dissolving Te pellets and Se pellets in TOP in a nitrogen-filled glovebox and stirred overnight. A solution of vacuum degassed BE and OA was mixed with TOP in a volume ratio of 15:1:1 BE:OA:TOP.

4.1.2.2 Zinc precursor preparation

1. 0.1 M Zn oleate solution was prepared by placing Zn acetate dihydrate in OA and BE solution with 9:1 OA:Zn molar ratio for the 2.4 nm cores and 2.5:1 OA:Zn molar ratio for the large cores. This was heated to 160°C under vacuum for 40 minutes and placed under nitrogen flow and then raised to 180°C until the solution was clear. In a typical reaction, 0.2195 g (1 mmol) of Zn acetate was placed in 9.369 ml BE and 0.621 ml (2.5 mmol) OA [157].

2. 0.1 M OLA/Zn oleate was made as (**1**) but with the following adjustment; The ratio of OLA:OA:Zn acetate was made to 2.5:2.5:1. In a typical reaction, 0.1835 g (1 mmol) of Zn acetate anhydrous was placed in 0.621 ml (2.5 mmol) OA, 0.7599 ml (2.5 mmol) OLA and 8.618 ml (2.5 mmol) BE [95].

3. 0.1 M Diethyl Zn TOP was prepared in a nitrogen-filled glovebox by placing 61 μl (0.598 mmol) diethyl Zn with 5.938 ml TOP [50].

4. 0.1 M Zn acetate TOP was prepared in a nitrogen-filled glovebox by placing 0.0918 g (0.5 mmol) of Zn acetate anhydrous with 5 ml TOP and stirred overnight [158].

5. 0.1 M Zn stearate was prepared as (**1**) with adjustment of 9.257 ml BE and 0.07112 g (2.5 mmol) SA [158]

4.1.3 Synthesis of ZnTe cores

4.1.3.1 Optimised Zhang method

This is a modified method based on the previously reported procedure [157]. In a typical reaction, 0.1756 g (0.8 mmol) of Zn acetate dihydrate was placed in a three-neck vessel with 15 ml BE and 1 ml OA. The solution was heated slowly to 150°C under vacuum for 40 minutes until the solution turned clear, and was then placed under nitrogen flow at 160°C for a further 10 minutes before being heated to the reaction temperature at 245°C. Separately, the Te precursor was prepared by reacting 1 ml of 0.8 M Te-TOP with 0.8 ml of 1 M superhydride OE in a nitrogen-filled glovebox, where it was allowed to react for 2-3 minutes at room temperature. The reacted turbid pink precursor solution was transferred from the glovebox via syringe into the hot reaction solution. The solution temperature was allowed to recover and kept at 245°C until the desired NC size was obtained, whereupon the solution was quenched using a water bath.

The core NC were cleaned by the addition of excess methanol and subsequent centrifugation for 10 minutes at 4000 rpm, followed by extraction of the supernatant and redispersion of the NC in hexane. All subsequent cleaning steps used methanol as the non-solvent and redispersed in hexane.

4.1.3.2 Xie method

This is a modified method based on the previously reported procedure [9]. In a typical reaction, 1.230 ml ODA was placed with 3.802 ml ODE and heated to 140°C for 45 minutes under nitrogen. The reaction solvent was heated to 280°C. In a glovebox, 0.976 ml of 0.1 M Te-TOP was mixed with 0.0010 ml (0.976 mmol) of diethyl Zn. This was injected into the reaction solvent and left to grow at 270°C. The NC were cleaned using the methanol:hexane method as in section 4.1.3.1.

4.1.3.3 Jiang method

This is a modified method based on the previously reported procedure [159]. In a typical reaction, 3 ml ODA was placed with 3 ml ODE and heated to 140°C for 45 minutes under nitrogen and was subsequently heated to 270°C. In a glovebox, a solution of 0.1 M diethyl Zn and anhydrous hexane was made. 0.3 ml of this solution was mixed with 0.6 ml of 0.04285 M Te-TOP and 0.058 g TOPO. This was injected into the reaction solvent at 270°C and left to grow at 260°C. The NC were cleaned using the methanol:hexane method as in section 4.1.3.1.

4.1.4 ZnSe shell growth using SILAR

To grow a specific shell thickness, typically 2 ml of the original ZnTe dispersion was cleaned as in section 4.1.3.1 and mixed with 2 ml of the BE:OA:TP (15:1:1) solution. This solution was subsequently placed under vacuum for 20 minutes at 100°C to remove low boiling point materials from the solution. The core reaction was empirically found to be quantitative and therefore the average diameter of the core, as determined through TEM, is used to calculate the concentration of the NC in the reaction solution using the

technique described previously in reference [9]. For these reactions, typically 0.708 μmol, 0.210 μmol and 0.101 μmol of ZnTe NC were used for the growth on the 2.4, 3.6 and 4.6 nm diameter cores respectively. Using the SILAR technique, aliquots of 0.1 M Zn oleate or 0.1 M Se-TOP were subsequently injected and heated to the growth temperature of 235-240°C. The temperature for each injection and growth was optimized to maximise the reactivity of the precursor whilst minimising the risk of Ostwald ripening. The smallest cores, for example, required the injection of the first precursor at a temperature of less than 180°C and then raised to 235°C for the first ML growth, whilst subsequent ML were injected and grown at 240°C. An Anglia Instruments high temperature *in situ* absorption dip probe was used to observe the evolution of the absorption peak to monitor shell growth. For a typical reaction, up to 25 minutes was required for selenium growth and 30 minutes for Zn growth. The core-shell NC were initially cleaned with an excess of a pre-made 3:1 methanol/butanol solution, centrifuged to enable the NC to precipitate out of the solution and the NC redispersed in hexane. Subsequent cleaning steps used only methanol solution as the non-solvent and redispersed with small amounts of hexane.

4.1.5 Variations of the standard ZnSe shell protocol

All the protocols below use the optimised Zhang synthesis method of section 4.1.3.1 to synthesise the ZnTe cores. Each ML was grown as in section 4.1.4 with the following modifications. The NC solution were cleaned using the standard butonol/methanol/hexane clean as described in 4.1.4.

Monolayer	1	2	3	4	5
2.4 nm Core					
Nominal diameter (nm)	2.98	3.53	4.10	4.66	5.24
Injection temperature (°C)	180	240	240	240	240
Growth Temperature (°C)	235	240	240	240	240
3.6 nm Core					
Nominal diameter (nm)	4.16	4.73	5.30	5.87	6.44
Injection temperature (°C)	180	240	240	240	240
Growth Temperature (°C)	240	240	240	240	240
4.6 nm Core					
Nominal diameter (nm)	5.17	5.73	6.30	6.86	7.40
Injection temperature (°C)	180	240	240	240	240
Growth Temperature (°C)	240	240	240	240	240

TABLE 4.1: The optimum temperature for each monolayers growth of ZnSe on a ZnTe core.

4.1.5.1 Successive Ion Layer Adsorption and Reaction — Thermal cycling (SILAR-TC) method

This is a modified method based on the previously reported procedure [54]. The crude NC dispersion was cleaned in the standard way described in section 4.1.3.1, the NC were redispersed in a 2 ml solution of pre-made 13:2:1 BE:OA:TOP solution. The NC solution was raised to 160°C where the pre-determined aliquot of 0.1 M Se-TOP was injected and left for 5 minutes, subsequently 0.1 M Zn oleate was injected and heated quickly to 240°C for 30 minutes and repeated.

4.1.5.2 Zinc oleate with oleylamine method

This is a modified method based on the previously reported procedure [9]. The crude NC dispersion was cleaned in the standard way described in section 4.1.3.1, the NC were redispersed in a 2 ml solution of premade 13:2:1:1 BE:OLA:OA:TOP solution. Using

the SILAR technique described in section 4.1.4 the 0.1 M Se-TOP and 0.1 M OLA-Zn oleate were alternately injected and grown at 240°C for 25 and 30 minutes respectively.

4.1.5.3 Zinc acetate/TOP and Se-TOP method

This is a modified method based on the previously reported procedure [158]. The crude NC dispersion was cleaned in the standard way described in section 4.1.3.1, the NC were redispersed in a 2 ml solution of premade 15:1 BE:TOP. The NC solution was raised to 180°C where an aliquot of 0.1 M Se-TOP was injected and left for 5 minutes, subsequently 0.1 M Zn oleate was injected 180°C and left to grow for 30 minutes. The NC was finally heated up to 240°C and annealed for 30 minutes [46, 158].

4.1.5.4 Diethyl zinc and Se-TOP method

This is a modified method based on the previously reported procedure [50]. The crude NC dispersion was cleaned in the standard way described in section 4.1.3.1, the NC were redispersed in a 2 ml solution of premade 15:1:1 BE:OA:TOP. The NC solution was raised to 220°C and using the SILAR technique described in section 4.1.4 aliquots of 0.1 M Se-TOP and 0.1 M diethyl Zn TOP were alternately injected and grown for 30 minutes at 220°C.

4.1.5.5 Zinc stearate and Se-TOP method

This is a modified method based on the previously reported procedure [158]. This uses the standard procedure described in section 4.1.4 with the substitution of SA for OA.

4.1.5.6 Diethyl zinc core method with zinc oleate Se-TOP shell method

Using the core synthesis method of section 4.1.3.2. The ZnSe shell was made using a modified shelling technique of reference [9, 160]. After the core synthesis at 270°C the reaction solution was reduced to 240°C. Using the SILAR technique described in section 4.1.4 aliquots of 0.1 M Se-TOP and 0.1 M Zn oleate (9:1 OA:Zn) were alternately injected and grown for 30 minutes.

4.1.5.7 Growth of alloyed nanocrystals

The crude NC solution was cleaned in the standard way; the NC solution was redispersed in the standard reaction solution of 15:1:1 BE:OA:TOP. In order to grow alloyed interfaces we modified the shelling procedure described above to make use of the growth kinetics as established by reference [46]. Starting with the solution of ZnTe cores, Te-TOP and Se-TOP were injected, each in quantities equivalent to one monolayer of growth, at 180°C. The solution was then heated to 240°C for a reaction time of 25 minutes. Then the equivalent of 4/3 ML of Zn oleate was injected and the reaction was allowed to proceed for a further 30 minutes. This sequence was repeated twice, omitting the Te-TOP, thus producing 4 ML of fully reacted growth with a graded composition from a Te-rich core interface to a Se-rich surface. Further ZnSe shell growth was then carried out using the SILAR technique described in section 4.1.4.

4.2 The synthetic method to graded alloyed CdZnSeS nanocrystals

All chemicals were purchased from Sigma Aldrich® without further purification or modification unless stated: CdO 99.5%, OA 99%, ODE 90%, S flakes 99.99%, Se pellets 99.9%, TOP 90%, Zn acetate anhydrous 99.99%. Reagent grade acetone, chloroform, hexane and methanol were desiccated by placing the solution with 3Å molecular sieves and left overnight. In a nitrogen-filled glovebox 0.007896 g (0.1 mmol) of Se and 0.003207 g (1 mmol) of S flake were dissolved in 3 ml TOP and stirred overnight. In a three-neck flask 0.051364 g (0.4 mmol) Cd oxide, 0.73392 g (4 mmol) Zn acetate, 5.6 ml OA and 20 ml ODE was degassed for 1 hour at 100°C under vacuum. The solution was placed under nitrogen flow and heated to 310°C. 3 ml S-Se TOP was injected in the reaction solution and allowed to grow for 5 minutes at 300°C. 2 ml aliquots were taken every minute.

The solidified cooled solution was redispersed with chloroform and was initially cleaned by precipitation with excess acetone and centrifuged for 10 minutes at 4000 rpm. The supernatant was then extracted and the NC redispersed using hexane. Subsequent cleaning steps washed the NC in a 1:1 hexane-methanol solution (equivalent to the original volume) and the methanol phase was extracted. A final centrifuge was conducted to highlight any excess methanol. Samples for TEM were prepared by further cleaning the NC using the following procedure three times: addition of excess methanol to allow precipitation; the sample was then centrifuged; supernatant extraction was extracted and redispersed in small amounts of hexane.

4.3 Physical characterisation

4.3.1 TEM, electron dispersive X-ray spectroscopy (EDX), Selected area electron diffraction patterns (SAED) and XRD characterisation

Samples for TEM were cleaned 4 times and drop cast onto a 400 mesh Cu grid with an ultra thin carbon film. TEM images and 'selected area electron diffraction patterns' (SAED) were taken using a JEOL 2010 TEM operating at 200 kV and electron dispersive X-ray spectroscopy (EDX) with a Oxford Instruments EDX detector. HRTEM images were taken using a JEOL 4000EX TEM operating at 400 kV or a JEOL 2010 TEM operating at 200 kV. A gold nanoparticle reference was used to calibrate the microscope. XRD patterns were taken using a Philips PW 1830 with Cu Kα source.

4.3.2 X-ray photoelectron spectroscopy (XPS) characterisation

Samples for XPS required a ligand exchange to the shorter chain butylamine to prevent excess charging during the measurements. These samples were prepared by adding excess butylamine to a cleaned NC solution and left over night at 50 °C under nitrogen. The samples were cleaned and redispersed with excess anhydrous methanol and hexane and stored under nitrogen. The samples were rapidly drop-cast onto Indium tin oxide (ITO) coated glass substrates in air, and immediately inserted into the vacuum system of the spectrometer. The total air exposure was less than 15 minutes, including the pumping time. These measures are effective in suppressing surface oxidation of the NC [161] and no significant surface oxidation was observed in XPS. The XPS experiments were carried out on the I511-1 beamline at MAX-lab, Sweden using a Scienta R4000

electron energy analyser. Photoemission spectra were recorded at room temperature at a total instrumental resolution of 170 meV (at 250 eV photon energy) to 450 meV (at 750 eV photon energy).

4.4 Optical characterisation

4.4.1 Ensemble absorption, photoluminescence (PL), photoluminescence excitation (PLE), quantum yield (QY) and lifetime measurements

Ensemble absorption spectra were recorded using a Varian Cary 5000 UV-visible-NIR spectrometer. Ensemble PL spectra were taken on a Varian Cary Eclipse Fluorescence Spectrometer or taken using an OceanOptics 2000X spectrometer excited with a 405 nm laser diode pen. Ensemble photoluminescence excitation (PLE) were taken on a Varian Cary Eclipse Fluorescence Spectrometer. The absolute QY were measured using 365 nm excitation from a diode laser, utilising a Labsphere integrating sphere and calculating the absolute QY using the method of de Mello *et al.* [162]. Ensemble lifetime measurements excited with a Picoquant 475 nm diode laser under CW or pulsed excitation with an intensity of less than 0.35 W cm^{-2} with a 70 picosecond pulse duration and with a repetition rate ranging between 2-5 MHz. The resulting signal is coupled from the spectrometer to a Perkin-Elmer SPCM-AQR-14-FC single-photon avalanche detector (SPAD) and the laser-driver pulse-timing signal is coupled to an Edinburgh Instruments TCC900 time-correlated single-photon counting (TCSPC) card.

4.4.2 Single nanocrystal spectroscopy

4.4.2.1 Sample preparation

All chemicals were used without further purification or modification unless stated: NC samples were prepared for spectroscopy by diluting the NC in solutions of anhydrous chloroform (Fisher HPLC grade), poly(methyl methacrylate) [PMMA] (Sigma Aldrich) and HDA (Sigma Aldrich) and spin cast on to a glass cover-slip. The optimum NC concentration was found empirically to be on the order of 50 pM.

ZnTe/ZnSe NC samples required the PMMA to be mixed with chloroform and placed under nitrogen reflux at 50°C until dry and redispersed with anhydrous degassed chloroform (Sigma Aldrich) then kept under nitrogen. HDA was heated to 100°C and placed under vacuum for 30 minutes and cooled then kept under nitrogen. Once cleaned ZnTe/ZnSe NC solution was then diluted with this solutions in a nitrogen-filled glovebox and spin cast as above.

4.4.2.2 Experimental setup and processing

SNS investigations were conducted using a purpose built epi-fluorescence system shown schematically in figure 4.1. The NC were excited with a Picoquant 475 nm diode laser under CW or pulsed excitation with an intensity of less than 25 W cm^{-2}. The signal was coupled to an Acton SpectraPro 2500i spectrometer with a 500 blazed grating or mirror grating and recorded using Princeton Instruments high-sensitivity liquid-nitrogen cooled Spec-10 100B/LN CCD. For lifetime measurements, the NC were excited with a 70 picosecond pulse duration and with a repetition rate ranging between 2-5 MHz. The resulting signal is coupled from the spectrometer to a Perkin-Elmer SPCM-AQR-14-FC

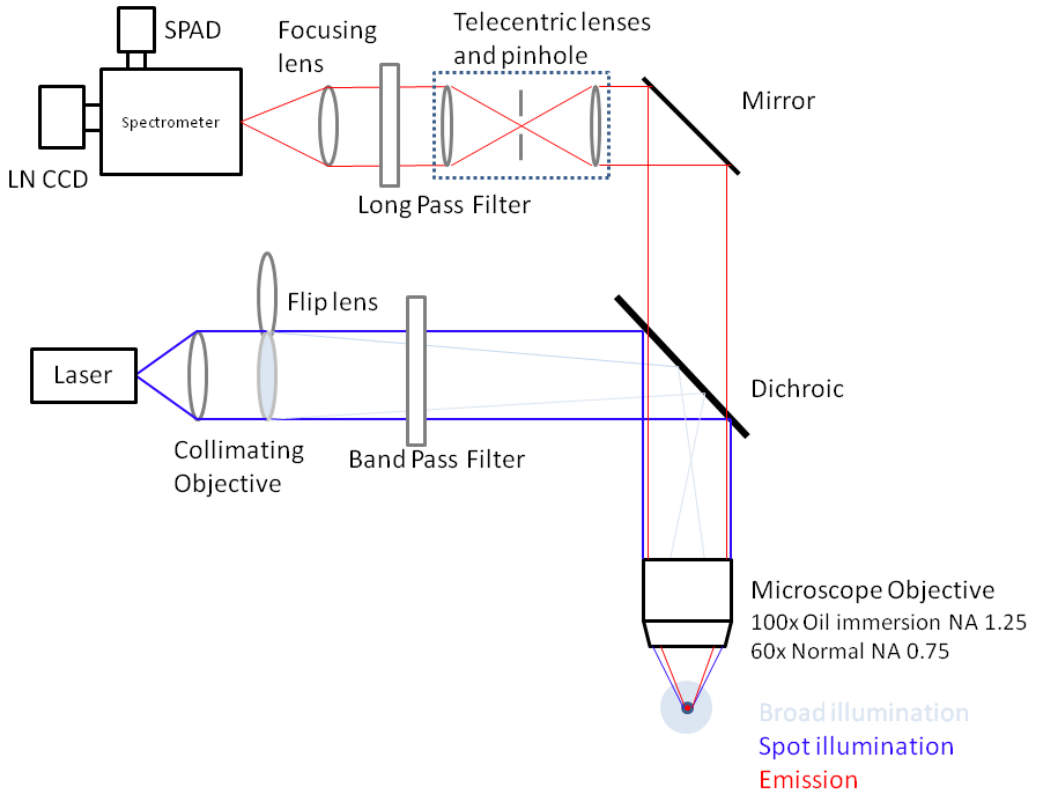

FIGURE 4.1: A schematic of the home built epi-fluorescence setup used for single NC spectroscopy.

SPAD and the laser-driver pulse-timing signal is coupled to an Edinburgh Instruments TCC900 TCSPC card. Lifetime, lifetime-time trajectories and intensity-time trajectories used the TCC900 in time tagging mode with 4096-channel binning. Hanbury Brown and Twiss (HBT) measurements were conducted by passing the fluorescence signal through an (1:1) optical fiber beam splitter and measuring the time delays between subsequent photon arrival events on two Perkin-Elmer SPADs and correlated with an Edinburgh Instruments TCC900 TCSPC card.

All analysis was conducted using Origin® except for lifetime-time, intensity-time trajectories and fluorescence lifetime-intensity distributions (FLID) which were analysed using self-developed code written in MATLAB®. To enable the lifetime to be measured within a one-second integration window, the binning resolution was reduced to between 256-512

channels or 0.39-1.95 ns depending on the time-tag range and the signal intensity.

Blinking statistics were calculated using a modified MATLAB® code initially developed by Benny Sher [163] which calculates the normalised probability distribution function $p(t_{\mathrm{off/on}})$ as initially described by Kuno *et al.* [164] which corrects the probability distribution for rare events that occur during the finite time of the investigation. This is described by the weighted probability distribution

$$p(t_{\mathrm{off/on}}) = \frac{N(t_{\mathrm{off/on}})}{N_{\mathrm{off/on}}^{\mathrm{total}}} \frac{1}{\Delta t} \tag{4.1}$$

where $N(t_{\mathrm{off/on}})$ is the number of off/on events of duration $t_{\mathrm{off/on}}$, $N_{\mathrm{off/on}}^{\mathrm{total}}$ is the total number of off/on events and Δt is the average time between nearest-neighbour events.

Chapter 5

Synthesis of type-II ZnTe/ZnSe nanocrystals

This chapter presents the first attempt to produce type-II ZnTe/ZnSe NC via a diethyl Zn-free synthesis method. It presents the general physical and optical properties of a size series of ZnTe/ZnSe NC and sets out to investigate the possible influence of strain within this structure through simulation. The chapter is split into two sections and sets out to show:

1. The development and comparison of a diethyl Zn and diethyl Zn-free ZnTe synthesis protocols which provide monodisperse NC with strong excitonic absorption features.

2. The general physical and optical properties of ZnTe/ZnSe NC grown using a diethyl Zn-free synthesis method. This section also sets out to compare the growth dynamics using a variety of Zn precursors and techniques. To provide evidence for

a strained structure, the physical and optical properties are simulated and compared to experiment. This section finally attempts to gain information through SNS of a single ZnTe/ZnSe NC.

5.1 Introduction & motivation

Since the seminal work of Kim *et al.* [62], the majority of type-II NC have been Cd chalcogenide based systems which show good optical performance over the red and N-IR regions of the spectrum. Previous attempts to synthesise ZnTe based type-II structures have mainly focused on lattice matched Cd chalcogenide shells enabling the emission to be tuned from 500 nm into the N-IR [9]. As Cd is heavily regulated due to its toxicity, the commercial application of Cd NC is severely limited [165]. More recently ZnTe/ZnSe NC has been produced as a Cd free alternative [50, 160]. An inspection of the relative bandgaps shows the potential to give a type-II structure that is tunable from the N-UV into the red region of the visible spectrum and thus could lead to potential commercial application within LEDs.

A potential limitation of this material combination is the large lattice mismatch of ∼7% between the ZnTe core and ZnSe shell material, which imposes considerable stresses in the structure. As discussed in section 2.2.2, strain is important in determining exciton energies of core-shell NC where the core has a small bulk modulus relative to the shell and is therefore easily compressed [20, 139]. Within the context of ZnTe/ZnSe NC, strain effects are predicted due to the differences in lattice constants and bulk moduli of the constituent materials (ZnTe: 6.10 Å, 50.5 GPa; ZnSe: 5.67 Å, 62.4 GPa respectively [14, 21]).

5.2 Development of synthetic techniques to ZnTe core nanocrystals

ZnTe offers a good platform to produce type-II structures due to its low ionisation potential (high valence band edge) and large intrinsic bandgap, giving the possibility to tune the effective bandgap over the whole visible spectrum. Unlike other II-VI semiconductors the number of protocols to synthesise ZnTe are severely limited and focus mainly on the hot injection method into non-polar solvents to produce zinc blende NC [9, 157, 159, 166]. Over the course of this project aqueous synthesis procedures have been developed [167, 168] that follow similar protocols to aqueous CdTe methods [169, 170]. As yet, these have not been able to compete in terms of size distribution, optical properties and yields when compared to the hot injection techniques. Therefore the hot injection, which is more mature, will be the focus of this project. Since this is the synthetic method attempted, the existing literature will first be discussed.

5.2.1 Previous related syntheses

The first recorded stable synthesis of ZnTe NC were recorded by Yun *et al.* [166] in 2001. ZnTe NC were synthesised using a phenyltellurolate Zn SSP complex, referred to as $[Zn(TePh)_2][TMEDA]$, into a TOP and dodecylamine reaction solvent. Observations of the NC under TEM showed an agglomerated solution which showed a clear large size distribution however no size distribution was quoted. This synthesis method to the SSP was shown to be highly complex and required highly reactive and pyrophoric reagents.

The most widely used synthetic method to produce ZnTe NC to date is the procedure developed by Xie *et al.* [9] and variants there of [50, 159, 160]. This method uses

the injection of a diethyl Zn & Se-TOP solution into a hot ODE/ODA solution. This procedure has been used to produce several type-II core-shell structures including Zn-Te/CdS ZnTe/CdSe ZnTe/CdTe NC [9] and also a variant to synthesise ZnTe/ZnSe NC [50, 160]. However, one draw back is that, in most cases, this produces large particle size distributions.

With the general trend towards greener synthesis techniques [39, 42, 158], attempts have been made to minimise the use of highly pyrophoric materials such as diethyl Zn. Following the trend of other II-VI semiconductors, Lee *et al.* attempted to make ZnTe NC using the decomposition of fatty Zn acids with Te phosphide precursors (e.g. Zn stearate with Te-TOP) in a variety of coordinating, non-coordinating solvents and at high temperatures [171]. The technique had limited success in producing spherical NC and only produced large NC or clusters of small NC (referred to as 'nanoflowers'). All the synthetic procedures described showed a smeared first excitonic feature indicative of large size distribution.

An attempt to describe the physical mechanism behind this large size distribution was conducted by Jiang *et al.* [159] in which the Xie *et al.* and Lee *et al.* methods were further investigated. It was hypothesized that the fatty acid precursor, even with amine activators, were not sufficiently active to enable homogenous nucleation of ZnTe NC thus the large size distributions. In contrast, the diethyl Zn precursor was consider to be too reactive and thus leads to uncontrolled growth. The hypothesis was that the addition of TOPO, a more tightly binding surfactant, hinders the fast growth of the diethyl Zn precursor and slows the rate of Ostwald ripening enabling a better size distribution.

A more recent technique employed by Zhang *et al.* [157] forgoes the use of highly pyrophoric diethyl Zn and uses ambient stable Zn oleate as the Zn precursor albeit

with the requirement of a strong reducing reagent of superhydride solution. A closer inspection of the reaction dynamics as described Zhang *et al.* showed a three step process, where the steps are described by:

$$\mathrm{Te_0} \underset{\text{Step1}}{\overset{\text{TOP+Superhydride}}{\rightleftharpoons}} [\mathrm{Te}^{2-}]^* \xrightarrow[\text{Step2}]{\mathrm{Zn(Ol)_2}} \mathrm{ZnTe_{(Cluster)}} \xrightarrow[\text{Step3}]{} \mathrm{ZnTe_{(NC)}} \tag{5.1}$$

1. Reactivity of the precursors; Te is dissolved in TOP to form a Te-TOP precursor. Without the reducing agent of superhydride the dynamic equilibrium within this reaction is set to a more unreactive Te compound. The addition of the superhydride serves to increase the reactivity of the precursor by producing $[\mathrm{Te}^{2-}]^*$.

2. Nucleation; The highly reactive nature of the $[\mathrm{Te}^{2-}]^*$ serves to help spontaneous nucleation of ZnTe clusters with the addition of Zn oleate ($\mathrm{Zn(Ol)_2}$) precursor.

3. Growth; Slow growth of the NC will predominantly be through Ostwald ripening assuming an almost complete reaction of the precursors.

Whilst superhydride itself is mildly pyrophoric due to its strong reducing nature, the overall stability of superhydride is significantly better and easier to use than diethyl Zn. The superhydride itself was not shown to measurably contribute to the final structure as seen by the lack of measurable B and Li in the EDX spectrum in figure D.1 in the Appendix.

5.2.2 Results and discussion

This section compares three of the most promising synthetic procedures to produce ZnTe as a core for the ZnTe/ZnSe core-shell structure. Here the methods of Zhang *et al.*, Xie *et al.* and Jiang *et al.* are used which have previously been reported to have reasonably pronounced excitonic features [9, 157, 159]. Specific emphasis is placed on the superhydride method of Zhang *et al.* as it does not use the highly pyrophoric diethyl Zn. Figure 5.1 shows a comparison of the absorption data using the three synthesis method. It is also noteworthy that the ZnTe NC observed little to no PL, consistent with the general lack of PL measurements in other reports. Thus to enable a degree of quantification between methods the spectral width of the second derivative of the absorption intensity (A) is utilised such that $\frac{\partial^2 A}{\partial \lambda^2} = 0$, which describes the points of inflection either side of the peak spectral absorption feature, akin to a FWHM within PL which is typically used as an indication of the size distribution [172].

Initial investigations into the superhydride method of Zhang *et al.* yielded a smeared excitonic feature, similar to those featured in the diethyl Zn synthesis protocols, implying a large size distribution. It was found through optimisation investigations of the reaction conditions, precursor concentrations and ratios, that the best excitonic features could be produced with a mild drop in the injection and growth temperature from 250°C to 245°C and an overall reduction in reactant concentration. Specifically an increase in the precursor to solvent volume ratio from 15:1 to 18:1, and overall decrease Te-TOP concentration from 1 M to 0.8 M. As seen by figure 5.1, our optimised superhydride method yielded much improved absorption excitonic features when compared to that of the Xie *et al.* and Jiang *et al.* method. This is specifically seen in the second derivative which shows a symmetric profile with a second derivative width ranging between 20 nm

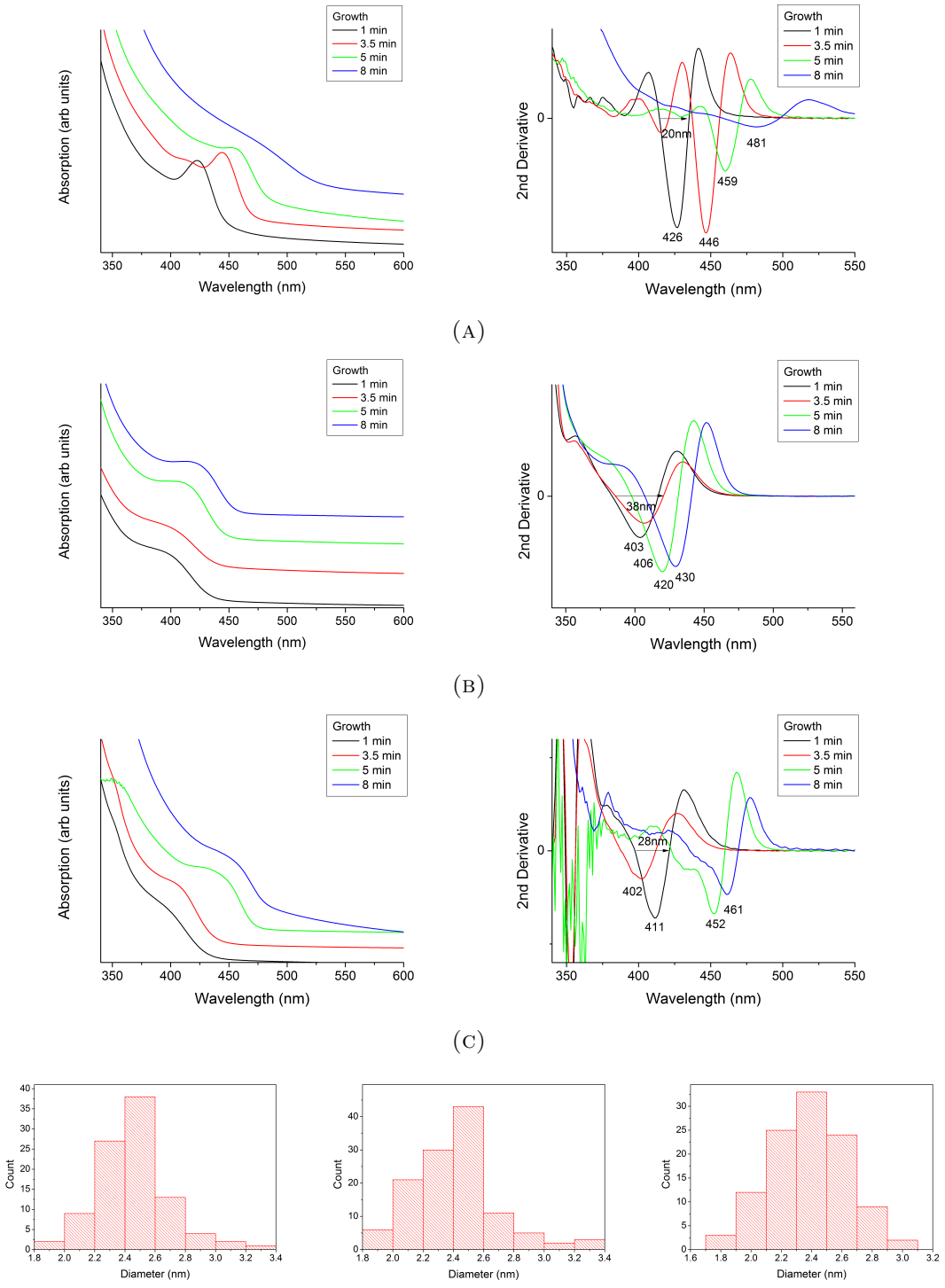

FIGURE 5.1: The evolution of the first excitonic absorption feature and the corresponding second derivative of ZnTe NC using a) the modified superhydride method of Zhang *et al.* b) the diethyl Zn TOP method of Xie *et al.* and c) the diethyl Zn TOPO method of Jiang *et al.* Bottom shows the size distribution histograms for ZnTe average ∼2.4 nm corresponding to 1 minute, 3.5 minutes and 3.5 minutes for the respective synthesis techniques. The respective standard deviations are 10%, 14% and 12%

to 22 nm and finally extending to 38 nm at long growth times. This was related to a size distribution of 10%, 7%, 9% and 14% for the 1, 3.5, 5 and 8 minutes growth respectively highlighting a size focusing regime for the first 3.5 minutes and a broadening mechanism thereafter. A comparison to the diethyl Zn highlights a blueshifted absorption spectra and non-symmetric second derivative shape consistent with a non-Gaussian size distribution. A comparison of like sized NC (2.4 nm Zhang, 2.3 nm Xie and 2.4 nm Jiang) showed the size distributions of 10%, 14% and 12% respectively relating to a second derivative width of 20 nm, 38 nm and 28 nm respectively and thus highlights the optimised superhydride method has the tightest size distribution of the synthetic methods attempted. An interesting point to note is the relative position of the absorption features of liked sized NC. These were seen to be 426 nm, 406 nm and 411 nm respectively. This variation is consistent with previous reports which use various ligands but still show a zinc blende structure for similar sizes [166–168]. It is thus theorised that ligands play a larger role on the effective bandgap, unlike Cd chalcogenide NC which on the whole show minimal shift with like length ligands for large NC [173]. Two postulates were proposed to account for the effect; firstly that this is due to the high conduction band of ZnTe and the unknown confinement effects of the supporting ligands at these energy levels. This is also supported by Xu *et al.* who theoretically showed that ligands play a large role on the the optical features within similar large bandgap of ZnSe [174]. Secondly that ligands, such as amines, induce a compressive stress on NC as high as 0.76 GPa within small core CdTe and CdSe NC [135, 175].

The other advantage of the superhydride method is that it is lab scalable without significant compromise on the size distribution quality. Here the superhydride method can routinely be used with in excess of 1 mmol of precursor, whilst the best size distribution for the diethyl Zn methods shown here could only be obtained with 0.1 mmol of

precursor. Due to the superior size distribution, strength of the optical features and the minimisation of pyrophoric precursors, the superhydride method was chosen as the core seed for ZnSe epitaxial shell growth.

5.3 Development of synthesis procedures towards ZnTe/ZnSe nanocrystals

This next section presents the capping methods to produce ZnTe/ZnSe NC and the SILAR synthesis method used here to cap the ZnTe cores. Further intricacies in using this technique are also described.

The only published methods for producing ZnTe/ZnSe NC to date are those of Bang *et al.* [50] and the MIT master thesis of Guan *et al.* [160]. These procedures use a modified version of the diethyl Zn method of Xie *et al.* for the ZnTe core seeds. Bang *et al.* uses the slow co-injection of diethyl Zn and Se-TOP at 220-240°C into HDA-ODE ZnTe NC reaction solution whilst Guan *et al.* uses the SILAR technique with Zn oleate and Se-TOP 240°C in an OLA-ODE solution. As mentioned in section 5.2.2, this thesis sets out to lessen the use of highly pyrophoric diethyl Zn and therefore the superhydride method is used to synthesise the ZnTe cores. Several over-coating procedures were attempted including procedures using diethyl Zn and Zn oleate with and without the addition of amines as described in section 4.1. Specific focus has been placed on Zn oleate without the addition of amines as a precursor to enable a common ligand combination to be used throughout the synthesis and characterisation, thus enabling a comparison to theoretical calculations without the need for ligand exchange. This was required as the ligand exchange protocols attempted did not maintain NC PL (not shown here).

Since the Zn oleate protocol without the use of amines is the primary focus of these investigations, it must be noted that to use Zn oleate as a Zn precursor makes the addition of ZnSe highly dependent on the reactivity of the Zn oleate precursor itself (which decreases with increasing ligand concentration) and the NC surface area to volume ratio (which decreases the reactivity with increasing size due to the enhanced steric hindrance

of the ligand). This means that up to 5 ML ZnSe could be grown with an oleic acid to Zn ratio of 9:1 whilst larger core diameters required 2.5:1 ratios. The full synthesis protocols are described in section 4.1.

The lattice mismatch of ∼7% between the core and shell materials introduces the potential for defects through inhomogeneous growth. Many techniques have been employed for shell growth, however recently SILAR has been shown to keep high QY by promoting homogeneous defect-free shells through ML growth whilst maintaining or enhancing the size distribution [51, 77]. To enable SILAR to be utilised both the core seed concentration and diameter need to be known. Unlike Cd based NC, no investigations between absorption and concentration have been conducted [172], fortunately all the ZnTe core methods attempted here use highly reactive precursors and it was empirically found that the ZnTe core reaction could be considered quantitative. Thus, the original core precursor stoichiometry and the core diameter as found by TEM, are sufficient to find the concentration of the ZnTe dispersion as similar described by Xie *et al.* [9]. Using this approach the shell could be grown to within ∼10% of the required shell thickness. If this was not the case, extra steps of atom absorption spectroscopy would be required to calculate the ZnTe concentration which would very time consuming [172].

As seen in figure 5.2a and 5.2b the anion/cation or cation/anion growth sequence makes negligible difference to the overall excitonic shift for the 1 ML growth. The initial injection of Se-TOP took 25 minutes to see a saturation of the redshift of the first excitonic absorption feature which implies the completion of the shell growth. The feature showed a redshift of 14 nm from the initial ZnTe absorption feature. The feature is further redshifted by 1 nm with the addition the Zn oleate after a growth period of 30 minutes. With the addition of Zn oleate, the first excitonic feature progressively becomes weaker without the loss of general form or significant redshift. The reverse

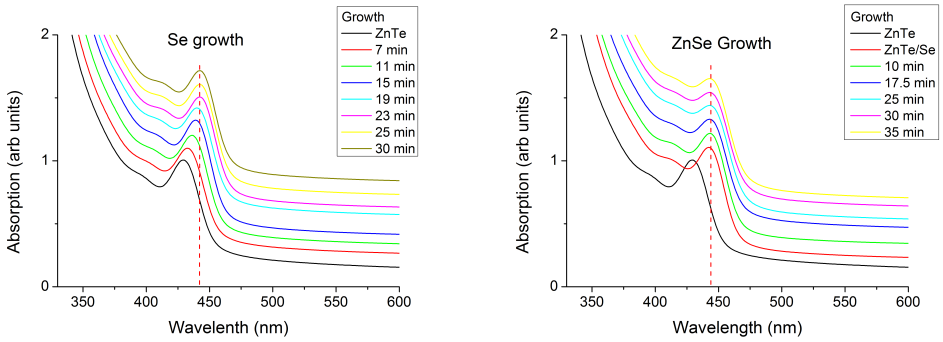

(A) Se-TOP then Zn oleate

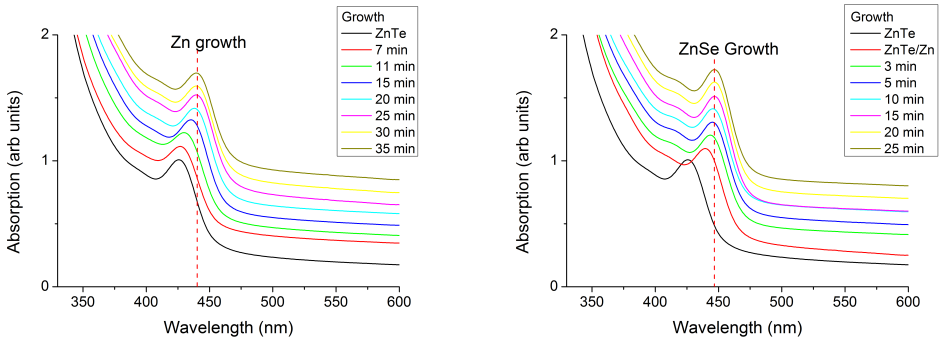

(B) Zn oleate then Se-TOP

FIGURE 5.2: Room temperature absorption spectra showing the evolution of the first excitonic feature with time using SILAR growth method, with the precursors sequence of a) Se then Zn b) Zn then Se. The red dotted line highlights the point of saturated redshift.

sequence produced an initial 10 nm redshift after 30 minutes of Zn oleate growth and then a further 6 nm redshift after 20 minutes of Se growth. The excitonic feature showed no significant weakening unlike the Se-Zn sequence. This thus implies that there is a faster transition to a type-II structure for the Se-Zn than the Zn-Se sequence and addition of Zn before Se produces a larger type-I structure.

As seen in figure 5.3, further investigation for subsequent ML shows that the Se produces the red shift whilst the Zn does not significantly redshift the excitonic feature. This is similarly true for the reverse sequence and has been similarly seen by Nemchinov *et al.* in the type-II structure of ZnSe/CdS [77]. This result is in contrast with co-injection shelling techniques which yields a smooth redshift [50, 77]. TEM investigations did show NC growth within this time implying that Zn growth was taking place. This therefore

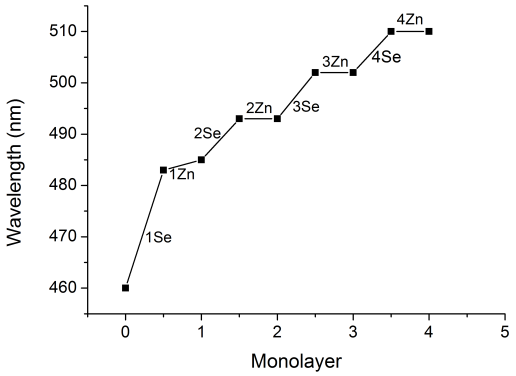

FIGURE 5.3: The evolution of first excitonic feature as determined by *in situ* absorption spectroscopy after each precursor injection and growth

supports the idea that the 4s atomic orbital of the Zn cation which contributes to the conduction band does not significantly modify the overall electronic structure in the type-II heterojunction whereas the 4p atomic orbital of the Se anion which contributes to the valence band does significantly modify the overall electronic structure [101].

Whilst 235-240°C was found to be the reaction temperature of the precursors, Ostwald ripening only occurred in excess of 245°C for the 2.4 nm diameter core but as the NC size increases past 3.6 nm the Ostwald ripening temperature also increases to 250°C. Once one ML of Se had been grown, it was found that no more Ostwald ripening took place up to 270°C as identified by a lack broadening in the PL FWHM. This result is consistent with other ZnSe non-amine activated synthesis protocols which require reaction temperatures in excess of 280°C [42, 171]. Table 4.1 shows the optimum reaction temperatures to minimise Ostwald ripening and enable the precursors to react.

5.4 Physical characterisation of ZnTe/ZnSe nanocrystals

This section sets out to demonstrate the physical properties of ZnTe/ZnSe NC focusing on the techniques of TEM, HRTEM, XRD and XPS. TEM investigations highlight the growth dynamics for various capping techniques. Subsequent HRTEM and XRD investigations set out to explore crystal structure and the role of strain in the structures. Further investigations using synchrotron XPS highlight the quality of the core-shell interface. HRTEM, XRD and XPS simulations and critical radius calculations have also been conducted to help identify and account for strain effects within the experimental results.

5.4.1 TEM characterisation

TEM investigations of the as-grown ZnTe cores show that the NC are largely spherical, only occasionally showing the non-spherical NC that one might expect from a zinc blende structure (Figures 5.4a, 5.4d and 5.4g). As described perviously the core size distributions can be as low as 7-9% with sharp size distribution profiles as seen by the inset of figures 5.4. This figure shows that the addition of ZnSe using the SILAR technique maintains the the size distribution profile and size distribution of the core as will be discussed further in table 5.3 in section 5.5.1. The shell procedure also produces spherical or quasi-spherical particles for all core sizes, except for core diameters above 3.6 nm with shell thicknesses over 3-4 ML (Figure 5.4).

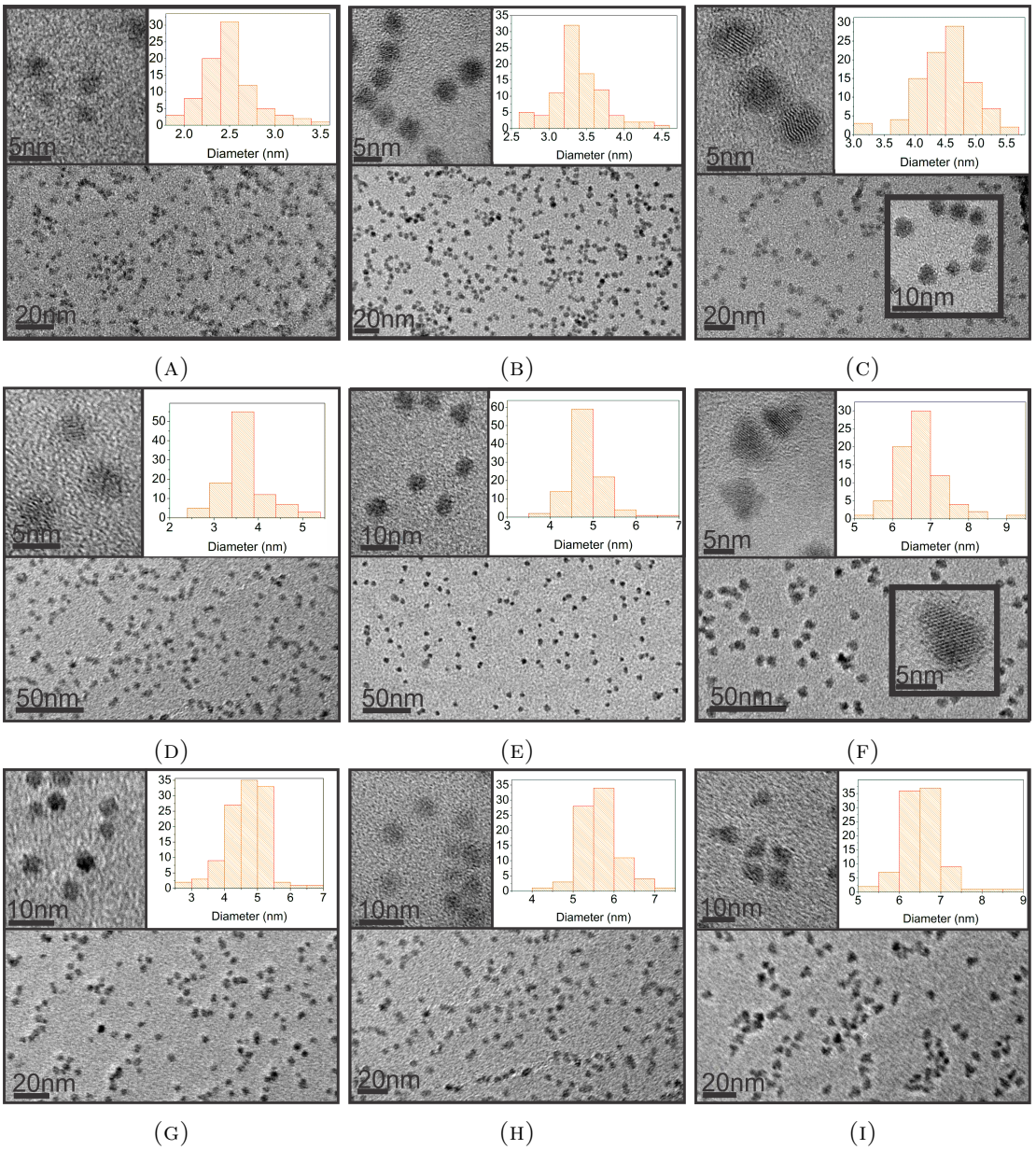

FIGURE 5.4: a,d,g) TEM images showing spherical a] 2.4 nm, d] 3.6 nm, and g] 4.6 nm ZnTe diameter cores. b-c) TEM images of ZnTe/ZnSe core-shell NC with a 2.4 nm core continuing to show spherical behaviour with b] 2 ML and c] 4 ML ZnSe shell growth. e,h,f,i) TEM images of ZnTe/ZnSe core-shell NC with a 3.6 nm and 4.6 nm diameter cores showing spherical structures with e,h] 2 ML ZnSe shell, and f,i] anisotropic tetrahedral or cubic structures observed with 5 ML ZnSe shell growth respectively. The insets show high magnification images to confirm the shape including some high resolution images and the corresponding size distributions.

For the largest core diameters and largest shells, anisotropic cubic or quasi tetrahedral structures are formed as seen in figures 5.4f and 5.4i. To test the robustness of these growth behaviours several shelling techniques were attempted including SILAR-TC [54]

and the use of various Zn precursors [9, 46, 95, 158] and conditions which have been shown by others to produce spherical NC growth in other Zn based systems.

Figure 5.5 highlights the NC shape with ∼5 ML shell growth using the following techniques;

1. SILAR-TC using Zn oleate and Se-TOP at 160°C and raised to 240°C (Figure 5.5a) [54].
2. Oleylamine activated Zn oleate and Se-TOP at 220°C and 240°C (Figure 5.5b) [9, 95, 160].
3. Zn acetate TOP and Se-TOP: each ML was injected at 160°C and left for 30 minutes and heated up to 240°C (Figure 5.5c) [46, 158].
4. Diethyl Zn and Se-TOP as shell precursor at 220°C (Figure 5.5d) [50].
5. Zn stearate and Se-TOP at 240°C (Figure 5.5e) [158, 176].
6. Using the diethyl Zn core synthesis method of Xie *et al.* and Zn oleate and Se-TOP shell growth at 240°C (Figure 5.5f) [9].

The proposed mechanism behind each scheme can be described in the following way:

Scheme 1, SILAR-TC, was shown by Blackman *et al.* to overcome specific facet growth which produced 'peanut' shape in CdS/CdSe and CdSe/CdTe NC [54, 65]. This technique heated the reaction solution quickly from a temperature that was significantly lower the reaction temperature of the precursor to the reaction temperature. The theory surmised by Blackman [54] which is a development of theories of Peng *et al.* [38], suggest that elongated NC are preferentially grown when the reaction solution has a high monomer concentration and thus the solution environment has a high chemical potential.

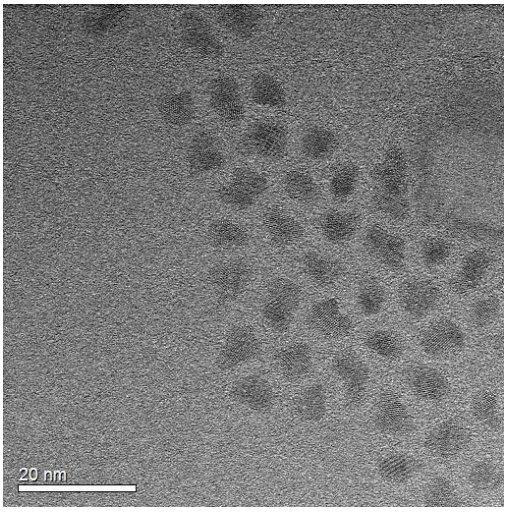

(A) SILAR-TC

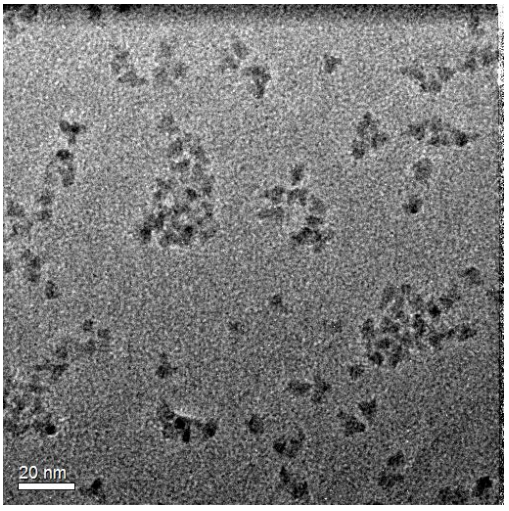

(B) Oleylamine Zn oleate Se-TOP

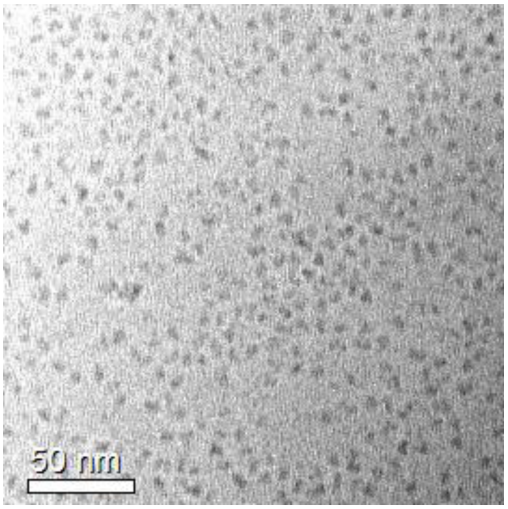

(C) Zn Acetate TOP and Se-TOP

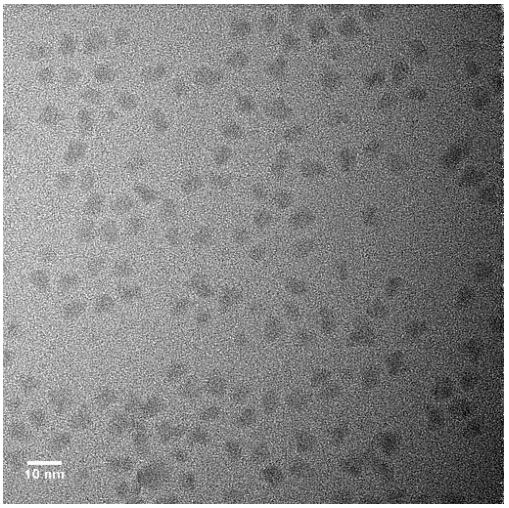

(D) Diethyl Zn and Se-TOP

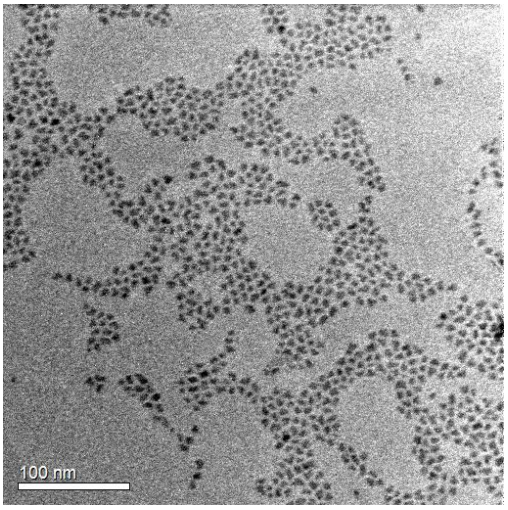

(E) Zn Stearate Se-TOP

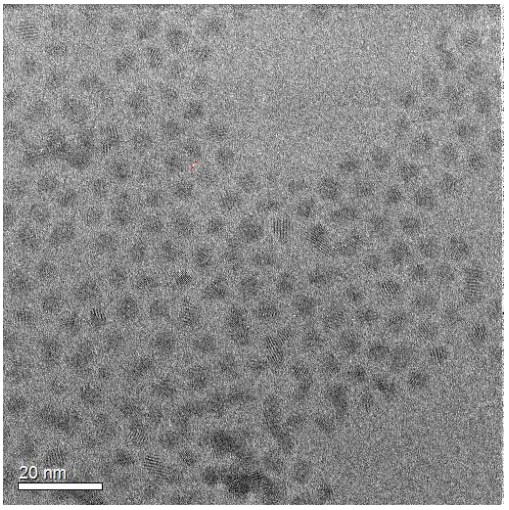

(F) Xie method ZnTe cores, Zn oleate/Se-TOP shell

FIGURE 5.5: TEM images showing anisotropic growth with ∼5 ML of ZnSe using a variety of Zn precursors growth.

SILAR-TC has the potential to "offer the monomers sufficient time to be adsorbed onto the surface of the existing nanocrystals in the solution prior to the growth" [54]. Schemes 2, 3 and 4 serve to change the reactivity of the precursors [9, 46, 95, 158]. Scheme 2 uses oleylamine to activate the Zn oleate and is in keeping with the ZnTe/ZnSe synthesis of Guan *et al.* and other known capping techniques [9, 51, 158, 160]. Scheme 3 proposes to use Zn acetate which naturally decomposes at 237°C and at lower temperatures in the presence of ligands [46, 158]. Scheme 4 uses diethyl Zn which is generally known to be highly reactive and was used by Bang *et al.* to produce ZnTe/ZnSe NC. Scheme 5 serves to investigate the steric hinderance of saturated and unsaturated surfactants where the double bond within oleic acid can produce an interwoven surface providing better steric hinderance when compared to the straight chain of the stearic acid [176]. Scheme 6 serves to test the potential unseen anisotropy of the core and thus anisotropic growth in the shell by synthesising cores via the diethyl Zn Xie method.

Since these techniques produced similar anisotropic growth and are comparable to observations reported by Guan *et al.* for ZnTe/ZnSe NC and Ivanov *et al.* for CdS/ZnSe NC [46, 160]. It was therefore postulated that strain could be effecting the growth dynamics. To test whether strain could be a contributing factor to shell growth dynamics, NC were synthesised with an alloyed interface which would mitigate strain effects at the core-shell interface [46]. Alloying the shell with 10% of Te (equivalent to 1 ML ZnTe growth) over first 4 ML showed a marked improvement in the spherical nature of large NC with thick shells (Figure 5.6) and highlights a possible reason for the anisotropic growth. It is interesting to note that growing the NC with 5% of alloying (equivalent to 0.5 ML ZnTe growth) still had a significant amount of anisotropic growth, highlighting this amount of alloying was insufficient to overcome the core-shell strain.

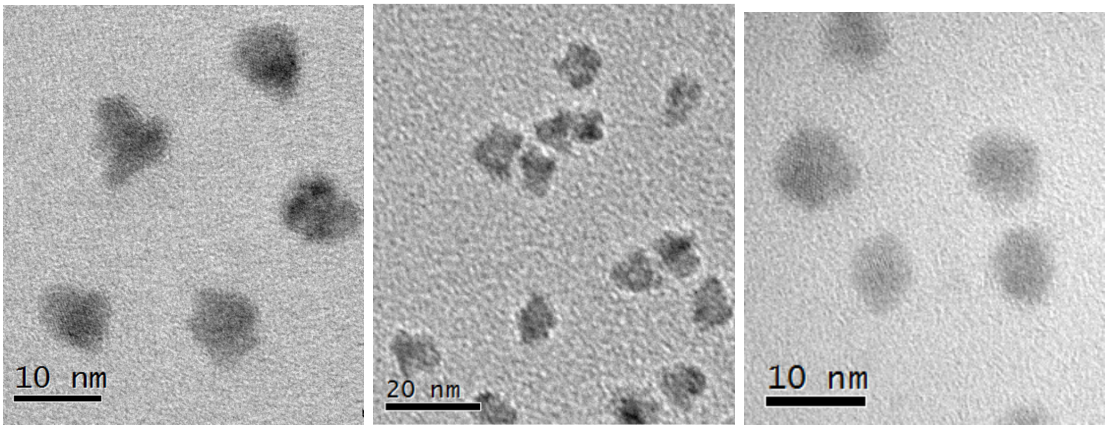

(A) (B) (C)

FIGURE 5.6: TEM images of 4.6 nm diameter ZnTe core NC with a) 5 ML ZnSe b) 5% alloying of the interface c) 10% alloying of the interface.

5.4.2 High resolution TEM (HRTEM) characterisation

Figure 5.7 shows high resolution images for all the core sizes with large shell thickness. Figure 5.7a shows an almost constant lattice constant over the whole NC for the smallest core diameter. The fast Fourier transform (FFT), which highlights the periodicity between atomic planes in reciprocal space akin to a diffraction pattern, shows an almost constant reciprocal interplane distance over the whole NC and corresponds to a zinc blende lattice structure with a lattice constant of 5.83(±0.05) Å. Figure 5.7b and 5.7c shows HRTEM images of the largest core diameters and shell thickness which show significant variations in lattice constant from the core to the shell. The corresponding FFT over the whole of NC shows an average lattice constant of 5.85(±0.05) Å and 5.92(±0.05) Å for 3.6 nm and 4.6 nm diameter cores respectively. However, a closer inspection of the centre and edge FFT, highlighted by the red squares in figure 5.7b and 5.7c, shows a variation lattice constant of 5.89(±0.13) Å to 5.67(±0.13) Å for 3.6 nm diameter core and 5.97(±0.13) Å to 5.85(±0.13) Å for the 4.6 nm diameter core respectively. This observation is consistent with the idea of a compressed core and lattice constant relaxation in a strained shell.

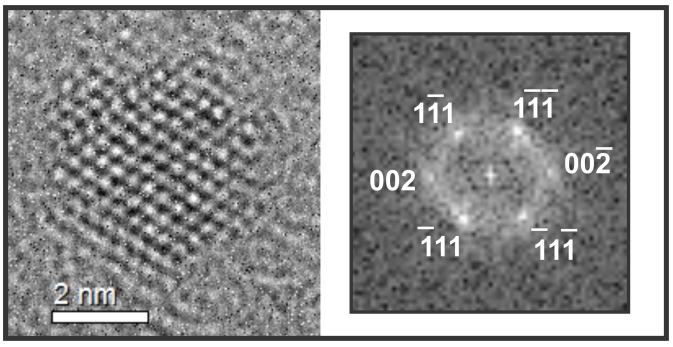

(A) 2.4 nm ZnTe core

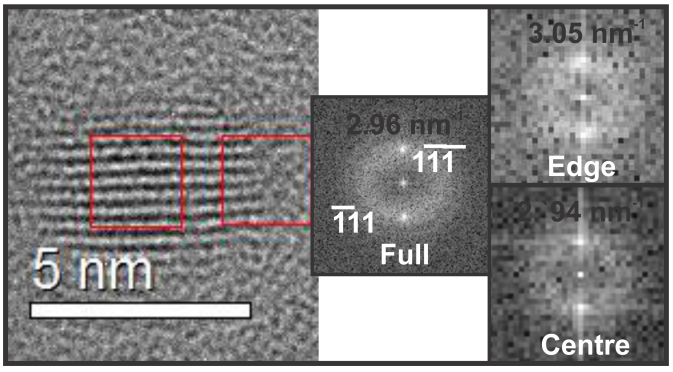

(B) 3.6 nm ZnTe core

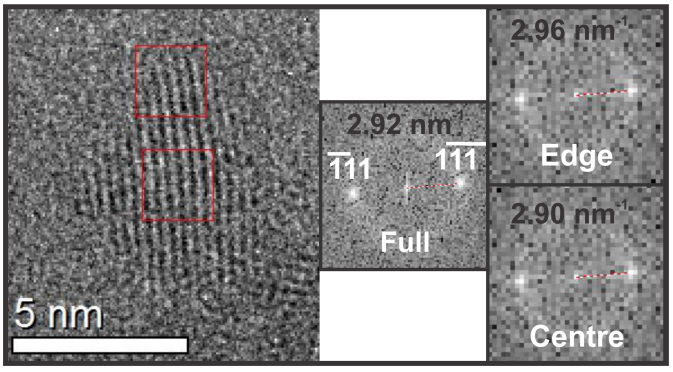

(C) 4.6 nm ZnTe core

FIGURE 5.7: HRTEM images of a) 2.4 b) 3.6 and c) 4.6 nm ZnTe core diameter NC with 4-5 ML ZnSe shell growth showing a) a spherical NC with FFT corresponding to zinc blende space group projected in the [022]. The indexed {111} reciprocal lattice plane distance of 2.97(±0.03) nm^{-1} corresponds to a zinc blende lattice constant of 5.83(±0.05) Å. b/c) A quasi spherical NC with an FFT showing a zinc blende space group. The indexed {111} reciprocal lattice plane distance showing an average lattice constant of 5.85(±0.05) and 5.92(±0.05) Å respectively but b-c) show lattice variation over the centre and edge of the NC relating where the reciprocal lattice plane distance is b) 2.94(±0.10) and 3.05(±0.10) nm^{-1} respectively for the 3.6 nm core which relate to a lattice constant of 5.89(±0.13) Å and 5.67(±0.13)Å respectively and c) 2.90(±0.10) and 2.96(±0.10) nm^{-1} respectively for the 4.6 nm ZnTe core and relating to a lattice constant of 5.97(±0.13) Å and 5.85(±0.13) Å respectively.

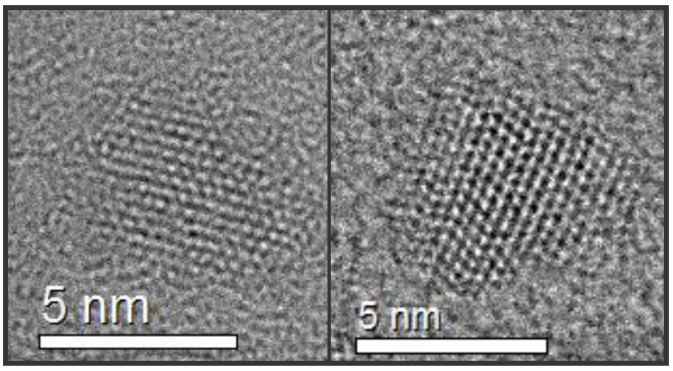

FIGURE 5.8: HRTEM images of 3.6 nm ZnTe core diameter NC with 4 ML ZnSe growth showing quasi-tetrahedral NC with a large amount of twinning stacking faults.

Figure 5.8 shows two quasi-tetrahedral NC with 3.6 nm diameter core NC with 4 ML ZnSe shell growth that show large amounts of stacking faults (predominantly twinning) which can potential be related to the observation of strain relaxation mechanism within the system.

5.4.3 Simulation of HRTEM data

Figure 5.9 shows a comparison of the experimental image shown in figure 5.7a and simulated micrographs of a 2.4 nm diameter ZnTe core NC with 4 ML ZnSe viewed in the [022] direction. A comparison of the two micrographs shows the NC to be slightly smaller (0.3 nm/0.52 ML) than average NC for this size however still within size distribution of the core. An inspection of the images and the corresponding FFT of figures 5.9c and 5.9d show that both NC have a zinc blende crystal structure with a lattice constant of 5.83($\pm$0.05) Å and 5.85($\pm$0.02) Å for the experimental and simulated images respectively. To account for the perceived single lattice constant one makes inspection of the atomistic structure used to model NC (Figure 5.9e). This figure highlights that strain is included in the model however the compression of the core is larger than large core diameters and thus the perceived accumulated shifts in atomic positions are small. Thus the electron wave only sees a slight deviation along the atom columns and a perceived single lattice constant is observed.

A further comparison of the images helps identify twinning stacking faults on the $(1\bar{1}1)$ and $(\bar{1}11)$ facets within the experimental image, potential highlighting the onset of anisotropic growth.

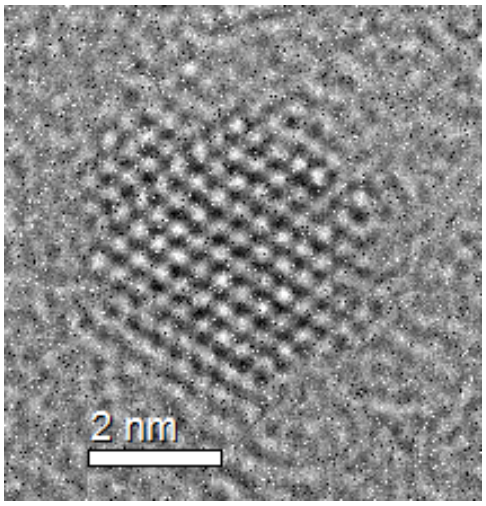

(A) Experimental micrograph

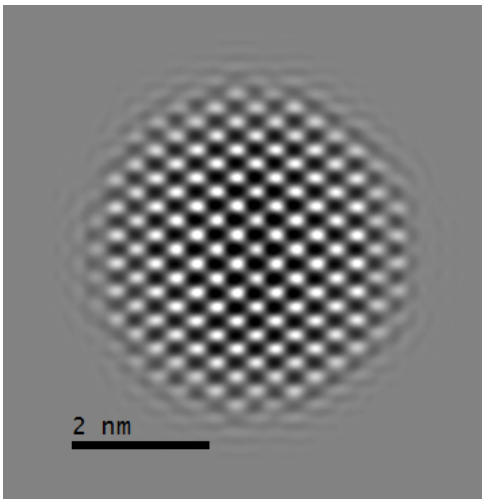

(B) Simulated strained NC micrograph

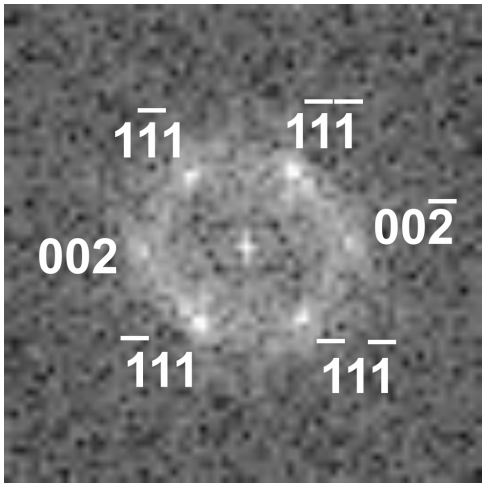

(C) FFT of [a]

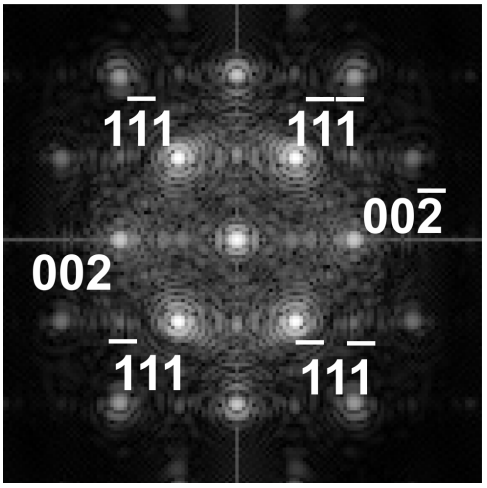

(D) FFT of [b]

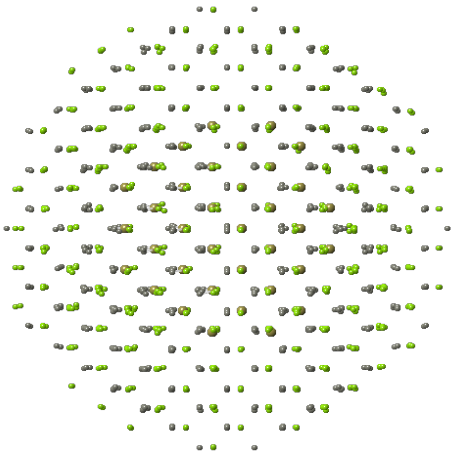

(E) Atomistic strain NC used in [b]

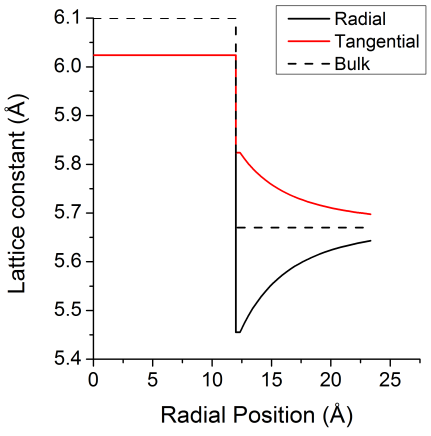

(F) Lattice constants used for [e]

FIGURE 5.9: a) HRTEM image of a 2.4 nm diameter ZnTe core NC with 4 ML ZnSe shell observed in the [022] direction. b) A simulated 2.4 nm diameter ZnTe NC with 4 ML ZnSe shell observed in the [022] direction (Images and simulations used a JEOL 4000EX HRTEM running at 400 kV. Defocus was taken to be -24 nm). c-d) The corresponding indexed FFT of the c) experimental image [a] and c) simulated image [b]. The reciprocal lattice distance to the {111} Bragg reflection for the experimental and simulated FFT are 2.97($\pm$0.03) nm^{-1} and 2.96($\pm$0.01) nm^{-1} respectively. This corresponds to a zinc blende lattice constant of 5.83($\pm$0.05) Å and 5.85($\pm$0.02) Å respectively. e) The atomistic model used to simulate figure [b] viewed in the [022]. f) The radial and tangential lattice constants used in the atomistic model of [e].

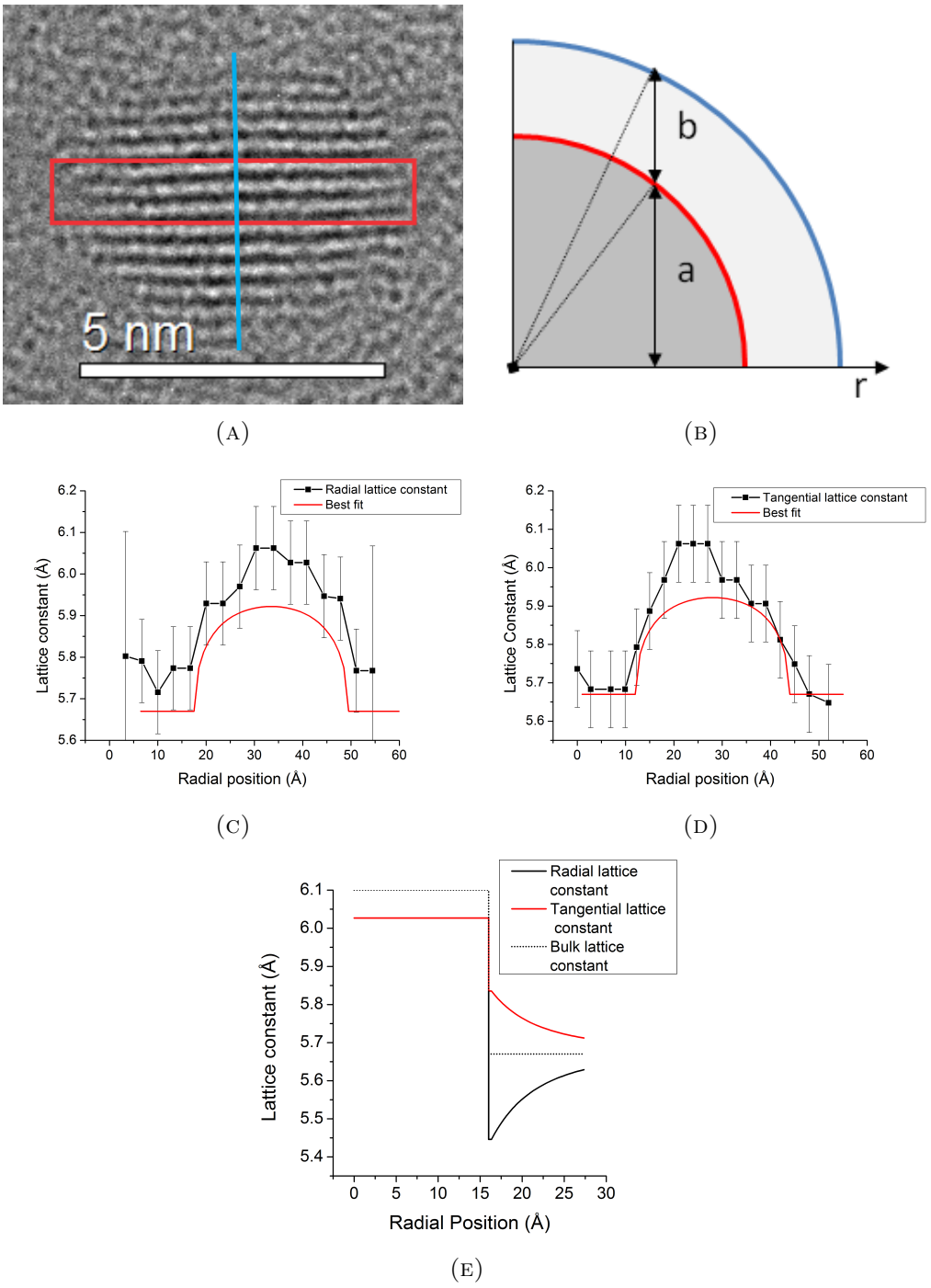

FIGURE 5.10: a) A HRTEM image of 3.6 nm diameter ZnTe core NC with 4 ML ZnSe shell highlighting the radial (Blue) and tangential (Red) regions investigated. b) A schematic of the simple compositional model used to calculate the best fit lattice constants in figure [c-d]. The observed lattice constants along c) the radial and d) tangential components of the NC. e) The predicted radial and tangential lattice constant using the continuum elasticity model for a 3.2 nm diameter ZnTe core NC with 4 ML ZnSe shell.

Figure 5.10 shows that larger NC do show variations of lattice constant and, in some

cases, a spherical geometry which allows for further analysis. Figure 5.10a shows a 3.6 nm diameter ZnTe core NC with 4 ML shell growth which was chosen for analysis. An inspection of the inter-plane distance at regular intervals over the radial (Blue line figure 5.10a) and tangential (Red box figure 5.10a) axis, as seen in figure 5.10c and 5.10d, shows a slow transition from the core lattice constant to the shell which is not consistent with the sharp lattice constant interface predicted within the pure continuum elasticity model in figure 5.10e. To account for this gradual transition to the shell, a basic assumption was applied, namely a TEM image is a 2-D projection of a 3-D object and the lattice constant observed will be the average lattice constant of the composition that the electron travels through as seen in figure 5.10b (i.e. Vegard's law applied to each electron pathway). Figure 5.10c and 5.10d show the predicted lattice constants with respect to the experimental lattice constants seen in figure 5.10a. Applying this seemingly simple model and sweeping the core and shell radii, gives lattice constant trends which are very similar to a NC with a 3.2 nm diameter core and an average shell thickness of 4 ML. Whilst this smaller than average core diameter can be attributed to the lower end of the size distribution of the original cores (i.e. The 3.2 nm diameter core NC can be explained by the average lattice constant being 3.6 nm diameter core with a standard deviation of 10%), the change of lattice constant of the core from bulk seen in figure 5.10c and 5.10d could indicate that there has been a compression of the core as shown by figure 5.10e. Using the continuum elasticity model, the strain on the core at 4 ML shell thickness would be 11% (Figure 3.2b) which could account for the observed 3.2 nm diameter core assuming an original core diameter of 3.6 nm. Thus, the NC is simulated with the reduced core diameter of 3.2 nm with a shell thickness of 4 ML.

An interesting observation is the experimental lattice constants in the shell. Figure 5.10c shows the tangential experimental lattice constant in the shell to be 5.67($\pm$0.15) Å, which

corresponds exactly to the bulk ZnSe value. The corresponding radial component in the shell has a larger lattice constant of 5.78(±0.15) Å (Figure 5.10d). This is counter intuitive assuming the lattice constants predicted by the continuum elasticity model of figure 5.10e, which would predict a larger tangential component and a smaller radial component. This highlights that the direct comparison of the continuum elasticity model and experiment cannot be made. Thus, TEM simulations were performed using strained and unstrained models.

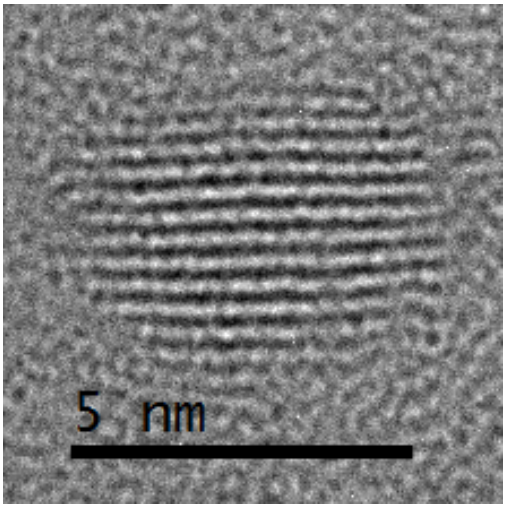

(A) Experimental HRTEM image

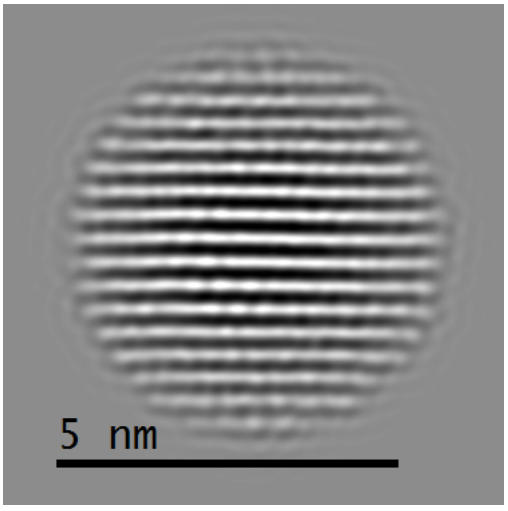

(B) Simulated HRTEM image: Strained

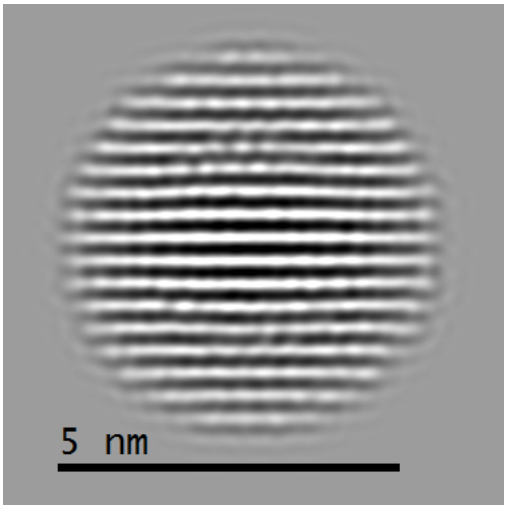

(C) Simulated HRTEM image: Unstrained

FIGURE 5.11: A comparison of the a) experimental, b) strain simulated and c) unstrained simulated HRTEM images for a 3.2 nm diameter ZnTe core NC with 4 ML ZnSe shell.

As seen by figure 5.11b and 5.11c, the strained and unstrained simulations provide subtly

different results. For the strained simulation, a subtly changing lattice constant from the core to shell is observed, whereas the unstrained simulation shows an more distinct interface around the core.

Figure 5.12a shows the lattice constants along the radial component of the experimental image and TEM simulations, and highlights a gradual transition from the core lattice constant to the shell for the strained model which shows very good agreement with experiment throughout the core and shell. The lattice constants along the radial component of the unstrained TEM simulation show an unexpected drop in the lattice constant at the core-shell interface before returning to the expected ZnSe lattice constant which does not follow experiment.

Figure 5.12b shows a comparison of the lattice constants along the tangential component for the strained and unstrained model and shows different trends when compared to radial component seen in figure 5.12a. The average experimental lattice constant within the core is 6.06($\pm$0.15) Å which shows very good agreement with the strained model which has an average lattice constant of 6.04($\pm$0.10) Å. Whilst the core follows a strained model, the experimental lattice constant shows a gradual transition to a shell lattice constant of 5.67($\pm$0.15) Å and follows the unstrained model accurately.

These results suggest that the NC is strained around the core and the radial component of the shell. Within the tangential component of the shell, the NC follows more closely with an unstrained model highlighting the possibility of dislocations within this region which would release strain. Following this interpretation, figure 5.13 shows four red dotted lines which highlight areas of least continuity along the planes and indicates possible stacking faults.

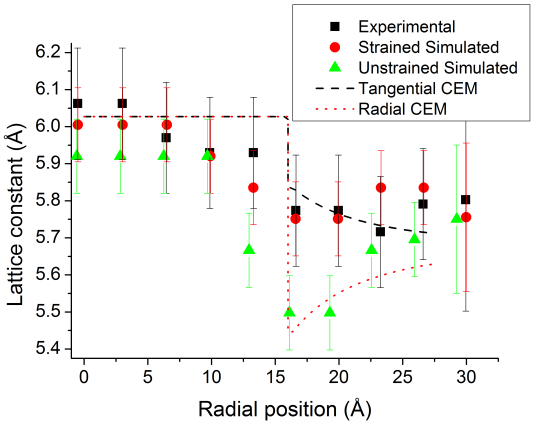

(A) Radial axis

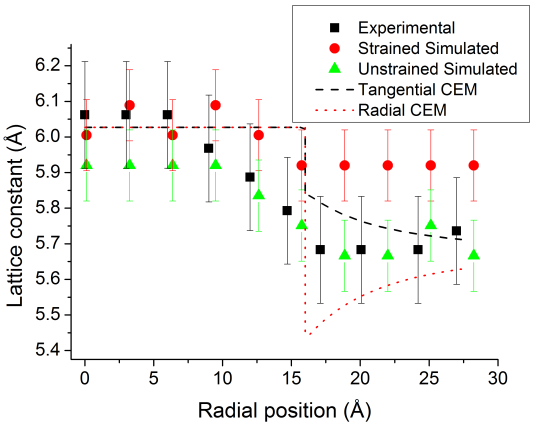

(B) Tangential axis

FIGURE 5.12: A comparison of the lattice constant obtained along the a) Radial and b) Tangential components, within the experimental, strained simulated and unstrained simulated HRTEM images. A comparison is also made to the tangential and radial component of the continuum elasticity model (CEM).

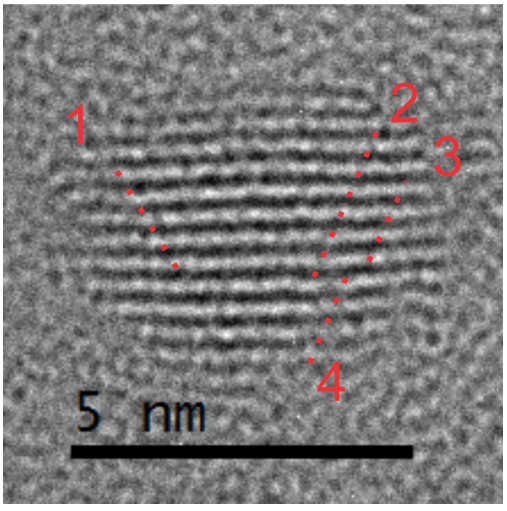

FIGURE 5.13: Four proposed stacking faults (Red dots) in a 3.6 nm diameter ZnTe core NC with 4 ML ZnSe shell.

For the interested reader, the Appendix E.1 describes further exploratory simulation work I have conducted to understand what further strain information could be obtained within core-shell NC using aberration-corrected microscopy and geometric phase correction.

5.4.4 XRD characterisation

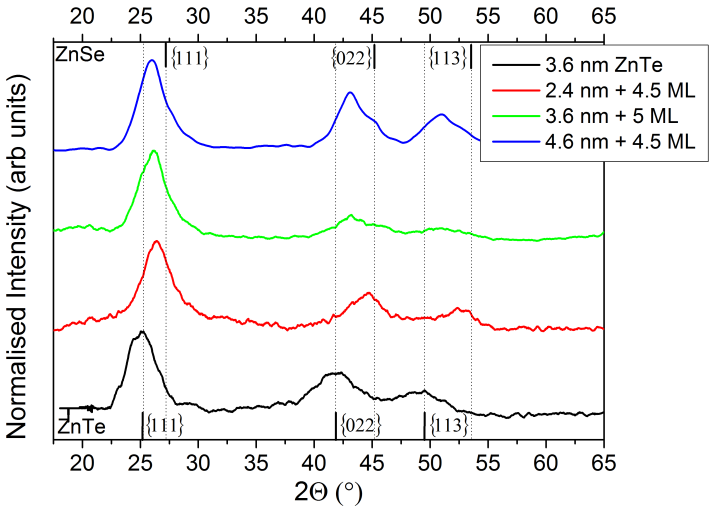

(A)

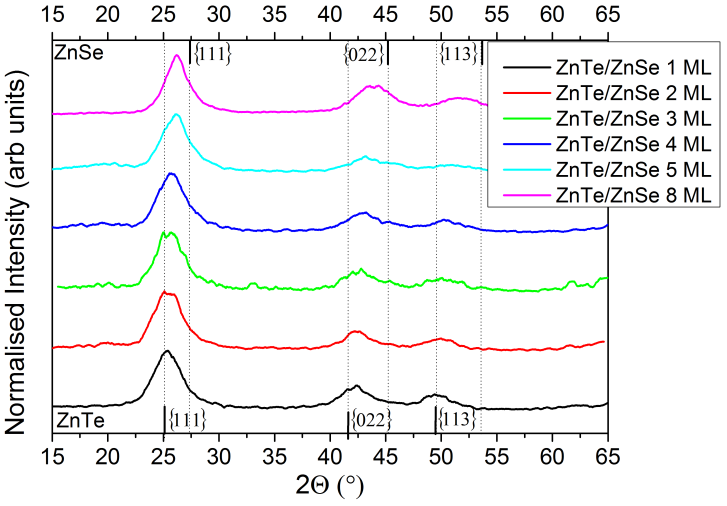

(B)

FIGURE 5.14: a) A comparison of the XRD powder diffraction patterns of 3.6 nm diameter ZnTe cores (Black) and ZnTe with large ZnSe shells with 2.4 nm diameter cores (Red), 3.6 nm diameter cores (Green) and 4.6 nm diameter cores (Blue). b) A comparison of the XRD diffraction patterns of 3.6 nm ZnTe core NC with 1 ML shell thickness (Black) increasing to 8 ML (Magenta) ZnSe shell thickness. The bulk diffraction peaks of ZnTe and ZnSe are highlighted at the bottom and top of the plot respectively.

Figure 5.14 shows the XRD patterns for ZnTe/ZnSe NC with various core diameters and a nominally constant shell thickness (Figure 5.14a) and a constant core diameter with increasing shell thickness (Figure 5.14b). These diffraction patterns are indicative

of zinc blende structure for all core and shell thickness.

Figure 5.14a shows that there is a shift from the ZnTe core diffraction pattern towards the diffraction pattern of ZnSe with increasing shell thickness. The smallest core diameter (Red: 2.4 nm diameter + 4.5 ML) shows the biggest shift towards the ZnSe lattice constant whereas the largest core diameter (Blue: 4.6 nm diameter + 4.5 ML) shows the smallest shift. The associated average lattice constant, as seen in table 5.1, is 5.78 Å, 5.91 Å and 5.93 Å for the 2.6 nm, 3.6 nm and 4.6 nm diameter cores with large shell thicknesses respectively. This variation between the smallest and the largest core diameters, is in part due to the composition of the NC, where, as is shown by table 5.1, the 'Precursor' molar ratio between the ZnTe and ZnSe materials for each core diameter is 10:90, 20:80 and 27:71 respectively and is consistent with epitaxial growth as seen previously in references [7, 9, 20]. As seen in figure 5.14b, a similar trend occurs for the shell thickness size series on a 3.6 nm diameter core. A calculation of these lattice constants using the {111} peak, seen in table 5.2, highlights a decrease in lattice constant from 6.10($\pm$0.03) Å for the core, to 5.88($\pm$0.03) Å for the largest shell thickness.

Whilst the {022} and {113} peaks seen in figure 5.14b are weak and no reliable peak width information can be gained, peak width information can be gained from the {111} peak. It is known that if the particle size is the only contributing factor to the peak width, the Scherrer equation gives a lower bound to the particle size [177]. The measured widths and calculated Scherrer diameters are seen in table 5.2 and show increasing disagreement with observed diameters (determined through TEM) with increasing shell thickness. The Scherrer diameters are smaller than the observed diameters, highlighting that the diffraction peaks are broader than excepted if one just considers a homogenous system. To account for this broadening, it is known that the inhomogeneous strain broadens the XRD peak [177], however application of a standard single material strain

	ZnTe:ZnSe ratio (%)	$a_{(Vegard)}$ (Å)	{111} Plane(Å)	{111} 2Θ (°)	{022} Plane (Å)	{022} 2Θ (°)	{113} Plane(Å)	{113} 2Θ (°)
2.4 nm Core 4.5 ML shell								
TEM	10:90	5.71	3.30	27.01	2.02	44.83	1.72	53.12
Precursor	10:90	5.71	3.30	27.01	2.02	44.83	1.72	53.12
XRD results	23:77	Ave.(5.78)	3.34(5.81)	26.57	2.04(5.76)	44.47	1.74(5.77)	52.60
3.6 nm Core 5 ML shell								
TEM	15:85	5.73	3.2	26.85	2.03	44.56	1.73	53.80
Precursor	20:80	5.76	3.33	26.79	2.04	44.46	1.74	52.64
XRD results	55:45	Ave.(5.91)	3.40(5.90)	26.12	2.09(5.92)	43.16	1.80(5.91)	51.22
4.6 nm Core 4.5 ML shell								
TEM	23:77	5.77	3.33	26.78	2.04	44.44	1.74	52.64
Precursor	29:71	5.80	3.35	26.62	2.05	44.17	1.75	52.32
XRD results	60:40	Ave.(5.93)	3.41 (5.91)	26.10	2.09(5.92)	43.16	1.79(5.95)	50.85

TABLE 5.1: A table relating the observed diffraction peaks of ZnTe/ZnSe NC in figure 5.14a to diffraction planes distances and lattice constants $a_{(Vegard)}$. The experimental diffraction peaks (XRD results) are related to the Vegard's law lattice constants obtained through ratio of the injected precursors ('Precursor') and the relative experimental TEM volumes of the core and shell (TEM).

term gives strain values that can be un-physically high (∼50%). Since this is a binary system the inclusion of a simple strain term would not be sufficient to account for peak broadening observed. Thus, XRD simulation is required and will be discussed in the next section.

	XRD {111} Peak Θ (°)	Lattice Constant (Å)	FWHM Θ (°)	Scherrer Diameter (nm)	TEM Diameter (nm)
2.4 nm diameter core					
4.5 ML	26.57	5.81	2.70	4.49	4.89
3.6 nm diameter core					
ZnTe*	25.28	6.10	3.20	3.60	3.60
1 ML	25.31	6.09	2.84	4.19	4.17
2 ML	25.45	6.06	3.06	3.80	4.73
3 ML	25.50	6.04	2.98	3.93	5.30
4 ML	25.72	5.99	2.91	4.04	5.87
5 ML	26.12	5.90	2.94	4.01	6.44
8 ML	26.21	5.88	2.13	6.25	8.14
4.6 nm diameter core					
4.5 ML	26.10	5.91	2.50	4.95	7.15
4.6 nm alloy diameter core with 5 ML ZnSe plus X% ZnTe					
5%	26.09	5.91	2.28	5.68	7.74
10%	25.48	6.05	2.13	6.23	8.05

TABLE 5.2: A table comparing the Scherrer diameter as determined through XRD and equation D.8, to the experimental diameter as determined through TEM. (*) The instrument broadening for the system was taken using ZnTe core diffraction the known diameter 3.6 nm.

One further point of note is the shape of the {111} diffraction peaks. Whilst the larger core diameters have a trend towards anisotropic {111} diffraction peaks with increasing shell thickness the peaks tend to maintain or broaden from the core as seen in table 5.2, the smallest core diameter with larger shell thickness (Red in figure 5.14a) shows no anisotropy and an almost Lorentzian line shape consistent with a single phase material [177]. This smallest core diameter diffraction peak also shows a narrowing in contrast to the other larger core diameter NC (Green and Blue figure 5.14a) and, as can be seen in table 5.2, correlates to a Scherrer diameter of 4.49 nm in reasonable agreement with TEM

found diameter of 4.89 nm. This result could indicate alloying of the core-shell interface NC. To analyse whether the NC are homogeneously alloyed, the XRD patterns can be analysed using Vegard's law (the underlying theory and calculations are described in the Appendix D.1.2). Table 5.1 shows the calculated 'Precursor' ratio and the composition ratio as determined by calculating relative volumes of the core and shell, and assuming no compression of the core as determined through 'TEM'. The relative composition and associated lattice constants are compared to those as determined by XRD. A comparison of this data shows the smallest cores have the closest lattice constant to a homogenously alloyed system, however there is still a significant variation (10:90 'Theoretical' versus 23:77 'Experimental'). Indeed none of the NC investigated show a purely homogenously lattice constant (Table 5.1). Whilst these results are indicative of strain effects, none are conclusive. To establish whether strain is a contributing factor to the XRD results, XRD simulation was conducted and is the subject of the next section.

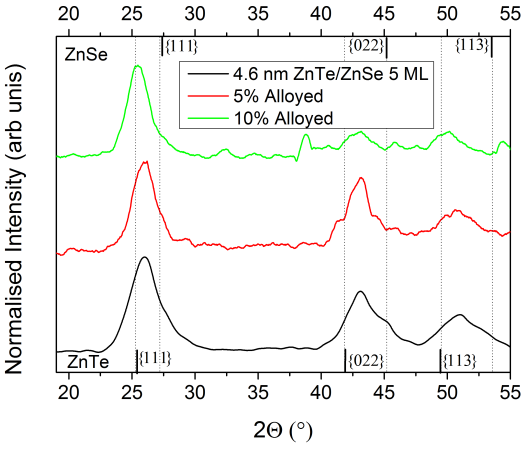

FIGURE 5.15: The XRD patterns for a 4.6 nm diameter ZnTe core with 5 ML ZnSe NC with a) an as-grown core-shell interface, (Black), b) 5% of alloying (Red) and c) 10% of alloying (Green) over the first 3 ML growth.

Further inspection of the alloyed interfaced XRD patterns continues to show a zinc blende crystal structure but there is a general narrowing and shift of the peaks towards the ZnTe lattice constant (Figure 5.15). The 5% alloyed shell shows no significant shift

from the original sharp core-shell interface (Red in figure 5.15). This implies that most of the Te has been incorporated into the first ML growth which does not significantly alter the overall structure of the NC. Incorporation of 10% alloying shows a significant shift towards bulk ZnTe lattice constant when compared to core-shell reference (Green in figure 5.15). As shown in table 5.2, the Scherrer diameters of the alloyed samples show significantly improved agreement to the TEM diameter when compared to sharp core-shell interface, thus implying that strain is a contributing factor to the broadening of the XRD peaks and further shows that the alloying mitigates strain.

5.4.5 XRD simulation

This sections describes the simulation of the XRD patterns using the strained NC model described in section 3.2 with the program *'DISCUS'* [144, 145]. These simulations use the Debye equation approach described in section 3.2 and accounts for thermal contributions by applying the Debye-Waller factors [145]. These simulations do not accounted for instrument broadening.

This section initially investigates unstrained structures to enable comparison to strained structures which are discussed later. Figure 5.16 shows the diffraction for two types of ZnTe/ZnSe NC in the simplest unstrained case. The first approach describes a 'two-layer' system with the form shown in figure 5.16c and gives the diffraction patterns of figure 5.16a. The second uses a 'core-shell' system as seen from figure 5.16d and gives the diffraction pattern seen in figure 5.16b. Both these approaches have nominally equal volumes of ZnTe and ZnSe respectively as seen in the projected models seen in figures 5.16c and 5.16d. The XRD patterns of the 'two-layer' system shows two superimposed diffraction patterns which can be easily identified as the bulk ZnTe and ZnSe diffraction patterns respectively with ZnSe diffraction peaks increasing in relative amplitude with increasing shell thickness. This diffraction pattern is akin to two independent phases. An inspection of the 'core-shell' simulations shows an initial ZnTe diffraction pattern that shifts with increasing shell thickness towards that of ZnSe. To explain this slow transition from ZnTe to ZnSe one must consider the close proximity of the core and shell atoms, thus, scattered X-rays will build constructive interference between the two materials giving rise to a perceived average of the two diffraction patterns. The 'core-shell' diffraction patterns have other interesting features marked such as $(*)$ in figure 5.16b, in which a new peak arises at smaller angles compared to the $\{111\}$ diffraction

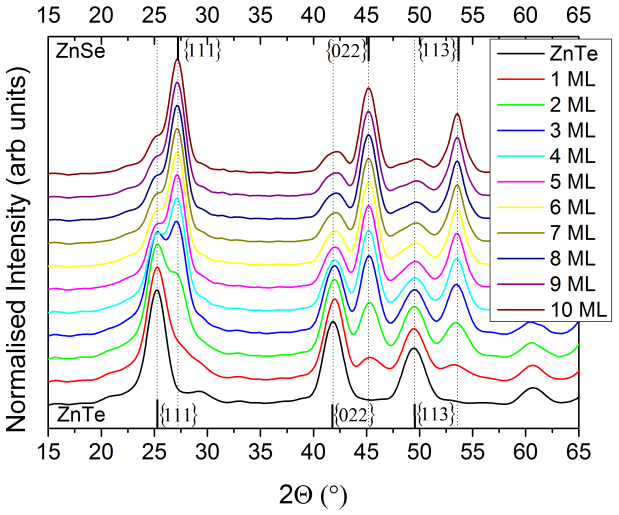

(A) Two-Layer

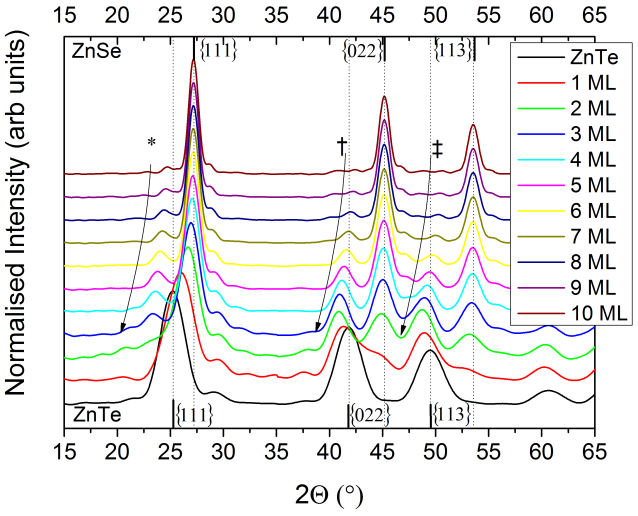

(B) Core-shell

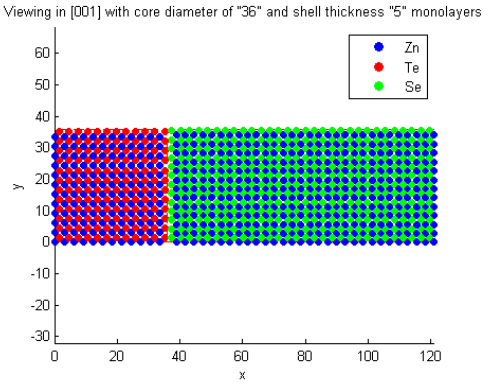

(C) Two-layer model

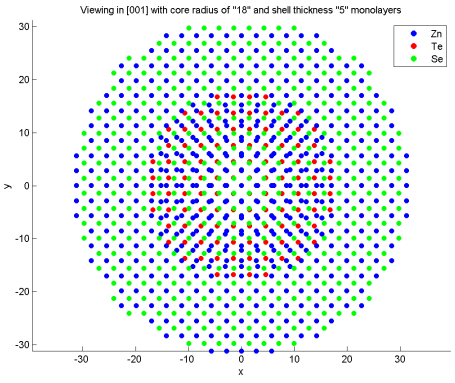

(D) Core-shell model

FIGURE 5.16: Simulated XRD patterns for a size series of unstrained ZnTe/ZnSe NC with 3.6 nm diameter cores and various shells in a) a 'two-layer' geometry and b) non-interacting 'core-shell' geometry. c) and d) show the corresponding atomistic models with 5ML of shell growth for simulation in figure [a] and [b] respectively.

peak. A further interesting feature is the initial shift to smaller angles of the {022} and {113} peaks marked (†) and (‡) respectively, these peaks then shift to larger angles for the larger shell thickness. These features are due to intrinsic stacking faults within the simple model used and will be discussed in further detail below.

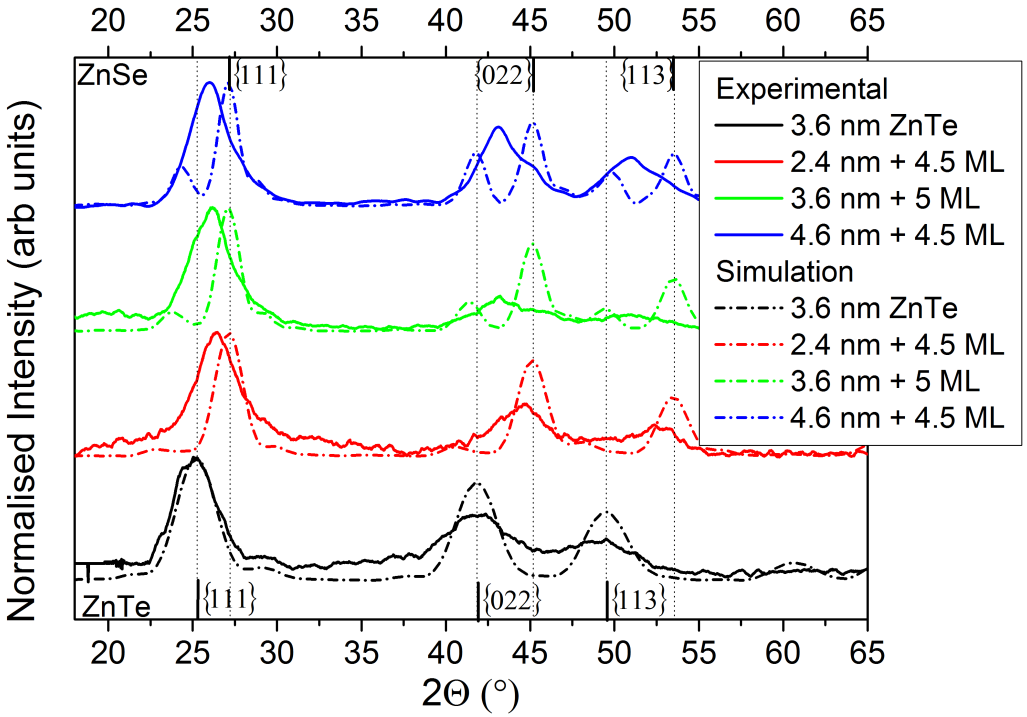

(A) Unstrained model 1: Non-interacting core-shell

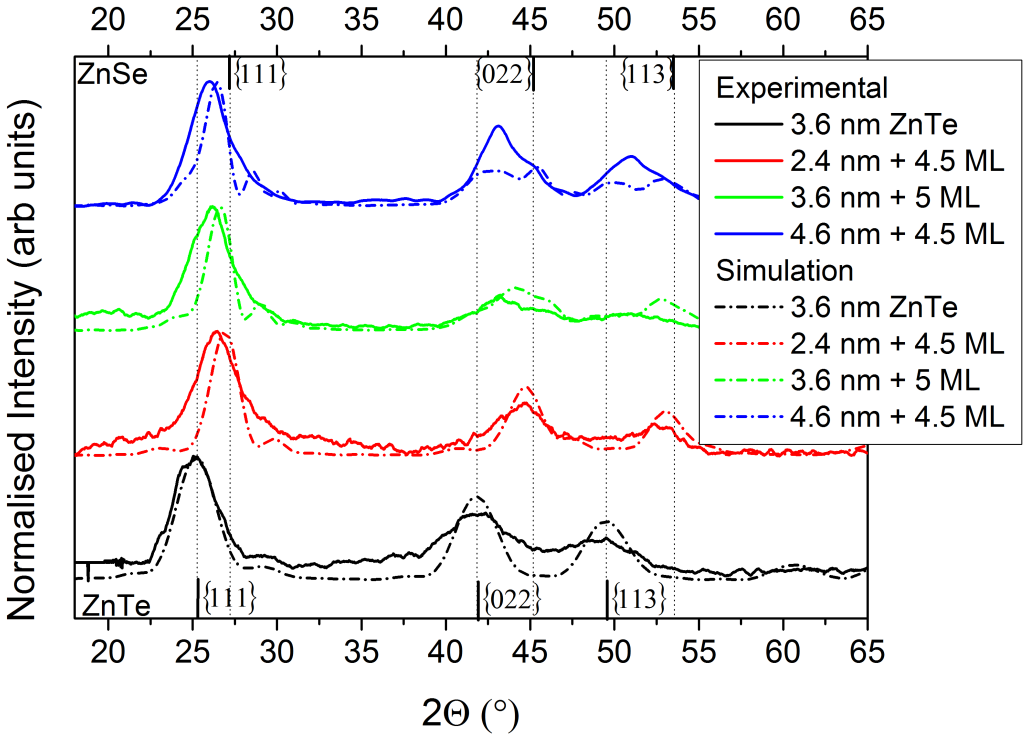

(B) Unstrained model 2: Quasi-epitaxially growth

FIGURE 5.17: Unstrained model 1 and 2: Simulated XRD patterns (Dotted line) for 3.6 nm diameter ZnTe cores (Black), 2.4 nm diameter ZnTe cores with 4.5 ML ZnSe shell (Red), 3.6 nm diameter ZnTe cores with 5 ML ZnSe shell (Green) and 4.6 nm diameter ZnTe cores with 4.5ML ZnSe shell (Blue), assuming a) a non-interacting core-shell and b) quasi-epitaxial growth. A comparison to the experimental diffraction patterns (Solid line) is also shown. The bulk diffraction peaks of ZnTe and ZnSe are highlighted at the bottom and top of the plot respectively.

One of the difficulties is to associate a strained model with an unstrained model. Since coherent unstrained growth within a lattice mismatched system is impossible, two simplifications can be considered.

1. Assumes a 'non-interacting' core and shell. i.e. the core and shell are built independently and the core and shell volumes are overlayed. (Figure 5.17a).

2. Assumes 'quasi-epitaxial growth' (Figure 5.17b). This uses the scheme 1 as seen in figure 3.5 in section 3.4 but it is noted that for large core diameters this system will break down.

The corresponding XRD simulations of the above schemes can be seen in figure 5.17a and 5.17b. The unstrained 'non-interacting' or 'quasi-epitaxial growth' models see larger shifts to the ZnSe lattice constant with increasing shell thickness than those seen in experiment (Figure 5.17a and 5.17b). Both simulations also see the appearance of two phases for the {022} and {113} diffraction peaks with increasing core diameter. For the 'non-interacting model' of figure 5.17a these peaks can be easily identified as bulk peaks, whereas the 'quasi-epitaxial growth' model of figure 5.17b sees a single peak for the smallest core diameter and almost two peaks for the largest diameter.

A comparison of the unstrained models highlights the role of stacking faults and dislocations in the XRD peaks. The 'non-interacting' model has exclusively stacking faults at the interface, thus the phase of the scattered X-rays in the interface region will be considerably different and will consequently not produce constructive interference to produce a single peak. The 'quasi-epitaxially growth' model has a more coherent interface and therefore has less stacking faults, thus the phases of the scattered X-rays will produce constructive interference to form a single superposition peak. It is also interesting to note the 'quasi-epitaxial growth' model has more dislocations with large core diameters

and produces the two {022} and {113} diffraction peaks. This, therefore indicates the limit of the 'quasi-epitaxial growth' approximation.

A strained NC can be modeled in two ways;

1. A 'full strained' model assumes that strain in the core and shell is described continuum elasticity mechanics and using building scheme 2 as discussed in section 3.2.

2. A 'faceted growth' model is described as model **1** above, but there is no compression of the core but strain in the shell. This considers a system where there is individual 'faceted growth' which would limit stress on the core.

The corresponding XRD simulations for the 'full strained' model and 'faceted growth' model can be seen in figure 5.18a and 5.18b respectively. Here the 'full strained' model of figure 5.18a shows better agreement with the experimental data diffraction peak maxima than the unstrained models of figure 5.17. This shows that strained epitaxial growth is required to accurately simulate the experimental diffraction patterns. The 'full strained' model (Figure 5.18a) and 'faceted growth' model (Figure 5.18b) show similar diffraction patterns for the smallest two core diameter. However on inspection on the 4.6 nm diameter core and 4.5 ML pattern shell (Blue figures 5.18a and 5.18b), the 'full strained' model describes the experimental diffraction peaks more accurately than the 'faceted growth', however the variation is small. These results imply that the shell is strained however there are still questions whether the core is strained or not.

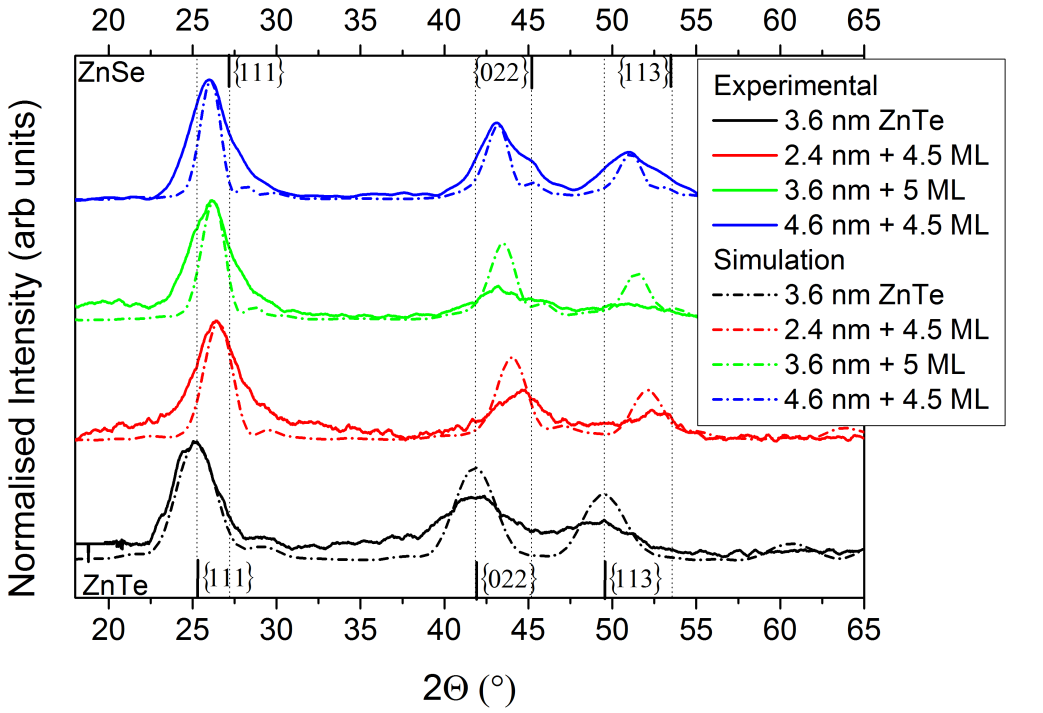

(A) Full strained model

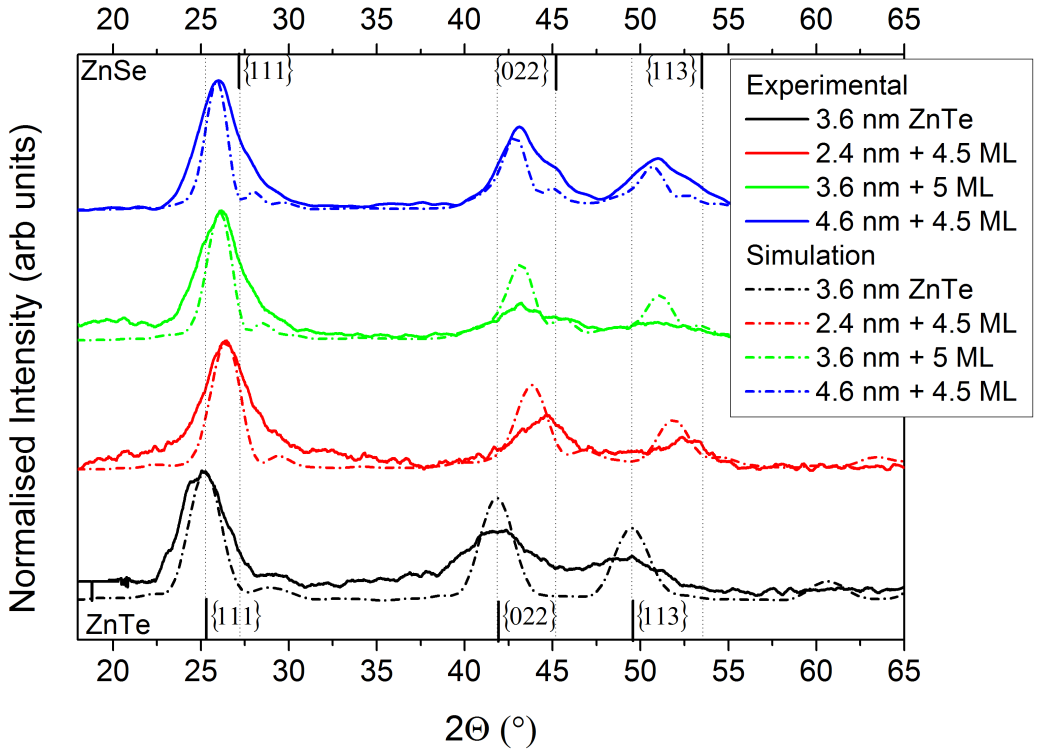

(B) Faceted growth model

FIGURE 5.18: Simulated XRD patterns (Dotted line) for 3.6 nm diameter ZnTe cores (Black), 2.4 nm diameter ZnTe cores with 4.5 ML ZnSe shell (Red), 3.6 nm diameter ZnTe cores with 5 ML ZnSe shell (Green) and 4.6 nm diameter ZnTe cores with 4.5 ML ZnSe shell (Blue), assuming a) a full strain model and b) faceted growth model. A comparison to the experimental diffraction patterns (Solid line) is also shown. The bulk diffraction peaks of ZnTe and ZnSe are highlighted at the bottom and top of the plot respectively.

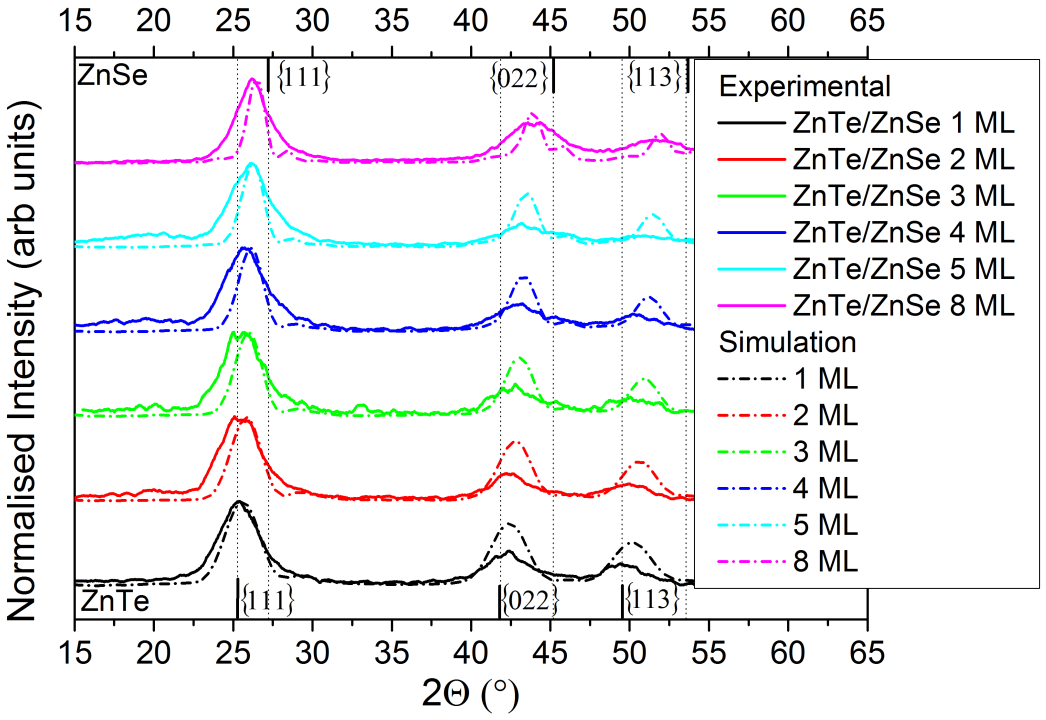

(A) Full strain model

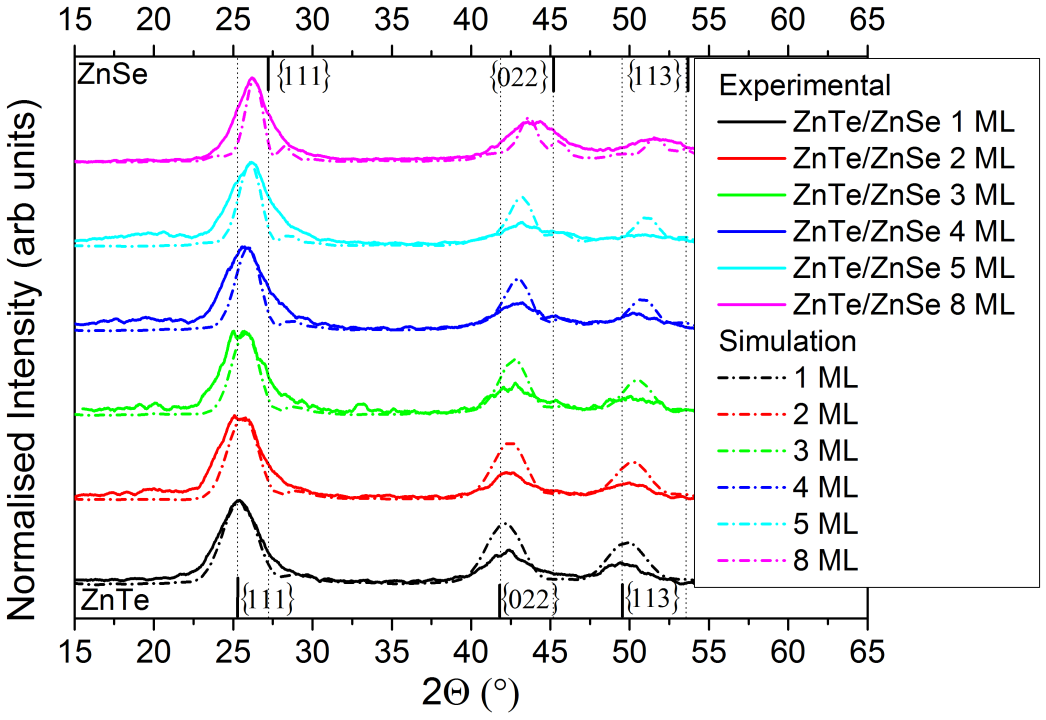

(B) Faceted strained model

FIGURE 5.19: Simulated XRD patterns (Dotted line) for a size series of ZnTe/ZnSe with 3.6 nm diameter cores and various shells for a) a full strain model and b) faceted growth model. A comparison to the experimental diffraction patterns (Solid line) is also shown. The bulk diffraction peaks of ZnTe and ZnSe are highlighted at the bottom and top of the plot respectively.

By simulating an entire shell thickness size series for a constant core diameter, as seen in figure 5.19a, it can be seen that the 'full strained' model shows an inferior fit at small shell thickness when compared to the experimental data. The 'full strained' model only accounts for the higher angle portion of each diffraction peak. To account for this lack of agreement, a 'faceted growth' model was considered, which shows improved agreement to the experimental data however the 'faceted growth' model still does not match with the experimental peak maxima (Figure 5.19b). Several explanations could be used to explain this lack of agreement at small shell thicknesses including alloying, defects and a breakdown of the continuum elasticity theory.

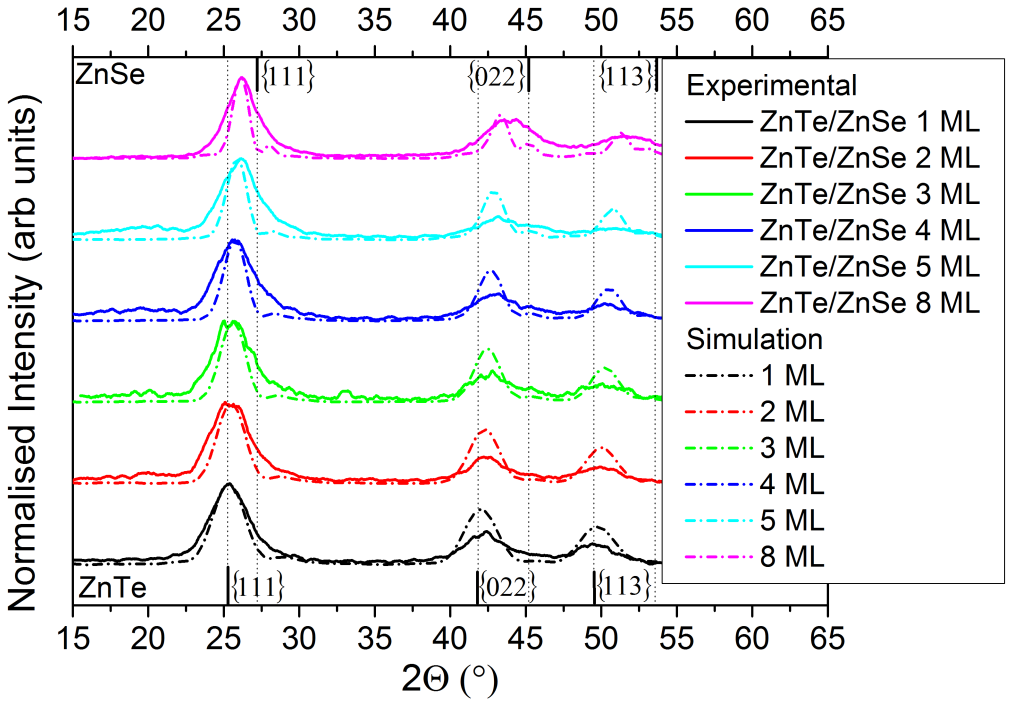

FIGURE 5.20: Simulated XRD patterns (Dotted line) for a size series of ZnTe/ZnSe with 3.6 nm diameter cores and various shells using the best fit parameters used to calculate the interface alloying. A comparison to the experimental diffraction patterns (Solid line) is also shown. The bulk diffraction peaks of ZnTe and ZnSe are highlighted at the bottom and top of the plot respectively.

To account for alloying, a coincidental error in inputting the materials parameters gave rise to an almost perfect fit at small shell thickness as seen in figure 5.20. These best

fit parameters are given in table B.3 and only influence the strain on the system. An inspection of the lattice constant seen in figure 5.21a shows that this change in parameter gives rise to mildly higher lattice constant profile over the NC (Red figure 5.21a) when compared to the 'full strained' model (Black figure 5.21a). It could be postulated that if the core is not alloyed and the continuum elasticity theory holds for small shell thickness, then the lack of compression of the core is due to a 'reduced pressure' from the shell. This reduced overall pressure will also reduce the strain in the shell, therefore to account for the best fit lattice constant in the shell, the difference in strain from the best fit and the reduced pressure, ($\Delta\epsilon$), must account for alloying. As seen in figure 5.21b, the interface pressure for this best fit lattice constant is almost 0.91 GPa more than half the 'full strained' model (2.1 GPa) for large shell thickness. Approximating the change in lattice constant to the tangential component only, this residual strain and thus lattice constant (Figure 5.21c) can be converted to composition by use of Vegard's law. Using this approximation, figure 5.21d shows the fraction of ZnTe within the ZnSe shell as a function of shell thickness. Initially there is alloying of 40% but this reduces below 10% by the 5 ML growth. The average amount of alloying can be calculated to be 21%. This amount of alloying is significantly higher than expected and borderline unfeasible considering the size and stoichiometry of the system. It must be noted that the core is assumed not alloyed in these calculations and thus to account for amount of alloying in the shell one needs to consider alloying from the interatomic diffusion of atoms across the core-shell interface which has been recently reported by others [129, 139, 178].

Ultimately these results show that there is agreement between the larger shell thickness and the strained model that the continuum elasticity model holds. However questions remain over the validity over the model at small shell thickness and whether alloying is taking place which should be the focus of further work.

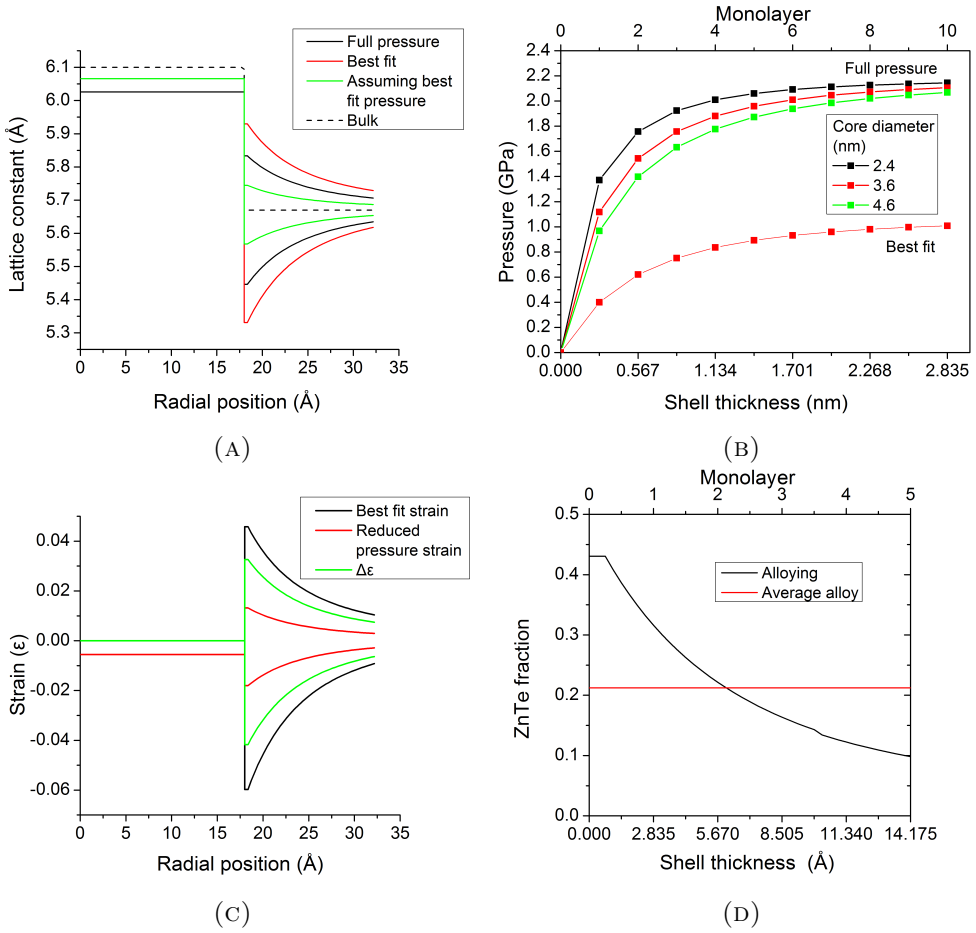

FIGURE 5.21: a) The radial and tangential lattice constants profiles of the full pressure model (Black), Best fit parameters used for figure 5.20 (Red) and the residual pressure model (Green) for a 3.6 nm diameter core with 5 ML shell. b) The pressure on the core as a function of shell thickness assuming a 'full pressure' model and 'residual pressure' model c) The tangential strain in the shell of the best fit model (Black), residual strain model (Red) and the variation between the two models (Blue), as a function of radial position for a 3.6 nm diameter core with 5 ML shell. d) The alloying and average alloying as function of radial position.

It is noteworthy to highlight that the experimental XRD patterns have broader peaks than those seen in the simulated diffraction patterns. Whilst it was shown in section 5.4.4 that the experimental diffraction pattern widths does not follow the Scherrer equation, these simulated patterns do follow the Scherrer equation and do partially follow the anisotropic peak shapes seen in the experimental diffraction peaks. To account for this lack of agreement it must be noted the model presented here assumes a perfect elastically strained system where only the atomic positions have been predicted. The simulation has not accounted for instrument broadening, shape variation, stacking faults/defects

and anisotropy within the NC ensemble. Whilst instrument broadening and shape can be accounted for, these would be minor when compared to the effect of defects and stacking faults. The nature of the program built here makes stacking faults too complex to be incorporated easily. It is also noteworthy to consider that defects not only affect the atomistic position through stacking faults but can also release strain, however adding wurtzite stacking faults into similar strained systems has accounted for some broadening and intensity drops [20]. This thus should be the focus of future work.

5.4.6 XPS characterisation

As shown in section 5.4, it was theorised that the formation of anisotropic core-shell NC in large core diameter systems could be related to strain. It is interesting to note that for the smallest cores with large shells that the NC are still largely spherical. It was shown that alloying the interface can produce spherical NC, thus this section investigates the quality of the core-shell interfaces in our smallest NC using XPS. This work was conducted by Wendy Flavell's group from the University of Manchester at MAXLab, Sweden. The analysis of the XPS data and the development of the corresponding model was conducted by Darren Graham of the University of Manchester. The resulting interpretation of the XPS results are my own work.

XPS is a critical tool in analysing surface composition. This technique utilises the photoelectric effect, as discovered by Einstein in the early 1900s, whereby incident X-rays eject electrons from the surface. The energy of electrons have characteristic energies which relate to binding energies of specific elements. Synchrotron-XPS makes use of the tunability of the source which enables the kinetic energy of the photo-emitted electrons to be varied. Tuning of the X-ray energy enables depth-resolved studies as there is dependence of the photoelectron inelastic mean free path on kinetic energy [161, 179–181]. Figure 5.22a shows the normalised XPS intensities of the characteristic Te 4d and Se 3d core levels as a function of photon energy for a 2.4 nm diameter core NC with 4 ML shell. An inspection of the relative intensities shows a marked increase in Te signal with increasing photon energy indicative of Te rich core.

Further analysis by Darren Graham enabled the compositional ratio, as function of photon energy, to be obtained by correcting for the relative photoionisation cross-sections with photon energy [182]. Figure 5.22b and 5.22c show the same experimental data

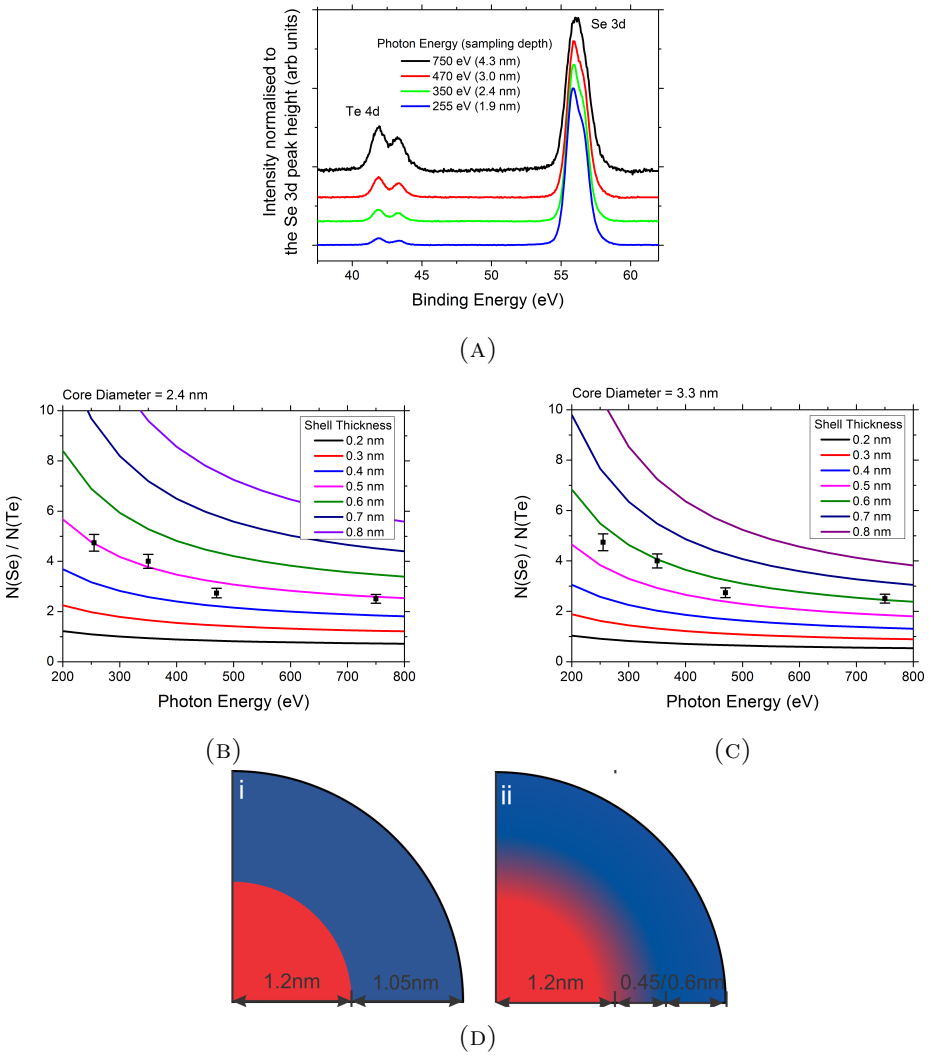

FIGURE 5.22: a) Core-level XPS showing the Te 4d and Se 3d signals as a function of X-ray photon energy for ZnTe/ZnSe NC with 2.4 nm diameter core and 4 ML shell. Estimated sampling depths are given in brackets. The signal intensity has been normalised to the Se 3d elemental peak. b-c) The elemental ratio N(Se)/N(Te) as a function of X-ray photon energy (Squares) compared with the trends predicted by the spherical core-shell model, for a core diameter of b) 2.4 nm and c) 3.3 nm with shell thicknesses ranging from 0.2 nm to 0.8 nm. d) A schematic showing a core-shell structure i] assuming no alloying at the core-shell interface and ii] the proposed alloying at the core-shell interface as deduced using the results of [c].

(Squares) and highlights the largest ratio of Se:Te is with low photon energy (low sampling depth), which decreases in Se:Te ratio with increasing photon energy (deepest sampling depth). This unambiguously highlights a system with Te rich core and more importantly highlights that the particle is not homogeneously alloyed. Since both the absorption of X-rays and the emission of electrons rely on Beer-Lambert's law, the technique does not naturally discriminate between a two-layer film from a core-shell geometry. An analytic model was developed by Darren Graham which expanded on previous models [183, 184] accounting for the core-shell nature of the NC and the observable compositional ratios as a function of photon energy could be predicted. Figure 5.22b and 5.22c highlights the experimental composition ratio and corresponding model with core diameter of 2.4 nm (Figure 5.22b) and 3.3 nm (Figure 5.22c) with a shell thickness ranging from 0.2 nm to 0.8 nm. It can be initially seen that the general trend of the compositional ratio with photon energy follows the analytic model, giving strong evidence for a core-shell geometry. However, a closer inspection of figure 5.22b shows the experimental data correlates to a shell thickness of 0.5 nm with core diameter of 2.4 nm. This gives an overall diameter of 3.4 nm which does not correlate with the observed diameter of 4.5 nm determined through TEM.

To correlate a total diameter of 4.5 nm with the observed compositional ratio, a core diameter of 3.3 nm with a shell thickness of 0.6 nm was required (Figure 5.22c). The observation of a larger core size in XPS than in TEM suggests that some alloying is taking place and that the difference between the core size, determined through XPS and determined from TEM, suggests there is an alloyed region of around 0.45 nm thickness between the core and shell materials, as shown schematically in figure 5.22d.

The thickness of the alloyed layer is consistent with similar observations in CdSe/CdS and CdTe/CdSe NC using similar synthesis methodology [129, 139]. Other recent reports

have seen considerable alloying occur at 240-250°C within ZnSe/ZnS and Mn-ZnSe/ZnS [185] but also at other lower and higher temperatures as discussed in section 2.3.6. From these results and those recently published, it can be implied that the alloying at the core-shell interface is due to the interatomic diffusion of Te and Se atoms.

5.4.7 Critical radius calculations

Using theory from section 3.5 and the material parameters in table B.1, this section presents the critical radius for a full, Frank partial and Shockley partial dislocation for ZnTe/ZnSe in effort to correlate these critical radii with the observed physical and optical features.

Whilst the dislocation core parameter (α) of 4 is typically used in equation 3.26 [15, 20], it has been stated that this value can range between 1-4 [15], thus, this parameter is swept for this new material of ZnTe/ZnSe. Figure 5.23 shows the critical radius for ZnTe/ZnSe NC as function of core radius and shell thickness for several α. The general trend sees the critical thickness increase in both the core and shell thickness with increasing α. It is seen for all core radii that at least 1-2 ML (0.28-0.56 nm) ZnSe can be grown without a partial dislocation being formed and 1.5-2.5 ML (0.45-0.70 nm) ZnSe without a full dislocation being formed. Core radii below 1.1-1.5 nm can grow ZnSe indefinitely without a full dislocation and core radii below 0.8-1.1 nm without a partial dislocation.

Experimental results have shown that the onset of stacking faults could be seen within the smallest 1.2 nm radii cores with 4 ML (1.134 nm) of shell thickness, marked as ($*$), which closely corresponds to a the boundary of a full dislocation in figure 5.23a with $\alpha = 1$, the Frank partial dislocation boundary in figure 5.23b with $\alpha = 2$ and Shockley partial dislocation boundary within figure 5.23c with $\alpha = 4$. Further comparison could be made with the observed onset of anisotropic growth and a high density of twin dislocations in large core radii with 3-4 ML (0.85-1.13 nm) of shell thickness seen in figure 5.4 marked as ($+$). This observation follows closely with the full dislocation boundary in figure 5.23b with $\alpha = 2$ and with the Shockley partial dislocation boundary in 5.23c with $\alpha = 4$. As will be shown in the next section, the highest QY was in the

region 1.5-3 ML (0.43-0.85 nm), marked as (‡), which can be related to Frank partial or Shockley partial within figures 5.23a-5.23c with $\alpha = 1$, 2 or 4. Whilst not all the observed features correlate to a dislocation boundary, the dislocation parameter of 2 or 4 shows the best agreement with the observed features and highlights the potential of partial dislocations as a cause for some of the observed features.

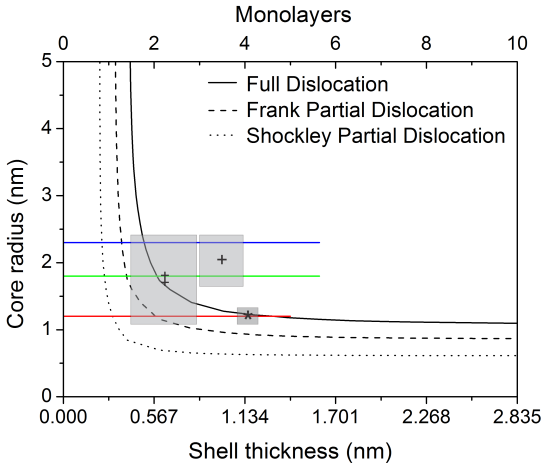

(A) $\alpha = 1$

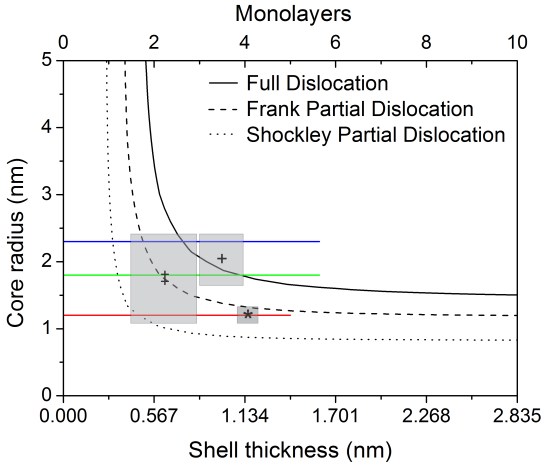

(B) $\alpha = 2$

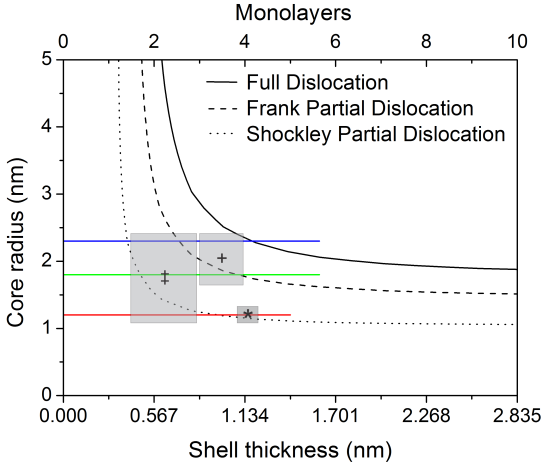

(C) $\alpha = 4$

FIGURE 5.23: The full, Frank partial and Shockley partial dislocation critical radii boundaries for ZnTe/ZnSe NC with α = a) 1, b) 2 and c) 4. The coloured lines show regions that have been investigated experimentally with core radii of a 1.2 nm (Red), 1.8 nm (Green) and 2.3 nm (Blue). The region of interest marked by ($*$) highlights the region where stacking faults within a 2.4 nm diameter core NC with 4 ML shell growth are observed, ($+$) highlights the onset of anisotropic growth in large-core large-shelled ZnTe/ZnSe NC and ($\ddagger$) highlights the region of highest QY.

5.5 Optical characterisation

This section presents the general optical properties of ZnTe/ZnSe and ZnTe/ZnTeSe alloyed NC through absorption, PL and PL lifetime studies. The observed exciton energies are further characterised by comparison to a (2-6)-band effective mass model in effort to distinguish between strained and unstrained system and various absorption transitions to be identified. The section finishes by presenting results from SNS on ZnTe/ZnSe NC.

5.5.1 General optical characterisation

Figure 5.24 shows the absorption and PL spectra for ZnTe/ZnSe up to 5 ML in shell growth for 2.4 nm, 3.6 nm and 4.6 nm core diameters. The spectra show the characteristic redshift and weakening of the absorption feature expected from a type-II structure. Redshifts of 124 nm, 97 nm and 65 nm are seen in the first excitonic absorption feature for 2.4 nm, 3.6 nm, and 4.6 nm diameter cores with up to ∼5 ML of shell thickness respectively.

The ZnTe core-only structures show little to no PL whilst the addition of a small amount of the Zn precursor enables weak excitonic PL to be observed implying that tellurium surface trap sites are responsible for rapid non-radiative recombination of the exciton, similar to the radiative trap site emission seen in CdS [39, 40]. The PL intensity increases markedly as the shell is made thicker, with the highest quantum yields of 12% occurring with the addition of 1.5-3 ML ZnSe. This result is in reasonable agreement with that of Bang *et al.* who observed the highest quantum yield at 1.4 ML [50], albeit with lower absolute QY. The PL from the first ML growth shows a redshift of 102 nm, 72 nm, and 82 nm for each 2.4 nm, 3.6 nm and 4.6 nm diameter cores respectively.

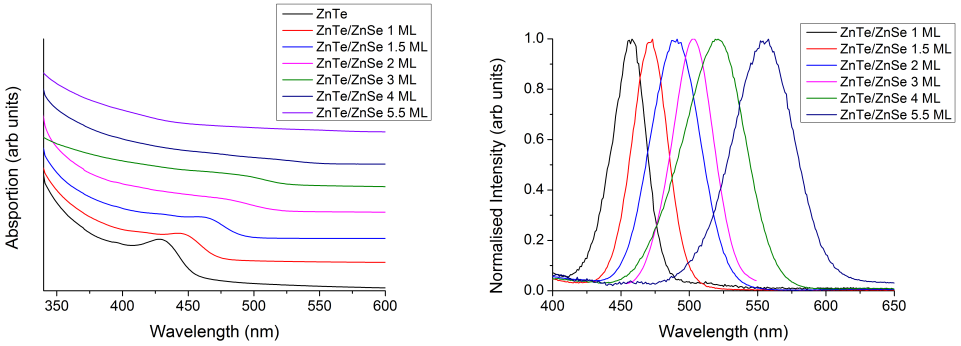

(A) 2.4 nm diameter ZnTe core.

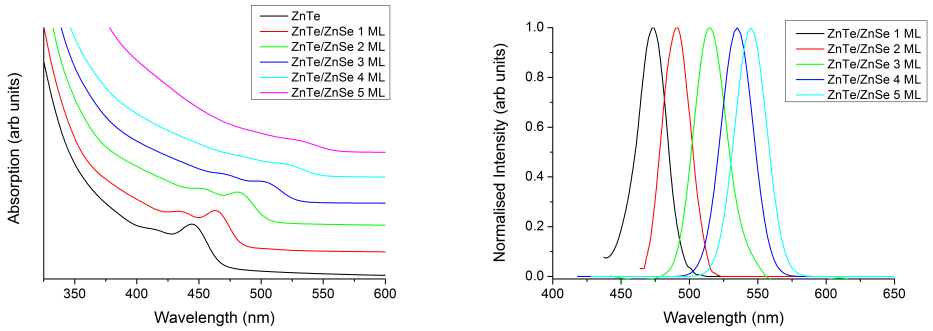

(B) 3.6 nm diameter ZnTe core.

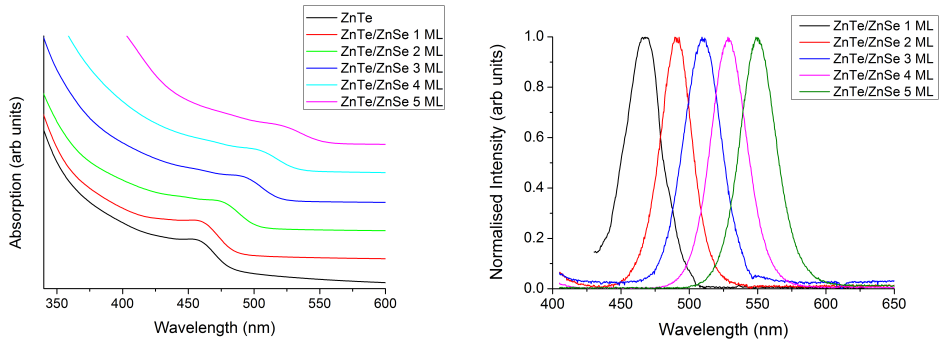

(C) 4.6 nm diameter ZnTe core.

FIGURE 5.24: The absorption and PL spectra of ZnTe/ZnSe NC with a) 2.4 nm, b) 3.6 nm, and 4.6 nm ZnTe core diameters with increasing shell thickness.

The general trend and magnitude in redshift of the optical features alongside a weakening of the absorption features are consistent with type-II structures and specifically comparable to ZnTe/ZnSe NC reported by Bang *et al.* and Guan *et al.* [50, 160]. A comparison of the ZnTe/ZnSe NC with a 4.6 nm diameter core, shown here in figure 5.24c, and on 4.4 nm diameter ZnTe cores Bang *et al.* and Guan *et al.* NC show correlating trends. Both sets of NC see a redshift of the absorption features from 430-450 nm to 550-580 nm. A quantitative comparison of the PL range can be made from the first ML

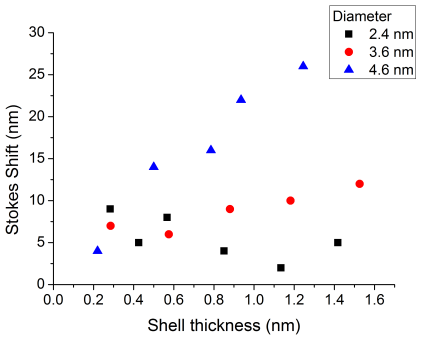

FIGURE 5.25: The Stokes shift for 2.4 nm, 3.6 nm and 4.6 nm diameter ZnTe core NC as a function ZnSe shell thickness.

to the 5th ML shell growth which both show redshifts of ∼80 nm. However, there are some subtle differences in the optical features. Firstly, both Bang *et al.* and Guan *et al.* have a core diameter of 4.4 nm which has a first excitonic feature situated at ∼430 nm in contrast to the 459 nm seen in the 4.6 nm diameter of figure 5.24c or the 426 nm feature of our 2.4 nm diameter cores seen in figure 5.24a. Whilst it is noted that ZnTe NC are a very difficult material to image through TEM due to the small Z-contrast, the variation in absorption feature seen here is better explained by the influence of ligands described previously. Secondly, there is a discrepancy in the onset of the first excitonic feature of the first 1 ML growth in which the Bang data is redshifted by roughly ∼15 nm when compared to the 1 ML growth seen in figure 5.24c and Guan *et al.* is blueshifted by ∼15 nm. A close inspection of the 2 ML and 4 ML optical features in figure 5.24c and Guan *et al.* and the 1 ML and 2 ML to be seen in Bang *et al.* see almost direct correlation. This highlights a possible inconsistency in defining a ML growth. From these results we conclude that in Bang *et al.* uses a full lattice constant (0.567 nm) rather than the half lattice constant considered here or by Guan *et al.* (0.284 nm). Ultimately past 1 ML growth all the reported optical data shows good correlation.

As seen in figure 5.25 and table 5.3, there is a mild decrease in Stokes shift for the smallest cores with increasing shell thickness (9 nm to 5 nm). Larger core diameters see

significant increases in Stokes shift with increasing shell thickness (7-12 nm for 3.6 nm diameter cores and 4-26 nm for 4.6 nm diameter cores). Experimental and theoretical reports have shown both trends in Stokes shift [54, 186]. The magnitude of the Stokes shift can be accounted for by three factors; firstly, the difference in energy between the strongest lowest energy optical allowed absorption transition and the ground state emission transition which typically describes the variations in the fine structure in a type-I system [187], secondly, phonon interactions [101] and thirdly, size inhomogeneity and shape [187]. Type-II systems are further complicated: it must also be noted that spatially direct transitions are going to be stronger than spatially separated transitions of the lowest energy transition, thus the strongest absorption feature may not be the closest to the band edge as most notably seen by Blackman *et al.* [54].

With this in mind the decrease in Stokes shift for the smallest NC can be related to observations seen in both type-I NC [187] and theoretically small cored type-II NC [186] in which the decrease in quantum confinement with increasing shell thickness decreases the effective energy between the closest energy optical allowed transitions (typically in the fine structure) and the band edge emission transition.

In NC with larger core diameters, the wavefunction overlap dominates the Stokes shift thus higher energy transitions can be stronger than lower energy transitions giving rise to a larger Stokes shift. Further reasons for increased Stokes shifts in large cores could also be due to the shape of the NC which is seen to become more anisotropic in the ZnTe/ZnSe seen here and this change in shape is known to increase the splitting of the fine structure in other structures [187].

The associated PL FWHM averages are 30 nm, 26 nm, and 31 nm which can be related to an average size distribution of 9%, 8% and 10% for the 2.4 nm, 3.6 nm and 4.6 nm

diameter cores respectively. These values are an improvement on the ZnTe/ZnSe NC produce seen by Bang which saw a PL FWHM of 30-50 nm and size distributions of 14-10% [50]

As seen from figure 5.26, the associated alloying decreases the redshift in absorption and PL spectra. The overall range of absorption is from 84 nm for the sharp core-shell interface structure to 74 nm and 65 nm for the 5% and 10% alloy respectively. Whilst an increase in shell conduction band energy using the ideas of Vegard's law for the electronic structure can go some way to explain optical data, this is not supported for homogenously alloyed NC as seen through the XRD Vegard's law lattice constants (Table 5.1). One postulate could be the lack of compression on the core as will be discussed in section 5.5.4.

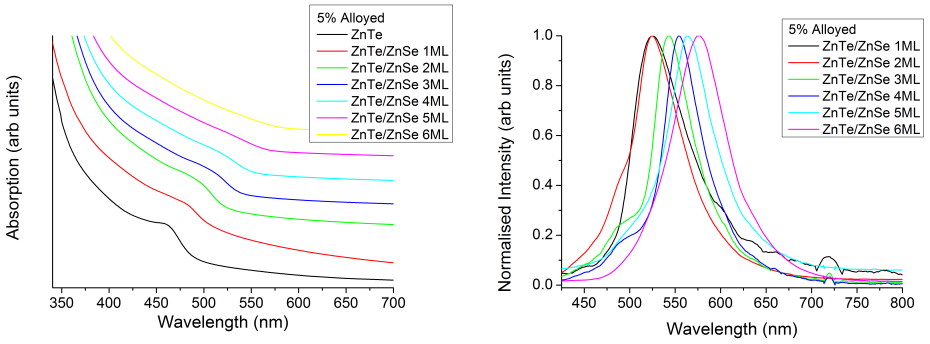

(A) 5% Alloying

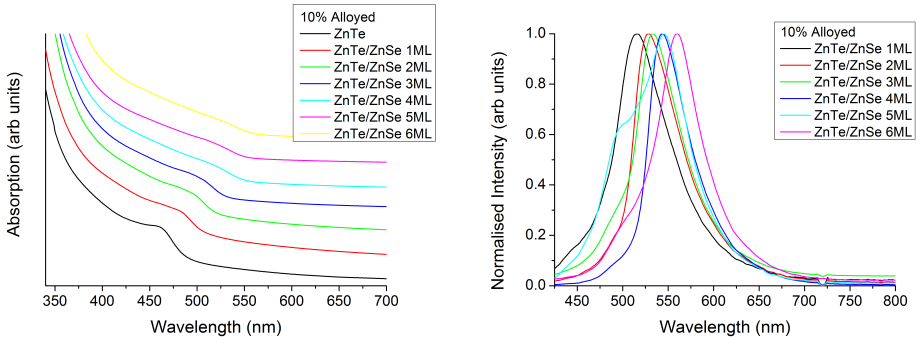

(B) 10% Alloying

FIGURE 5.26: The absorption and PL spectra of 4.6 nm diameter ZnTe core NC with a) 5% alloying and b) 10% alloying of core-shell interface with increasing shell ZnSe thickness.

ML	Abs (nm)	PL (nm)	Stoke shift (nm)	FWHM (nm)	Size distribution (%)
2.4 nm diameter core					
0	426	-	-	-	10
1	448	457	9	30	9
1.5	466	471	5	25	9
2	482	490	8	50*	13
3	498	502	4	34	9
4	518	520	2	55*	13
5.5	550	555	5	54*	13
3.6 nm diameter core					
0	446	-	-	-	7
1	465	472	7	25	8
2	484	490	6	26	8
3	505	514	9	27	8
4	524	534	10	29	8
5	533	545	12	25	7
4.6 nm diameter core					
0	459	-	-	-	9
1	462	466	4	30	10
2	477	491	14	30	10
3	494	510	16	35	10
4	506	528	22	31	9
5	524	550	26	31	9

TABLE 5.3: A table showing the first excitonic features, peak PL, Stokes shift and FWHM for 2.4 nm, 3.6 nm, and 4.6 nm diameter ZnTe cores with various shell thicknesses.

5.5.2 Exciton dynamics

This section utilises a qualitative and quantitative approach in an effort to show a reduction in oscillator strength expected by a type-II NC.

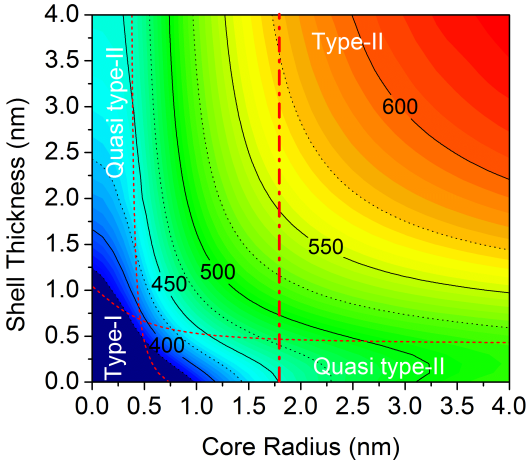

FIGURE 5.27: A contour plot of the theoretical absorption wavelength of the $1S^{(e)}_{1/2}1S^{(h)}_{3/2}$ transition in the strained regime showing the type-I, type-II and quasi type-II regions.

A qualitative approach can be made by comparing the weakening of the exciton features in the absorption spectrum to the calculated onset of the type-II regime as determined by using the effective mass theory and energy level argument described in section 2.4.2. Figure 5.27 shows a contour plot of the calculated $1S^{(e)}_{1/2}1S^{(h)}_{3/2}$ exciton energies as a function of core radius and shell thickness in the strained regime. The figure highlights the type-I, quasi-type-II, and type-II localisation regimes which describe the degree of wavefunction overlap between the two charge carriers. For comparison figure 5.27 also highlights, with the thick dashed line, the trend line that corresponds to the experimental data in figure 5.24b. As seen in figure 5.27 the onset of type-II regime is at 1.83 ML (0.52 nm) shell thickness which is in reasonable agreement with onset of the weakening of the first excitonic feature past 2 ML shell growth.

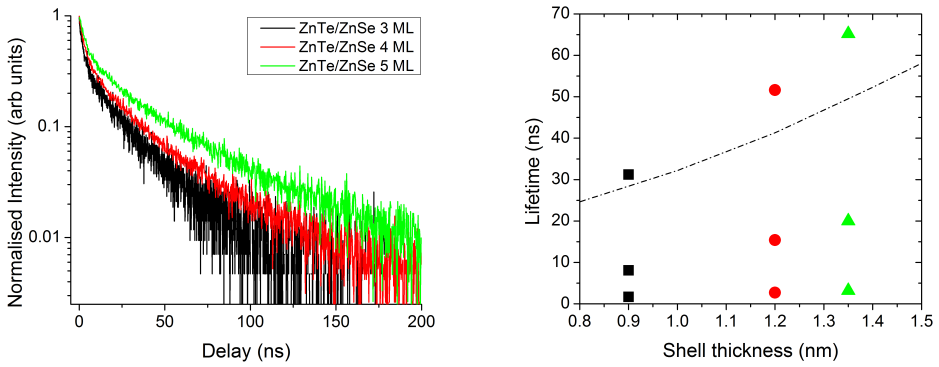

(A) (B)

FIGURE 5.28: a) The PL lifetime decays for a 3.9 nm diameter ZnTe core NC with 3, 4 and 5 ML of ZnSe shell. b) The extracted tri-exponential lifetime components as a function of shell thickness with a comparison to the proposed theoretical lifetime (Dashed black line). Full fittings can be found in Appendix D.1.7

A more quantitative approach can be made by using the PL lifetimes in which an increase in PL lifetime is expected. Due to limitations of the excitation source and associated optical setup only larger shell thickness NC with PL emission higher than a wavelength of 510 nm could be investigated. Figure 5.28 shows the PL decay with increasing shell thickness where the PL lifetimes could be extracted using tri-exponential fits. Figure 5.28b shows that all lifetime components increase with increasing shell thickness and the longest components exhibit similar trends to that predicted by theory. The figure also highlights the longest lifetime component transition from 31.2 ns to 65.2 ns for 3 ML to 5 ML growth respectively, indicative of a type-II system and a significant reduction in the wavefunction overlap [50, 62, 73]. This 65.2 ns lifetime is also comparable to the long components lifetime observed by Bang/Guan *et al.*, 97/57 ns albeit for larger core sizes and larger/smaller shell thickness respectively [50, 160].

Whilst the lack of a clear single long exponential tail in the decay could be due to size inhomogeneity, this observation along side the shorter lifetime components could also suggest other mechanisms are contributing to the decay such as charging or charge trapping effects [115, 131]. This is further supported by surface charging observed within

transient absorption spectroscopy measurements of this material which is reported in a joint publication in Phys. Chem. Chem. Phys. with David Bink's group at the University of Manchester [188].

5.5.3 PL stability

PL stability is one of the major issues within this structure. Whilst this section describes the stability of NC with 1 ML shell thickness these investigations highlight a general trend for ZnTe/ZnSe NC and can be seen in some of the PL spectra in section 5.5.1. Figure 5.29 shows the PL stability of 3.8 nm diameter ZnTe core NC with 1 ML ZnSe shell growth that has been cleaned once using methanol/butanol precipitation and redispersed in hexane using commercial degassed anhydrous solvents in inert atmosphere. The cleaned solution was placed in two cuvettes within a nitrogen environment, one was then exposed to ambient conditions just before investigation. The crude dispersion of NC showed no loss of PL for months/years for the same glove box atmosphere exposure ruling out oxygen exposure within the glove box as a root cause.

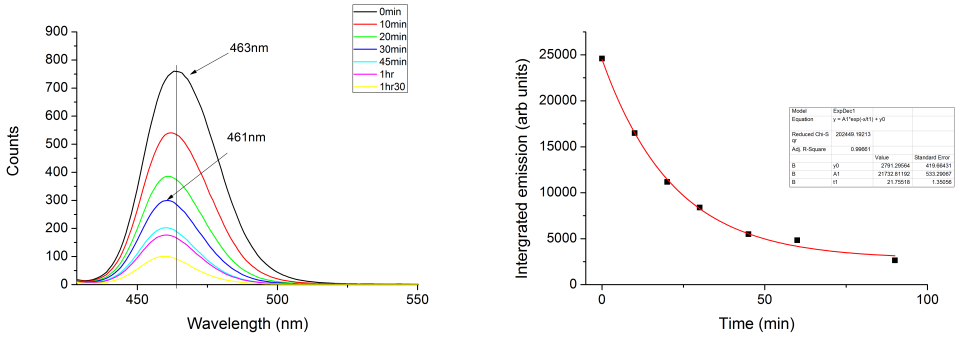

(A) No exposure to atmosphere

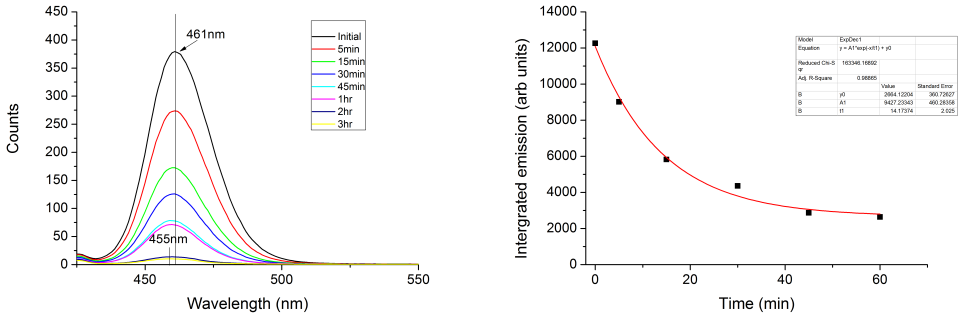

(B) Exposure to atmosphere

FIGURE 5.29: PL stability of 3.8 nm diameter core NC with 1 ML ZnSe shell after 1 methanol:butanol precipitation clean without and with exposure to ambient conditions showing integrated emission intensity exponential decays, with lifetimes of 13 and 22 minutes respectively

As seen from figure 5.29a there is marked reduction in PL with and without exposure ambient conditions. The reduction in PL magnitude coincides with a blueshift of up to 5-8 nm in peak PL position however there was no observable change in the absorption spectrum. The reduction in integrated emission intensity can be related to an exponential decay with lifetimes of 13 and 22 minutes respectively. The fact that the degradation in PL have similar decay lifetimes suggests that the effect of oxidation is minimal.

One possible reason could be associated with cleaning the NC. The methanol/butanol clean used here is essential to precipitate the NC and removes OA fluorescence. This compares to standard methanol cleans which produce an oil phase rather than a precipitant. Other cleaning techniques such as chloroform/methanol phase extraction and precipitation from other polar solvents such as acetone or ethyl acetate, either did not remove the ligand fluorescence or totally quenched PL/agglometrated the NC solution. Cleaning the NC can push the dynamic equilibrium of ligand association from one that has full coverage, to ligand dissociation from the NC (the underlying theory is described in section D.1.8). This is especially true in the case of OA which is known to be a relatively weakly binding ligand/Lewis base and is typically easily exchanged to other ligands for application [4, 189, 190]. Dissociation of ligands will lead to detrimental effects such as surface trap sites, the potential for agglomeration and an ease of oxidation. A change of ligand or the addition of ZnS to stabilise the solution showed substantial shifts in excitonic energy due to the intrinsically large band gaps, bandgap alignment and strain effects. It must also be noted that the ligand exchanges attempted were detrimental to the PL. Since the ultimate goal was to compare ZnTe/ZnSe NC it was decided to keep a constant ligand combination of OA and TOP.

5.5.4 (2-6)-band effective mass simulation

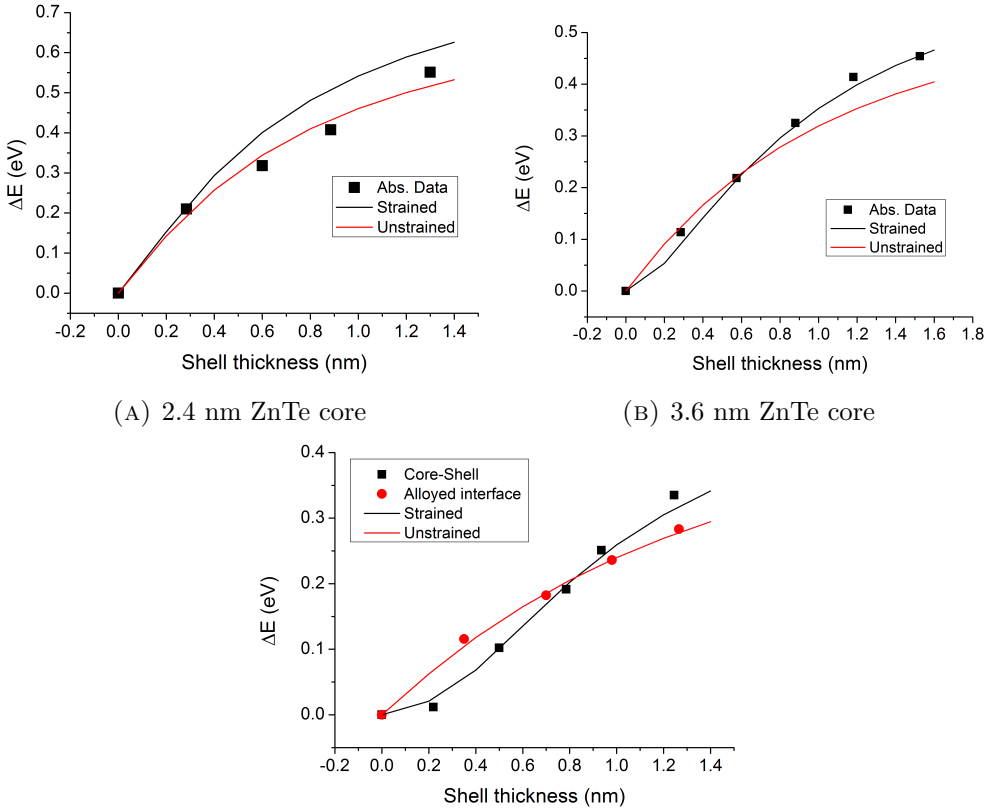

(A) 2.4 nm ZnTe core

(B) 3.6 nm ZnTe core

(C) 4.6 nm ZnTe Core

FIGURE 5.30: A comparison of the energy deviation, ΔE, of the $1S^{(e)}_{1/2}1S^{(h)}_{3/2}$ exciton energy from the core absorption feature calculated with and without strain (Lines) and compared to the first absorption feature from the experimental data (Squares) for a) 2.4 nm, b) 3.6 nm and c) 4.6 nm diameter ZnTe core NC as a function of ZnSe shell thickness. c) Also shows the energy deviation trend for the ZnTe/$ZnTe_{0.1}Se_{0.9}$ alloyed interface NC.

Whilst the observed redshift in optical features seen in figure 5.24 can be related to type-II structure, questions remain over whether the strain inflicted by the 7% lattice mismatch between the core and the shell enhances this redshift.

Utilising the first exciton feature obtained from the second derivatives of the absorption spectra seen in figure D.3 Appendix, figures 5.30 shows the deviation of the exciton energy from the core exciton energy with increasing shell thickness. A comparison is made to the predicted deviation for the calculated strained and unstrained cases utilising the effective mass approximation as discussed in section 3.6. A comparison of the two

models reveals the addition of strain to the system can cause a redshift of ∼55 meV for the thickest shells. The significance of the strain can be seen when comparing the model (Lines) to the observed variation of the first excitonic feature (Squares) for the largest core sizes of figure 5.30c. The strained model (Black lines) shows a plateau feature at small shell thicknesses which accurately describes the experimental data. This plateau feature is due to two competing factors: the bandgap energy increases due to the hydrostatic compression of the shell on the ZnTe core and the increasingly type-II nature of the overall NC. To quantify the improved agreement between experiment and calculation, the value of the sum of squared residuals between the model and the measured band edge absorption features were calculated. For the largest core size, the inclusion of strain in the model improves the agreement by more than an order of magnitude (see Appendix C.1.2) and highlights that the core is being actively compressed. Experimental data for the 3.6 nm diameter NC shows better agreement with the strained model rather than the unstrained model. However there is better agreement with the unstrained model with decreasing core diameter (Figure 5.30a-5.30b). From these results it can be hypothesised that there is light alloying of the interface which does not significantly modify the core-shell structure, as shown from XPS, however reduces the strain and compression on the core and therefore mitigates the associated shift in exciton energy. To test whether alloying can significantly influence the manifestation of strain within the system, the interface of the largest cores NC was actively alloyed over the first 4 ML. Using the 10% alloy data of figure 5.26b, the red circles in figure 5.30c show a very different dependence on thickness which is much closer to that predicted for an unstrained system. This result suggests that alloying mitigates the compressive strain on the core and highlights the significance of compression of the core on the exciton energy.

Due to the low size distribution, figure 5.24b shows several higher-order optical features. Here an attempt is made to identify further exciton features resulting from higher energy 'hot-exciton' transitions using the strained model. Figure 5.31a shows the second derivative of the absorption data for a core diameter of 3.6 nm with varying shell thickness. Minima in the second derivative are taken to be resonances in the absorption. Two strong

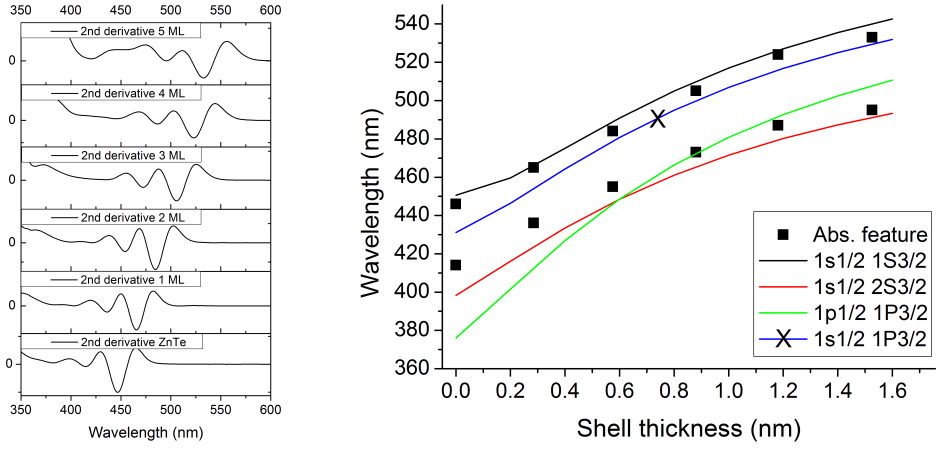

(A) (B)

FIGURE 5.31: a) The second derivative of the absorption data for the 3.6 nm diameter ZnTe core NC with increasing shell thickness. b) The mapped absorption features as a function of shell thickness with the theoretically calculated exciton transitions.

features can be seen in the absorption spectra of the ZnTe core through to 5 ML of shell thickness. Figure 5.31b highlights the calculated energies for the allowed and forbidden electric dipole transitions within the vicinity of the experimental data. In addition to the first absorption feature showing good agreement to the $1s_e(1/2) - 1S_h(3/2)$ transition consistent with many other NC [99, 191–193], quite good agreement is obtained between the second absorption feature and the $1s_e(1/2) - 2S_h(3/2)$ transition and is consistent with other zinc blende structures. Whilst there is variation between experimental $1s_e(1/2) - 2S_h(3/2)$ transition it has very recently been shown that $1s_e(1/2) - 2S_h(3/2)$ transition is dependent on ligands with up to 40 meV variations for the same length primary amines and carboxylic acids and could account for this variation [173].

Whilst some higher energy features are weak in the second derivative, an inspection of the fourth derivative shows two or three weaker further features. Whilst these are used with caution, a comparison of the relative transition energies sees a potential agreement with the highest energy feature with the $1s_e(1/2) - 3S_h(3/2)$ transition. However, it must be noted some of these identified transitions may also have contributions from other dipole allowed transitions such as $1s_e(1/2) - 1S_h(1/2)$, $1p_e(1/2) - 1P_h(3/2)$, $1p_e(1/2) - 1P_h(1/2)$, $1p_e(3/2) - 1P_h(3/2)$ and $1p_e(3/2) - 1P_h(1/2)$, which follow similar trajectories but have weaker oscillator strengths.

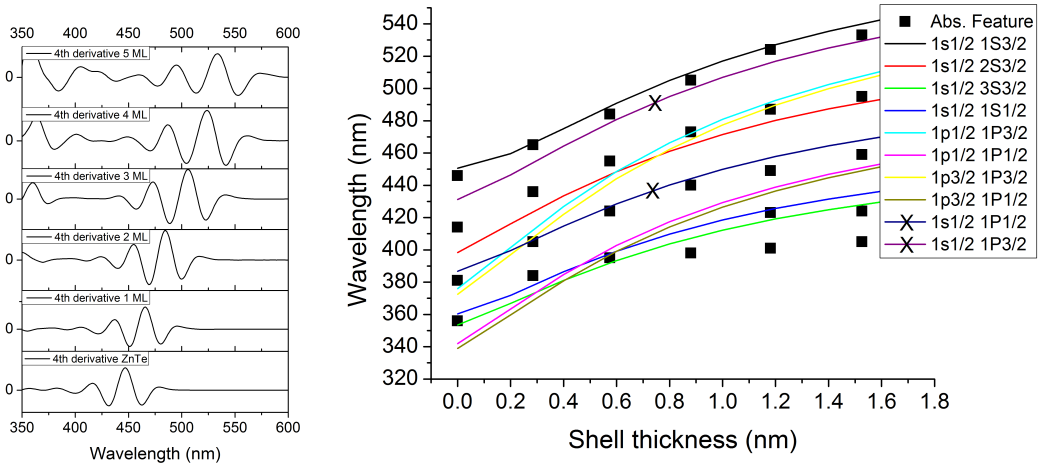

(A) (B)

FIGURE 5.32: a) The fourth derivative of the absorption data for the 3.6 nm diameter ZnTe core NC with increasing shell thickness. b) The mapped absorption features as a function of shell thickness with the theoretically calculated exciton transitions.

Interestingly the transition commencing at 380 nm and finishing 440 nm does not follow any of the calculated dipole allowed transition energies, but does appear to agree quite well with the predicted energies of the dipole forbidden $1s_e(1/2) - 1P_h(1/2)$ transition. Much discussion has been made in other systems with regards to the potential observation of optically forbidden transitions (with conflicting results for PbSe NC [194, 195]), however there is tangible evidence for optically forbidden transition within wurtzite CdSe NC and zinc blende InP NC which have both shown an optically active

$1s_e(1/2) - 1P_h(1/2)$ transition [193, 196]. The manifestation of transitions that are forbidden in spherically symmetric confinement potentials may result from the presence of an internal electric field in the nanocrystals that lowers the symmetry [196, 197]. The internal piezoelectric field is known to be as large as $42D$ for ZnSe and other zinc blende structures, and can potentially be enhanced by strain effects due to a shell [197, 198], thus providing a possible explanation for the observation of this absorption feature. However, further PLE measurement at 4 K are required to fully support these observations and theory [199].

5.5.5 Single nanocrystal spectroscopy of ZnTe/ZnSe nanocrystals

As was shown in section 2.5.2.2, SNS on type-II NC is limited. Here the reasonably high QY of our ZnTe/ZnSe NC enables some of the first single NC investigation on type-II NC. Figure 5.33a shows a typical single NC spectrum observed at room temperature and excited at 8 W cm^{-2}. The figure shows a Lorentzian emission line shape with a peak at 592 nm with a FWHM of 16.9 nm as expected from a single NC. This FWHM can be related to the homogeneous line width at room temperature and is comparable to type-I NC (see chapter 6). Since the FWHM of the ensemble emission is the convolution of the homogeneous line width and inhomogeneous broadening due to the NC size distribution, an estimation of the size inhomogeneity of the ensemble PL can be made. Comparing homogeneous line width with the inhomogeneous line width of ∼30 nm seen in the ensemble PL spectrum in figure 5.24b suggests that the spectral contribution by the inhomogeneous size distribution is less than 25 nm, evaluating the two spectra in quadrature. Using this result and the model in section 3.6 enables us to estimate the size inhomogeneity to be about 1-2 ML (a diameter change of 0.57-1.14 nm) depending on shell thickness, slightly larger than the size distribution measured through TEM.

Figure 5.33b, highlights the spectral evolution of a single NC PL over time and shows that the NC have good initial optical stability with very little blinking and spectral diffusion. However within about a minute of continued photo-excitation, spectral blueing is observed with a loss of intensity and enhanced blinking which can be related to photo-induced oxidation of the NC. This oxidation can be attributed to the exposure of the matrix to ambient conditions and the diffusion of oxygen into the matrix and thus in to the NC. A NC was also shown to have two-peak emission, as demonstrated in figure 5.33c, where a strong emission peak was seen at 580 nm and a secondary emission at

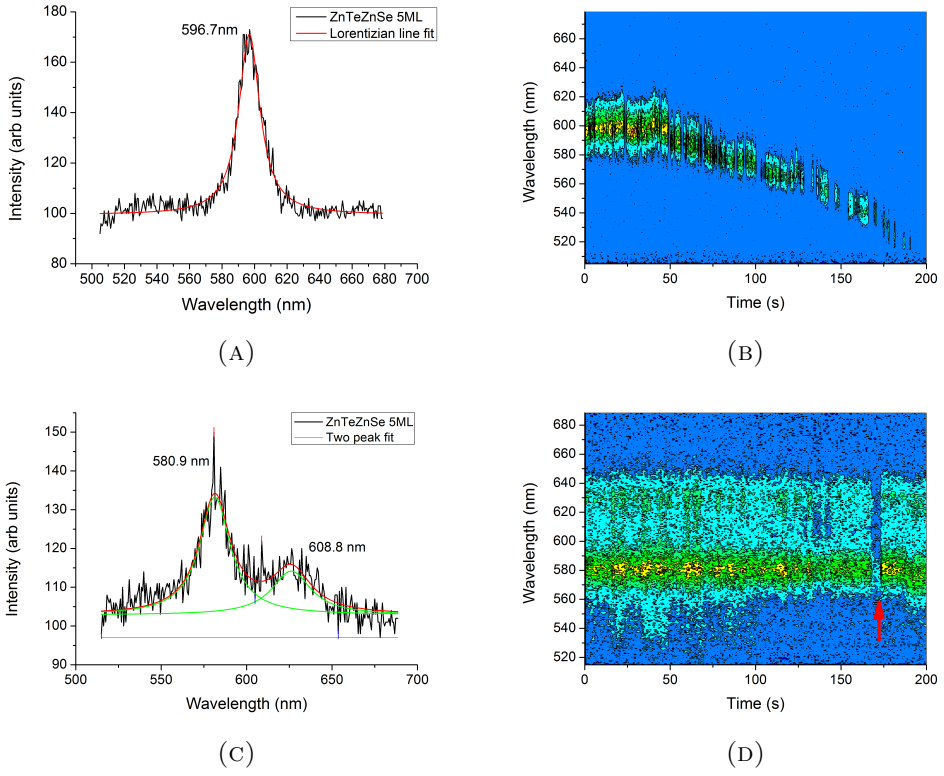

FIGURE 5.33: Spectral time trajectories and individual spectra of 3.8 nm diameter ZnTe core and 5 ML ZnSe shell highlighting, a-b) initial stable single Lorentzian peak emission at 596.7 nm with a FWHM of 15.9 nm. This emission is stable for the first 45 seconds before spectral blueing. c-d) Two-peak emission with a primary peak at 580.9 nm and a secondary peak at 608.8 nm. The red arrow indicates a common blink at 170 seconds.

608 nm. This two-peak emission can be related to a single NC by looking at figure 5.33d in which constant emission can be seen up to 170 seconds. The lack of emission thereafter (indicated by the Red arrow) suggests a common blink and therefore a high probability of being a single NC. As was described in section 2.5, multi-peak emission has been seen in other non-blinking systems as demonstrated by Wang *et al.* in the quasi type-II CdZnSe/ZnSe NC and by Kloper *et al.* in the quasi type-II regime within CdTe/CdSe NC and have been related to trion emission [88, 122]. It is unfortunate to note this is a very limited study and that the many attempts to reproduce these results failed. This is presumed to be due to optical stability issues of the NC.

5.6 Conclusion

In conclusion, this chapter demonstrates that using a modified superhydride ZnTe synthetic method provides a diethyl Zn-free method towards ZnTe NC. The method shows superior size distributions and optical characteristics when compared to diethyl Zn synthesis methods. Large amounts of ZnTe NC can be produced on a laboratory scale without the loss of optical performance and size distribution. This chapter demonstrates the synthesis of a size series of ZnTe/ZnSe NC, producing some of the highest QY for this structure, and shows the synthesis of ZnSe on the smallest ZnTe cores known to date. Due to the quantitative nature of the ZnTe core reaction, the SILAR technique can be used to grow ZnSe within 10% of the desired shell thickness whilst maintaining the size distribution of the core. ZnTe/ZnSe NC can be synthesised using Zn oleate and Se-TOP as precursors without the need for diethyl Zn as a precursor or amines as ligands, leading to a 'greener' synthetic route to ZnTe/ZnSe NC. Various Zn precursors and shell synthetic techniques showed anisotropic growth. HRTEM and XRD also revealed that NC with large core diameter and large shells observe strain effects through lattice bowing in TEM and peak broadening within XRD which led to the hypothesis that the anisotropic growth has a strain component. An attempt to support this hypothesis showed that actively alloying the shell over 4 ML produced spherical NC, highlighting that strain is a contributing factor to the growth dynamics.

Development of a strained atomistic model has enabled the direct comparison of TEM and XRD data with simulations. The comparison of simulations with experimental data shows trends towards a strained NC but also reveals that the NC have stacking faults and dislocations which have the potential to release strain. TEM and XRD simulations also support the observation of a single lattice constant for small core diameters with

large shell thicknesses and can be related to the small relative accumulated shifts of the atoms in the shell to the core. Full and partial dislocation critical radius calculations were developed and were compared to the observed physical and optical features. Whilst not fully conclusive, this technique does highlight that both partial and full dislocations could be a cause for the observed physical and optical features. XPS of the smallest core diameter with the largest shell thickness show the existence of 0.45 nm of alloying at the core-shell interface which is indicative of the interdiffusion of anions.

The main synthetic route investigated produced a size distribution of 7-10%, enabling the PL emission to maintain a narrow FWHM and maintaining good identification of absorption features. The effective bandgap can be tuned from the N-UV and into the visible spectrum with increasing shell thickness. The absorption data showed a weakening of the first excitonic feature and an increase in PL lifetime with larger shell thickness, indicative of type-II system. The onset of the weakening of the absorption feature and the lifetimes observed are comparable to those regimes predicted by (2-6)-band effective mass approximation that incorporates the idea of strain. Using the (2-6)-band effective mass approximation can distinguish between the as-grown 'sharp' and 'alloyed' interfaces and also indicates that the alloyed structures incorporate reduced strain. The sharp exciton features seen in the absorption data could also be used with the effective mass approximation to identify four excitons transitions albeit two tentatively. One of these transitions was also tentatively identified as the optically forbidden $1s_e(1/2) - 1P_h(1/2)$ transition. SNS enabled the homogenous linewidth to be identified as less than 17 nm, relating the inhomogeneous broadening within the ensemble PL due to the size distribution to be 1-2 ML in shell thickness. One particular problem of this structure is PL stability. PL studies and reported ultra-fast transient absorption experiments show that the stability issues are most probably due to the disassociation of the ligands from the

surface and therefore charging effects.

Chapter 6

Single-nanocrystal optical investigations of highly luminescent alloyed and commercially-available type-I nanocrystals

6.1 Introduction

As was shown in chapter 2, since the first NC studies much work has been conducted to understand the carrier dynamics within NC in an effort to maximise the specific exciton processes for application [3, 101, 111, 200]. Type-I NC have shown great promise for optoelectronic and biological applications with the most widely-studied structure of

CdSe/ZnS displaying good emission efficiencies, but have been marred by phenomena such as excessive charging and blinking which have hindered application. None more so than the application of biological tagging and the potential use of NC as single-photon sources which both require coherent efficient single-particle emitters with good optical stability free from blinking, blueing and spectral drift [119, 201].

The improvements in synthetic techniques and understanding of material design has enabled a wide range architecture to be synthesised with large QY. Strain mitigated core-shell-shell and graded alloyed systems have been shown to enhance QY as described in section 2.3.4 and have the potential to produce non-blinking emitters.

Whilst ensemble measurements can reveal much information about the carrier dynamics, these measurements are hampered by inhomogeneous broadening due to the intrinsic size distribution of the NC ensemble. The large QY of the NC investigated here allow for meaningful SNS studies to be undertaken with good signal to noise ratios and also enables optical features to be resolved which can often be masked in an ensemble measurement. This enables the exciton dynamics to be probed spectroscopically, through intensity-time trajectories (Blinking studies), lifetime-time trajectories and accumulated lifetime measurements. These techniques investigate specific processes within the NC which are highlighted below;

- Spectral-time trajectories investigate the spectral emission of the NC over time and can show 'spectral diffusion', in which discrete jumps in the peak emission are seen. Sharp spectral diffusion is associated with a charge carrier in a trap state within close proximity of the NC core, where the electric field of the trapped charge induces a changes the effective bandgap through the 'quantum confined stark effect' (QCSE) [202, 203]. Spectral-time trajectories can also highlight spectral blueing

which describes a process of non-reversible photoinduced oxidation that spectrally blueshifts the peak wavelength over time [204]. Spectral-time trajectories can also be used as the first step to investigate blinking behaviour.

- Intensity-time trajectories investigate the blinking behaviour of the NC with millisecond resolution. The 'on' and 'off' durations can be collated over 10-30 minute investigations to form 'on' and 'off' duration probability distributions which are usually described by power law distributions as described in section 2.5.2. Investigation of these statistics can yield evidence for potential trapping mechanisms or recombination dynamics.

- PL lifetime measurements can be used to highlight the multitude of radiative and non-radiative recombination dynamics. As was shown in section 2.5.2, the very new technique of comparing lifetime-time and intensity-time trajectories within the NC field to produce FLID statistics can be used to distinguish between Auger processes and the activation of non-radiative recombination centres [130, 131].

This chapter presents exploratory SNS studies alongside standard ensemble characterisation studies in an effort to understand the carrier dynamics within:

- graded alloyed CdZnSeS NC; which uses a facile synthetic method to produce highly luminescent NC.

- within a size-series of commercially available CdSe/ZnS NC; which have been shown by our commercial collaborator to have very high QY.

6.2 A facile synthetic method to highly-luminescent graded alloyed nanocrystals: From synthesis to single nanocrystal investigations

6.2.1 Introduction and motivation

As was shown in section 2.5.2, several techniques have recently discovered to produce non-blinking NC, the potential hindrance for application of these protocols is the complex synthetic procedure which can have long growth times in excess of 40 hours for 'giant' NC and three reaction steps for non-blinking graded NC [53, 88]. Bae *et al.* have produced brightly-emitting graded alloyed CdZnSeS NC with QY as high as 80% that only require a reaction time of a matter of minutes[89]. It is thought that this alloying plays two roles; firstly, it mitigates strain effects which have been shown to have a large influence on both the optical, physical and electronic properties; secondly, it leads to a graded band gap potential which has be shown to be the premise for non-blinking NC [88]. Limited work has been conducted investigating the exciton dynamics within one-pot alloyed structures [205–207] and thus these NC are a promising candidate for blinking studies which could lead to a facile synthesis method to non-blinking NC.

The work presented here builds on a preliminary optical study conducted by myself using graded alloyed material provided by Katayune Presland from the Paul O'Brien group at the University of Manchester [208] which showed good optical performance and where the NC tended to be in the 'on' state rather than the 'off' state but could have been compromised through processing. These results are reported in Katayune Presland's thesis [208]. This section presents the extension of this preliminary work and explores the general physical and optical properties of alloyed NC made in-house using

the same synthesis method provided by Katayune Presland. As described in section 4.2, the synthetic method requires an excess of cation precursors in a ratio of 4:1 and thus utilises the natural reaction dynamics of the system, as described in section 2.3.6, to produce a predominately CdSe core with ZnS shell with a graded alloy in-between [89]. The expected structure should be CdSe 9.1% CdS 27.2% and ZnS 63.6%. It must be noted that this is an idealistic interpretation of the system, in reality it has been shown by Bae *et al.* that the core is predominately CdSe with a S content of less than 6% however the final shell is ZnS within detectable limits [89].

6.2.2 Results

These section present the general physical and optical characterisation of the as synthesised CdZnSeS NC in an effort to provide further evidence for an alloyed structure before finally investigating the recombination dynamics of these NC through SNS.

6.2.2.1 Physical characterisation

Figure 6.1 shows the TEM images of the CdZnSeS NC after 1 minute, 3 minutes and 5 minutes growth and highlight an increase in size from an average diameter of 6.3 nm, 7.9 nm and 9.1 nm respectively. These have corresponding size distributions of 10%, 9%, and 9% respectively. The NC are largely quasi-spherical for 1 minute growth but increase to quasi-cubic/tetrahedral structures with increasing growth time. Inspection of the SAED patterns seen in figure 6.2 show a clear increase in ring radius with increasing NC size. Interpretation of the SAED, whilst difficult, suggests a predominately zinc blende crystal structure but also shows signs of possible wurtzite stacking faults. A qualitative interpretation of these results can be made considering the the first ring to

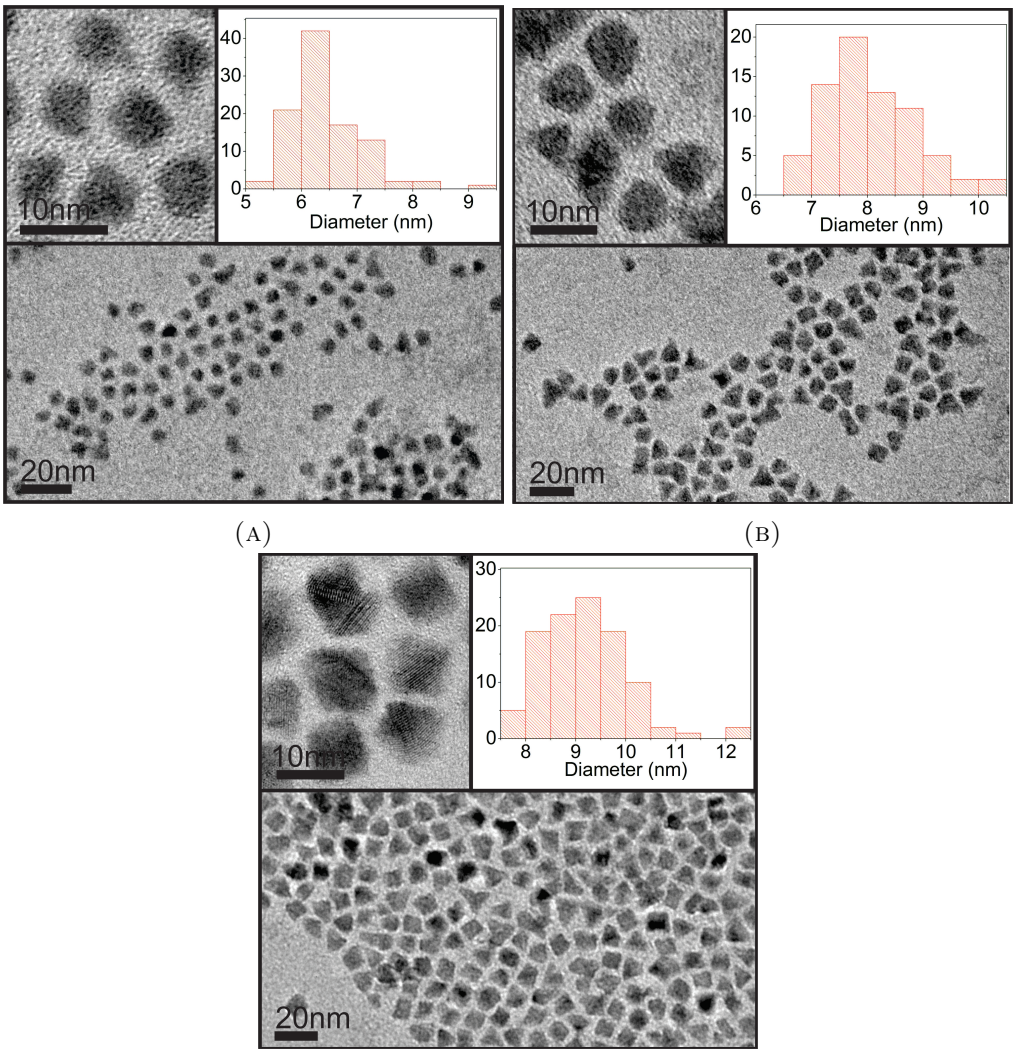

(A) (B)

(C)

FIGURE 6.1: TEM images and the corresponding size distribution histograms, inset, for CdZnSeS NC after a) 1 b) 3 and c) 5 minutes growth.

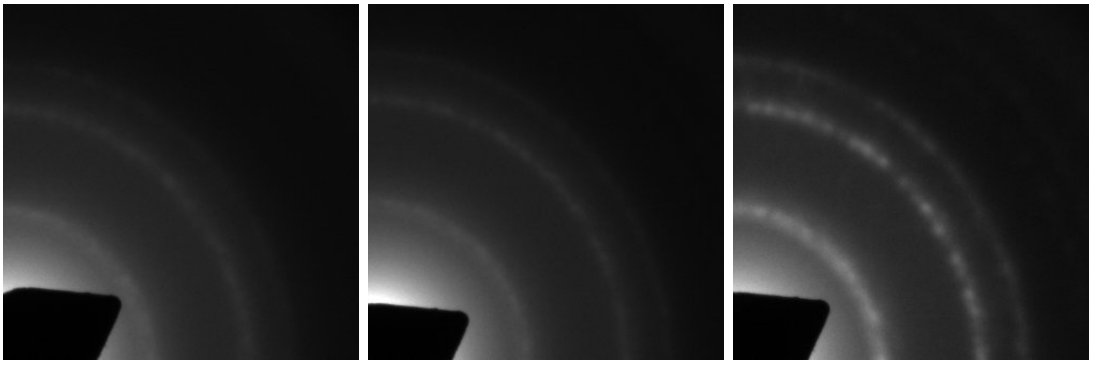

(A) 1 minute (B) 3 minutes (C) 5 minutes

FIGURE 6.2: Selected area electron diffraction patterns for CdZnSeS NC after a) 1 minute b) 3 minutes and c) 5 minutes growth.

be the zinc blende {111} which would correspond to NC lattice constant of 5.72 Å, 5.62 Å and 5.56 Å for 1 minute, 3 minutes and 5 minutes growth respectively. This highlights a general trend from the largest possible crystal structure of CdSe (6.08 Å) that the NC could be, through ZnSe (5.67 Å) to the smallest possible lattice constant of ZnS (5.41 Å) and thus supports a varying structure with increasing shell thickness that builds on the reaction dynamics of the individual precursors.

Figure 6.3 shows HRTEM images of CdZnSeS with 3 minutes and 5 minutes growth. Indexing the FFT was intrinsically difficult due to three different distances to the Bragg spot pairs where at least two matching distance pairs are expected. This observation of three Bragg distances could highlight a potential strain releasing mechanism or preferential alloying direction/orientation as was seen in reference [209].

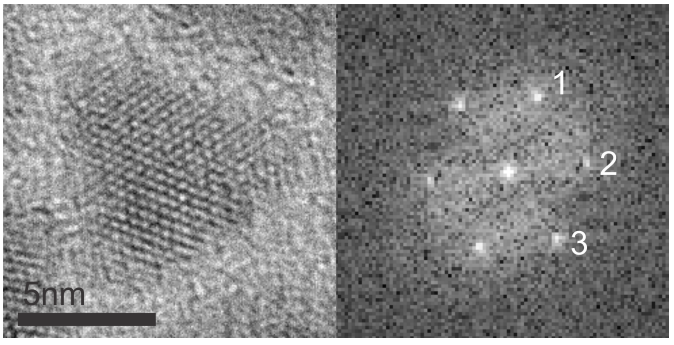

(A) 3 minutes

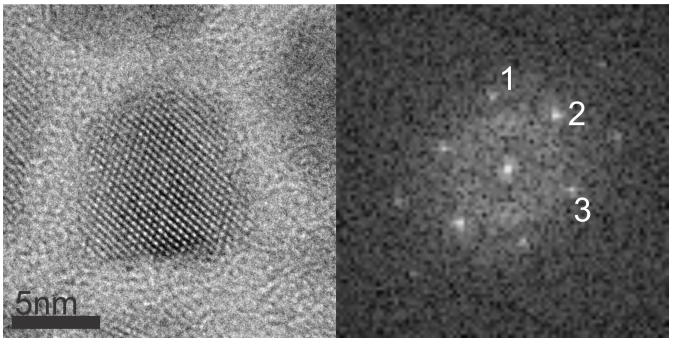

(B) 5 minutes

FIGURE 6.3: HRTEM images of CdZnSeS NC after a) 3 minute and b) 5 minutes growth. The images are shown with the corresponding FFT and index Bragg reflections distances of a) $1_a = 2.90$ nm^{-1}, $2_a = 2.76$ nm^{-1} and $3_a = 2.81$ nm^{-1} and b) $1_b = 3.04$ nm^{-1}, $2_b = 2.89$ nm^{-1} and $3_b = 2.66$ nm^{-1}.

6.2.2.2 Ensemble optical properties

Figure 6.4a shows the evolution of the absorption spectra highlighting a redshift of the first exciton from 614 nm to 638 nm with increasing growth time and size. PL showed a similar redshift in peak wavelength from 615 nm to 641 nm. As can be seen in figure 6.4d these shifts coincide with an interesting variation in Stokes shift which varied markedly from 1 nm down to 0 nm back up to 3 nm with increasing NC size and highlights a potential crossing of the energy levels in the fine structure [187]. The PL FWHM decreases with size from 32 nm to 30 nm in support of the small reduction in size distribution seen in figure 6.1.

To provided further support for a single graded CdSe-ZnS structure, PLE, measured at the PL peak intensity, showed the wavelength dependent emission intensity spectra which correlated to the observed absorption spectra as seen in figure 6.4a. This highlights that the absorption spectra do not mask any other NC or non-emissive structures and that the optical feature in the absorption spectra are coupled to the bandedge emission. The NC were excited with a wavelength as high as 340 nm with no observation of PL from other NC, further supporting the fact that no other NC made solely from one of the constituent material NC. To see if the redshift follows a purely CdSe NC behaviour, a comparison was made to the particle size predicted using the first excitonic absorption feature and the empirical fitting parameter determined in reference [43] (Figure 6.4d). The comparison showed the experimental data to be significantly blueshifted when compared to theoretical CdSe NC. This highlights the synthesised NC have a larger than expected bandgap, consistent with either a core-shell CdSe/ZnS structure or a graded CdSeS/CdZnSe alloy.

Ensemble lifetime measurements were used to show a type-I system. Whilst the lifetime

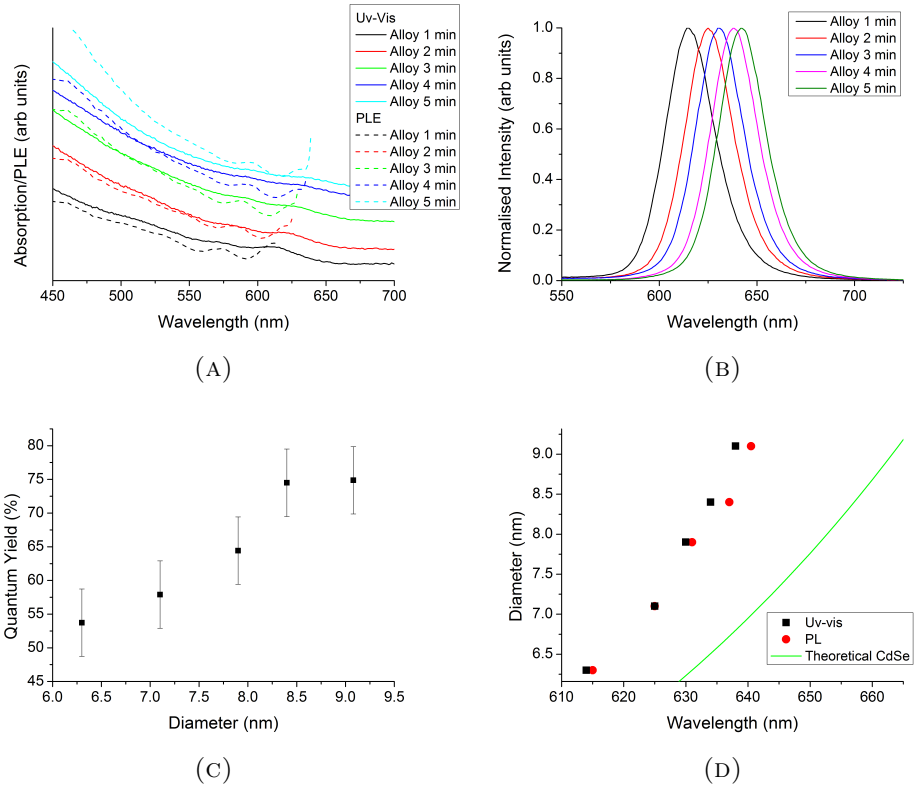

(A) (B)

(C) (D)

FIGURE 6.4: The ensemble optical properties for the growth series of CdZnSeS NC. a) Ensemble absorption and PLE spectra b) PL spectra excited at 400 nm c) QY and d) a comparison of the ensemble PL with first excitonic feature highlighting the Stokes shift. For comparison the theoretical diameter of CdSe as calculated using empirical fitting parameter determined in reference [43] and the first excitonic feature.

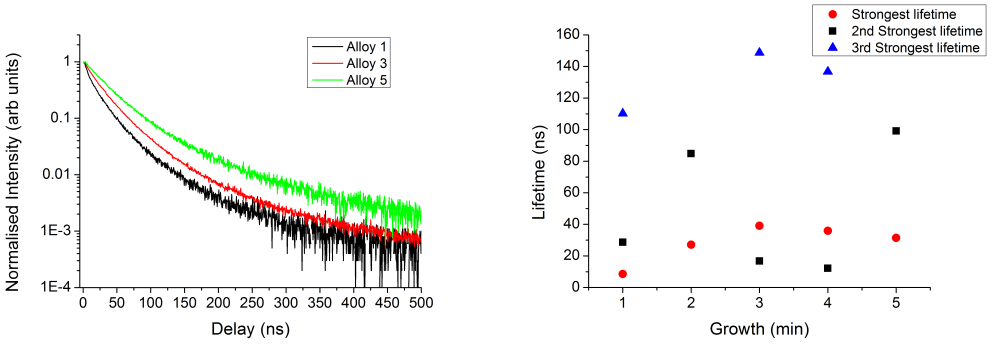

(A) (B)

FIGURE 6.5: a) Ensemble lifetime measurements for CdZnSeS after 1, 3 and 5 minutes growth. b) The bi- and tri-exponential lifetime for each growth time. These are highlighted by relative amplitude strength. Full fitting parameters can be found in the Appendix F.1

measurements show either bi- and tri-exponential fitting as seen in figure 6.5a, the strongest lifetime components saw a rise from 8.6 ns to 39.1 ns and then a subsequent fall to 31.4 ns with increasing size (Red dots figure 6.5b). The 8.6 ns lifetime is comparable with a CdSe core only structure [129] and 39.1 ns is comparable to CdSe/CdS structure with 4 ML shell (∼40 ns [129]). If a CdSe/CdS can be assumed, using the theoretical calculations of reference [126] for CdSe/CdS structures indicates that these NC can be potentially be classed as quasi type-II. It is interesting to note the subsequent drop in lifetime for large NC, this could be due to either a decrease in non-radiative lifetime, however this would also see a reduction in QY, or strain/alloying/natural band alignment effects changing wavefunction overlap to a more type-I geometry.

As seen in figure 6.4c, the QY increased significantly from 53% to 75% for 1 and 5 minutes growth respectively which plateaus after 4-5 minutes growth. This remarkably high QY of 75% is comparable to some of the best ternary type-I NC [79, 80], and thus, a good candidate for SNS.

6.2.2.3 Single nanocrystal spectroscopy

This section conducts SNS on the CdZnSeS NC with 5 minutes growth which have shown the highest QY.

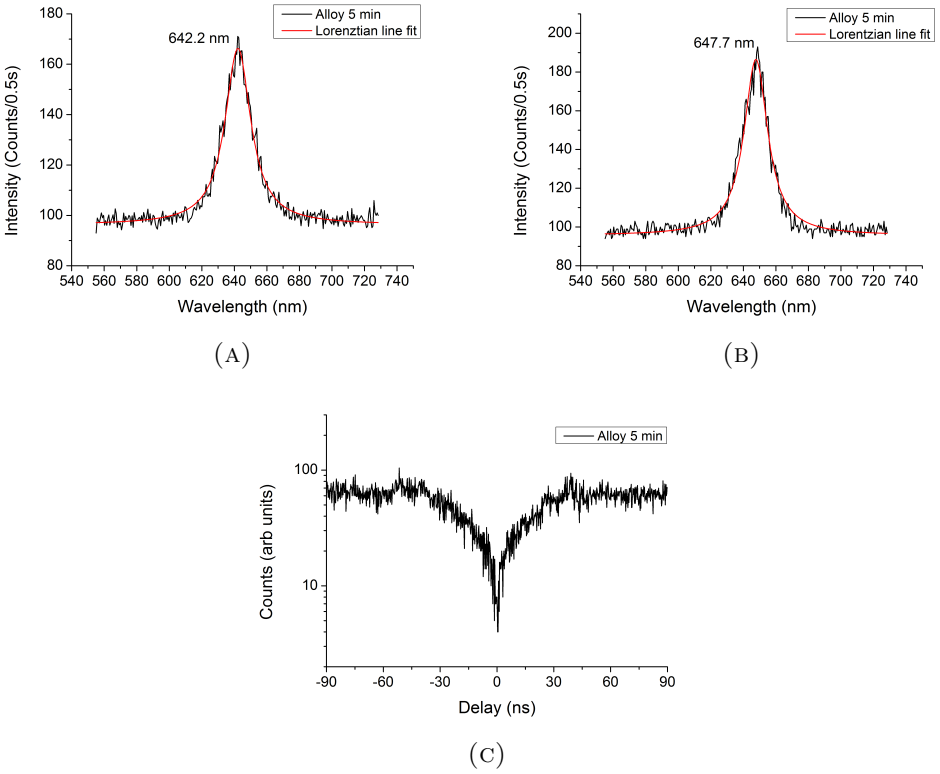

FIGURE 6.6: a-b) Representative spectra of two CdZnSeS 5 minutes NC showing Lorentzian line emission with FWHM of 19.2 nm and 17.8 nm respectively. c) Hanbury Brown Twiss measurement on a NC showing a FWHM of 20 nm showing a $g^{(2)}$ correlation drop at 0 ns to 9% of the total intensity.

Figure 6.6 shows the representative spectra for CdZnSeS 5 minutes NC which show Lorentzian line shapes. These have a FWHM range between 15 nm and 22 nm and an average of 18.3 nm with a standard deviation of 2.6 nm. Whilst all the NC showed Lorentzian line shapes, which is consistent with a single NC emitter, a FWHM over 20 nm could highlight the emission of a small cluster of NC. Thus, a HBT measurement can be conducted to confirm a single emitter [210]. Figure 6.6c shows a HBT measurement for a NC with a FWHM of 20 nm which has a characteristic dip in the $g^{(2)}$ signal at zero

delay time. This dip falls to 9% of the highest count rate, considerably lower than the 50% required to describe a single photon emitter.

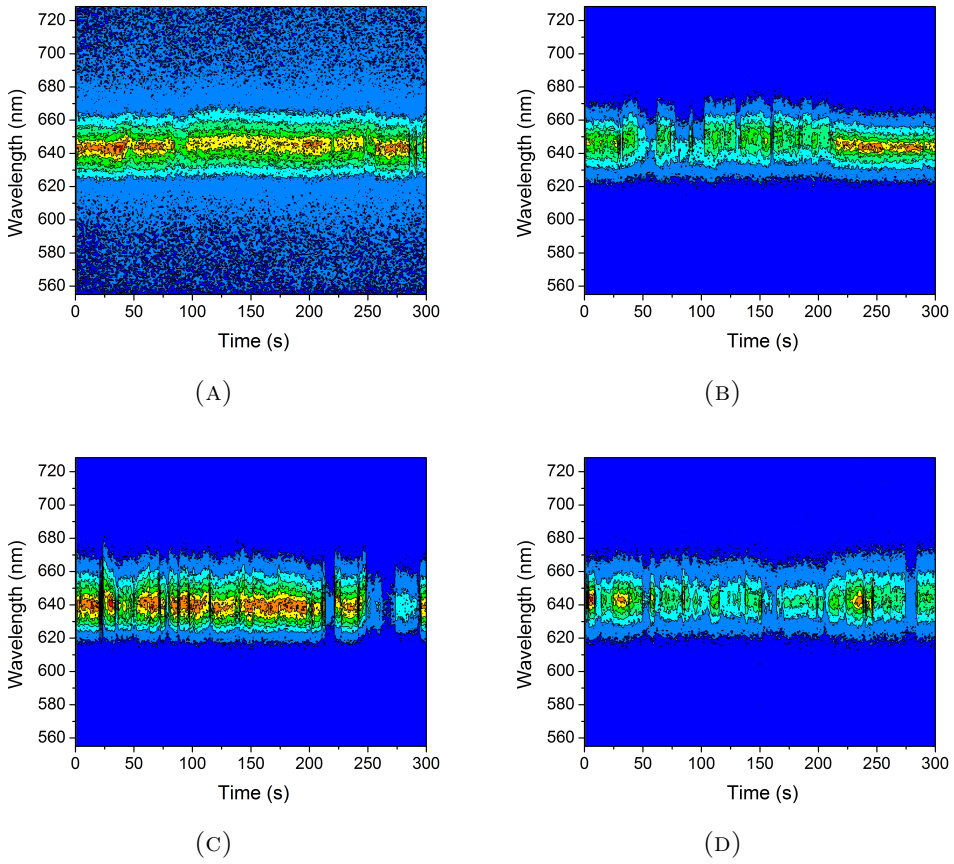

FIGURE 6.7: Spectral trajectories of four separate CdZnSeS NC highlighting a) NC with good stable emission b-c) NC predominately in the 'on' state with small amount of spectral diffusion d) NC showing a large amount of blinking.

Figure 6.7 shows representative spectral trajectories of four single NC. 25% of the 30 NC observed showed a large amount of blinking as seen in figure 6.7d. The majority of the NC showed good emissive qualities with NC largely in the 'on' state as seen in figure 6.7a-6.7c. A large amount of spectral diffusion could be seen which often coincided with blinking event as seen in all the NC in figure 6.7. This spectral diffusion could be as large as 5-7 nm as seen in figure 6.7b-6.7d which can be related to a surface/shell trapping mechanism seen by Empedocles *et al.* [203].

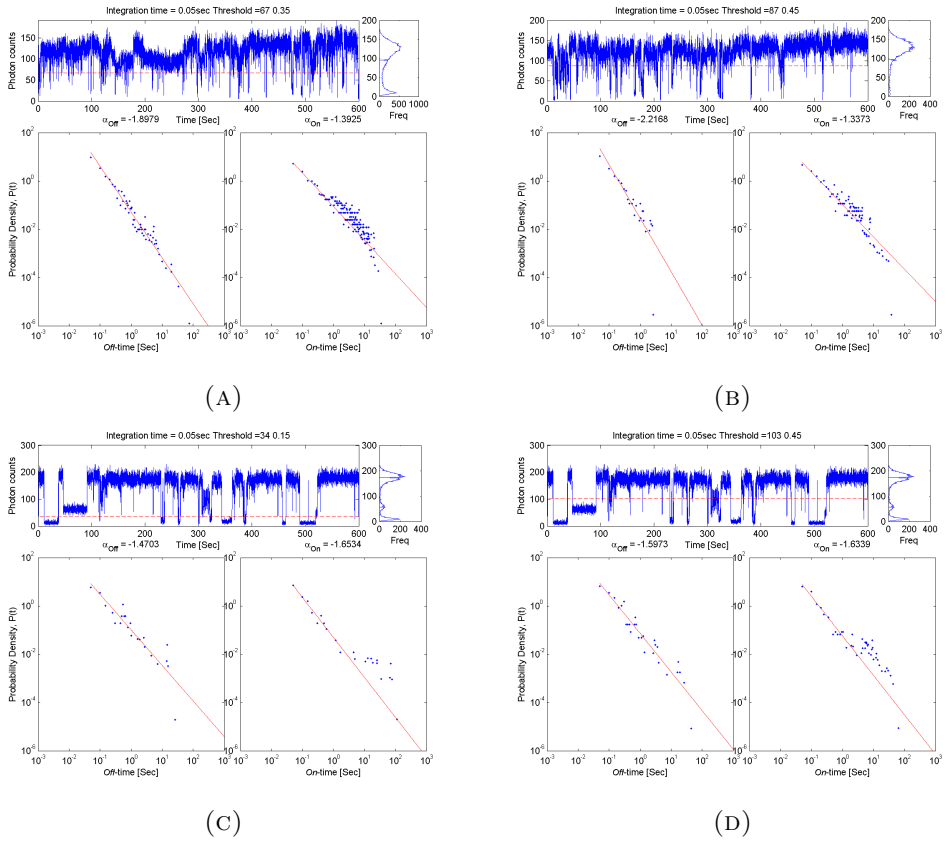

FIGURE 6.8: Intensity-time and blinking statistics of three CdZnSeS NC investigated over 10 minutes showing a-b) nearly non-blinking NC showing 'off'/'on' power law exponents of a) -1.90 and -1.39 b) -2.22 and -1.34 respectively. c-d) the blinking statistic of the same NC showing a 'off'/'on' power law exponents with a threshold of c) 34 counts of -1.47 and -1.65 and d) 105 counts of -1.60 and -1.63 respectively.

The intensity-time trajectories of figure 6.8 highlight a wide variety of blinking properties. The 'off' and 'on' probability distribution for all the observed NC showed a power law dependence. The 'off' exponent ranged between -1.3 to -2.3 with an average of -1.88 and a standard deviation 0.27 whilst the 'on' ranged between -1.0 and -1.7 with an average -1.26 with standard deviation and 0.19. The nearly non-blinking NC as seen in figure 6.8a and 6.8b saw 'off' and 'on' exponents that deviated away from the expected blinking exponent of -1.5 towards -2 and -1 respectively. Such exponents are indicative of a high probability of a small 'off' and large 'on' duration. In general, the 'off' exponent is larger than the 'on' exponent and the 'on' component is generally below -1.5, however figure 6.8c and 6.8d highlight the first observation within these studies where

this was not the case and the 'off' exponent was smaller than the 'on'. It is interesting to note that whilst most blinking statistics are only mildly dependent on threshold, figure 6.8c-6.8d highlights largely different 'off' exponents for the various thresholds. It will been shown later in figure 6.11 that these thresholds take into consideration two different blinking processes where the higher threshold of 103 counts in figure 6.8d incorporates both A- and B-type blinking whereas the lower threshold of 34 counts in figure 6.8c incorporates just A-type blinking.

As can be seen in figures 6.9b-6.12b, the single NC lifetime were seen to be mildly bi-exponential with a strong component that ranged over 18-40 ns with an average of 26.0 ns and standard deviation of 5.8 ns. This is in comparison to the strongest component of the ensemble lifetime which was measured to be 31.0 ns. A further weak shorter lifetime component was observed in the single NC accumulated lifetime which had an average lifetime of 6 ns with a standard deviation of 3.2 ns. The unfortunate nature of the ensemble lifetime makes this component incomparable to single NC observations here.

Figure 6.9 highlights the intensity-time and lifetime-time trajectories for a nearly non-blinking NC which shows only a few drops in intensity. An inspection of the corresponding lifetimes at points **d**, **e** and **f** in figures 6.9d-6.9e shows mono-exponential decay within each specific time bin and that the lifetime can vary considerably with intensity. FLID enables general trends in intensity-lifetime to be observed. Figure 6.9c identifies that the NC mode lifetime to be in the high-intensity 'on' state which has a mode lifetime of 26 ns that is consistent with the accumulated lifetime of 27.0 ns seen in figure 6.9b and in reasonable agreement to the strong component lifetime in the ensemble lifetime. This lifetime is indicative of single exciton emission. The majority of the 'off' states can be related to short lifetimes with lifetimes of ∼5-7 ns which is

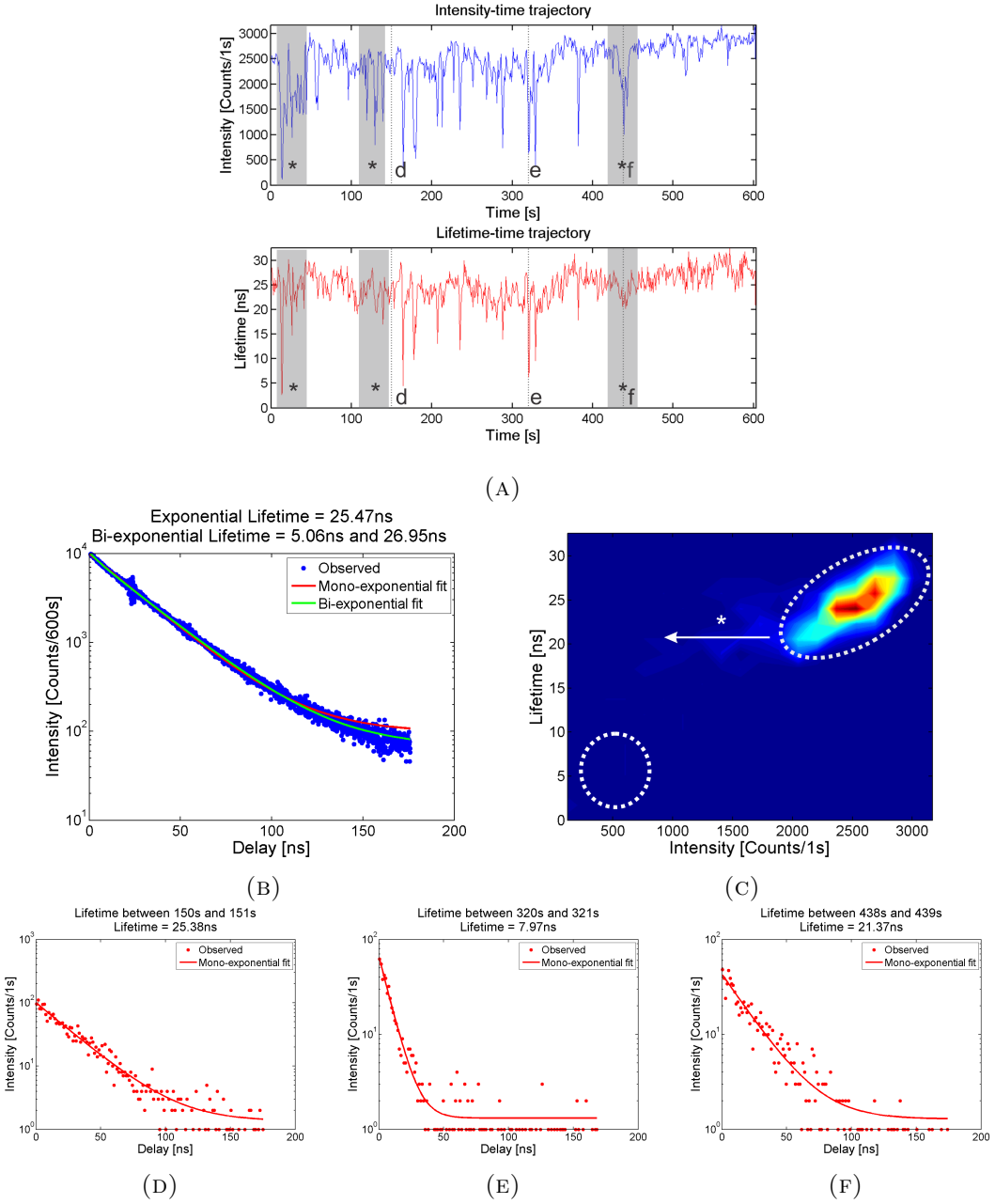

FIGURE 6.9: a) A comparison of the intensity-time and lifetime-time trajectories for a CdZnSeS NC under pulsed excitation with a repetition rate of 5 MHz and investigated for 10 minutes with a 1 second integration. b) The accumulated lifetime over a 10 minute integration. c) A FLID using the data from [a]. The lifetime between d) 150 s and 151 s e) 320 s and 321 s and f) 438 s and 439 s

most notably highlighted by point **e** in figure 6.9a and the corresponding lifetime figure 6.9e. The general trend of this emission within FLID gives a second mode, albeit small, with a low-intensity low-lifetime. As was shown in section 2.5.2 this type of emission is indicative of A-type blinking and highlights the possibility of trion emission. A second

trend in emission characteristic can be seen in the regions marked (∗) in figure 6.10a which has large drops in intensity but no real change lifetime (∼22-25 ns). This is more clear by comparing the lifetime at point **d** and **f** in figure 6.9d and 6.9f. This emission characteristic is an indication that B-type blinking is present within these NC.

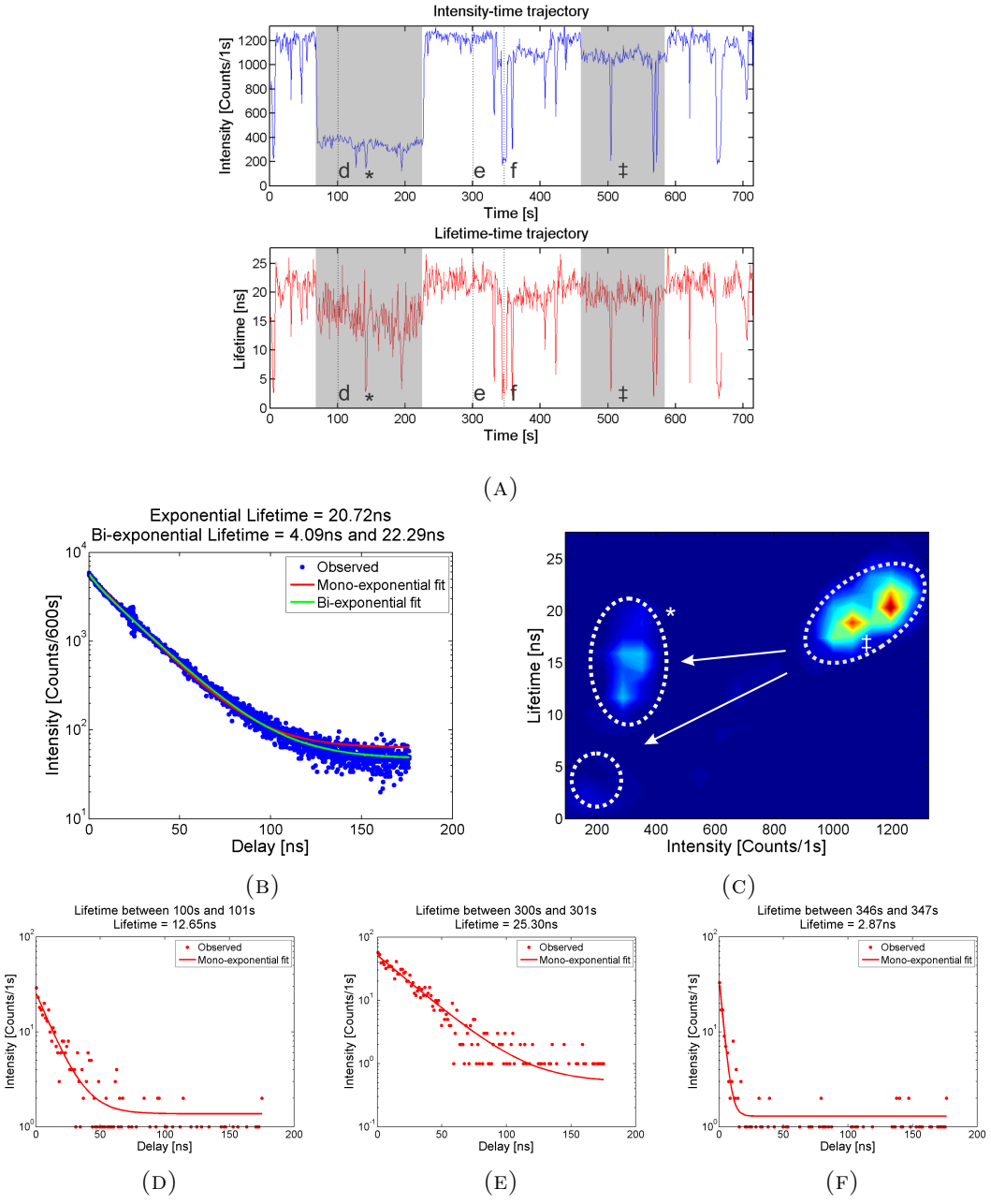

FIGURE 6.10: a) A comparison of the intensity-time and lifetime-time trajectories for a CdZnSeS NC under pulsed excitation with a repetition rate of 5 MHz and investigated for 10 minutes with a 1 second integration. b) The accumulated lifetime over a 10 minute integration. c) A FLID using the data from [a]. The lifetime between d) 100 s and 101 s, e) 300 s and 301 s and f) 346 s and 347 s

Figure 6.10 and 6.11 show two NC which show increased amount of blinking and show better examples of the previous trends. The majority of the blinks could be correlated to drops in lifetime to ∼5 ns as can be seen by comparing lifetimes at points **e** and **f** in figure 6.10 and **d** and **f** in figure 6.11. This is again indicative of A-type blinking which gives a mode at low intensities-lifetimes within the FLID figures 6.10c and 6.11c. The two modes in the FLID figure 6.10c and 6.11c show lifetimes of 4 ns and 21 ns, and 3 ns and 22 ns respectively, which show good agreement with accumulated lifetime components of 3.07 ns and 23.32 ns, and 4.09 ns and 22.29 ns seen in figures 6.10b and 6.11b respectively.

Both FLID figures also show regions where a drop in intensity but no significant drop in lifetime are seen. These regions are marked by (∗) and are extremely evident in the intensity-time trajectories of figure 6.10a and 6.11a and the specific lifetimes of point **d** in figure 6.10d and **e** in 6.11e. These regions are indicative of B-type blinking and can be long lived (Several 10's of seconds). It is interesting to note that the B-type blinking marked as (*) in figure 6.10a also showed a slowly decreasing lifetime which highlights another temporary process such as QCSE that influences the blinking and lifetime.

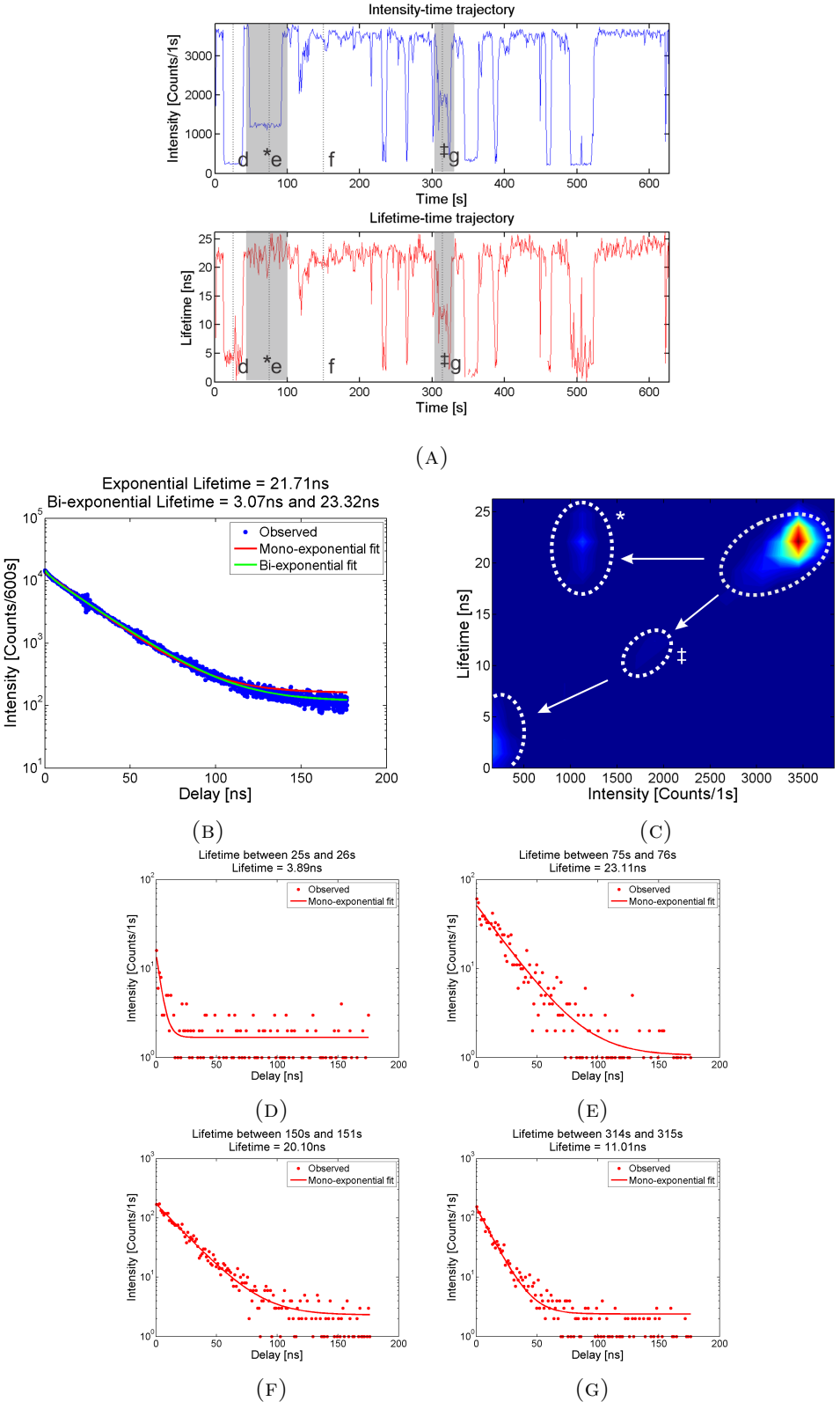

FIGURE 6.11: a) A comparison of the intensity-time and lifetime-time trajectories for a CdZnSeS NC under pulsed excitation with a repetition rate of 5 MHz and investigated for 10 minutes with a 1 second integration. b) The accumulated lifetime over a 10 minute integration. c) A FLID using the data from [a]. The lifetime between d) 25 s and 26 s, e) 75 s and 76 s, f) 150 s and 151 s and g) 314 s and 315 s.

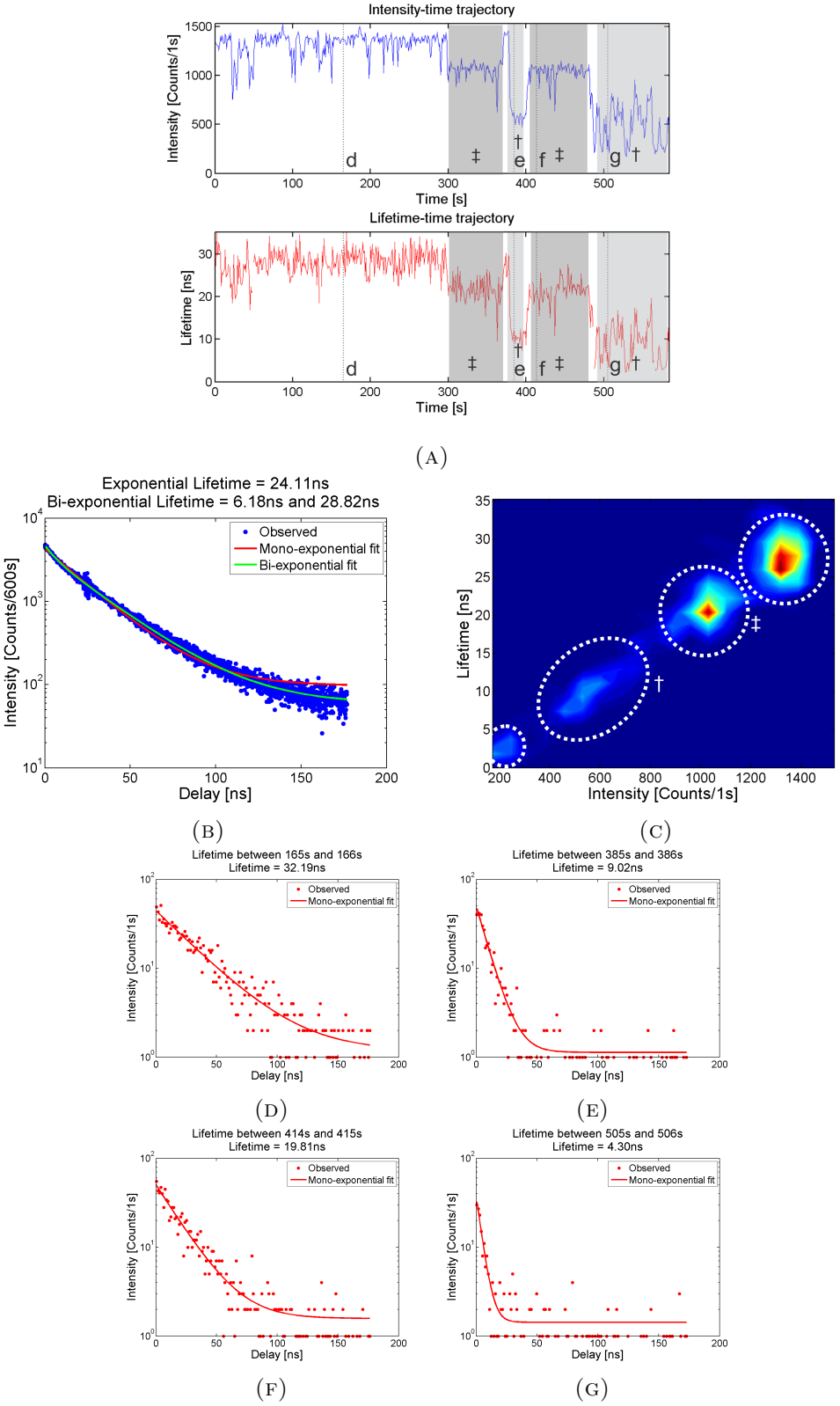

FIGURE 6.12: a) A comparison of the intensity-time and lifetime-time trajectories for a CdZnSeS NC under pulsed excitation with a repetition rate of 5 MHz and investigated for 10 minutes with a 1 second integration. b) The accumulated lifetime over a 10 minute integration. c) A FLID using the data from [a]. The lifetime between d) 165 s and 166 s, e) 385 s and 386 s, f) 414 s and 415 s and g) 505 s and 506 s.

Figure 6.10a-6.12a show NC which show some stepwise intensity changes which corresponds to linear drops in lifetime as seen in the regions marked (‡) and (†). The lifetime within these regions (Figure 6.11g, 6.12e and 6.12f) consistently show mono-exponential decays highlighting a single recombination mechanism for the system within these time bins. Whilst two or three modes are expected in the FLID, which should be attributed to single exciton recombination and to A- or B-type blinking (or grey state emission), the observation of more modes which scale linearly with intensity and lifetime highlights other recombination dynamics. Since there was little spectroscopic change with these NC before intensity time investigation, it could be assumed that these changes in recombination dynamics could be due to the anisotropic shape of some of the NC, as was seen from TEM, or localisation of charges (either single exciton or multi-exciton or trapped charge carriers).

6.2.3 Summary

A one-pot synthesis method was used to produce CdZnSeS NC which provides strong emitters with QY as high as 76% and a ensemble FWHM of less than 32 nm which correlates closely the small size distribution ∼9% in observed in TEM. The optical and physical characterisation show that the formed NC have broadly similar bandgaps and composition from CdSe to ZnS. Rather unsurprisingly the synthesis does yield a wide range of emission recombination dynamics as seen by the variety of blinking properties and the lifetime range. SNS of the highest QY NC showed the majority of the NC to be predominantly in the ‘on’ state with some spectral diffusion present. The blinking ‘off’ state is predominantly trion A-type blinking however B-type blinking is still present highlighting the activation of recombination centres. Multiple ‘grey’ state emission was identified for some of the NC the intensity of which has a linear dependence with lifetime.

6.3 eBioscience eFluor®nanocrystals

6.3.1 Introduction and motivation

eBioscience is a commercial company specialising in fluorescent labels for biological application with specific emphasis on labels for flow cytometry studies [211]. This sections presents an exploratory study of a size series of eBioscience eFluor® NC with the goal to give further insight into the optical properties of eFluor®NC which will help with the design of future NC with specific focus on the recombination dynamics within single NC excited well below the single exciton limit.

6.3.2 Stated properties and composition

These NC are synthesised under licence from Evident using the method described in US Patent No. 7,482,059 and are stated to consist mainly of a CdSe core and ZnS shell [211]. The patented synthesis method claims a "metal layer...reduce[s] the lattice mismatch between the semiconductor core and shell" [212]. These NC were provided in toluene and are TOPO capped [211]. All other composition information is proprietary.

Product name	Sample code	Peak PL (nm)	FWHM (nm)	QY
eFluor® 605 nm	Y0002	608	27	79
eFluor® 625 nm	Y0004	625	28	90
eFluor® 640 nm	Y0005	641	22	90+
eFluor® 650 nm	Y0007	646	29	88

TABLE 6.1: The eFluor®NC samples and quoted optical properties.

Table 6.1 and figure 6.13 show the stated optical properties and spectral features of the size series of eFluor® NC investigated. These NC show impressive optical properties in terms of FWHM as low as 22 nm and QY in excess of 90%.

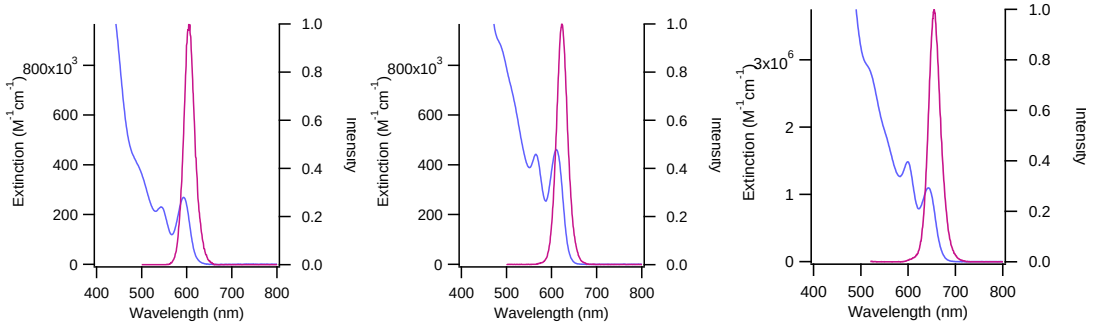

FIGURE 6.13: Extinction coefficient (Pink) and PL spectra (Purple) for a) eFluor®605 nm b) eFluor®625 nm and c) eFluor®650 nm NC [211].

6.3.3 Results

6.3.3.1 Ensemble lifetimes

Ensemble lifetime measurements of figure 6.14 and table 6.14 highlight that the eFluor®NC have a mild bi- or tri-exponential decay with strong lifetime component in the region of 19-26 ns. Two weaker components can also be observed one with a short lifetime of 4-9 ns and long lifetime component of 39-52 ns.

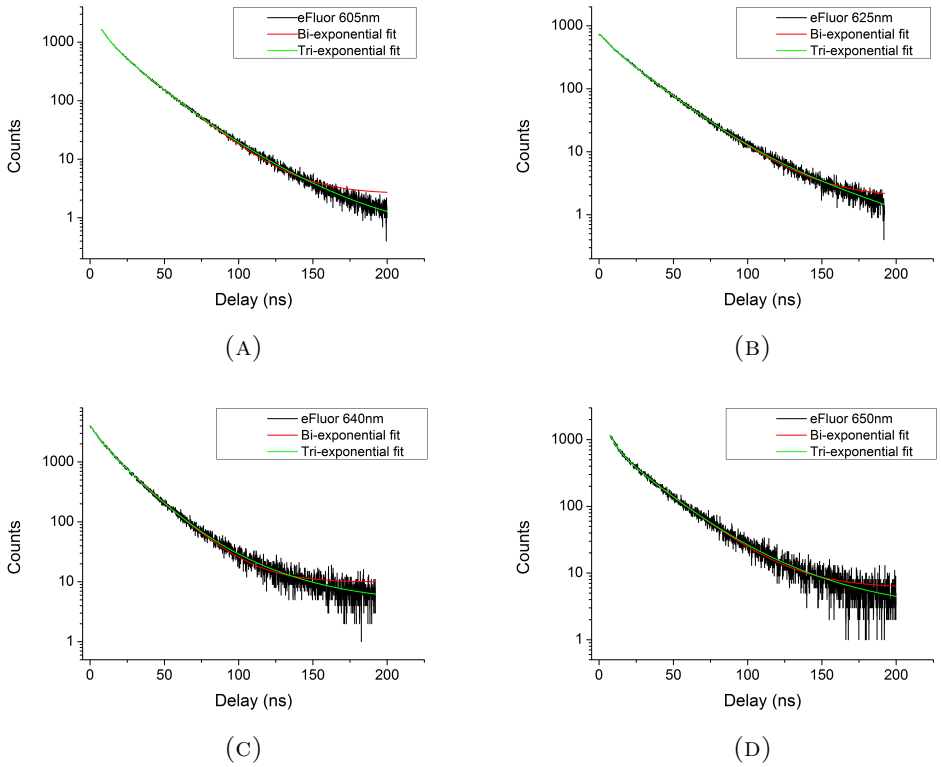

FIGURE 6.14: Ensemble lifetime data for a) eFluor®605 nm b) eFluor®625 nm c) eFluor®640 nm and d) eFluor®650 nm NC.

Lifetime	Amplitude τ_1	τ_1 (ns)	Amplitude τ_2	τ_2 (ns)	Amplitude τ_3	τ_3 (ns)
eFluor®605 nm						
Bi-exponential	6226.5	6.8	10301.5	22.1		
Tri-exponential	5988.2	6.8	11707.1	19.9	735.9	46.4
eFluor®625 nm						
Bi-exponential	2165.5	9.0	5138.7	25.7		
Tri-exponential	1341.9	8.8	5208.8	22.7	159.1	52.0
eFluor®640 nm						
Bi-exponential	1604.9	7.8	2425.0	20.0		
Tri-exponential	878.4	7.9	2654.8	19.1	878.4	39.0
eFluor®650 nm						
Bi-exponential	518.2	5.4	736.5	25.5		
Tri-exponential	369.8	4.8	671.1	22.1	88.7	49.3

TABLE 6.2: The bi- and tri-exponential lifetime components for the lifetime trajectories of figure 6.14.

6.3.3.2 TEM images of eFluor® nanocrystals

Figures 6.15-6.18 show HRTEM images of the eFluor®605 nm, 625 nm 640 nm and 650 nm NC. It can be seen from figure 6.17 that eFluor®640 nm NC are predominately spherical NC whilst the eFluor®605 nm, 625 nm and 650 nm shows quasi-spherical/tetrahedral NC (Figure 6.15, 6.16 and 6.18). A closer inspection of the HRTEM images of figures 6.15-6.18 highlight infrequent observations of stacking faults within the spherical eFluor®640 nm NC whilst a higher proportion of eFluor®605 nm, 625 nm and 650 nm NC showed stacking faults which appeared to coincide with anisotropic growth, as most notably seen in figure 6.18.

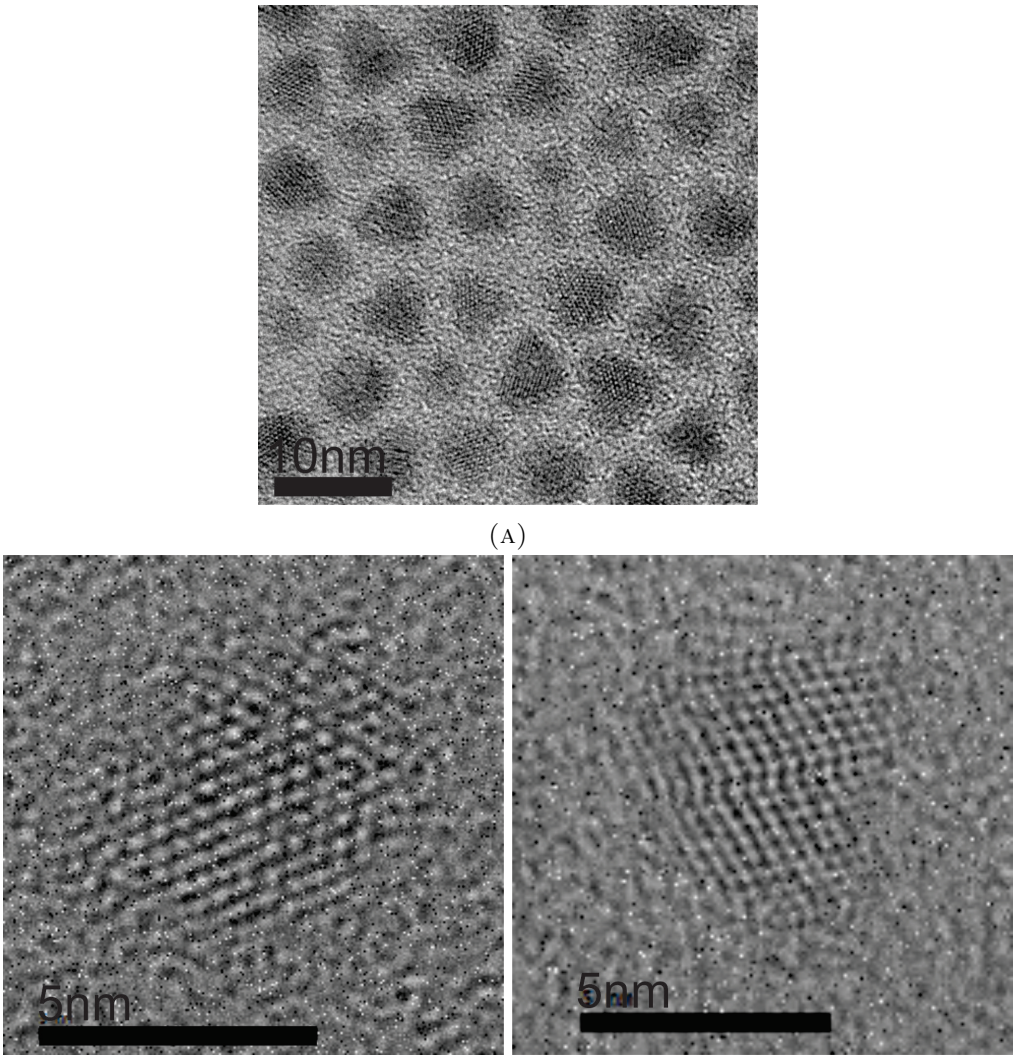

(A)

(B) (C)

FIGURE 6.15: TEM images of eFluor®605 nm NC showing limited number of twinning stacking faults.

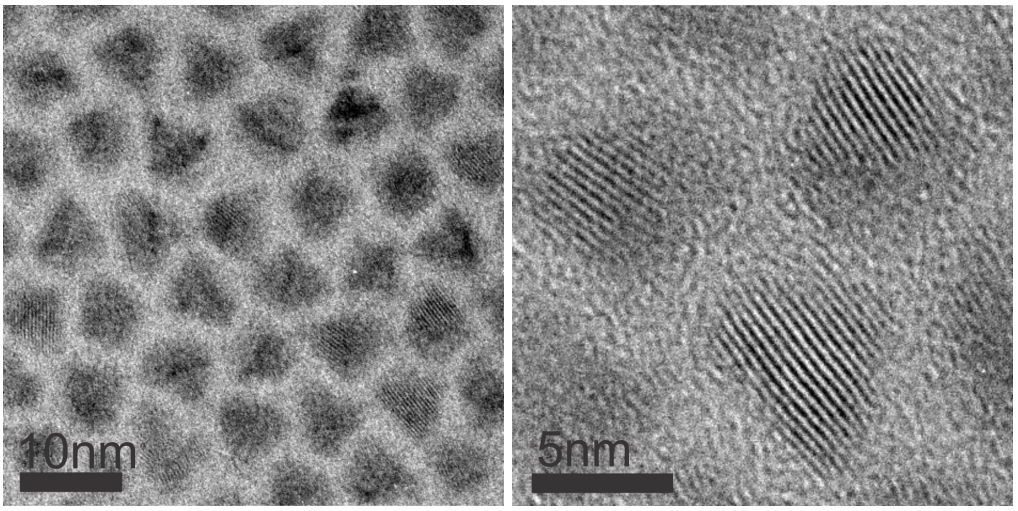

(A) (B)

FIGURE 6.16: TEM images of eFluor®625 nm NC showing a mixture of coherent and incoherent crystals structures.

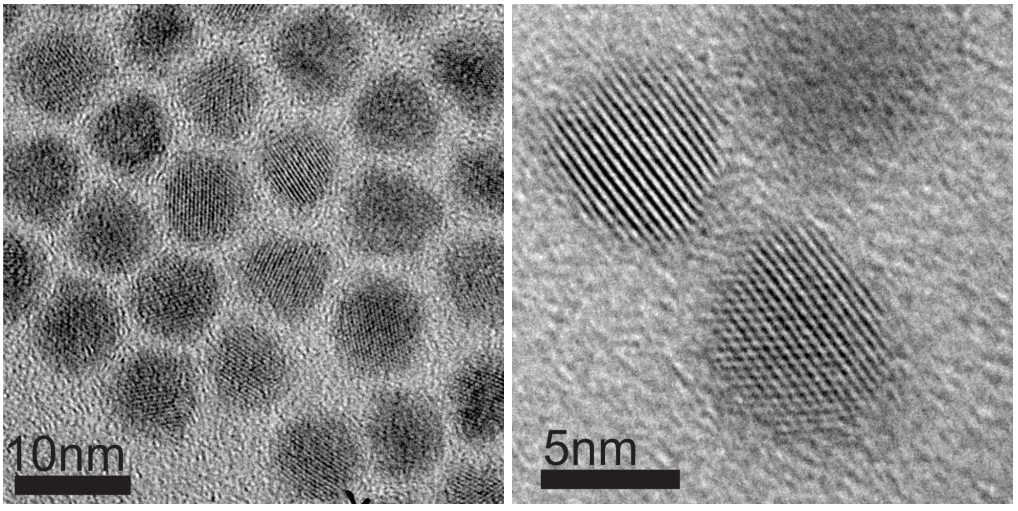

(A) (B)

FIGURE 6.17: TEM images of eFluor®640 nm NC showing predominently coherent crystals structures.

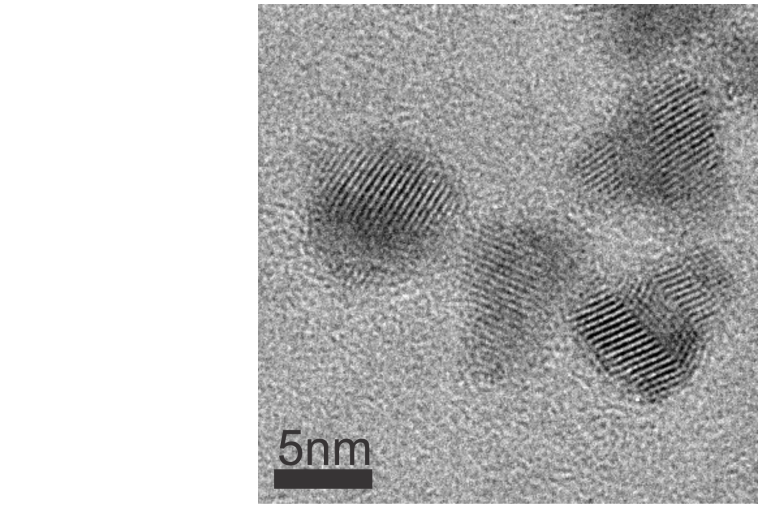

(A)

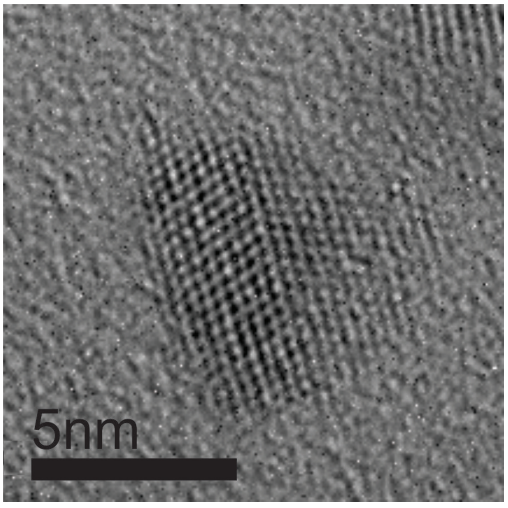

(B)

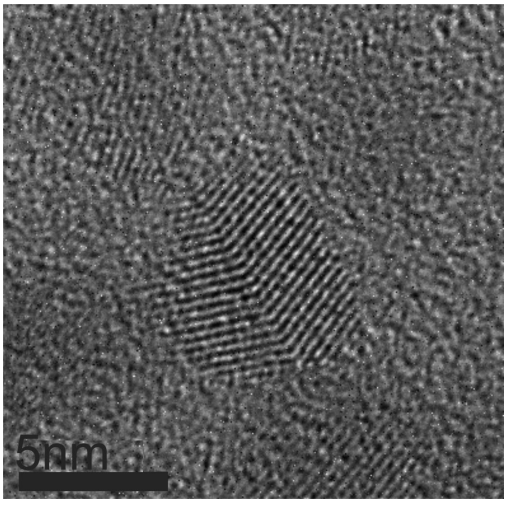

(C)

FIGURE 6.18: HRTEM images of eFluor®650 nm NC showing twinning stacking faults.

6.3.4 Single nanocrystal spectroscopy

This section presents the SNS investigations on eFluor®NC in numeric order however it most be noted that the most studied NC are the eFluor®625 nm, 640 nm and 650 nm. Utilising the extinction coefficients given in figure 6.13, it was calculated that all the NC were excited below 0.1 exciton per 200 ns in CW excitation or 0.1 exciton per pulse in pulsed excitation[213].

6.3.4.1 eBioscience eFluor® 605 nm nanocrystals

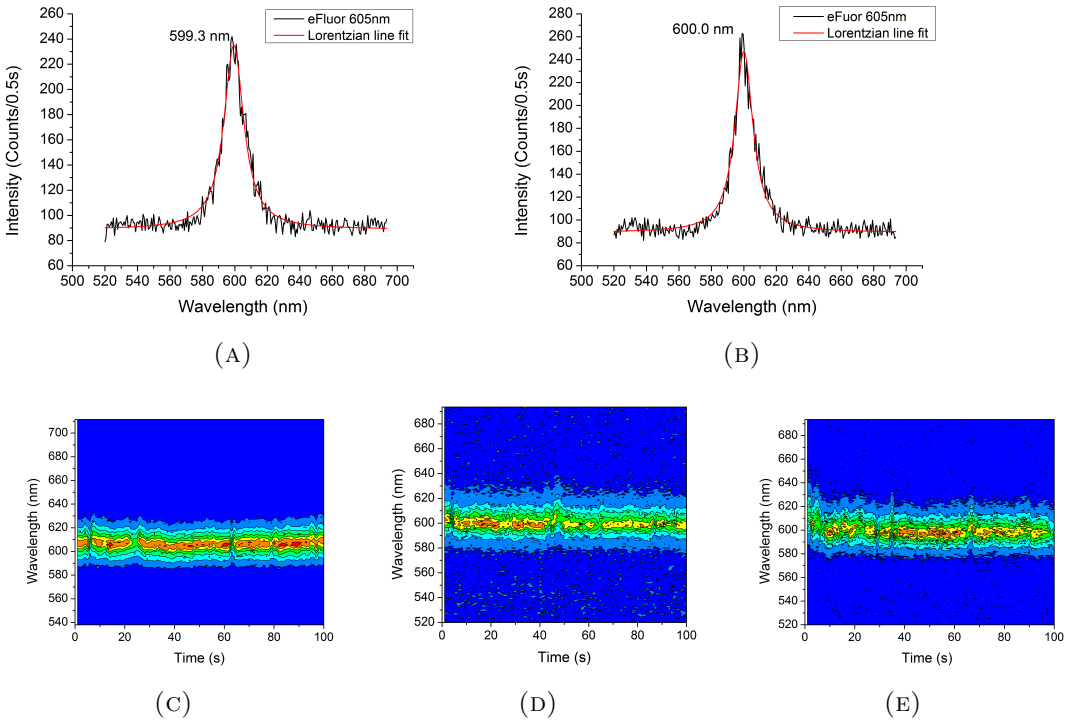

FIGURE 6.19: Representative spectra of single eFluor®605 nm NC a-b) show the spectra of single eFluor®605 nm NC with a Lorentzian line fit highlighting FWHM of 14.8 nm and 13.5 nm respectively. c-e) Spectral trajectories of eFluor®605 nm NC highlighting c-e) good optical performance with mild spectral diffusion.

Figure 6.19 shows the representative optical properties of single eFluor®605 nm NC which show Lorentzian line-shape emission with a FWHM of between 13-18 nm with an average of 15.1 nm and standard deviation of 1.0 nm (Figure 6.19a and 6.19b). Out of

the 18 NC spectral trajectories, 72% of the spectral trajectories showed no blinking or limited blinking on time scale larger than 0.5 seconds as seen by figure 6.19c and 6.19e). These figures show slowly varying spectral diffusion with typical shifts of less than 4 nm within non-blinking NC.

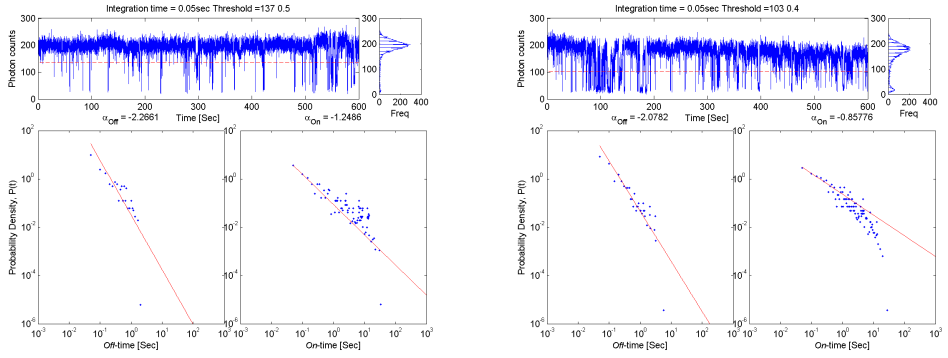

(A) (B)

FIGURE 6.20: Intensity-time trajectories and blinking statistics of two different eFluor®605 nm NC under continuous wave excitation showing a) a good optical stability and power law exponent of -2.27 and -1.24 for the 'off' and 'on' exponents respectively and b) large blinks with power law exponents of -2.08 and -0.86 for the 'off' and 'on' exponents respectively

Figure 6.20 shows the blinking studies under CW excitation which show the NC do blink on the order of tens of milliseconds. These had blinking power law behaviour, the 'off' exponent ranged between -1.8 to -2.9 with an average of -2.15 and standard deviation of 0.43, the 'on' time exponent ranged between -1.0 and -1.3 with an average of -1.15 of standard deviation 0.11.

Lifetime measurements of single NC showed predominantly single exponential or mildly bi-exponential fitting behavior (Figure 6.21b and 6.22b) which showed a lifetime/strong lifetime component ranging between 20-31 ns with an average lifetime of 23.4 ns and a standard deviation of 3.0 ns. The NC with bi-exponential lifetimes saw a smaller lifetime component with an average lifetime 4.6 ns which was less than 20% weaker in amplitude when compared to the stronger longer lifetime. The lifetime correlates reasonably to the

ensemble measurement which shows a tri-exponential fit with lifetimes of 6.8 ns, 22.1 ns and 46.4 ns (Figure 6.14).

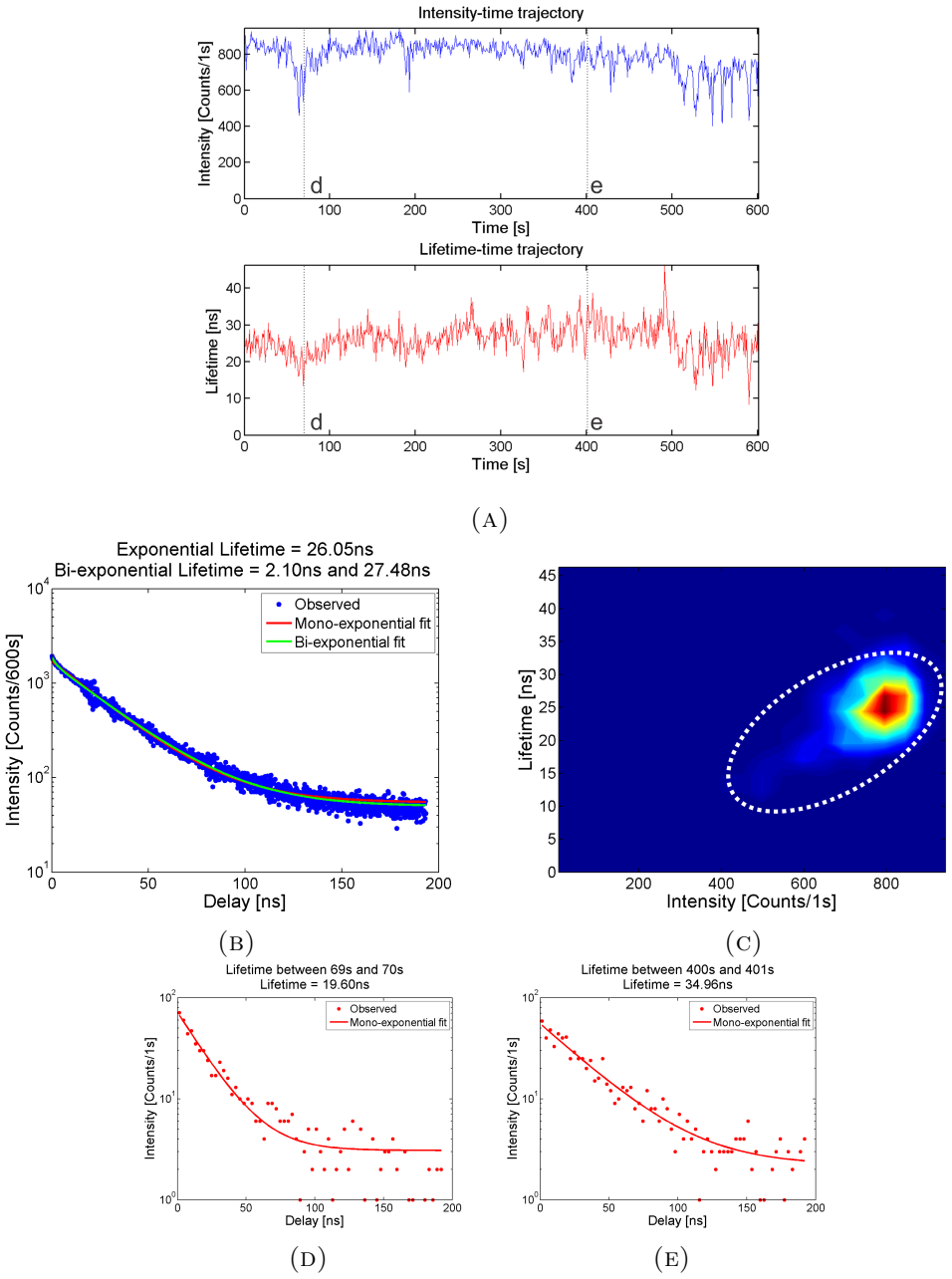

FIGURE 6.21: a) A comparison of the intensity-time and lifetime-time trajectories for an eFluor®605 nm NC under pulsed excitation with a repetition rate of 5 MHz and investigated for 10 minutes with a 1 second integration. b) The accumulated lifetime over a 10 minute integration. c) A FLID using the data from [a]. d) The lifetime between 69 s and 70 s and e) 400 s and 401 s.

Figure 6.21a shows a comparison of the lifetime-time and intensity-time trajectories for a non-blinking NC. The lifetimes ranged from 15-35 ns (Figure 6.21d-6.21e). FLID

highlights the main mode to be 26 ns in the 'on' state consistent with strong component in the accumulated lifetime of 27.5 ns.

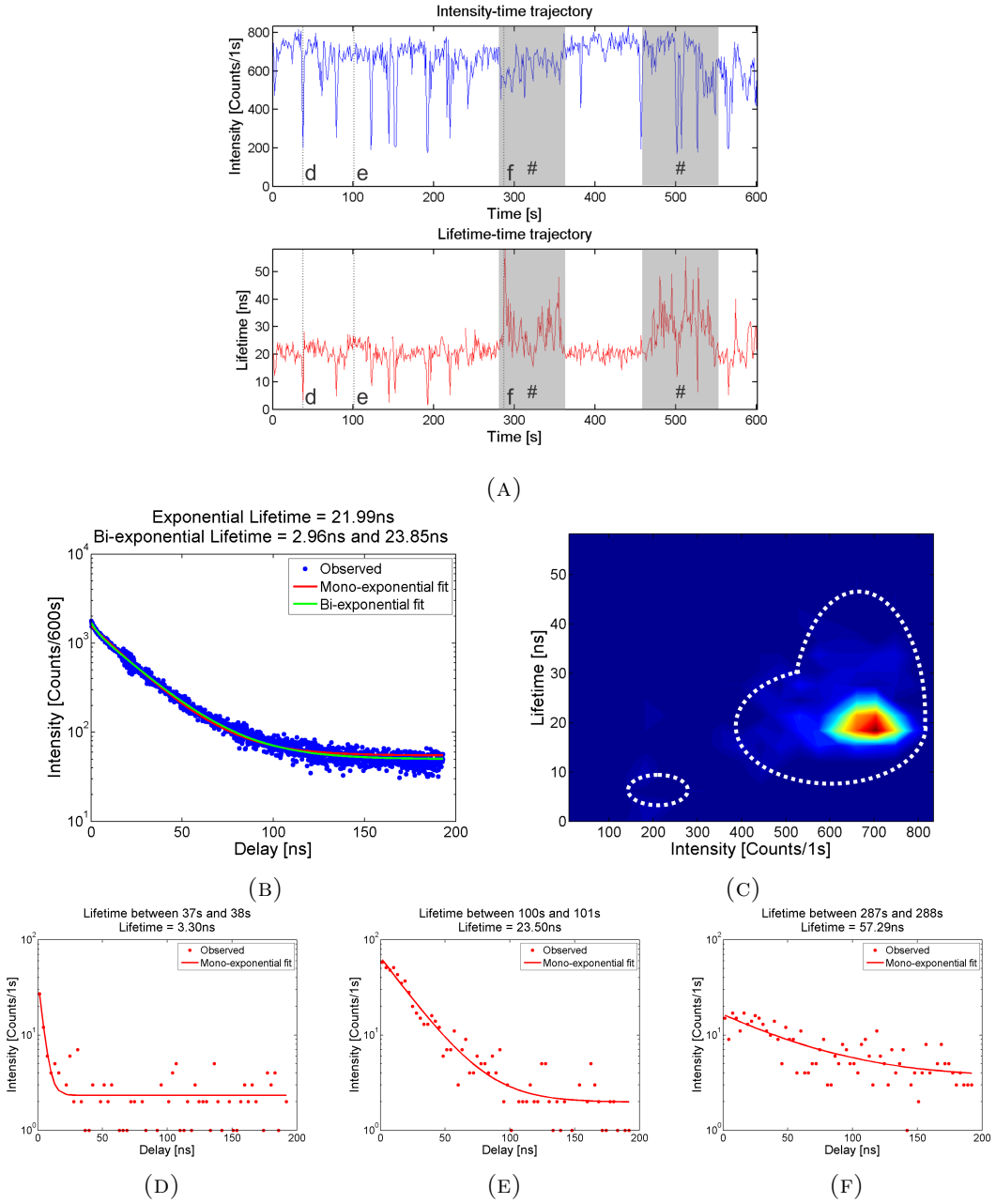

FIGURE 6.22: a) A comparison of the intensity-time and lifetime-time trajectories for an eFluor®605 nm NC under pulsed excitation with a repetition rate of 5 MHz and investigated for 10 minutes with a 1 second integration. b) The accumulated lifetime over a 10 minute integration. c) A FLID using the data from [a]. d) The lifetime between 37 s and 38s and e) 100 s and 101 s and f) 287 s and 288 s.

Figure 6.22 shows a comparison of lifetime-time and intensity-time trajectories for a blinking NC thats shows distinct drops in lifetime which correspond to 'off' states within

the intensity-time trajectory (Figure 6.22a). The lifetime within these blinks drops to as low as 3 ns as seen in figure 6.22d which supports the small lifetime component seen in the accumulated lifetime fit (Figure 6.22b). Interestingly, figure 6.22a also shows an increase in lifetime marked as (#) which is as high as 57 ns (Figure 6.22f). This increase in lifetime also corresponds to a mild decrease in the corresponding intensity.

Whilst the FLID figure 6.21c sees a trend to larger lifetimes due to the long lifetimes state, the general trend within the FLID for both NC sees a trend from a high-lifetime and high-intensity towards a low-lifetime and low-intensity (Figure 6.21c and 6.22c).

6.3.4.2 eBioscience eFluor® 625 nm nanocrystals

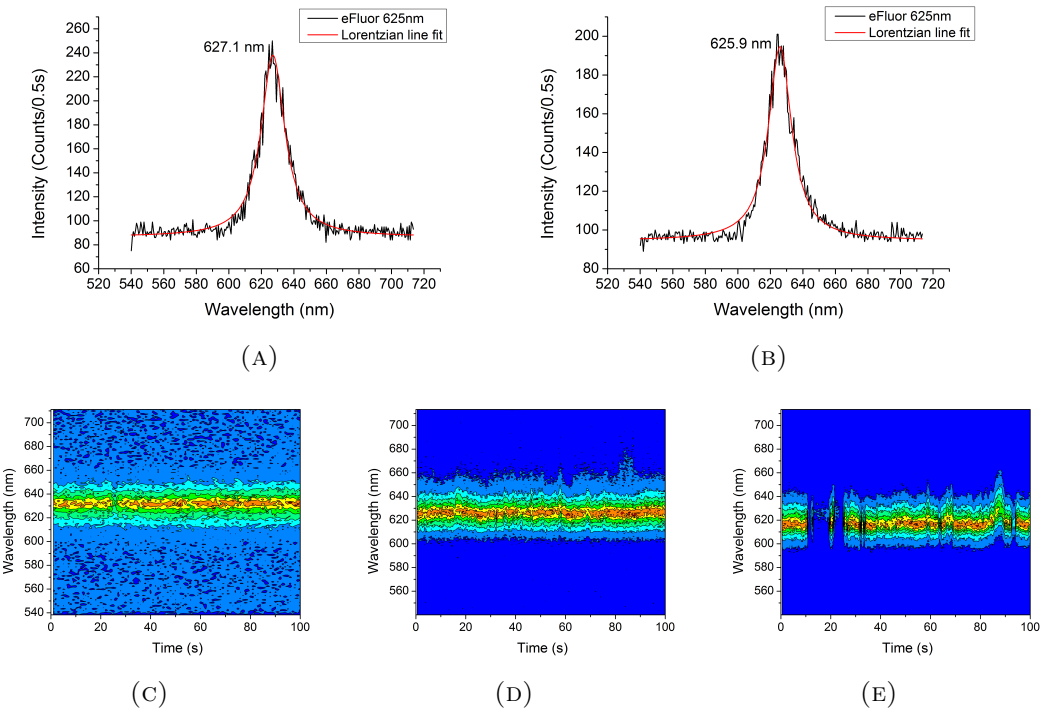

FIGURE 6.23: Representative spectra for eFluor®625 nm NC a-b) show the spectra of single eFluor®625 nm NC with Lorentzian line fits and FWHM of 17.9 nm and 17.4 nm respectively. c-e) Spectral trajectories of eFluor®625 nm NC highlighting c-d) good optical performance and e) blinking and spectral diffusion.

Figure 6.23 shows the representative optical properties of single 625 nm eFluor®NC which show Lorentzian line-shape emission with a FWHM that ranged between 16-20 nm with an average of 18.2 nm and standard deviation of 1.0 nm (Figure 6.23a and 6.23b). Out of 20 spectral trajectories more than 75% showed no blinking on a time on scale of larger than 0.5 seconds (Figure 6.23c and 6.23d) whilst a few NC showed long blinks as shown in figure 6.23e. As seen from figure 6.23c-6.23d mild spectral diffusion could be seen with typical shifts of less than 5 nm within non-blinking NC however larger shifts were observe in one trajectory as seen by figure 6.23e.

Blinking studies under CW excitation show the NC do blink on the order of tens of milliseconds (Figure 6.24). These had blinking power law behaviour with an 'off' exponent ranging between -1.6 to -2.7 with an average of -2.01 and standard deviation of

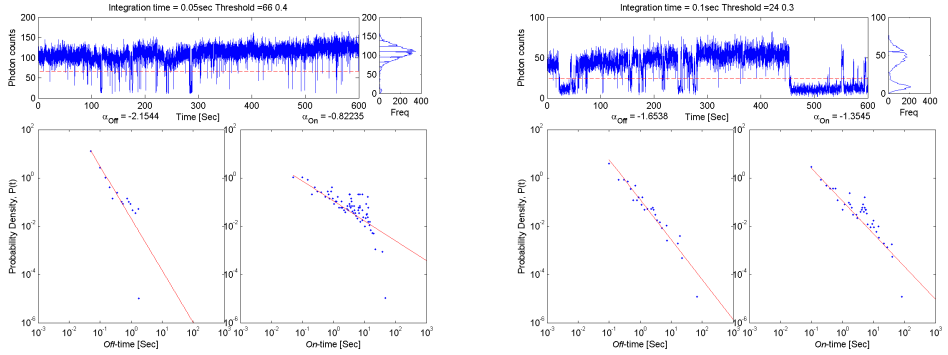

(A) (B)

FIGURE 6.24: Intensity-time trajectories and blinking statistics of two different eFluor®625 nm NC under continuous wave excitation showing a) a good optical stability and power law exponent of -2.15 and -0.82 for the 'off' and 'on' exponents respectively and b) large blinks with power law exponents of -1.65 and -1.35 for the 'off' and 'on' exponents respectively.

0.28 and an 'on' time exponent ranging between -0.7 and -1.3 with an average of -1.06 and standard deviation of 0.17. As can be seen by figure 6.24b, NC with poor blinking performance have power law exponents closer to the generally considered 'normal' blinking exponent of -1.5 whilst the NC showing nearly non-blinking performance, as seen in figure 6.24a, showed exponents closer to -2 and -1 respectively.

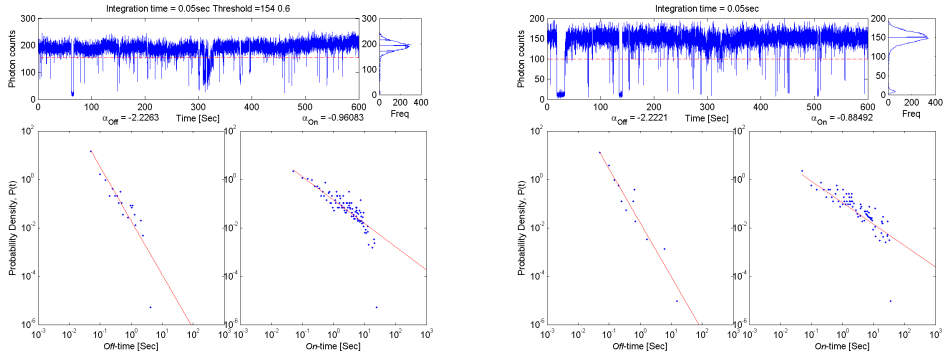

(A) (B)

FIGURE 6.25: Intensity-time trajectories and blinking statistics of the same eFluor®625 nm NC under 8 W cm^{-2} excitation with a) continuous wave excitation showing power law 'off' and 'on' exponents of -2.23 and -0.96 respectively b) pulsed excitation showing 'on' power law exponents 'off' and 'on' exponents of -2.22 and -0.88.

To highlight consistency between two investigation techniques figure 6.25 shows the blinking statistics of the same NC under CW excitation and pulsed excitation for the

same power. An inspection of the blinking statistic shows similar power law exponent, with the CW excitation showing 'on' and 'off' exponents of -0.96 and -2.23 respectively whilst the pulsed excitation had a power law of -0.88 and -2.22. This trend was consistent with the five other NC investigated.

Single NC lifetimes measurements showed predominantly single exponential or mildly bi-exponential fitting behavior (Figure 6.26b and 6.27b) which showed a lifetime/strong lifetime component ranging between 21-39 ns with an average lifetime of 26.3 ns with a standard deviation of 5.5 ns and a shorter bi-exponential component with average lifetime 2.6 ns which is less than 20% weaker in amplitude when compared to the longer component. This compares to an ensemble lifetime which shows tri-exponential lifetimes of 9 ns, 22.7 ns and 52 ns (Figure 6.14b).

Figure 6.26 and 6.27 show lifetime-time and intensity-time comparisons for two NC which show blinking within the intensity-time trajectory. The intensity-time trajectories show the NC to be in a predominately 'on' state whilst the lifetime-time trajectories shows a slowly varying lifetimes ranging between 20-30 ns and 30-40 ns respectively. Figure 6.26b and 6.27b show the accumulated lifetime with a strong lifetime component of 25 ns and 35 ns respectively which is comparable to the strong mode seen in the FLID as seen by figure 6.26c and 6.27c. Both NC see a distinct drop in lifetime to 10 ns as seen by figure 6.26e and 6.27e which correspond to blinks in intensity and highlight a trend within the FLID from a high-lifetime high-intensity towards a low-lifetime low-intensity (Figure 6.26c and 6.27c).

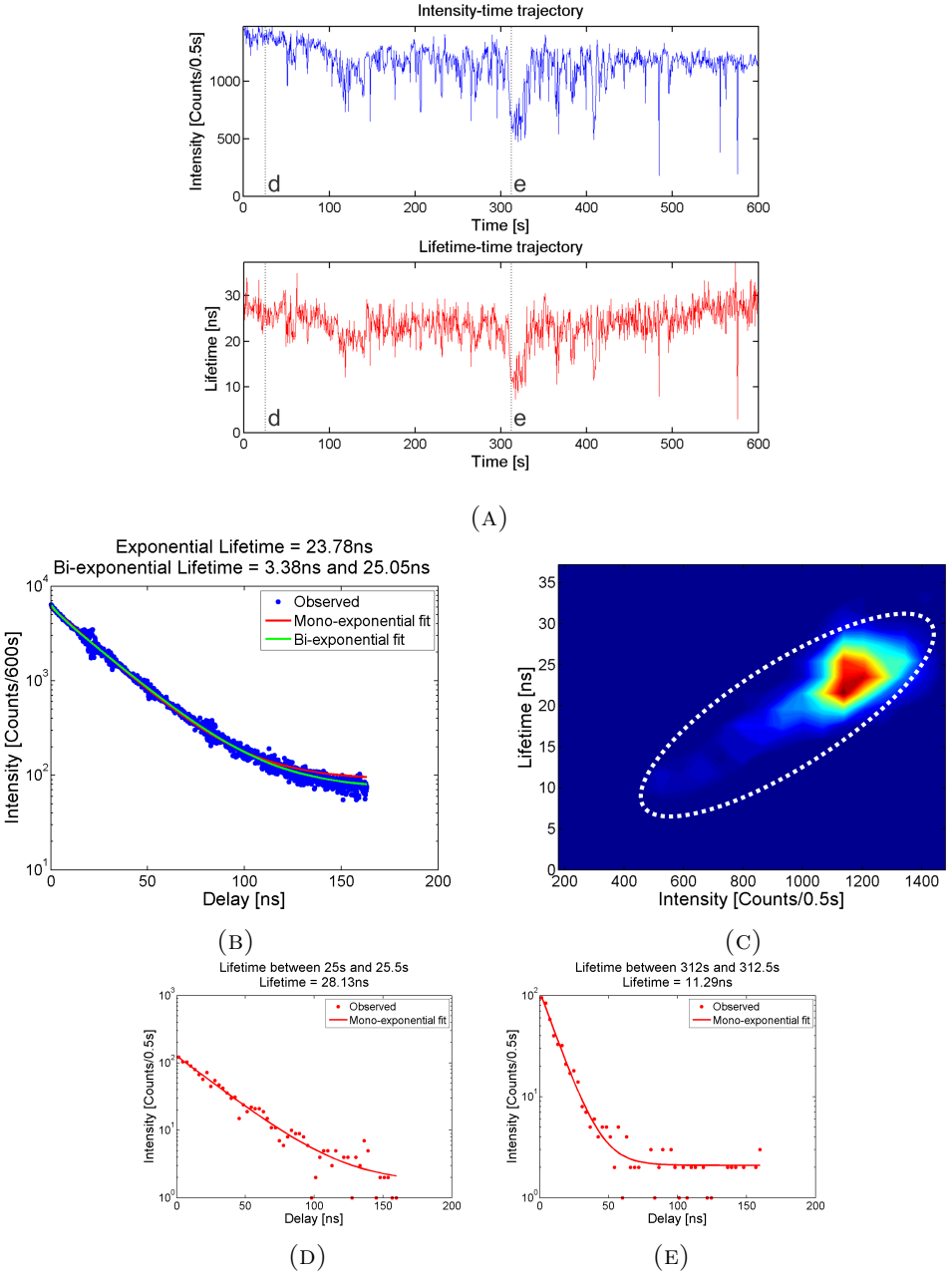

FIGURE 6.26: a) A comparison of the intensity-time and lifetime-time trajectories for an eFluor®625 nm NC under pulsed excitation with a repetition rate of 5 MHz and investigated for 10 minutes with a 1 second integration. b) The accumulated lifetime over a 10 minute integration. c) A FLID using the data from [a]. d) The lifetime between 25 s and 25.5 s and e) 312 s and 312.5 s.

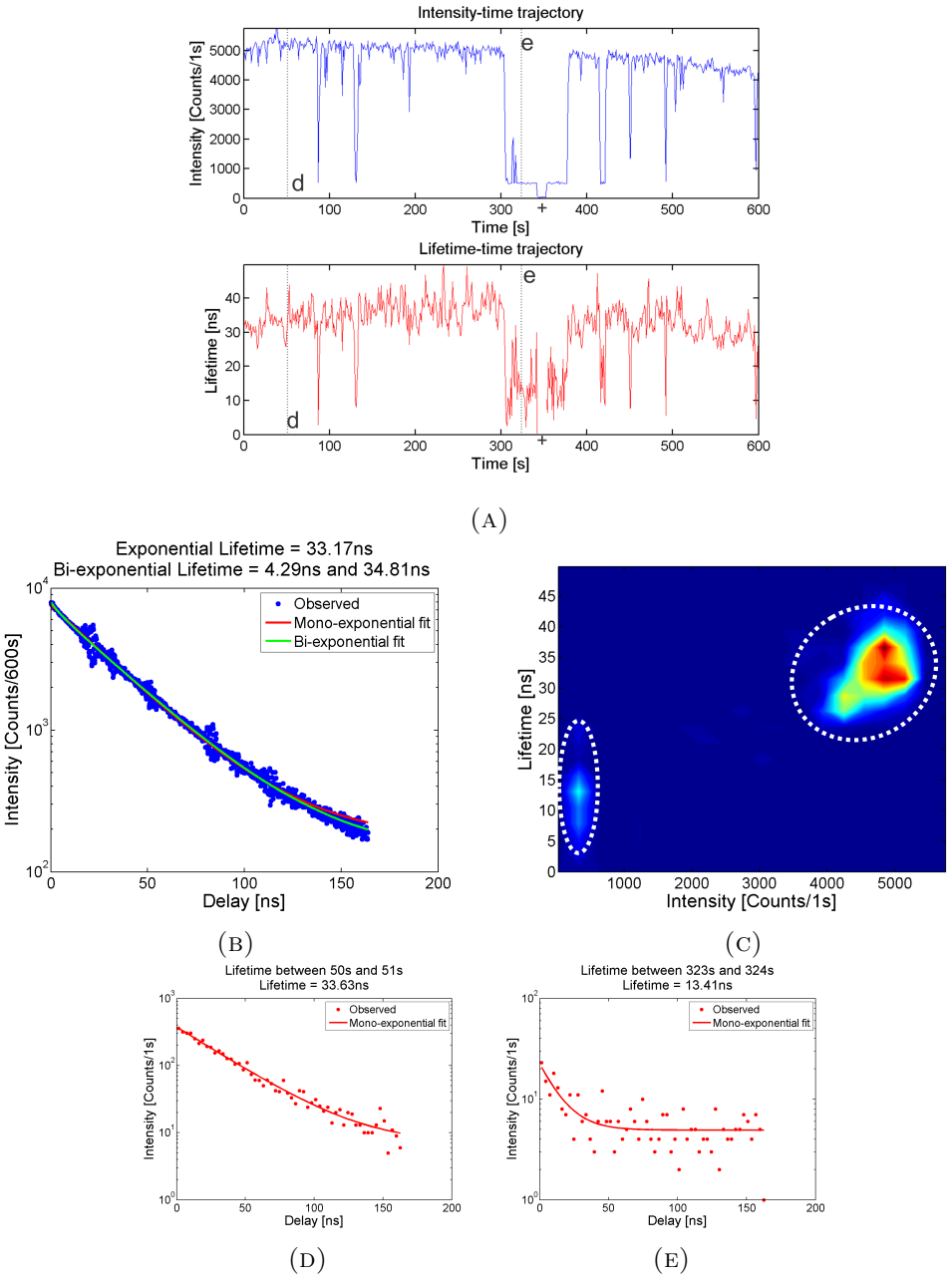

FIGURE 6.27: a) A comparison of the intensity-time and lifetime-time trajectories for an eFluor®625 nm NC under pulsed excitation with a repetition rate of 5 MHz and investigated for 10 minutes with a 1 second integration. b) The accumulated lifetime over a 10 minute integration. c) A FLID using the data from [a]. d) The lifetime between 50 s and 51 s and e) 323 s and 324 s. (+) indicates a switch back to image mode to ensure to no positional drift had occurred.

6.3.4.3 eBioscience eFluor® 640 nm nanocrystals

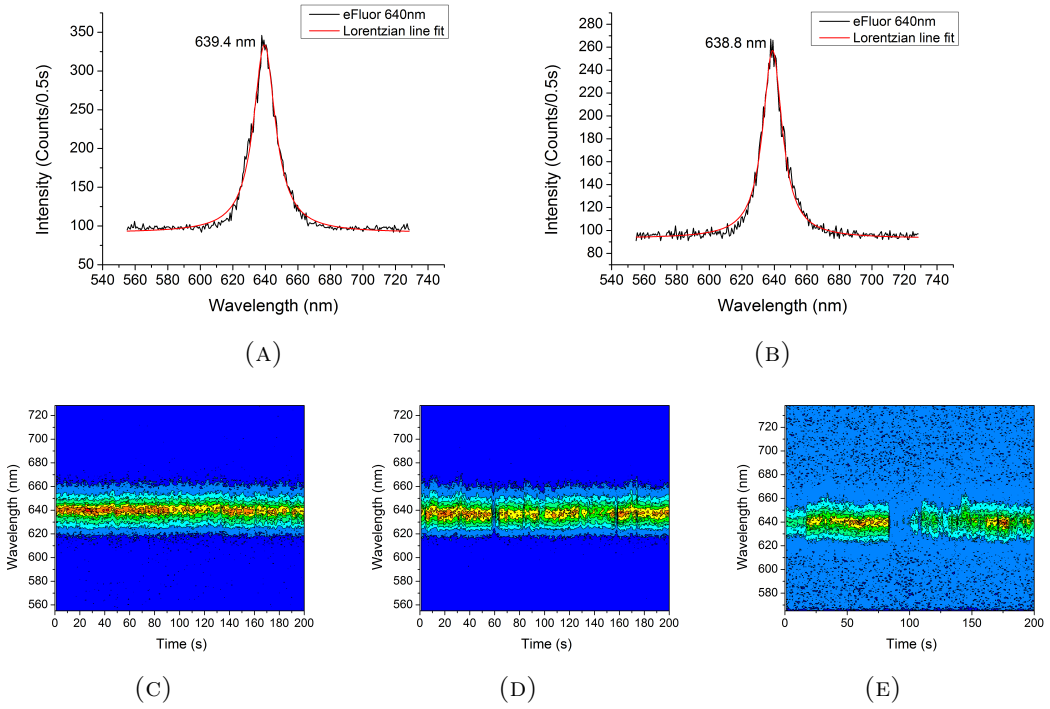

FIGURE 6.28: Representative spectra for eFluor®640 nm NC a-b) show the spectra of single eFluor®640 nm NC with Lorentzian line fits and FWHM of 16.3 nm and 14.5 nm respectively. c-e) Spectral trajectories of single eFluor®640 nm NC highlighting c) good optical performance d) a few blinks and e) a blinking NC.

Figure 6.28 shows the optical properties of single eFluor®640 nm NC which show Lorentzian line-shape emission with a FWHM of between 14-19 nm with an average of 16.2 nm with a standard deviation of 1.5 nm (Figure 6.28a and 6.28b). Out of the 20 spectral trajectories more than 80% of the spectral trajectories showed less than one blinking on time scale larger than 0.5 seconds (Figure 6.28c and 6.28d) whilst a few NC showed long blinks as shown in figure 6.28e. Figure 6.28c-6.28d highlights minimal spectral diffusion with typical shifts of less than 6 nm with figure 6.28e.

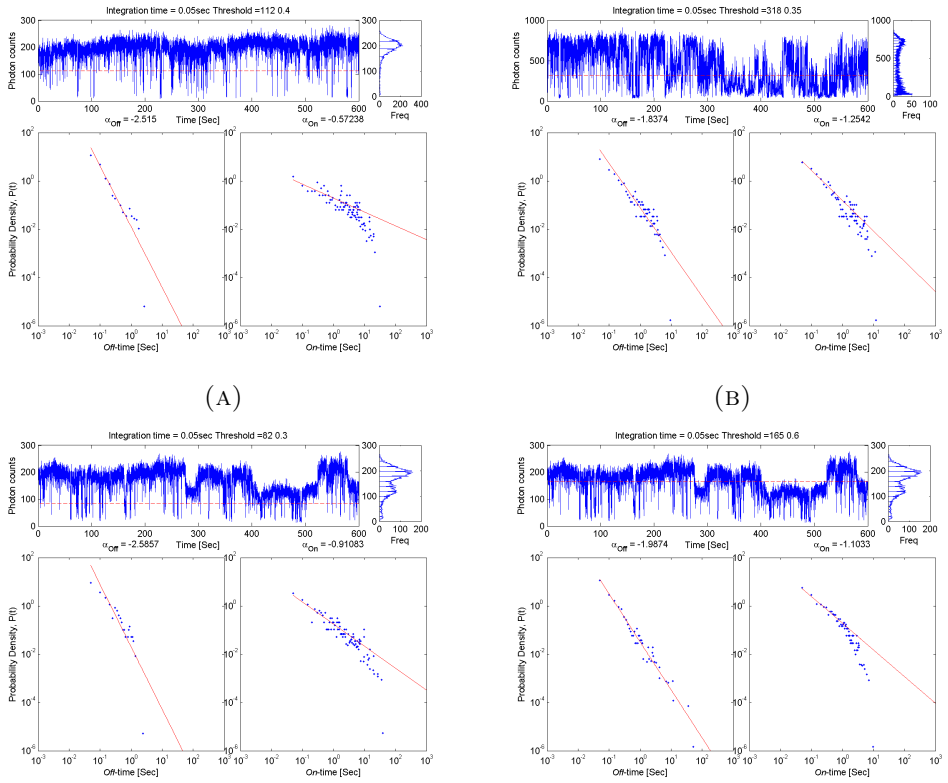

FIGURE 6.29: Intensity-time trajectories and blinking statistics of two different eFluor®640 nm NC under continuous wave excitation showing a) a good optical stability and power law exponent of -2.52 and -0.57 for the 'off' and 'on' exponents respectively and b) large blinks with power law exponents of -1.84 and -1.25 for the 'off' and 'on' exponents respectively. c-d) Show the same intensity-time trajectory which has grey state emission but has c) a blinking statistic threshold below the grey state emission giving power law exponents of -2.59 and -0.91 for the 'off' and 'on' exponents respectively and d) a blinking statistic threshold above the grey state emission giving power law exponents of -1.98 and -1.10 for the 'off' and 'on' exponents respectively.

Blinking studies under CW excitation show the NC do blink on the order of tens of milliseconds with rare long blinks (Figure 6.29). The NC showed power law behaviour with an 'off' exponent ranging between -1.6 to -2.9 with an average of -2.42 and standard deviation of 0.20 and an 'on' time exponent ranging between -0.5 and -1.3 with an average of -1.02 and standard deviation of 0.20. Interestingly, the largely blinking NC of figure 6.29b still exhibits similar power exponents to other non-blinking NC observed. As seen in figure 6.29c a few NC exhibited 'grey' state emission in which the NC did not fully go into a total 'dark' state. With such blinking, choosing a threshold value is problematic.

Thus two threshold values were chosen, one below the 'grey' state (Figure 6.29c) and one between the 'grey' state and the 'on' (Figure 6.29d). These revealed two slightly difference power law exponents of -2.59 and -1.99 for the 'off' exponent respectively and, -0.91 and -1.10 for the 'on' exponent.

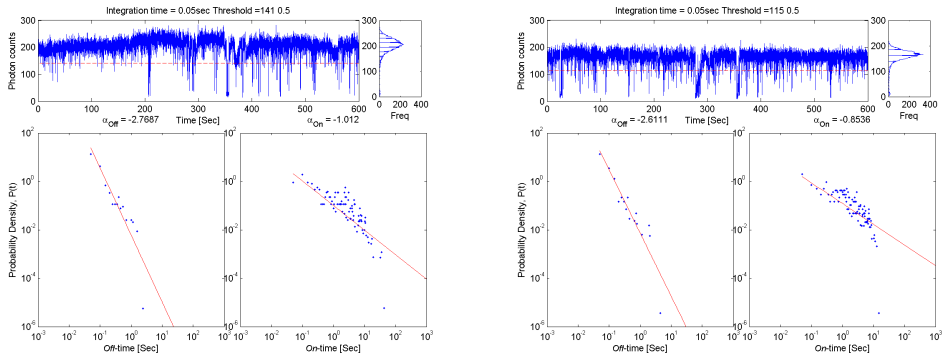

(A) (B)

FIGURE 6.30: Intensity-time trajectories and blinking statistics of the same eFluor®640 nm NC under 8 W cm^{-2} excitation with a) continuous wave excitation showing power law 'off' and 'on' exponents of -2.77 and -1.01 respectively b) pulsed excitation showing 'on' power law exponents 'off' and 'on' exponents of -2.61 and -0.85.

Pulsing the excitation for the same power within CW excitation shows similar power law exponents. For the example case of figure 6.30, the continuous wave 'on' and 'off' exponents were -1.01 and -2.77 respectively whilst the pulsed excitation had a power law exponents of -0.85 and -2.61 showing very similar blinking statistics.

Lifetime measurements showed predominantly single exponential or mildly bi-exponential fitting behavior (Figure 6.31b and 6.32b) which showed a very strong lifetime component ranging between 18-35 ns with an average lifetime of 25.8 ns and standard deviation of 4.6 ns. A shorter bi-exponential component with average lifetime of 2.7 ns which is typically less than 20% weaker in amplitude when compared to the longer component was observed. This compares to an ensemble lifetime which shows tri-exponential decay with 6.9 ns, 19.1 ns and 39.0 ns (Figure 6.14c).

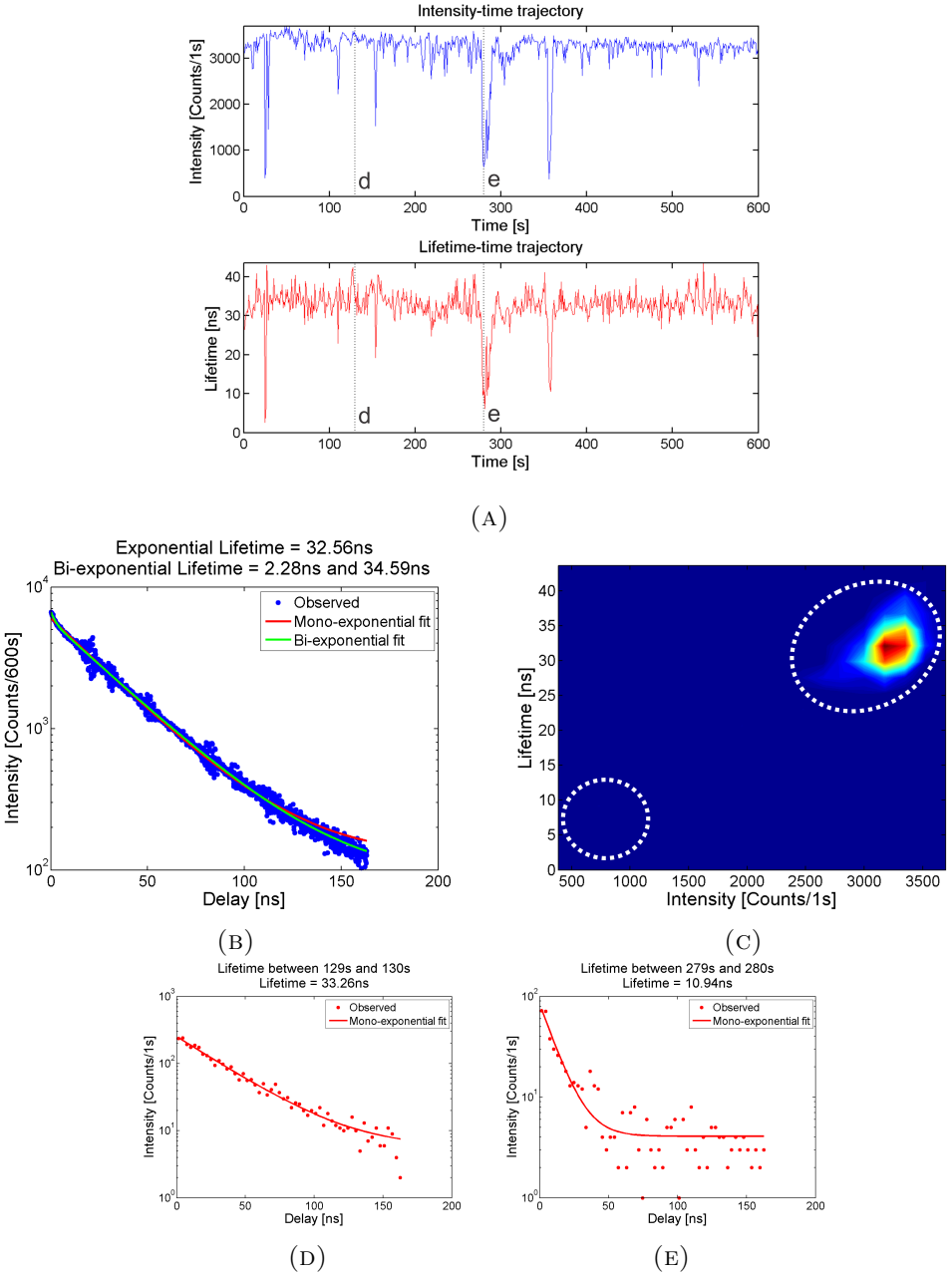

FIGURE 6.31: a) A comparison of the intensity-time and lifetime-time trajectories for an eFluor®640 nm NC under pulsed excitation with a repetition rate of 5 MHz and investigated for 10 minutes with a 1 second integration. b) The accumulated lifetime over a 10 minute integration. c) A FLID using the data from [a]. d) The lifetime between 129 s and 130 s and e) 279 s and 280 s.

Figure 6.31 shows a comparison of the lifetime-time and intensity-time trajectories for predominantly non-blinking NC which maintains a good emission intensity and lifetime stability. Several distinct drops in lifetime are observed to as low as 2 ns which also correspond to blinking events. This is shown the FLID in figure 6.31c as a general trend

from a high-lifetime and high-intensity mode towards a low-lifetime and low-intensity mode highlighting A-type blinking.

Figure 6.32 shows a NC predominantly in the 'on' state however the figure does show drops intensity and lifetime. The FLID of figure 6.32c shows two interesting modes marked as (∗) and (‡) which can be related to specific regions with the intensity-time trajectories. The region marked as (∗), sees drops in intensities but with no change in lifetime and is indicative of B-type blinking.

The region marked as (‡) shows a slightly weaker intensity than the 'on' state which could be referred to as 'grey' state emission. The lifetimes in this region was seen to be ∼16 ns and was seen to be mono-exponential (Figure 6.32f). This is in comparison to single exciton recombination lifetime (>20 ns) seen in figure 6.32d but larger than those seen with totally 'dark' off states as seen in previous NC (<10 ns) and seen in figure 6.32g.

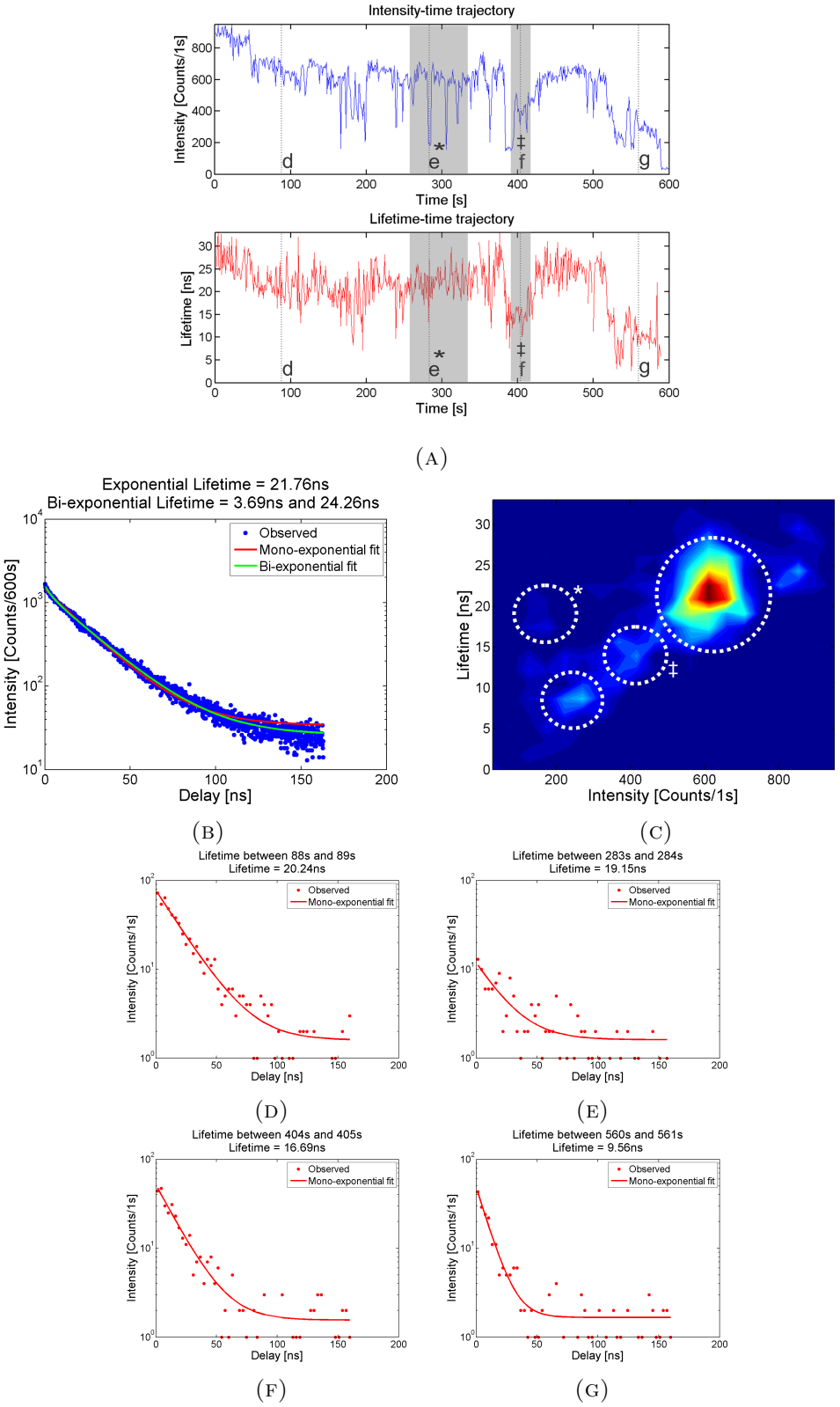

FIGURE 6.32: a) A comparison of the intensity-time and lifetime-time trajectories for an eFluor®640 nm NC under pulsed excitation with a repetition rate of 5 MHz and investigated for 10 minutes with a 1 second integration. b) The accumulated lifetime over a 10 minute integration. c) A FLID using the data from [a]. d) The lifetime between 88 s and 89 s, e) 280 s and 284 s, f) 404 s and 405 s and g) 560 s and 561 s.

6.3.4.4 eBioscience eFluor® 650 nm nanocrystals

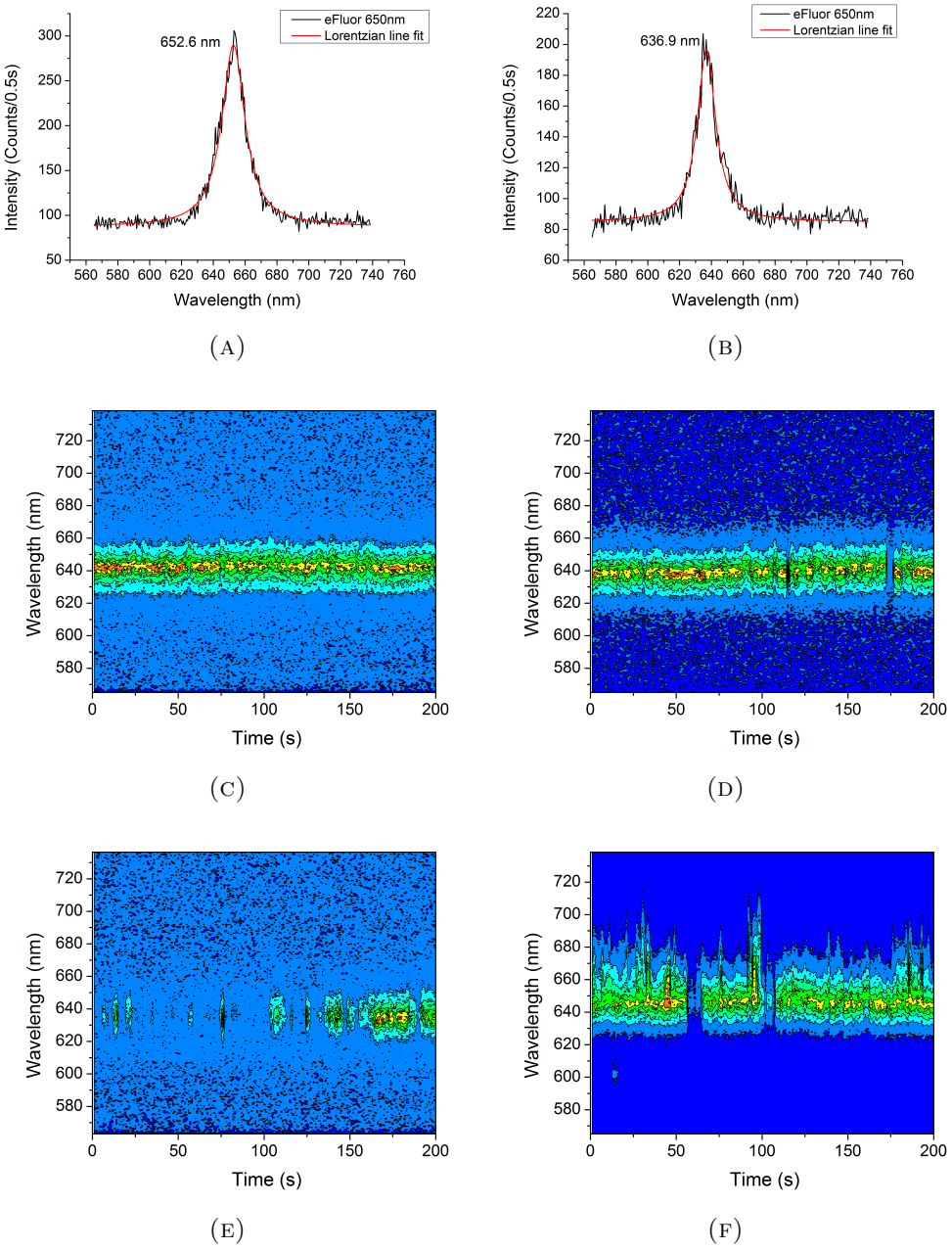

FIGURE 6.33: Representative spectra for eFluor®650 nm NC a-b) show the spectra of single eFluor®650 nm NC with Lorentzian line fits and FWHM of 17.7 nm and 14.2 nm respectively. c-e) Spectral trajectories of single eFluor®650 nm NC highlighting c) good optical performance d) a few blinks and e) a blinking NC.

Figure 6.33 shows the optical properties of single eFluor®650 nm NC which show typical Lorentzian line-shape emission with a FWHM of 13-20 nm with an average of 16.2 nm and standard deviation of 2.6 nm. The eFluor®650 nm NC showed varied emission

properties, four of which are seen in figure 6.33c-6.33f. 45% of the 30 spectral trajectories observed showed non-blinking NC or NC with less than two large 0.5 second blinks as seen in figure 6.33c-6.33d, the majority of NC showed a blinking characteristic with a significant portion showing poorer optical performance, the poorest were seen to blink as seen in figure 6.33e. The NC typically showed predominately slow spectral diffusion of less than 5 nm as seen in figure 6.33c-6.33d; however, examples did see large sharp spectral diffusion as large as 7 nm as seen in figure 6.33f.

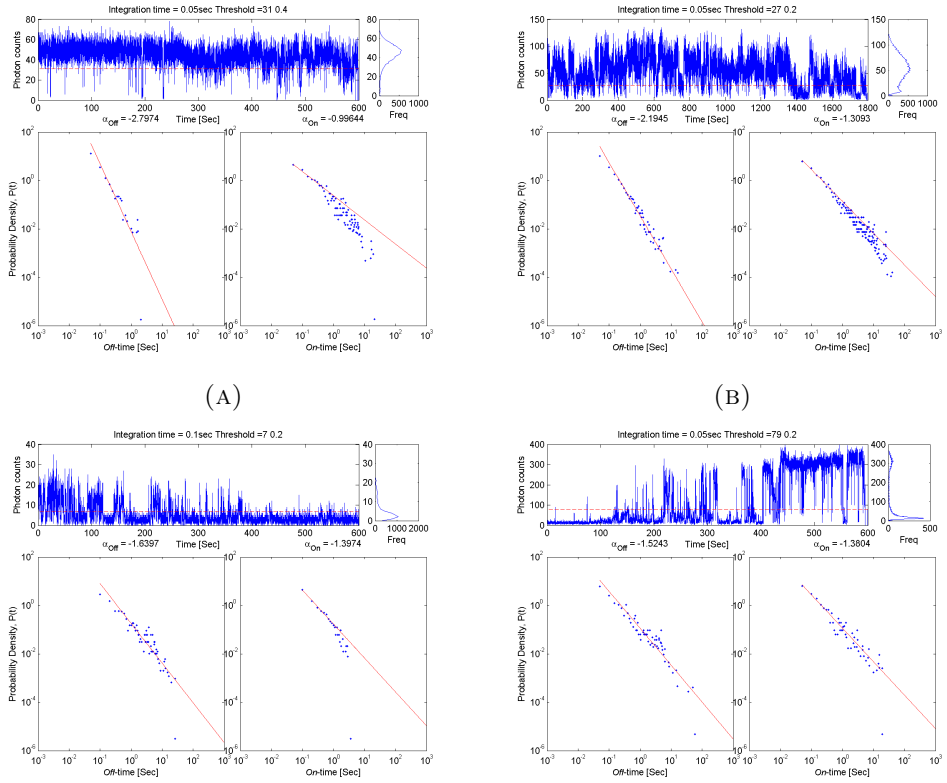

FIGURE 6.34: Intensity-time trajectories and blinking statistics of four different eFluor®650 nm NC under continuous wave excitation showing a) a good optical stability and power law exponent of -2.80 and -1.00 with exponential tail-off for the 'off' and 'on' exponents respectively, b) large blinks and grey states with power law exponents of -2.19 and -1.31 for the 'off' and 'on' exponents respectively c-d) blinking NC with power law exponents of -1.64 and -1.52 for the 'off' exponent and -1.40 and -1.38 for the 'on' exponent respectively.

The wide variety of intensity-time trajectories gave a wide variety of blinking statistics as seen in figure 6.34. Figure 6.34a-6.34b shows predominantly non-blinking NC with 'off'

exponents ranging from -1.9 to -2.8 and 'on' exponents ranging from -0.9 to -1.3 with an average of -2.49 and -1.10 respectively consistent with previously observed eFluor®NC. Figure 6.34c-6.34d shows the NC blink with power law exponents ranging from -1.5 to -1.7 for the 'off' exponents and ranging from -1.3 to -1.5 for the 'on' exponents. These had an average of -1.59 and -1.39 for the 'off' and 'on' exponents respectively. The lifetime of the eFluor®650 nm NC showed single or mildly bi-exponential with a lifetime/ strongest lifetime component in the range of 18-29 ns, with an average lifetime of 23.5 ns and standard deviation of 2.9 ns. The bi-exponential lifetimes saw a further small lifetime component, this was on average 3.9 ns which was typically less than 20% of the lifetime amplitude. This is comparable to the ensemble lifetime which showed a tri-exponential fit with a lifetime of 4.8 ns, 22.1 ns and 49.3 ns (Figure 6.14d). Tri-exponential decays were seen on two occasions and corresponded to NC that were seen to predominantly be in the 'off' state, as will be seen in figure 6.36.

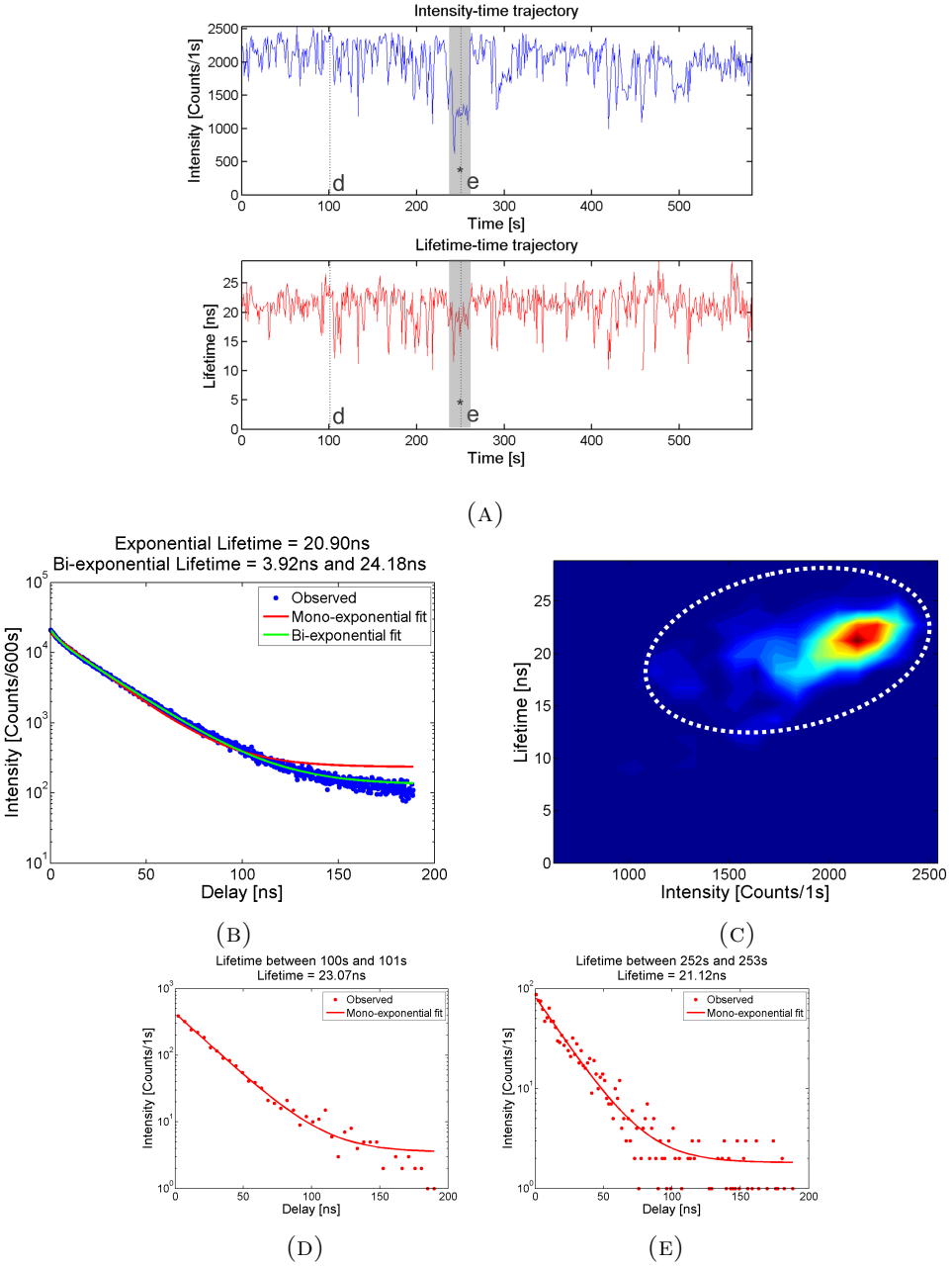

FIGURE 6.35: a) A comparison of the intensity-time and lifetime-time trajectories for an eFluor®650 nm NC under pulsed excitation with a repetition rate of 5 MHz and investigated for 10 minutes with a 1 second integration. b) The accumulated lifetime over a 10 minute integration. c) A FLID using the data from [a]. d) The lifetime between 100 s and 101 s and e) 252 s and 253 s.

Figure 6.35 highlights a NC in the predominantly 'on' state which saw only minor fluctuations within the intensity-time and lifetime-time trajectories. The lifetime fluctuations ranged between 14-28 ns of which two examples can be seen in figure 6.35d-6.35e. The majority of the lifetimes held closely to 22 ns as can be seen in the intensity-lifetime

histogram in figure 6.35c corresponding closely to the accumulated lifetime of 24 ns seen in figure 6.35b. The region marked (∗) highlighted a marked drop in intensity but no significant change in lifetime as can be seen by figure 6.35e.

Figure 6.36 highlights a NC in the predominantly 'off' state which saw a large variation of lifetimes corresponded closely to the intensity fluctuations. The lifetime ranged between 2 ns and 24 ns with the majority of the states being in the short component 1-3 ns, as can be seen the FLID in figure 6.36c, which follows closely to the accumulated lifetime of figure 6.36b. Examples of the varying lifetimes trajectories can be seen in figure 6.36d-6.36f.

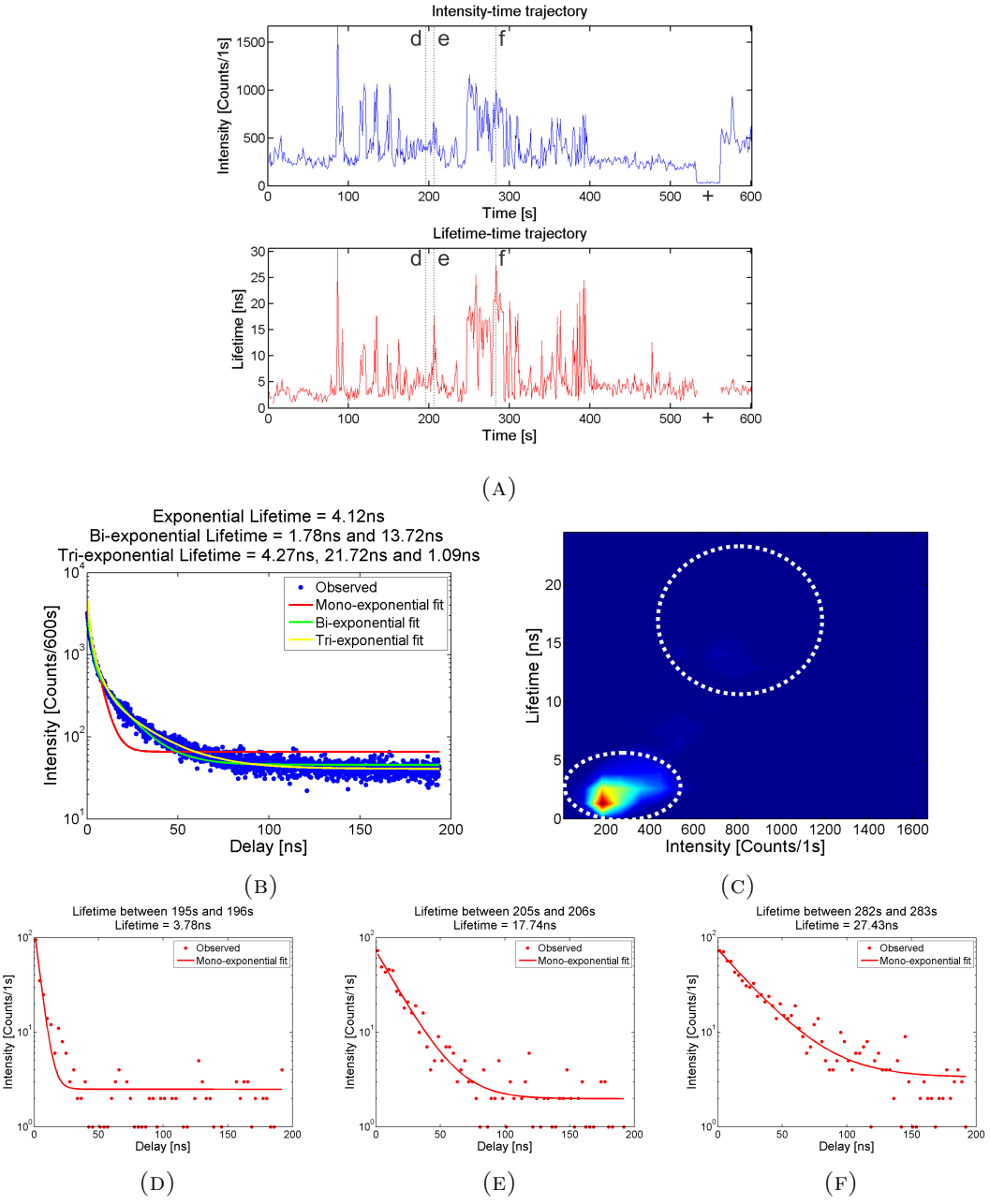

FIGURE 6.36: a) A comparison of the intensity-time and lifetime-time trajectories for an eFluor®650 nm NC under pulsed excitation with a repetition rate of 5 MHz and investigated for 10 minutes with a 1 second integration. b) The accumulated lifetime over a 10 minute integration. c) A FLID using the data from [a]. The lifetime between d) 100 s and 101 s, e) 205 s and 206 s and f) 282 s and 283 s. (+) indicates a switch back to image mode to ensure to no positional drift had occurred.

6.3.5 Summary

This exploratory study shows the eBioscience eFluor®605 nm, 625 nm, 640 nm and 650 nm NC to be extremely stable and efficient emitters which show Lorentzian line shape emission with an average FWHM of 16.4 nm and show a small amount of slowly varying spectral diffusion which is related to the electric field variations in the surrounding matrix. A high proportion of NC did not blink on long time scales and thus should be considered as nearly 'non-blinking' NC on long time scales. Closer investigation revealed some blinking on the 10's of milliseconds, the 'on' and 'off' duration followed power law probability statistics with 'on' and 'off' exponents close to -1 and -2 respectively. Development of intensity-time and lifetime-time trajectory techniques has enabled the observation of several recombination mechanisms to be observed on one second time resolution. The most prominent mechanism being single exciton decay which corresponds to the 'on' state, whilst the 'off' state is dominated low-intensity low-lifetime emission consistent with A-type blinking. The eFluor®625 nm and 640 nm NC also showed a higher intensity 'off' state emission. B-type blinking was rarely observed but mainly seen in longer wavelength NC. An interesting observation of a longer lifetime components was seen for one eFluor®605 nm NC. There was also poorer optical performance from the eFluor®650 nm NC.

6.4 Discussion

Both the CdZnSeS and eFluor® NC in general showed extremely bright stable emission with similar optical behaviour. The spectra highlight Lorentzian line shape emission with an average FWHM of below 18.5 nm which is consistent with bandedge emission expected from a single NC emitter. Whilst the majority of the CdZnSeS NC where in the 'on' state, blinking was still prevalent in most NC. The majority eFluor®NC showed superior non-blinking performance and no significant sharp spectral diffusion. These NC did show a slow variation in peak emission which can be related to electric field variations around the NC. This was especially noticeable in the eFluor®605 nm NC. Further experiments conducted on the eFluor®605 nm NC highlighted peak emission shifts of 3 nm could be obtained with electric fields as high as ± 60 kV cm^{-1} (see Appendix G.1). These changes in electric field can give rise to variation lifetimes by up to 3 ns and can be related to the QCSE demonstrated Empedocles *et al.* [202].

A limited number of CdZnSeS NC and eFluor®605 nm, 625 nm and 650 nm NC saw spectral diffusion as large as 7 nm which often coincided with a blinking event. Reports for other materials have seen similar spectral diffusion which has been correlated to a charge carrier entering a trap state which gives rise to large electric fields within the NC [204]. This event results in a charging effect which enables trion recombination to take place and placing the NC in darker state.

Intensity-time studies highlight that the eFluor®605 nm, 625 nm, 640 nm NC show very good optical performance in terms of emission stability and a very low probability of long blinks. This is highlighted by almost constant emission seen in the spectral trajectories and the intensity-time trajectories. Intensity-time trajectories of the NC highlight short blinks on time scale of milliseconds and give blinking duration probability densities

that provide power law probability distributions. These NC showed 'on'/'off' power law exponents of around -1 and -2 respectively and highlight the high probability of short 'off' states and the high probability of long 'on' states. These exponents are consistent with 'quasi-giant' CdSe/CdS NC, which also show good non-blinking behaviour, and yielded similar <0.9 and >2.2 'on' and 'off' power law exponents respectively [214]. These exponents are in stark contrast to the exponents reported for blinking CdSe/ZnS NC where both exponents are closer to -1.5 [214, 215]. Whilst the CdZnSeS NC on average showed good optical performance, the blinking performance ranged more significantly when compared to the eFluor®NC and did not shows as low/high exponents as the eFluor®NC. The wide range of blinking exponents could be due to B-type blinking as was seen in figure 6.8 however a quantitative comparison can not yet be made and should be the subject of future work.

The accumulated single NC lifetimes see mildly bi-exponential decay with a strong lifetime component between 13-40 ns and can be related to single exciton recombination. The broad range of single NC lifetimes can go some way to explain the tri-exponential decay profiles seen in the ensemble lifetime.

Pulsing the excitation for the same power showed similar blinking characteristics implying that the same mechanism exists in the NC under CW and pulsed excitation enabling time dependent lifetimes to be calculated simultaneously with intensity-time trajectories. Emission intensity in the current experimental setup, which is still in development, limits the FLID statistics to a 0.5-1 second resolution but reveal much about the optical properties on the longer time scales. FLID enables the general trends to be observed and thus enable identification of blinking mechanism which could be easily missed by inspection of a purely intensity-time and lifetime-time time trajectory. The FLID figures typically show a prominent high-intensity long-lifetime emission process that has

a lifetime and intensity which can be associated with single exciton recombination. A very close inspection of the FLID sees the general trend from single exciton emission to a lower-lifetime with a lower-intensity. This lifetime drops to as low as 1-6 ns for the eFluor®605 nm and 650 nm NC but also as high as ∼10 ns for the eFluor®625 nm and 640 nm NC which is most notably seen in figure 6.32 and 6.36. The corresponding FLID trend from high-intensity high-lifetime to low-intensity low-lifetime are consistent with the trion emission seen in 'quasi-giant' CdSe/CdS NC [130]. A noticeable fraction of the eFluor®625 nm and 640 nm NC show 'grey' state emission rather than full 'dark' state emission, this 'grey' state corresponds to reasonably long lifetime (∼10 ns) highlighting the non-radiative recombination process is a long process within this system and is comparable to others reports which have seen non-blinking and 'grey' state emission NC [125, 131]. Previous reports have shown that, in the perfect regime, trion emission should be half the single exciton lifetime [131]. It can be implied that the trion Auger recombination lifetime is significantly longer in the eFluor®625 nm and 640 nm NC than in the eFluor®605 nm and 650 nm NC.

Similar observation were also seen in the CdZnSeS NC but also highlighted multiple 'grey' states. Whilst still requiring further investigation, this observations could highlight the ability of the NC to extend past the singly charged trion state into the doubly and triply charged states. This would give rise to multiply modes in the FLID due to the shorter lifetimes and faster Auger recombination lifetimes of the multiply charged states [131]. This effect could be due to the anisotropic shape of the CdZnSeS NC, as observed in the TEM.

Since the FLID technique is still in development, direct quantification of the efficiency of the trion emission has not yet been achieved thus only enabling a qualitative interpretation of the Auger recombination lifetimes. Obtaining the efficiency of the trion emission

will enable a calculation of the trion Auger recombination lifetime to be performed and should the subject of further work [129].

Whilst A-type blinking is predominantly seen for all eFluor®NC, B-type blinking was also seen in the CdZnSeS NC and a few of the eFluor®640nm and 650nm NC highlighting the possibility of the activation of recombination centres. The exact mechanism behind B-type blinking is still the subject of much interest and debate. Whilst further evidence will be discussed later it is in complete and thus the investigation of B-type blinking should be the subject of further work.

6.4.1 Reserved analysis: Further discussion on Auger lifetimes through knowledge of the composition

This section focuses on potential reasons why the trion emission is efficient within these CdZnSeS and eFluor® NC. It builds on knowledge of the composition of the NC. As was shown in section 6.2.1 the CdZnSeS NC consist of a CdSe core, an alloyed CdS intermediary shell and ZnS outer shell. The eFluor® NC structure consists of CdSe and ZnS with a proprietary amount of CdS between the core and shell. With this knowledge a comparison can be made to CdSe/CdS NC which has been extensively researched recently and can give large insight into the general mechanism behind the CdZnSeS and eFluor® NC [126, 129–131]. Whilst the interfacial layer is known to reduce strain in the system, an increase in CdS on CdSe has been shown to produce quasi type-II NC which increases the single exciton lifetime from 7 ns for the core-only structure to 20 ns and 46 ns with 2 ML and 4 ML CdS growth, in reasonable agreement with lifetimes observed in the CdZnSeS and eFluor® NC [129]. This decrease in wavefunction overlap enables a significant increase in Auger recombination lifetime, as was shown by Oron et al. *and*

García-Santamaría et al. *[114, 129]. It is interesting to note that some of the trion lifetimes seen here are slightly larger than some NC seen previously for similar structures [130]. Thus potentially highlighting greater than volume scaling of the Auger recombination lifetime. It must be noted that greater than volume scaling of the Auger lifetimes has been observed in CdSe/CdS NC and was shown to be the result of an alloying of the core-shell interface through interatomic diffusion [129]. Whilst the exact synthesis procedure of eFluor® NC is unknown to the author, it can be assumed that if TOPO was involved in the synthesis, the reaction temperature was around 240° C consistent with other reports. As was described in section 2.5.2.3, García-Santamaría* et al. *and Cai* et al. *showed that at temperatures around 240° C a significant amount of interatomic diffusion occurs[129, 139]. The resulting interatomic diffusion will grade the interface potential and thus relax the Auger recombination criterion thus the potential to give the large trion lifetimes seen in the eFluor® NC [121].*

It is notable that some eFluor®605 nm NC show infrequent long lifetimes with high intensities as seen in figure 6.21. These were in NC which showed typical bandedge emission and did not show spectral drift when initially investigated. The absence of spectral change highlights a process that still leads to efficient radiative bandedge emission. Whilst investigation into this long component are still on going, these limited results already rule out QCSE and the activation of fast non-radiative trap sites due to the lack of spectral drift and the loss of intensity. Thus, three possibilities exist to explain this phenomenon, firstly the observed emission in these NC with a lifetime of ∼20 ns is due to trion emission and the larger lifetime is a charge neutral state which could be supported by very recent reports of Galland *et al.* [131]. Secondly, there is a spontaneous increase in the non-radiative lifetime highlighting the NC have longer radiative lifetimes and the system is non-radiative lifetime limited. Thirdly, there is a

long-lived trap site capturing the charge carrier and subsequently enabling de-trapping for radiative bandedge recombination. This phenomenon should be the subject of further work.

In general the eFluor®650 nm NC showed weaker optical performance when compared to the rest of the size series. Exploratory investigations into the cause of the poorer performance show two possible causes, firstly the NC-ligand stability and secondly, the effect of dislocations and stacking faults.

The NC-ligand stability was highlighted by the observation that the NC solution agglomerated at 4°C (Appendix G.2 for image). The other eFluor®NC at 4°C and the same solution at room temperature revealed no agglomeration issues over a 6 month period and showed the optical performance reported here. The relatively large NC diameter of ∼8 nm (as determined by TEM) may highlight that the agglomeration could be associated with colloidal dispersion dynamics. When reheated to room temperature, the solution required vigorous stirring to recover the suspension and the optical performance after this process was remarkably weak. This could highlight the dissociation dynamics of the ligands at low temperature in which there was insufficient thermal energy to enable TOPO to be reabsorbed to the surface. Thus, there are many free dangling bonds enabling more oxidation or surface trap site recombination to occur. Similar processes, albeit at a slower rate, could occur at room temperature enabling a larger degree of dangling bands and mechanism to enable oxidation.

The dislocation argument can be supported by HRTEM investigation which revealed a large amount twinning stacking faults within the eFluor®650 nm NC. This observation could highlight potential vacancies within the NC which have been reported to reduce

optical performance [81]. It can be easily thought that either of these observation could cause recombination centres and B-type blinking.

6.4.2 Reserved analysis: Critical radius calculations

To see whether these stacking faults are intrinsic to the NC design, the critical radius, as described in section 3.5, is calculated for zinc blende CdSe/CdS and CdS/ZnS figure 6.37a and 6.37b respectively. Knowledge of the composition and inspection of the critical radius limit in figure 6.37a highlights that all the CdSe/CdS NC synthesised where below the critical threshold for a full dislocation. By considering the CdSe/CdS internal structure to be the total inner radius on the CdS/ZnS then an inspection of figure 6.37b shows this structure forms a full stacking fault after 2 ML of ZnS. If this approximation is correct then stacking faults are possible in all the NC observed. The lack of stacking faults in the other structures could be due to increased alloying at the interface which would mitigate strain effects and also increase the Auger recombination lifetime, vide supra.

Ultimately, the overall performance of the eFluor®NC rival some of the best in the field and show a consistency in emission and recombination dynamics that can not be obtained when compared to the CdZnSeS NC. This highlights that the eFluor®NC could easily be used for multiple applications including FRET and optoelectronic devices. Whilst the CdZnSeS NC are bright emitters with a specified wavelength, thus these NC could be used for applications such as a basic biological tag due to the relatively unknown composition produced from the synthetic method. This also highlights that a full understanding of the CdZnSeS NC may not be possible.

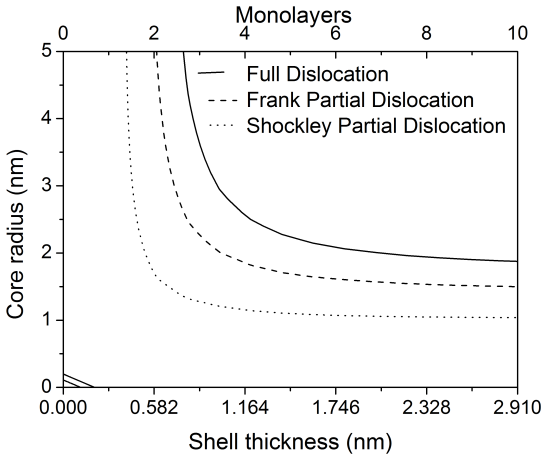

(A)

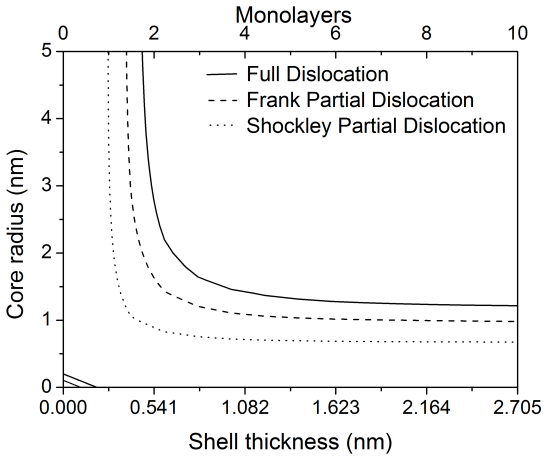

(B)

FIGURE 6.37: The full, Frank partial and Shockley partial dislocation critical radii for a) CdSe/CdS NC and b) CdS/ZnS NC for $\alpha = 4$.

6.5 Conclusion

In conclusion, this chapter presents exploratory studies into exciton dynamics within graded alloyed CdZnSeS NC via a facile synthesis method and a size series of eBioscience eFluor® NC.

SNS investigations demonstrate that all the NC investigated are bright single emitters that shows some slowly varying spectral diffusion. This slowly varying spectral diffusion can be related to variations in electric field in the surrounding matrix. Rare sharp spectral diffusion were also observed which coincide with a blink which indicated surface trapping of the charge carrier as seen be others. Intensity-time investigations show the NC to predominantly be in the 'on' state but do show blinking on the short time scale. The 'on' and 'off' durations follow a power law probability distribution with exponents close to -1 and -2 for the 'almost non-blinking' NC respectively and both close to -1.5 for the 'blinking' NC.

FLID highlights that both sets of NC have predominantly single exciton emission however the 'off' states have a combination of A-type and B-type blinking. Whilst in most cases this blinking is A-type and could be related to the presence of a trion, B-type blinking was also evident, albeit less dominant, and mostly seen in the CdZnSeS NC and longer wavelength eFluor®NC which potential have more defects within the structure.

The CdZnSeS NC unsurprisingly have a varied recombination dynamic which could be related to the variable composition and anisotropic growth from the synthetic method. This compares to eFluor®NC which show nominally uniform recombination dynamics across all eFluor®NC, as expected from a commercial product. Further interesting

recombination dynamics were seen in some of the CdZnSeS NC and eFluor®605 nm NC which can not be readily explained and thus warrant further investigation.

Chapter 7

Conclusion and future work

7.1 Conclusion

This thesis set out to investigate the carrier dynamics within NC through direct core-shell engineering and observe how a strained or alloyed core-shell interface can influence these carrier dynamics.

This was achieved by producing monodisperse ZnTe/ZnSe NC via a diethyl Zn-free synthetic method highlighting the 'greenest' synthetic route to ZnTe/ZnSe NC to date. HRTEM and XRD investigations showed that strain, induced from the 7% lattice mismatch, could be seen through lattice bowing in TEM and peak broadening within XRD. The incorporation of continuum elasticity theory into a strained atomistic model enabled the HRTEM and XRD data to be simulated and compared. The comparison supported evidence for a strained NC but also revealed potential stacking faults and dislocations within these NC. Anisotropic growth was seen for various Zn precursors within SILAR and SILAR-TC techniques for the largest cores. It was hypothesised that strain could be a contributing factor to anisotropic growth. An attempt to support this hypothesis

showed that actively alloying the shell over 4 ML produced spherical NC highlighting that strain could have a potential influence on growth dynamics. Synchrotron XPS further supported this hypothesis by the identification 0.45 nm of alloying at the core-shell interface within smallest core diameter structures which showed a spherical geometry.

Ensemble optical investigations showed the effective bandgap of ZnTe/ZnSe NC could be tuned from the N-UV into the visible spectrum with increasing shell thickness which has a characteristic weakening of the absorption feature and an increase of the long PL lifetime component indicative of type-II NC. This synthetic procedure produced QY as high as 12%, one of the highest QY of this material to date but is hindered by photostability issues. Using a (2-6)-band effective mass model the exciton energy shift with shell thickness was effectively simulated and thus identified the effect of strain on the exciton energy and the potential for alloying in the structure. Intentionally alloying 4 ML at the core-shell interface reduced the anisotropic growth but also mitigated the strain-induced excitonic shifts highlighting a potential cause for the observed features. The (2-6)-effective mass approximation also allowed two transitions to be identified through the second derivative of the absorption spectrum whilst two further transitions could tentatively be identified through the fourth derivative.

Further exploratory studies into highly luminescent alloyed CdZnSeS NC via a facile synthesis method and a size series of eBioscience eFluor®CdSe/ZnS type-I NC showed these NC to be nearly 'non-blinking'. These NC showed blinking 'on' and 'off' durations that followed power-law probability distributions and exponents consistent with other nearly 'non-blinking' NC. The late development FLID enabled the intensity-time and lifetime-time trajectories to be compared, albeit with a second resolution, and highlighted that the major mechanism for recombination during a blink was through trion recombination but also revealed that recombination centres were still active in these NC.

Ultimately this broad thesis synthesises novel structures and develops new analytical tools to help to investigate the physical and optical properties of NC, giving insight into the growing knowledge of the carrier dynamics within NC.

7.2 Future work

7.2.1 Further synthesis of ZnTe/ZnSe nanocrystals

Whilst high QY have been achieved, further experiments are required to increase the stability and reproducibility of this structure. With increased stability further SNS investigations into two peak emission can take place whilst also enabling PLE experiments to verify hot exciton transitions.

This thesis has shown that strain is a component in producing anisotropic NC, however it could be considered that a understanding of anisotropic growth within ZnTe/ZnSe NC might not be complete. Further synthesise of ZnTe/ZnSe NC via a dropwise addition method prove useful [80, 95]. Whilst in theory this should be similar to SILAR-TC, it could potentially yield a different result. Another possibility would be to change the TOP ligand to TBP or Se-ODE or the purity of the TOP where it is known that TOP does contain some phosphoric acid groups and that at high concentrations has been known to produce branched structures or vary crystal structure [216].

7.2.2 Interatomic diffusion of Te in ZnTe/ZnSe nanocrystals

The identification of interatomic diffusion is becoming a large discussion point within the field as shown by the alloying described here and by others [129, 217, 218]. Determining the rate of interatomic diffusion will be crucial in understanding the NC architecture. A very recent report by Cia *et al.* [139] showed a good example of how to investigate this phenomenon using time/temperature dependent optical studies which could be implemented for ZnTe/ZnSe NC. This uses optical investigations alongside theoretical effective mass calculations to quantify the diffusion process.

Whilst synchrotron XPS would be ideal for this investigation, access is difficult. Another route to identify interatomic diffusion is using standard XPS and measuring the Te concentration at the surface. During the writing of this thesis standard XPS and Monte Carlo simulations have shown a "Thermodynamic instability [217]" in ZnSe/ZnS core-shell NC which showed noticeable high theoretical and experimental interatomic diffusion coefficients at 250°C [217, 218]. It was further predicted that within ZnTe/ZnSe NC the Te will have a greater tendency to move to the surface [178]. If this hypothesis is correct, this could highlight a different interpretation of the PL stability issues described in section 5.5.3.

7.2.3 Development of type-II structures

Type-II structures offer a unique ability to spatially separate charge carriers and have long exciton lifetimes which offers exciting potential within magnetically doped NC to investigate single carrier $sp-d$ interactions with the Mn state and observe enhanced 'Giant Zeeman splitting' [219]. Whilst not shown in this thesis, my investigations into doping Mn in standard type-II combinations like CdS/ZnSe and ZnSe/CdS have not enabled the effective band to be tuned through the 585-600 nm Mn transition due to the specific band alignments, thus, new structures such as Mn-ZnTe or Mn-CdTe or alloy variants could be used to produce doped type-II NC. This is the focus of my post-doc.

7.2.4 Further work on strain modeling

From this thesis it is inherently clear that strain and stacking faults play a role in the general physical and optical properties of NC. Whilst the atomistic model developed here goes a long way to help identifying strain in XRD and TEM images, this model

can further be developed to include stacking faults. After much thought, the best approach would be to have a predefined homogenous lattice constant structure within which random stacking faults are placed and then a strain field is applied

Ultimately direct measurement of strain within NC should be the goal of the field. My investigation utilising the use of aberration corrected TEM and geometric phase analysis (GPA) could be used to investigate strain (see Appendix section E.1). Initial investigations have shown reasonable correlation to the simulated input parameters but due to the nature of GPA, does suffer from thickness effects. This technique could be enhanced by applying GPA over a defocus series which could yield an average strain. Whilst the relatively non-evasive technique of TEM could be potentially be used to observe strain, high angle annular dark field STEM (HAADF-STEM) tomography has already been used to produce 3-D compositional maps and therefore with refinement, may enable strain to be directly measured but might be hindered by high irradiation damage [136].

7.2.5 Further work on single nanocrystal spectroscopy

SNS is a powerful technique when investigating the optical properties of NC. The late development FLID within this thesis has given a great insight into the recombination dynamics of these NC. This technique warrants further development in an effort to achieve 10-100 ms resolution which have been quoted elsewhere [130, 131].

With the development of this technique further exciting extensions of this work could be made to investigate doubly charged or multi-exciton dynamics within these NC, which is known to vary from NC to NC even if there is similar single exciton QY NC [127, 214]. These investigations and subsequent understanding could enable direct engineering of

the multi-exciton lifetimes and point directions to enable large multi-exciton QY to be realised.

Appendix A

A.1 Derivation of the critical radius calculations

This sections sets out to derive the critical thickness as described by Balasubramanian *et al.* [15].

All critical thickness/radius calculation serve to calculate the point at the energy of coherent state, $E_{Coherent}$, is lower than energy incoherent state $E_{Incoherent}$(i.e. $0 > \Delta E = E_{Coherent} - E_{Incoherent}$). Here we define the energy associated with fully coherent growth to be purely elastic energy $E_{Elastic}$ and thus

$$E_{Coherent} = E_{Elastic} \tag{A.1}$$

In an incoherent state the energy required to produce a defect, E_{Defect}, sets to release some of the elastic energy of the system, thus leaving a residual elastic energy $E_{Residual}$. The energy in the system can be defined as

$$E_{Incoherent} = E_{Residual} + E_{Defect} \tag{A.2}$$

Using the notation described in section 3.1 it can be found that the elastic energy can be described by [15]

$$E_{Elastic} = (\pi a^3 p^2)\left[\frac{1-\nu_c}{1+\nu_c}\frac{1}{\mu_c} + \frac{1-2\nu_s}{1+\nu_s}\frac{1}{\nu_s}\frac{c}{1-c} + \frac{1}{2\mu_c(1-c)}\right] \tag{A.3}$$

In an incoherent state, we describe the energy to create a full dislocation as the energy to produce a dislocation loop E_{Loop} [15].

$$E_{Defect_{full}} = E_{Loop} \tag{A.4}$$

where E_{Loop} is defined as [15]

$$E_{Loop} = 2\pi r_{loop}\left(\frac{\mu_i |\mathbf{b}|^2}{4\pi(1-\mu_i)}\right)\ln\left(\frac{8\alpha r_{loop}}{|\mathbf{b}|} - 1\right) \tag{A.5}$$

where α is dislocation core parameter, r_{loop} is the radius of the dislocation loop being considered and $\mu_i = 2\mu_c\mu_s/(\mu_c + \mu_s)$ as the average shear modulus at the interface. As the largest strain is at the core-shell interface, we take r_{loop} to be radius of the dislocation loop around the core shell interface.

We can further extend the model by considering the energy required to form partial dislocations. Here we consider the energy required for the partial dislocation loop and the intrinsic stacking fault energy loop that encompasses the partial dislocation $E_{Stackingfault}$.

$$E_{Defect_{Partial}} = E_{Loop} + E_{Stackingfault} \tag{A.6}$$

Here we define the energy require to create the intrinsic stacking fault energy as

$$E_{Stackingfault} = \pi r_{loop}^2 \gamma \tag{A.7}$$

where γ is the stacking fault energy of the shell material.

The energy released by the formation of the dislocation is considered by the interaction energy $E_{Interaction}$ which can be generally described as

$$E_{Interaction} = \pi r_{loop}^2 p(a, a_s)|\mathbf{b}| \tag{A.8}$$

where we defined $p(a, a_s)$ as p is section 3.1 and note here that p is a function of the core radius a and the shell thickness a_s and thus, the residual energy in the system can be considered by

$$E_{Residual} = E_{Elastic} - E_{Interaction} \tag{A.9}$$

Using equations A.1 to A.9 we show the critical radius for the full partial and partial dislocations the critical energy can be written as

$$\Delta E_F = 0 = 2\pi r_{loop}\left(\frac{\mu_i|\mathbf{b}|^2}{4\pi(1-\mu_i)}\right)\ln\left(\frac{8\alpha r_{loop}}{|\mathbf{b}|}-1\right) - \pi r_{loop}^2 p(a, a_s)|\mathbf{b}| \tag{A.10}$$

$$\Delta E_P = 0 = 2\pi r_{loop}\left(\frac{\mu_i|\mathbf{b}|^2}{4\pi(1-\mu_i)}\right)\ln\left(\frac{8\alpha r_{loop}}{|\mathbf{b}|}-1\right) - \pi r_{loop}^2 p(a, a_s)|\mathbf{b}| + \pi r_{loop}^2\gamma \tag{A.11}$$

Here we see that the critical radius is function of core radius (a) and shell thickness (a_s) by virtue of the interface pressure at the core-shell interface and r_{loop} which is the core radius a in this case.

A.2 Critical radius calculations for CdSe/ZnS nanocrystals

This section show the critical radius for the widely studied system of CdSe/ZnS that has a 12% lattice mismatch. Figure A.1 shows the critical radius for zinc blende CdSe/ZnS NC for various α and suggests that ZnS can only be grown dislocation free for shell thickness below 0.3 nm (1.14 ML). It is also seen that within the $\alpha = 4$ model that a core radii below 0.7 nm can grow ZnS dislocation free whilst within the $\alpha = 1$ model no ZnS can be grown with more than 1 ML without a form of dislocation. To enable comparison we show the highest quantum yield obtained from Daboussi *et al.* [7] and Smith *et al.* [20] were obtained for core radii 2nm and 1.9nm the largest QY with 1.3 ML (0.35 nm) and 1.5 ML (0.40 nm) of ZnS shell respectively which shows the best agreement with the full dislocation boundary of $\alpha = 4$ (Figure A.1c). This prediction is considerably better than previous predictions using Matthews-Blakeslee theory [152] which predicts a critical radius of 1 nm[137, 151].

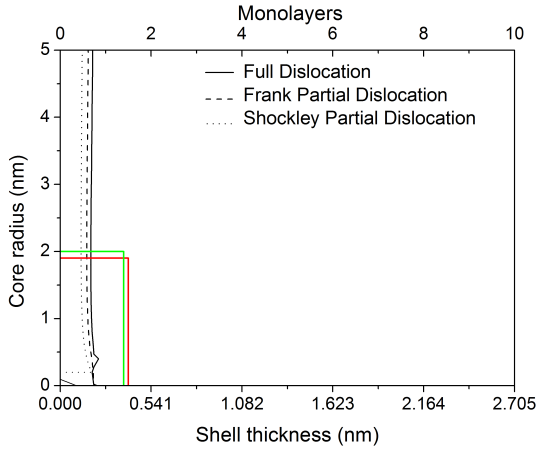

(A) $\alpha = 1$

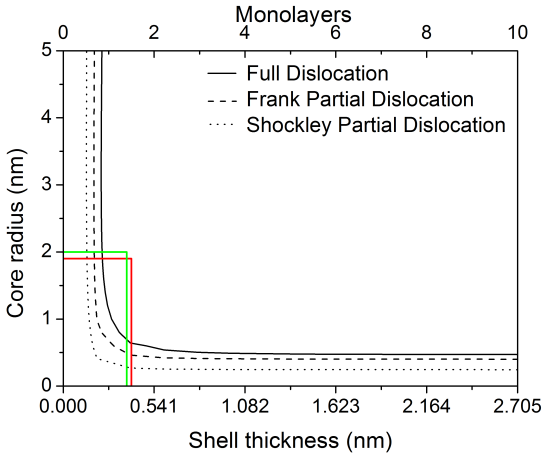

(B) $\alpha = 2$

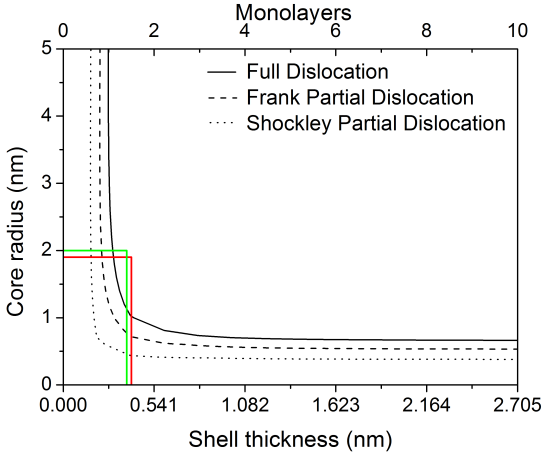

(C) $\alpha = 4$

FIGURE A.1: The critical radius for CdSe/ZnS for a full, Frank partial and Shockley partial dislocation for $\alpha =$ a) 1, b) 2 and c) 4. Inset shows the highest quantum yield as shown by Daboussi *et al.* [7] (Green) and Smith *et al.* (Red) [20]

Appendix B

B.1 Materials parameters for all strain model simulations and critical radius calculations

Parameters	ZnTe	Ref.	ZnSe	Ref.
E (GPa)	43.94	[220]	75.5	[221]
ν	0.363	[222]	0.38	[223]
K (GPa)	50.9	[21]	62.4	[21]
μ (GPa)	28.6	[224]	18.35	[225]
a_0 (nm)	0.610	[14]	0.567	[14]
γ(mJ m^2)			12.4	[226]

TABLE B.1: Material parameters used to model the effect of strain in ZnTe/ZnSe nanocrystals.

Parameters	CdSe	Ref.	ZnS	Ref.
E (GPa)	61.20	[227]	86.2	[228]
ν	0.345	[18]	0.331	[18]
K (GPa)	55.7	[227]	77	[18]
μ (GPa)	28.6	[227]	33.3	[228]
a_0 (nm)	0.605	[18]	0.54	[18]
γ(mJ m^2)			4	[226]

TABLE B.2: Material parameters used to model critical radius CdSe and ZnS.

Parameters	Core	Shell
E (GPa)	75.5	43.94
ν	0.38	0.363
K (GPa)	62.4	-
μ (GPa)	32.9	24.8
a_0 (nm)	0.610	0.567

TABLE B.3: Best fit parameters material parameters used to model the effect of strain in ZnTe/ZnSe core-shell nanocrystal

Appendix C

C.1 (2-6)-band effective mass model.

This section is for completeness and is the work of Edward Tyrrell.

C.1.1 General effective mass model

The effective mass parameters of the unstrained bulk materials are shown in table C.1. We use the energy-dependent two-band electron and six-band hole radial Hamiltonians of Pokatilov *et al.* [156] for QD heterostructures to calculate single-particle levels which are eigenstates of total angular momentum j and parity p. We label the nanocrystal core radius a and the shell thickness a_s. Quoted Luttinger parameters used here are experimental values.

Parameters	ZnTe	Ref.	ZnSe	Ref.
E_g (eV)	2.26	[229]	2.7	[230]
E_p (eV)	19.1	[231]	24.2	[231]
Δ (eV)	0.92	[231]	0.43	[231]
$m_e(m_0)$	0.11	[232]	0.14	[233]
γ_1^L	4.07	[234]	2.45	[235]
γ_2^L	0.78	[234]	0.61	[235]
γ_3^L	1.59	[234]	1.11	[235]

TABLE C.1: Effective mass parameters

Electron (hole) energies calculated for the unstrained band profile are denoted $E^{(0)}_{e(h)}$. We note that there is a range of values for the ZnTe/ZnSe valence band offset E_v in the literature, including calculated values of 1.08 eV [236], 0.73 eV [237] and 0.84 eV [238]. Due to the uncertainty in this value and the fact that the effective band gaps of type-II NC are known to be strongly influenced by the valence band offset, we treat E_v as a fitting parameter. We also find single particle energies to be significantly affected by the band gap E_{g3} of the external medium due to the wide band gap ZnTe/ZnSe NC materials which increase penetration of the wave functions into the surroundings compared to narrower gap semiconductors. Due to the uncertainty in E_{g3}, we similarly treat it as a fitting parameter.

The Coulomb interaction is calculated as a first order perturbation to the single particle states with the numerical method of Bolcatto and Proetto [239]. This model assumes a spatial dielectric constant $\epsilon(r)$ that changes smoothly from the core value ϵ_{ZnTe} to the shell value ϵ_{ZnSe} over a distance of $2\delta_1$, and from ϵ_{ZnSe} to the external value ϵ_{out} over a distance of $2\delta_2$. We use $\delta_1 = \delta_2 = 0.1$ nm, $\epsilon_{ZnTe} = 7.3$ [240], $\epsilon_{ZnSe} = 5.9$ [240] and $\epsilon_{out} = 2$.

We calculate the sum of squared residuals S deviation of the ground state exciton energy with increasing shell thickness when compared to the original core exciton energy ZnTe/ZnSe NC with a =1.2, 1.8 and 2.3 nm cores to find the parameters that give the best fit as E_v is varied from 0.4 to 1 eV and E_{g3} is varied from 0.5 to 10 eV. The individual best fit for each core and global best fit are shown in C.3.

Parameters	ZnTe	Ref.	ZnSe	Ref.
a_v^c (eV)	-6.95	[21]	-5.93	[21]
a_v^v (eV)	-2.28	[21]	-1.97	[21]

TABLE C.2: Material parameters used to model the effect of strain in ZnTe/ZnSe core-shell nanocrystal

C.1.2 Strained effective mass model

To model the effect of strain on the electronic structure of the nanocrystal we use a similar approach to Smith *et al.* [20] This involves calculating the stress and strain fields in the heterostructure using the continuum elasticity model of Balasubramanian *et al.* [15], and then applying the model-solid theory of Van de Walle [19] to find the resulting band alignments of the strained structure. This is done by converting the fractional volume changes of the materials due to hydrostatic strain to shifts in the conduction (valence) band energy $E^{c(v)}$ using

$$a_v^{c(v)} = \frac{dE^{c(v)}}{d\ln v} \tag{C.1}$$

where $d\ln v$ is the fractional volume change and $a_v^{c(v)}$ is the conduction (valence) band volume deformation potential. The deformation of the crystal lattice changes the conduction and valence band edges because they depend on the bond strength in the crystal.

Using the strain equations for the core and shell (equations 3.4, 3.9 and 3.10 derived in section 3.1) we define the fractional volume change in the core as

$$\frac{\Delta\Omega}{\Omega} = \epsilon_{rr} + \epsilon_{\theta\theta} + \epsilon_{\phi\phi} = \frac{3p_i}{E_c}(2\nu_c - 1). \tag{C.2}$$

and in the shell as

$$\frac{\Delta\Omega}{\Omega} = \frac{3cp_i}{E_s(1-c)}(1-2\nu_s) + \frac{2cp_i}{E_s(1-c)}\left(\frac{a+a_s}{r}\right)^3(1-2\nu_s). \tag{C.3}$$

Following the approach of Van de Walle [19], we modify the existing unstrained conduction and valence band profiles by uniform shifts due to the 'homogeneous' (r-independent) strain in each region. This gives the size-dependent band gap

$$E_g(a, a_s) = \begin{cases} E_{g1} + \frac{3p_i}{E_c}(2\nu_c - 1)(a_v^c - a_v^v) & \text{for } r < a \\ E_{g2} + \frac{3cp_i}{E_s(1-c)}(1 - 2\nu_s)(a_v^c - a_v^v) & \text{for } a < r < a_s \end{cases} \tag{C.4}$$

where E_{g1} and E_{g2} are the unstrained core and shell band gaps. These shifts mean the conduction and valence band profiles change as a function of a and a_s. Since the shifts are independent of r the radial wave functions remain spherical Bessel or Hankel functions. We take into account the effect of the size dependent band-gap $E_g(a, a_s)$ on the parameters α, γ^L, γ_1^L and χ in the single particle Hamiltonians[156]. For example for the conduction band parameter α, $\alpha \to \alpha(a, a_s)$ where

$$\alpha(a, a_s) = \frac{m_0}{m_c} - \frac{E_p}{3}\left(\frac{2}{E_g(a, a_s)} + \frac{1}{E_g(a, a_s) + \Delta}\right) \tag{C.5}$$

and the band gap in the core and shell are given by C.4.

Single particle energies $E_{e(h)}^{(1)}$ and wave functions $\psi_{e(h)}^{(1)}$ of the modified potentials are then calculated. Finally the inhomogeneous (r-dependent) part of the strain in the shell region is added as a perturbation:

$$H^{c(v)} = \frac{2cp_i}{E_s(1-c)}\left(\frac{a + a_s}{r}\right)^3 (1 - 2\nu_s)a_v^{c(v)} \tag{C.6}$$

The corresponding first order energy shifts $E_{p,e(h)}$ are defined as

$$E_{p,e(h)} = \langle \psi_{e(h)}^{(1)} | H^{c(v)} | \psi_{e(h)}^{(1)} \rangle \tag{C.7}$$

We note that all of the strain-dependent energy shifts of the conduction and valence band profiles maintain the spherical symmetry of the confining potential for electrons and holes. Therefore electron and hole eigenstates retain the same symmetry as before the strain was added. For ZnTe/ZnSe NC, we find that $E_{p,h} \sim -1$ meV for $nS^{(h)}_{3/2}$ states ($n = 1, 2, 3$), while $E_{p,e}$ can reach ~ -50 meV for the $1S^{(e)}_{1/2}$ state. In other words the inhomogeneous strain in the shell affects electron states to a much greater extent than hole states due to the much greater conduction band deformation potential. Therefore for hole states we approximate the valence band profile by a flat band in the shell and use the wave functions $\psi^{(1)}_h$. For the electrons new 'perturbed' wave functions could be calculated in first order perturbation theory using [241]

$$\psi^{(2)}_{e,n} = \psi^{(1)}_{e,n} + \sum_{l \neq n} \frac{H^c_{ln}}{E_{e,n} - E_{e,l}} \psi^{(1)}_{e,l}, \tag{C.8}$$

$$E^{(2)}_{e,n} = E^{(1)}_{e,n} + E_{p,e} \tag{C.9}$$

where n labels the ordinal number of a level with given symmetry, $H^c_{kn} = \langle \psi^{(1)}_{e,k} | H^c | \psi^{(1)}_{e,n} \rangle$ and the wave functions $\psi^{(2)}_{e,n}$ are normalised. However we find that since matrix elements H_{ln} are of the order of 10 meV for $n = 1$ and electron $ns_{1/2}$ levels are separated by several hundred meV for the considered nanocrystals $\psi^{(2)}_{e,n} \simeq \psi^{(1)}_{e,n}$ to a good approximation.

The exciton energies E_{ex} of the strained structure are then calculated as

$$E_{ex} = E^{(2)}_e - E^{(1)}_h + E^{(1)}_c + E^{(1)}_{s,h} + E^{(1)}_{s,e} \tag{C.10}$$

where $E_c^{(1)}$ and $E_{s,e(h)}^{(1)}$ are the interparticle Coulomb energy and electron (hole) self-energy defined as

$$E_c^{(1)} = \langle \psi_h^{(1)} | \langle \psi_e^{(1)} | V_c(\mathbf{r}_e, \mathbf{r}_h) | \psi_e^{(1)} \rangle | \psi_h^{(1)} \rangle \tag{C.11}$$

$$E_{s,e(h)}^{(1)} = \langle \psi_{e(h)}^{(1)} | V_s(\mathbf{r}_e) | \psi_{e(h)}^{(1)} \rangle. \tag{C.12}$$

To model the Coulomb interaction we use the parameters listed earlier. The electron and hole localisation regimes are identified using the 'energy criteria' used previously in other reports [46, 242]. The electron localisation boundary is found by numerically solving the equation $E_e^{(1)} = E_{c1}$ where E_{c1} is the strain-dependent conduction band edge energy of the core. The hole localisation boundary is found by numerically solving the equation $E_h^{(1)} = E_{v1}$ where E_{v1} is the strain-dependent valence band edge energy in the shell.

To fit the model to the data we again vary E_v from 0.4 to 1 eV and E_{g3} from 5 to 10 eV and calculate S for the ground states. In this case E_v is the ZnTe/ZnSe valence band offset of the heterostructure before strain is added. The individual best best fit for each core and global best fit are shown in C.3.

The PL radiative lifetimes were calculated using the procedure of de Mello Donegà *et al.* [243].

	S_{min} (nm^2)	best fit value of Eg3 (eV)	best fit value of Ev (eV)
1.2 nm Core			
Strained	110	7.77	0.579
Unstrained	100	5.078	0.876
1.8 nm Core			
Strained	26	6.73	0.716
Unstrained	68	6.357	0.789
2.3 nm Core			
Strained	13	8.45	0.678
Unstrained	175	7.267	0.728
Global fit			
Strained	235	6.031	0.710
Unstrained	478	6.479	0.760

TABLE C.3: Optimum E_{g3} (eV) and E_v (eV) values used model ZnTe/ZnSe NC.

Appendix D

D.1 Additional information for the ZnTe/ZnSe nanocrystals

D.1.1 EDX spectrum of ZnTe core-only nanocrystals

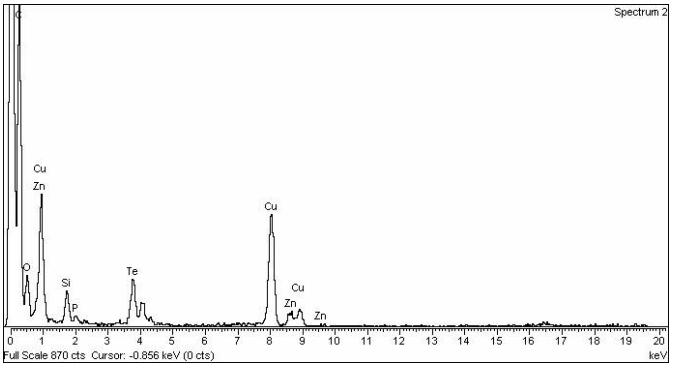

FIGURE D.1: An Energy-dispersive X-ray spectrum of core only ZnTe nanocrystals showing Zn, Te, P, C and Cu. This is expected from a ZnTe nanocrystals with a phosphine ligand on a Cu support. The spectra shows no detectable lithium or boron from the superhydride solution.

D.1.2 Vegard's Law

Vegard's law is an empirically derived relationship which determines the lattice constant of an alloy by knowing the relative composition of the materials and can extend to band gap energies if one assumes another bowing term. The relationship assumes a linear dependence between the relative molar fraction of the individual materials and the relative contribution of each bulk lattice constant to the alloyed lattice constant a_{alloy}. Mathematically this is described by

$$a_{alloy} = x_1 a_1 + y_2 a_2 \tag{D.1}$$

where a_i describes the bulk lattice constants of materials 1 and 2 and x_1 and y_2 describe the relative composition of the two materials.

D.1.3 XRD concentration values

The results in table 5.1 use the following approaches to get achieve the composition ratios

1. Use the stoichiometric ratio assuming full quantitative reactions of all precursors.
2. The composition ratio, as determined through the volumes densities, using the average diameter determined by TEM (assuming the ZnTe to have a constant volume throughout the shell growth).
3. To relate the observed diffraction peaks and thus global lattice constant of the NC to a Vegard ratio.

The TEM derived compositional ratio were calculated using the follow procedure

The volume (V) of the core and shell is found by

$$V_{(core)} = \frac{4}{3}\pi a^3 \tag{D.2}$$

$$V_{(shell)} = \frac{4}{3}\pi(a_s^3 - a^3) \tag{D.3}$$

The mass (M) of the core and shell can be found by multiplying the volume by the density ρ

$$M_{(core)} = V_{(core)} * \rho_{(core)} \tag{D.4}$$

$$M_{(shell)} = V_{(shell)} * \rho_{(shell)} \tag{D.5}$$

This can be related to the amount of moles (mol) by dividing the mass by the molar mass (A)

$$mol_{(core)} = \frac{M_{(core)}}{A_{(core)}} \tag{D.6}$$

$$mol_{(shell)} = \frac{M_{(shell)}}{A_{(shell)}} \tag{D.7}$$

The result of each core-shell investigated are shown in table D.1

D.1.4 Scherrer equation

Due to the finite size of the particle the coherence length of the periodic structural pattern is finite and can give a lower bound for the diameter of the NC (D) can be found through the Scherrer equation [244]

	Radius (nm)	Volume (nm^3)	Moles (zM)[10^{-21}]	Relative Concentration (%)
2.4 nm ZnTe core 4.5 ML ZnSe shell				
ZnTe	1.2	7.24	0.00212	10
ZnSe	1.2474	52.1	0.0197	90
3.6 nm ZnTe core 5 ML ZnSe shell				
ZnTe	1.80	24.4	0.715	15
ZnSe	1.418	115	4.19	85
4.6 nm ZnTe core 4.4 ML ZnSe shell				
ZnTe	2.3	51.0	1.49	23
ZnSe	1.276	141	5.12	77

TABLE D.1: The values used to obtain the TEM derived compositional ratio.

$$D = \frac{K\lambda}{(\Delta(2\theta) - B_i)\cos(\theta_{peak})} \tag{D.8}$$

Where λ is wavelength of the X-ray radiation (Cu $K\alpha$ 1.5405Å), K is the size factor which we take to be 1 for a spherical particle, $\Delta(2\theta)$ is the FWHM of the diffraction peak in 2θ radians and θ_{peak} is the Bragg angle of the peak in θ radians and B_i is the instrument broadening which we have taken to be 0.011 radians (0.68°). Here we take in consideration only the {111} peak, this is due to size effects making higher peak wavelength overlap and thus preventing easy identification of the peak width [134].

D.1.5 Additional ZnTe/ZnSe absorption data

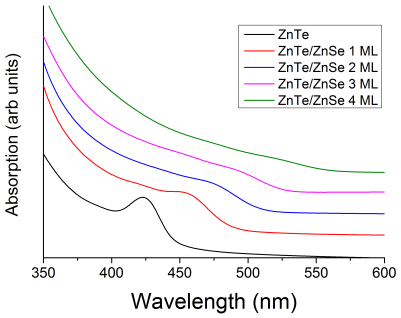

FIGURE D.2: The absorption spectra for ZnTe/ZnSe NC with 2.4 nm diameter ZnTe cores and upto 4 ML in ZnSe shell.

D.1.6 Full 2nd derivatives of the ZnTe/ZnSe absorption spectra

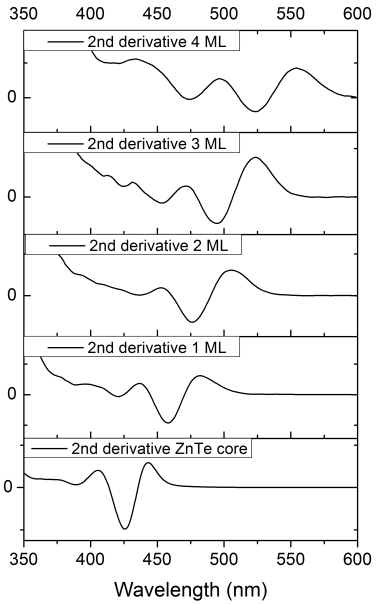

(A) 2.4 nm ZnTe core

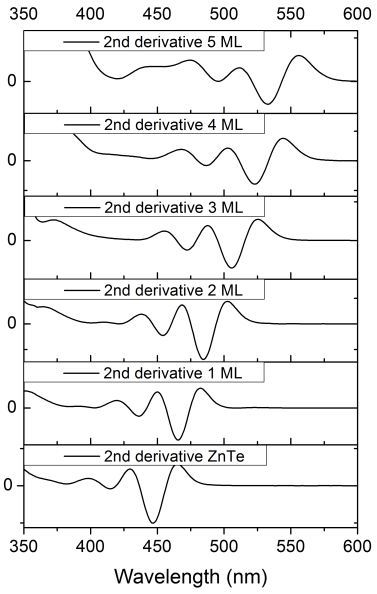

(B) 3.6 nm ZnTe core

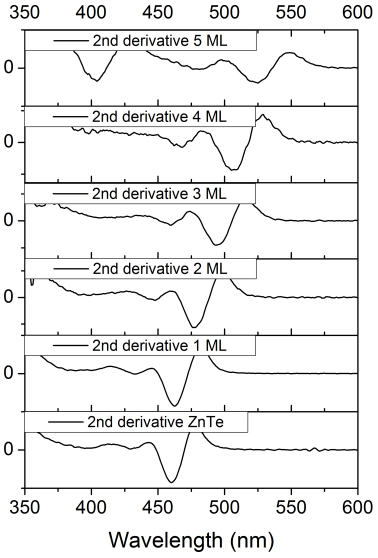

(C) 4.6 nm ZnTe core

FIGURE D.3: 2^{nd} derivative of the ZnTe/ZnSe absorption data.

D.1.7 Additional lifetime information for ZnTe/ZnSe nanocrystals

Lifetime	Amplitude τ_1	τ_1 (ns)	Amplitude τ_2	τ_2 (ns)	Amplitude τ_3	τ_3 (ns)
ZnTe/ZnSe 3 ML						
Tri-exponential	935.0	1.7	296.2	8.7	240.3	31.6
ZnTe/ZnSe 4 ML						
Tri-exponential	2166.1	2.4	679.6	15.7	275	51.6
ZnTe/ZnSe 5 ML						
Tri-exponential	1179.0	3.0	504.9	20.0	282	65.2

TABLE D.2: The tri-exponential lifetime components for the lifetime trajectories of ZnTe/ZnSe NC with a 3.9 nm diameter NC core of figure 5.28.

D.1.8 Disassociation constants and dynamic equilibrium

Here the dissociation dynamics for a typical NC solution can be described by dissociation reaction in equation D.9. If the reaction is in a state of dynamic equilibrium it can be understood that the tendency of the reaction to one state or the other is controlled through a dissociation constant K_d, which is defined through the concentration of its constituent parts. The relation of K_d is given by equation D.10 where $[NC \cdot Ligand_{(x)}]$ describes the concentration of a fully ligand covered NC, $[NC]$ describes a ligand free NC, $[Ligand]$ describes concentration of the ligand in solution and x the stoichiometric ratio of NC to ligand required to provide a full coverage of ligands around the NC. With all things being equal, the lower the $[NC \cdot Ligand_{(x)}]$concentration (and thus the lower the [Ligand] concentration) the higher the uncovered [NC] concentration. Using this theory, another scenario can be easily visualised through the addition/removal of excess ligands which will effect the [Ligand] concentration and therefore will lower/raise the uncovered [NC] concentration.

$$NC \cdot Ligand_{(x)} \overset{K_d}{\rightleftharpoons} NC + xLigand \tag{D.9}$$

$$K_d = \frac{[NC] \times [Ligand]^{(x)}}{[NC \cdot Ligand_{(x)}]} \tag{D.10}$$

Appendix E

E.1 Further strain analysis through TEM simulation

E.1.1 The strained and unstrained atomistic models for 3.2 nm diameter ZnTe core and 4 ML shell

It is worth noting some of unexplained features of figures 5.11 and 5.13 in terms of simulated atomistic positions seen in figure E.1a and E.1b. The larger than expected lattice constant in the shell within the tangential strained model can be accounted by the broad range of epitaxial growth routes to the shell and is most probably an artifact of building the strained system in octants. The large drop in lattice constant at the core-shell interface within the radial component of the unstrained model can be explained by two overlapping planes which would distort the observed lattice constant. It is also noteworthy that the core lattice constant of the strained NC shows a similar lattice constant to that of compositional model presented in figure 5.10c. This gives weight to the idea that Vegard's law can be applied, to a first approximation and with caution, when two materials with different lattice constants are overlayed.

(A) Strained (B) Unstrained

FIGURE E.1: The a) strained and b) unstrained atomistic models used for figures 5.11b and 5.11c.

E.1.2 Further characterisation through aberration corrected microscopy simulation

As was seen in section 5.4.3 the limited success of obtaining TEM images on a zone axis severely limits the possibility of investigating strain within these structures. The precision to which the lattice constant could be found was also limited by the microscope. By simulating these structure for a C(s) aberration corrected JEOL 2200 microscope, we set to increase the sharpness and information limit of the images, therefore, higher-order information can be obtained. The effect on image quality can be seen from figure E.2a and E.2b where the sharpness of the image is markedly increased. By placing the NC on the {111} zone axis we see distinct regions where atoms have diverged from a single column, highlighting strained regions. This is in the shell region for a strained NC (Figure E.2a) and at the core-shell interface for the unstrained case (Figure E.2b), as expected. An inspection of the corresponding FFT shows the general increase in image resolution in which Bragg reflections can resolved well past the {440} reflection. This can be compared to images from the JEOL 4000EX as seen in figure 5.9d, in which the

{440} Bragg reflection can only just be resolved. The FFT quality is such, that we can potentially identify forbidden reflection as seen by the indexed {110} Bragg peaks seen by figure E.2c. These forbidden reflections are associated with either double reflection of the electrons or a breaking of crystal symmetry and are therefore are typically associated with the formation of stacking faults/strained regions within the system. Whilst the image quality could still be enhanced using exit wave-restoration the information gathered will only set improve the resolution of analysis and identification of strain or defect regions.

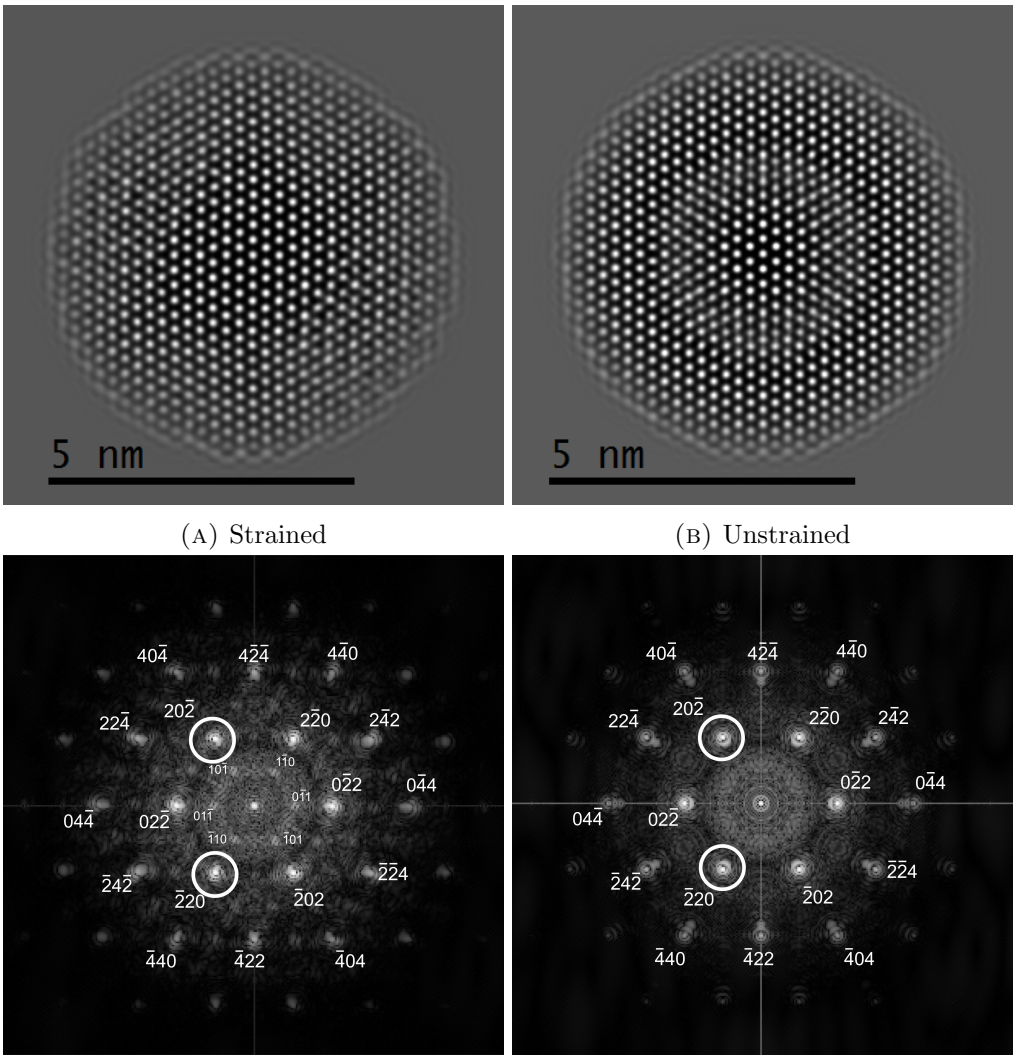

(A) Strained (B) Unstrained

(C) Strained (D) Unstrained

FIGURE E.2: A simulated HRTEM image for a) a strained and b) a unstrained 3.6 nm diameter ZnTe core with 5 ML ZnSe shell. Images were simulated for an the C(s) aberration corrected JEOL 2200 microscope running at 200 kV with a defocus of 28 nm. The corresponding indexed FFT of c) the strained and d) the unstrained images of [a] and [b] respectively.

E.1.3 Further characterisation through geometric phase analysis simulation

A further technique of geometric phase analysis (GPA) has been developed by Hÿtch *et al.* to analyse strain with HRTEM images [245, 246] and has been used to great effect to study strain within thin films[245], the intrinsic strain within gold dodecahedron

NC[247] and core-shell nano-plates[140]. A full description of this technique can be found in reference [248]. In brief, a HRTEM image is treated as the sum of many sets of interference fringes. The amplitude and phase variations of these fringes within a local area are fourier analysed and compared to a perfect reference. The amplitude variations reveal anti-phase boundaries (i.e transformations). Phase variations can be used to obtain the displacement between to fringes. To enable a 2-D displacement/strain map to be produced, we apply a Bragg filter to two Bragg reflections that are not on the same plane, and thus two fringe distance and fringe vectors are investigated. The Bragg filter for the strained and unstrained images are highlighted by a white ring around the $(20\bar{2})$ and $(\bar{2}20)$ Bragg reflections in the FFT images of figure E.2c and E.2d. We define the reference region as the centre of the NC All GPA processing used the '*FRWRtools*' plugin for '*Digital Micrograph*'[i].

[i] This is freely available add-on developed by Koch *et al.* at Stuttgart Center for Electron Microscopy and downloadable at `http://www.christophtkoch.com/strain/index.html`

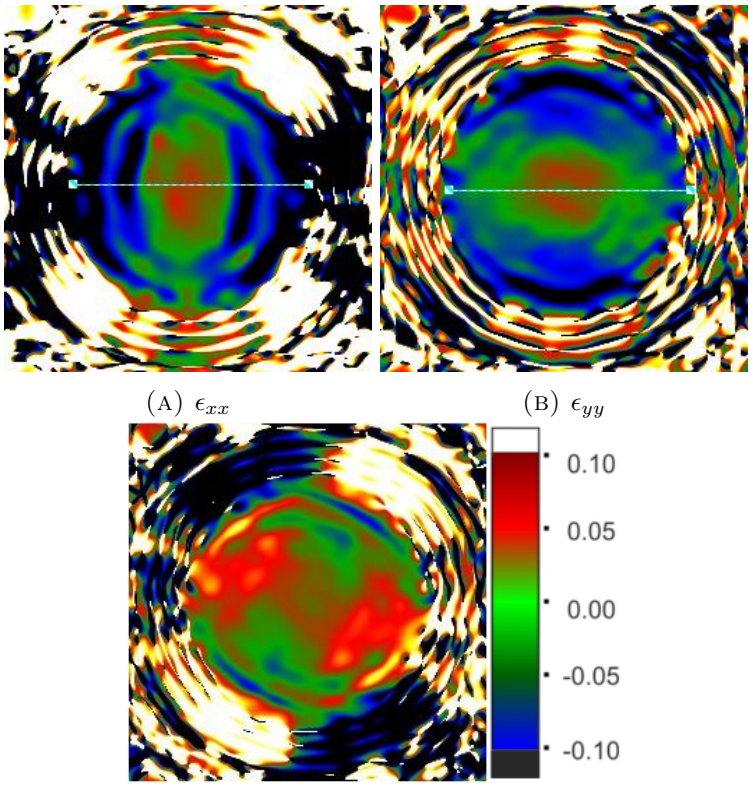

(A) ϵ_{xx} (B) ϵ_{yy}

(C) ϵ_{xy}

FIGURE E.3: a) ϵ_{xx} b) ϵ_{yy} and c)ϵ_{xy} strain tensor components as a function of position as calculated using GPA for the strained NC image in figure E.2a and using the Bragg filter of figure E.2c.

Figure E.3 and E.4 show the cartesian strain tensor components as a function of position for the strained and unstrained NC seen in figure E.2a and E.2b. From these figures, we can see the magnitude of compressive strain increase from the core to the shell, as expected. To quantify these results we inspect the strain magnitude profile for ϵ_{xx} and ϵ_{yy} over the breath of the NC. We relate ϵ_{xx} and ϵ_{yy} in this geometry to ϵ_{rr} and $\epsilon_{\theta\theta}$ respectively in a spherical coordinate system. From figure E.5a we see the magnitude of ϵ_{xx} varies from 0.005 for the core and then jumps to -0.13/-0.11 at the core-shell interface at x= 1.4 and x=4.7 respectively. The magnitude of the strain in the shell oscillates[ii] and finishes at a magnitude of ∼-10 in before a sharp increase at shell edge.

[ii] Investigations of core only NC revealed these oscillation to be thickness effects, however due to time constraints, procedures to overcome this effect have not been developed.

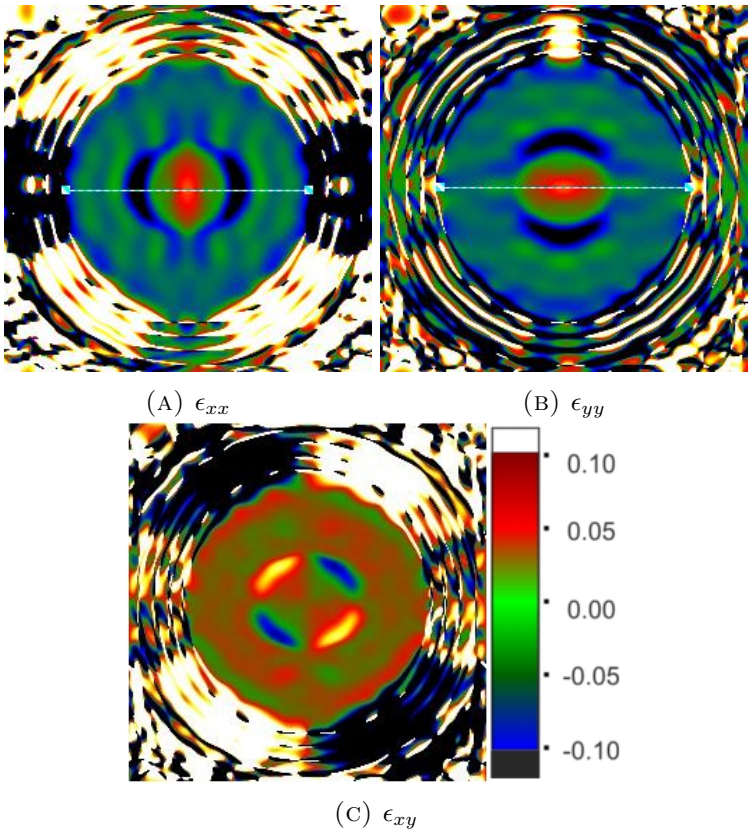

(A) ϵ_{xx} (B) ϵ_{yy}

(C) ϵ_{xy}

FIGURE E.4: a) ϵ_{xx} b) ϵ_{yy} and c)ϵ_{xy} strain tensor components as a function of position as calculated using GPA for the unstrained NC image in figure E.2b and using the Bragg filter of figure E.2d.

From figure E.3b we see the magnitude of the ϵ_{yy} varies from a core value of 0.004 to shell magnitude of -0.04.

To draw comparison we calculate theoretical relative strain from the continuum elasticity model and use the compressed core lattice constant value (6.02 Å) as the point of reference in calculating the relative strain. In the continuum elasticity model, the radial strain component jumps to magnitude of -0.10 which relaxes with increasing shell thickness to -0.065. The tangential component shows a slow transition to -0.05. We see the absolute magnitudes of the two are not the same, however the radial and tangential components show a similar trend to the ϵ_{xx} and ϵ_{yy} profiles.

In comparison the unstrained model sees ϵ_{xx} vary from 0.025 in the core and jump to -0.15 at the core-shell interface and then reduce to average magnitude of $\sim$-0.04. The

jump is consistent with a large amount of stacking fault. The ϵ_{yy} profile shows a similar trend to ϵ_{xx} albeit with a smoother transition and no peak at the core-shell interface. The variation of the strain from the core to shell is 0.065 and is in close that expected strain from the lattice mismatch of 0.071 (7.1%).

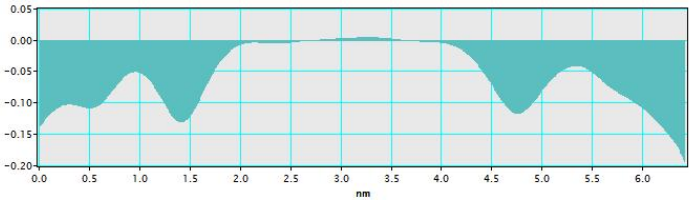

(A) Profile of strained ϵ_{xx}

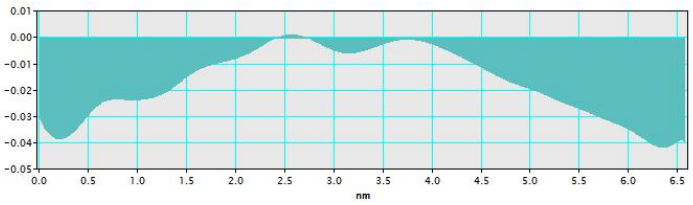

(B) Profile of strained ϵ_{yy}

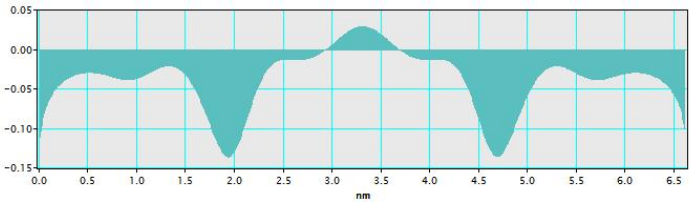

(C) Profile of unstrained ϵ_{xx}

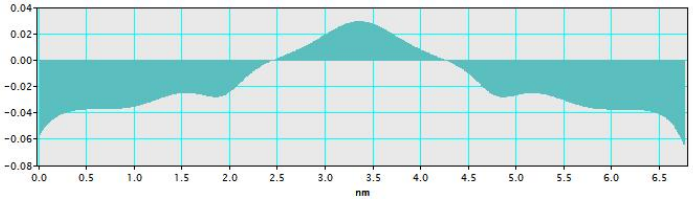

(D) Profile of unstrained ϵ_{yy}

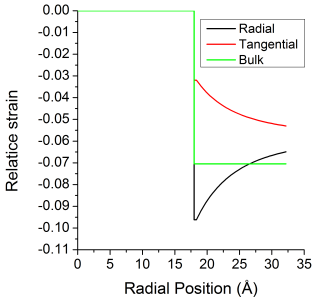

(E)

FIGURE E.5: a-d) The profiles of ϵ_{xx} and ϵ_{yy} along the x axis of the strained strain components of a) figures E.3a and b) E.3b, and the unstrained components of c) figures E.4a and d) E.4b. e) The predicted strain components profiles relative to the core lattice constant for a 3.6nm ZnTe core and 5ML ZnSe shell. Black and red are the relative radial and tangential strain components of the strained model assuming a 6.02Åcore lattice constant and Green is the relative strain of bulk lattice constants

Whilst the absolute magnitudes within the ϵ_{xx} and ϵ_{yy} profiles are higher(lower) than

that predicted for the strain(unstrained) NC, the trends in magnitudes do show reasonable agreement. To account for variations in absolute magnitude we note that we use the NC core as the local reference since the software is limited to a reference within the image. Whilst using the core region is a valid first approximation as it does shows minimal strain, we note that the core part of the image can have contributions from the shell which could and disrupt the accuracy of the result. To overcome this potential problem, we note that commercially available programs (e.g http://www.hremresearch.com), can account for a external reference and that using this external reference can considerable improve the reliability of the results. This highlights the potential of GPA as an analytical tool for strained core-shell NC however further experimental testing and procedures to account for strain oscilation/thickness effects should be taken consideration before using GPA as standard analytical technique.

Appendix F

F.1 Additional ensemble lifetime information for the CdZnSeS nanocrystals

Lifetime	Amplitude τ_1	τ_1 (ns)	Amplitude τ_2	τ_2 (ns)	Amplitude τ_3	τ_3 (ns)
CdZnSeS 1 minute						
Tri-exponential	7083.5	8.5	4290.6	26.2	4290.5	110.2
CdZnSeS 2 minutes						
Bi-exponential			6378.7	27.1	1058	84.7
CdZnSeS 3 minutes						
Tri-exponential	26575.9	16.7	28038	39.0	646.8	148.6
CdZnSeS 4 minutes						
Tri-exponential	30796.0	12.1	38036.3	35.9	1158.5	136.6
CdZnSeS 5 minutes						
Bi-exponential			4858.5	31.4	657.4	99.1

TABLE F.1: The bi and tri-exponential lifetime components of the CdZnSeS NC of figure 6.5.

Appendix G

G.1 eFluor®605 nm nanocrystals under electric fields

These results were obtained using an electrode designed and constructed by a summer student Charlotte Lynch. These experiments were conduct by myself on her behalf. An ensemble of 605nm NC in PMMA and HDA, were placed on a glass cover slip with two line electrodes separated by 35 μm. A potential difference of between $\pm$210 V was applied between the electrodes and the spectral and lifetime response were recorded.

Figure G.1a highlights the variation of spectral response for in which the peak emission was measured to be 606.9 nm, 608.6 nm and 609.0 nm for -60, 0 and +60 kV cm^{-1}. The lifetimes corresponding lifetimes were 11.5 ns, 14.3 ns and 13.8 ns respectively. These observations are consistent with observation seen CdSe NC in reference [202].

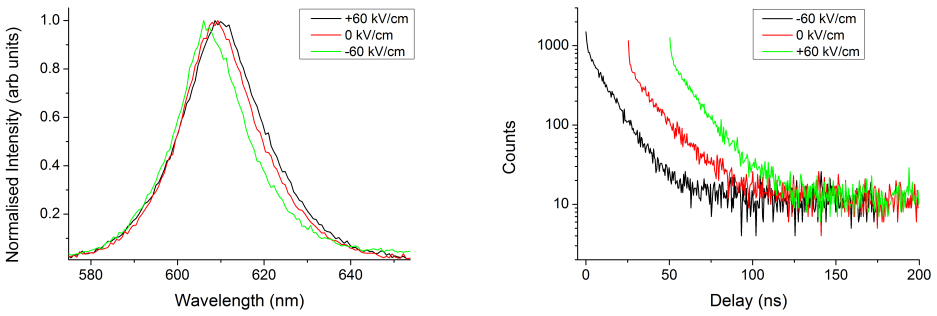

(A) (B)

FIGURE G.1: The a) spectral and b) lifetime variations of an ensemble of eFluor®605 nm under electric field of zero and ±60 kV cm^{-1}.

G.2 eFluor®650 nm nanocrystals agglomeration at 4°C

FIGURE G.2: The agglomeration of eFluor®650 nm nanocrystals at 4°C.

References

[1] Ekimov, A. I.; Onushchenko, A. A. *JEPT Lett.* **1981**, *34*, 345.

[2] Rossetti, R.; Nakahara, S.; Brus, L. E. *J. Chem. Phys.* **1983**, *79*, 1086–1088.

[3] Murray, C. B.; Norris, D. J.; Bawendi, M. G. *J. Am. Chem. Soc.* **1993**, *115*, 8706–8715.

[4] Debnath, R.; Bakr, O.; Sargent, E. H. *Energy Environ. Sci.* **2011**, *4*, 4870–4881.

[5] Chan, W. C. W., Ed. *Bio-Applications of Nanoparticles*; Springer, 2008.

[6] Colvin, V. L.; Schlamp, M. C.; Alivisatos, A. P. *Nature* **1994**, *370*, 354–357.

[7] Dabbousi, B. O.; Rodriguez-Viejo, J.; Mikulec, F. V.; Heine, J. R.; Mattoussi, H.; Ober, R.; Jensen, K. F.; Bawendi, M. G. *J. Phys. Chem. B* **1997**, *101*, 9463–9475.

[8] Hines, M. A.; Guyot-Sionnest, P. *J. Phys. Chem.* **1996**, *100*, 468–471.

[9] Xie, R.; Zhong, X.; Basché, T. *Adv. Mater.* **2005**, *17*, 2741–2745.

[10] Reiss, P.; Protière, M.; Li, L. *Small* **2009**, *5*, 154–168.

[11] Reiss, P. In *Semiconductor Nanocrystal Quantum Dots: Synthesis, Assembly, Spectroscopy and Applications*; Rogach, A., Ed.; Springer Wien New York, 2008.

[12] Gorkavenko, T.; Zubkova, S.; Makara, V.; Rusina, L. *Semiconductors* **2007**, *41*, 886–896.

[13] Pandey, A.; Guyot-Sionnest, P. *J. Chem. Phys.* **2007**, *127*, 104710–10.

[14] Madelung, O.; Schulz, M.; Weiss, H. *Landolt-Bornstein: numerical data and functional relationships in science and technology, new seriess, group III: crystal and solid state physics*; Springer Berlin, 1982; Vol. III/17b.

[15] Balasubramanian, S.; Ceder, G.; Kolenbrander, K. D. *J. Appl. Phys.* **1996**, *79*, 4132–4136.

[16] Tolbert, S. H.; Alivisatos, A. P. *Annu. Rev. Phys. Chem.* **1995**, *46*, 595–626.

[17] Eaglesham, D. J.; Cerullo, M. *Phys. Rev. Lett.* **1990**, *64*, 1943.

[18] Adachi, S. *Properties of Group−IV, III− V and II− VI Semiconductors*; John Wiley & Sons, 2005.

[19] Van de Walle, C. G. *Phys. Rev. B* **1989**, *39*, 1871–1883.

[20] Smith, A. M.; Mohs, A. M.; Nie, S. *Nat. Nanotechnol.* **2009**, *4*, 56–63.

[21] Wei, S.-H.; Zunger, A. *Phys. Rev. B* **1999**, *60*, 5404–5411.

[22] Murray, C. B.; Kagan, C. B.; Bawendi, M. G. *Annu. Rev. Mater. Sci.* **2000**, *30*, 545.

[23] de Mello Donegá, C.; Liljeroth, P.; Vanmaekelbergh, D. *Small* **2005**, *1*, 1152.

[24] Murray, C. B.; Kagan, C. B.; Bawendi, M. G. *Science* **1995**, *270*, 1335.

[25] Peng, Z. A.; Peng, X. *J. Am. Chem. Soc.* **2001**, *123*, 183–184.

[26] Washington II, A.; Strouse, G. *J. Am. Chem. Soc* **2008**, *130*, 8916.

[27] Ziegler, J.; Merkulov, A.; Grabolle, M.; Resch-Genger, U.; Nann, T. *Langmuir* **2007**, *23*, 7751–7759.

[28] Biju, V.; Itoh, T.; Anas, A.; Sujith, A.; Ishikawa, M. *Anal. Bioanal. Chem.* **2008**, *391*, 2469–2495.

[29] Park, J.; Joo, J.; Kwon, S. G.; Jang, Y.; Hyeon, T. *Angew. Chem. Int. Ed.* **2007**, *46*, 4630.

[30] LaMer, V. K.; Dinegar, R. H. *J. Am. Chem. Soc.* **1950**, *72*, 4847.

[31] Kelsall, R., Hamley, I. W., Geoghegan, M., Eds. *Nanoscale science and technology*; John Wiley & Sons, 2005.

[32] Kudra, S.; Carbone, L.; Manna, L.; Parak, W. In *Semiconductor Nanocrystal Quantum Dots: Synthesis, Assembly, Spectroscopy and Applications*; Rogach, A. L., Ed.; SpringerWien NewYork, 2008.

[33] Mullin, J. W. *Crystalization*; Oxford University Press, 1997.

[34] Peng, X.; Wickham, J.; Alivisatos, A. *J. Am. Chem. Soc.* **1998**, *120*, 5343.

[35] Ostwald, W. *Lehrbuch der allgemeinen chemie*; Leipzig, W. Engelmann, 1896; Vol. 2.

[36] Katari, J. E. B.; Colvin, V. L.; Alivisatos, A. P. *J. Phys. Chem.* **1994**, *98*, 4109–4117.

[37] Talapin, D. V.; Rogach, A. L.; Kornowski, A.; Haase, M.; Weller, H. *Nano Lett.* **2001**, *1*, 207–211.

[38] Peng, Z. A.; Peng, X. *J. Am. Chem. Soc.* **2002**, *124*, 3343.

[39] Yu, W. W.; Peng, X. *Angew. Chem. Int. Edit.* **2002**, *41*, 2368–2371.

[40] Chen, D.; Zhao, F.; Qi, H.; Rutherford, M.; Peng, X. *Chem. Mater.* **2010**, *22*, 1437–1444.

[41] Jasieniak, J.; Bullen, C.; van Embden, J.; Mulvaney, P. *J. Phys. Chem. B* **2005**, *109*, 20665–20668.

[42] Shen, H.; Wang, H.; Li, X.; Niu, J. Z.; Wang, H.; Chen, X.; Li, L. S. *Dalton Trans.* **2009**, 10534–10540.

[43] Yu, W. W.; Wang, Y. A.; Peng, X. *Chem. Mater.* **2003**, *15*, 4300–4308.

[44] Danek, M.; Jensen, K. F.; Murray, C. B.; Bawendi, M. G. *Chem. Mater.* **1996**, *8*, 173–180.

[45] Chan, W. C. W.; Nie, S. *Science* **1998**, *281*, 2016–2018.

[46] Ivanov, S.; Piryatinski, A.; Nanda, J.; Tretiak, S.; Zavadil, K.; Wallace, W.; Werder, D.; Klimov, V. *J. Am. Chem. Soc.* **2007**, *129*, 11708–11719.

[47] Tsay, J. M.; Pflughoefft, M.; Bentolila, L. A.; Weiss, S. *J. Am. Chem. Soc.* **2004**, *126*, 1926–1927.

[48] Chen, H.-S.; Lo, B.; Hwang, J.-Y.; Chang, G.-Y.; Chen, C.-M.; Tasi, S.-J.; Wang, S.-J. J. *J. Phys. Chem. B* **2004**, *108*, 17119–17123.

[49] Kudera, S.; Zanella, M.; Giannini, C.; Rizzo, A.; Li, Y.; Gigli, G.; Cingolani, R.; Ciccarella, G.; Spahl, W.; Parak, W.; Manna, L. *Adv. Mater.* **2007**, *19*, 548–552.

[50] Bang, J. et al. *Chem. Mater.* **2010**, *22*, 233–240.

[51] Li, J. J.; Wang, Y. A.; Guo, W.; Keay, J. C.; Mishima, T. D.; Johnson, M. B.; Peng, X. *J. Am. Chem. Soc.* **2003**, *125*, 12567–12575.

[52] Herman, M. A. *Molecular Beam Epitaxy: Fundementasl & Current Status (2nd ed.)*; Springer New York, 1996.

[53] Chen, Y.; Vela, J.; Htoon, H.; Casson, J. L.; Werder, D. J.; Bussian, D. A.; Klimov, V. I.; Hollingsworth, J. A. *J. Am. Chem. Soc.* **2008**, *130*, 5026–5027.

[54] Blackman, B.; Battaglia, D.; Mishima, T.; Johnson, M.; Peng, X. *Chem. Mater.* **2007**, *19*, 3815.

[55] Peng, X.; Manna, L.; Yang, W.; Wickham, J.; Scher, E.; Kadavanich, A.; Alivisatos, A. P. *Nature* **2000**, *404*, 59–61.

[56] Protière, M.; Reiss, P. *Nanoscale Res. Lett.* **2006**, *1*, 62–67.

[57] Ge, M.; Yue, Y.; Liu, Y.; Wu, J.; Sun, Y.; Chen, X.; Dai, N. *Colloids Surfaces A* **2011**, *384*, 574–579.

[58] Malik, M. A.; Revaprasadu, N.; O'Brien, P. *Chem. Mater.* **2001**, *13*, 913–920.

[59] Fan, D.; Afzaal, M.; Mallik, M. A.; Nguyen, C. Q.; OBrien, P.; Thomas, P. J. *Coordin. Chem. Rev.* **2007**, *251*, 1878–1888.

[60] Steckel, J. S.; Zimmer, J. P.; Coe-Sullivan, S.; Stott, N. E.; Bulovi, V.; Bawendi, M. G. *Angew. Chem. Int. Edit.* **2004**, *43*, 2154–2158.

[61] Peng, X.; Schlamp, M. C.; Kadavanich, A. V.; Alivisatos, A. P. *J. Am. Chem. Soc.* **1997**, *119*, 7019–7029.

[62] Kim, S.; Fisher, B.; Eisler, H.-J.; Bawendi, M. G. *J. Am. Chem. Soc.* **2003**, *125*, 11466–11467.

[63] Nonoguchi, Y.; Nakashima, T.; Kawai, T. *Small* **2009**, *5*, 2403–2406.

[64] Chen, C.-Y.; Cheng, C.-T.; Lai, C.-W.; Hu, Y.-H.; Chou, P.-T.; Chou, Y.-H.; Chiu, H.-T. *Small* **2005**, *1*, 1215–1220.

[65] Blackman, B.; Battaglia, D.; Peng, X. *Chem. Mater.* **2008**, *20*, 4847–4853.

[66] Reiss, P.; Bleuse, J.; Pron, A. *Nano Lett.* **2002**, *2*, 781–784.

[67] Balet, L. P.; Ivanov, S. A.; Piryatinski, A.; Achermann, M.; Klimov, V. I. *Nano Lett.* **2004**, *4*, 1485–1488.

[68] Zhong, X.; Xie, R.; Zhang, Y.; Basch, T.; Knoll, W. *Chem. Mater.* **2005**, *17*, 4038–4042.

[69] Pan, Z.; Zhang, H.; Cheng, K.; Hou, Y.; Hua, J.; Zhong, X. *ACS Nano* **2012**, *6*, 3982–3991.

[70] Shen, H.; Wang, H.; Tang, Z.; Niu, J. Z.; Lou, S.; Du, Z.; Li, L. S. *CrystEngComm* **2009**, *11*, 1733–1738.

[71] Kim, S.; Lim, Y. T.; Soltesz, E. G.; De Grand, A. M.; Lee, J.; Nakayama, A.; Parker, J. A.; Mihaljevic, T.; Laurence, R. G.; Dor, D. M.; Cohn, L. H.; Bawendi, M. G.; Frangioni, J. V. *Nat. Biotechnol.* **2004**, *22*, 93–97.

[72] Yu, K.; Zaman, B.; Romanova, S.; shan Wang, D.; Ripmeester, J. A. *Small* **2005**, *1*, 332–338.

[73] Chin, P. T. K.; de Mello Donega, C.; van Bavel, S. S.; Meskers, S. C. J.; Sommerdijk, N. A. J. M.; Janssen, R. A. J. *J. Am. Chem. Soc.* **2007**, *129*, 14880–14886.

[74] Wang, C. H.; Chen, T. T.; Chen, Y. F.; Ho, M. L.; Lai, C. W.; Chou, P. T. *Nanotechnology* **2008**, *19*, 115702–.

[75] Ning, Z.; Tian, H.; Yuan, C.; Fu, Y.; Qin, H.; Sun, L.; Agren, H. *Chem. Commun.* **2011**, *47*, 1536–1538.

[76] Chou, P.-T.; Chen, C.-Y.; Cheng, C.-T.; Pu, S.-C.; Wu, K.-C.; Cheng, Y.-M.; Lai, C.-W.; Chou, Y.-H.; Chiu, H.-T. *ChemPhysChem* **2006**, *7*, 222–228.

[77] Nemchinov, A.; Kirsanova, M.; Hewa-Kasakarage, N. N.; Zamkov, M. *J. Phys. Chem. C* **2008**, *112*, 9301–9307.

[78] Ivanov, S. A.; Nanda, J.; Piryatinski, A.; Achermann, M.; Balet, L. P.; Bezel, I. V.; Anikeeva, P. O.; Tretiak, S.; Klimov, V. I. *J. Phys. Chem. B* **2004**, *108*, 10625.

[79] Talapin, D. V.; Mekis, I.; Gotzinger, S.; Kornowski, A.; Benson, O.; Weller, H. *J. Phys. Chem. B* **2004**, *108*, 18826–18831.

[80] Reiss, P.; Carayon, S.; Bleuse, J.; Pron, A. *Synthetic Met.* **2003**, *139*, 649–652.

[81] McBride, J.; Treadway, J.; Feldman, L. C.; Pennycook, S. J.; Rosenthal, S. J. *Nano Lett.* **2006**, *6*, 1496–1501.

[82] Zhang, W.; Chen, G.; Wang, J.; Ye, B.-C.; Zhong, X. *Inorg. Chem.* **2009**, *48*, 9723–9731.

[83] Jack Li, J.; Tsay, J. M.; Michalet, X.; Weiss, S. *Chem. Phys.* **2005**, *318*, 82–90.

[84] Protire, M.; Reiss, P. *Small* **2007**, *3*, 399–403.

[85] Zhong, X.; Feng, Y.; Knoll, W.; Han, M. *J. Am. Chem. Soc.* **2003**, *125*, 13559–13563.

[86] Bailey, R. E.; Nie, S. *J. Am. Chem. Soc.* **2003**, *125*, 7100–7106.

[87] Swafford, L. A.; Weigand, L. A.; Bowers, M. J.; McBride, J. R.; Rapaport, J. L.; Watt, T. L.; Dixit, S. K.; Feldman, L. C.; Rosenthal, S. J. *J. Am. Chem. Soc.* **2006**, *128*, 12299–12306.

[88] Wang, X.; Ren, X.; Kahen, K.; Hahn, M. A.; Rajeswaran, M.; Maccagnano-Zacher, S.; Silcox, J.; Cragg, G. E.; Efros, A. L.; Krauss, T. D. *Nature* **2009**, *459*, 686–689.

[89] Bae, W. K.; Char, K.; Hur, H.; Lee, S. *Chem. Mater.* **2008**, *20*, 531–539.

[90] Yin, Y.; Alivisatos, P. *Nature* **2005**, *437*, 664.

[91] Li, L. S.; Pradhan, N.; Wang, Y.; Peng, X. *Nano Lett.* **2004**, *4*, 2261–2264.

[92] Fiore, A.; Mastria, R.; Lupo, M. G.; Lanzani, G.; Giannini, C.; Carlino, E.; Morello, G.; De Giorgi, M.; Li, Y.; Cingolani, R.; Manna, L. *J. Am. Chem. Soc.* **2009**, *131*, 2274–2282.

[93] Xie, R.; Kolb, U.; Basché, T. *Small* **2006**, *2*, 1454–1457.

[94] Manna, L.; Milliron, D. J.; Meisel, A.; Scher, E. C.; Alivisatos, A. P. *Nat. Mater.* **2003**, *2*, 382–385.

[95] Wu, Y. A.; Warner, J. H. *J. Mater. Chem.* **2012**, *22*, 417–424.

[96] Yeh, C.-Y.; Lu, Z. W.; Froyen, S.; Zunger, A. *Phys. Rev. B* **1992**, *46*, 10086.

[97] Shen, H.; Wang, H.; Chen, X.; Niu, J. Z.; Xu, W.; Li, X. M.; Jiang, X.-D.; Du, Z.; Li, L. S. *Chem. Mater.* **2010**, *22*, 4756–4761.

[98] Gaponenko, S. V. *Opitcal properties of Semiconductor Nanocrystals*; Cambridge University Press, Cambridge, 1998.

[99] Klimov, V., Ed. *Nanocrystal Quantum Dots*; CRC Press, 2010.

[100] Ekimov, A. I.; Hache, F.; Schanne-Klein, M. C.; Ricard, D.; Flytzanis, C.; Kudryavtsev, I. A.; Yazeva, T. V.; Rodina, A. V.; Efros, A. L. *J. Opt. Soc. Am. B* **1993**, *10*, 100–107.

[101] Klimov, V. I. *Annu. Rev. Phys. Chem.* **2007**, *58*, 635.

[102] Klimov, V. I.; McGuire, J. A.; Schaller, R. D.; Rupasov, V. I. *Phys. Rev. B* **2008**, *77*, 195324.

[103] Tyrrell, E. J.; Smith, J. M. *Phys. Rev. B* **2011**, *84*, 165328–165340.

[104] Klimov, V. I.; Mikhailovsky, A. A.; Xu, S.; Malko, A.; Hollingsworth, J. A.; Leatherdale, C. A.; Eisler, H.-J.; Bawendi, M. G. *Science* **2000**, *290*, 314–317.

[105] Zhao, J.; Bardecker, J. A.; Munro, A. M.; Liu, M. S.; Niu, Y.; Ding, I.-K.; Luo, J.; Chen, B.; Jen, A. K.-Y.; Ginger, D. S. *Nano Lett.* **2006**, *6*, 463–467.

[106] Nirmal, M.; Dabbousi, B. O.; Bawendi, M. G.; Macklin, J. J.; Trautman, J. K.; Harris, T. D.; Brus, L. E. *Nature* **1996**, *383*, 802–804.

[107] Kuno, M.; Fromm, D. P.; Hamann, H. F.; Gallagher, A.; Nesbitt, D. J. *J. Chem. Phys.* **2000**, *112*, 3117–3120.

[108] Anikeeva, P. O.; Madigan, C. F.; Halpert, J. E.; Bawendi, M. G.; Bulovi, V. *Phys. Rev. B* **2008**, *78*, 085434.

[109] Zhu, H.; Lian, T. *J. Am. Chem. Soc.* **2012**, *134*, 11289–11297.

[110] Frantsuzov, P.; Kuno, M.; Janko, B.; Marcus, R. A. *Nat. Phys.* **2008**, *4*, 519–522.

[111] Klimov, V. I.; Ivanov, S. A.; Nanda, J.; Achermann, M.; Bezel, I.; McGuire, J. A.; Piryatinski, A. *Nature* **2007**, *447*, 441–446.

[112] Kazes, M.; Oron, D.; Shweky, I.; Banin, U. *J. Phys. Chem. C* **2007**, *111*, 7898–7905.

[113] Htoon, H.; Hollingsworth, J. A.; Malko, A. V.; Dickerson, R.; Klimov, V. I. *Appl. Phys. Lett.* **2003**, *82*, 4776.

[114] Oron, D.; Kazes, M.; Banin, U. *Phys. Rev. B* **2007**, *75*, 1–7.

[115] Sher, P.; Smith, J.; Dalgarno, P.; Warburton, R.; Chen, X.; Dobson, P.; Daniels, S.; Pickett, N.; O'Brien, P. *Appl. Phys. Lett.* **2008**, *92*, 101111.

[116] Shimizu, K. T.; Neuhauser, R. G.; Leatherdale, C. A.; Empedocles, S. A.; Woo, W. K.; Bawendi, M. G. *Phys. Rev. B* **2001**, *63*, 205316.

[117] Margolin, G.; Protasenko, V.; Kuno, M.; Barkai, E. *Adv. Chem. Phys.* **2005**, *123*, 054704.

[118] Cichos, F.; von Borczyskowski, C.; Orrit, M. *Curr. Opin. Colloid In.* **2007**, *12*, 272–284.

[119] Lee, S. F.; Osborne, M. A. *ChemPhysChem* **2009**, *10*, 2174–2191.

[120] Krauss, T. D.; O'Brien, S.; Brus, L. E. *J. Phys. Chem. B* **2001**, *105*, 1725–1733.

[121] Cragg, G. E.; Efros, A. L. *Nano Lett.* **2009**, *10*, 313–317.

[122] Kloper, V.; Osovsky, R.; Cheskis, D.; Sashchiuk, A.; Lifshitz, E. *Phys. Status Solidi C* **2009**, *6*, 2719–2721.

[123] Mahler, B.; Spinicelli, P.; Buil, S.; Quelin, X.; Hermier, J.-P.; Dubertret, B. *Nat. Mater.* **2008**, *7*, 659–664.

[124] Malko, A. V.; Park, Y.-S.; Sampat, S.; Galland, C.; Vela, J.; Chen, Y.; Hollingsworth, J. A.; Klimov, V. I.; Htoon, H. *Nano Lett.* **2011**, *11*, 5213–5218.

[125] Spinicelli, P.; Buil, S.; Qulin, X.; Mahler, B.; Dubertret, B.; Hermier, J.-P. *Phys. Rev. Lett.* **2009**, *102*, 136801.

[126] García-Santamaría, F.; Chen, Y.; Vela, J.; Schaller, R. D.; Hollingsworth, J. A.; Klimov, V. I. *Nano Lett.* **2009**, *9*, 3482–3488.

[127] Htoon, H.; Malko, A. V.; Bussian, D.; Vela, J.; Chen, Y.; Hollingsworth, J. A.; Klimov, V. I. *Nano Lett.* **2010**, *10*, 2401–2407.

[128] Park, Y.-S.; Malko, A. V.; Vela, J.; Chen, Y.; Ghosh, Y.; García-Santamaría, F.; Hollingsworth, J. A.; Klimov, V. I.; Htoon, H. *Phys. Rev. Lett.* **2011**, *106*, 187401.

[129] García-Santamaría, F.; Brovelli, S.; Viswanatha, R.; Hollingsworth, J. A.; Htoon, H.; Crooker, S. A.; Klimov, V. I. *Nano Lett.* **2011**, *11*, 687–693.

[130] Galland, C.; Ghosh, Y.; Steinbruck, A.; Sykora, M.; Hollingsworth, J. A.; Klimov, V. I.; Htoon, H. *Nature* **2011**, *479*, 203–207.

[131] Galland, C.; Ghosh, Y.; Steinbrück, A.; Hollingsworth, J. A.; Htoon, H.; Klimov, V. I. *Nat. Commun.* **2012**, *3*, 908.

[132] You, L. H.; Zhang, J. J.; You, X. Y. *Int. J. Pres. Ves. Pip.* **2005**, *82*, 347.

[133] Tolbert, S. H.; Alivisatos, A. P. *Science* **1994**, *265*, 373–376.

[134] Bawendi, M. G.; Kortan, A. R.; Steigerwald, M. L.; Brus, L. E. *J. Chem. Phys.* **1989**, *91*, 7282–7290.

[135] Meulenberg, R. W.; Jennings, T.; Strouse, G. F. *Phys. Rev. B* **2004**, *70*, 235311.

[136] Bals, S.; Casavola, M.; van Huis, M. A.; Van Aert, S.; Batenburg, K. J.; Van Tendeloo, G.; Vanmaekelbergh, D. *Nano Lett.* **2011**, *11*, 3420–3424.

[137] Rosenthal, S. J.; McBride, J.; Pennycook, S. J.; Feldman, L. C. *Surf. Sci. Rep.* **2007**, *62*, 111–157.

[138] Sung, Y.-M.; You, M.; Kim, T. *J. Nanopart. Res.* **2012**, *14*, 1–6.

[139] Cai, X.; Mirafzal, H.; Nguyen, K.; Leppert, V.; Kelley, D. F. *J. Phys. Chem. C* **2012**, *116*, 8118–8127.

[140] Cassette, E.; Mahler, B.; Guigner, J.-M.; Patriarche, G.; Dubertret, B.; Pons, T. *ACS Nano* **2012**, *6*, 67416750.

[141] Stadelmann, P. JEMS. 2004; http://cimewww.epfl.ch/people/stadelmann/jemsWebSite/jems.html.

[142] Rietveld, H. M. *J. Appl. Crystallogr.* **1969**, *2*, 65–71.

[143] Buonsanti, R.; Llordes, A.; Aloni, S.; Helms, B. A.; Milliron, D. J. *Nano Lett.* **2011**, *11*, 4706–4710.

[144] Proffen, T.; Neder, R. B. *Diffuse Scattering and Defect Structure Simulations: A cook book using the program DISCUS*; Oxford University Press, 2008.

[145] Proffen, T.; Neder, R. B. *J. Appl. Crystallogr.* **1997**, *30*, 171–175.

[146] Hall, B. D. *J. Appl. Phys.* **2000**, *87*, 1666–1675.

[147] Van Der Merwe, J. H. *J. Appl. Phys.* **1963**, *34*, 123–127.

[148] People, R.; Bean, J. C. *Appl. Phys. Lett.* **1985**, *47*, 322–324.

[149] Ovid'ko, I. A.; Sheinerman, A. G. *Adv. Phys.* **2006**, *55*, 627–689.

[150] Huxter, V. M.; Lee, A.; Lo, S. S.; Scholes, G. D. *Nano Lett.* **2008**, *9*, 405–409.

[151] Chen, X.; Lou, Y.; Samia, A. C.; Burda, C. *Nano Lett.* **2003**, *3*, 799–803.

[152] Matthews, J. W.; Mader, S.; Light, T. B. *J. Appl. Phys.* **1970**, *41*, 3800.

[153] Hull, D.; Bacon, D. J. *Introduction to Dislocations*, 3rd ed.; Pergamon Press, 2001; Vol. 37.

[154] Föll, H. Defects in Crystals. 2012; http://www.tf.uni-kiel.de/matwis/amat/def_en/kap_5/backbone/r5_4_1.html.

[155] Ovid'ko, I. A.; Sheinerman, A. G. *Phys. Rev. B* **2002**, *66*, 245309.

[156] Pokatilov, E. P.; Fonoberov, V. A.; Fomin, V. M.; Devreese, J. T. *Phys. Rev. B* **2001**, *64*, 245328.

[157] Zhang, J.; Sun, K.; Kumbhar, A.; Fang, J. *J. Phys. Chem. C* **2008**, *112*, 5454–5458.

[158] Pradhan, N.; Goorskey, D.; Thessing, J.; Peng, X. *J. Am. Chem. Soc.* **2005**, *127*, 17586–17587.

[159] Jiang, F.; Li, Y.; Ye, M.; Fan, L.; Ding, Y.; Li, Y. *Chem. Mater.* **2010**, *22*, 4632–4641.

[160] Guan, J. Synthesis and structural characterization of ZnTe/ZnSe core/shell tunable quantum dots. M.Sc. thesis, Massachusetts Institute of Technology, 2008.

[161] Hardman, S. J. O.; Graham, D. M.; Stubbs, S. K.; Spencer, B. F.; Seddon, E. A.; Fung, H.-T.; Gardonio, S.; Sirotti, F.; Silly, M. G.; Akhtar, J.; O'Brien, P.; Binks, D. J.; Flavell, W. R. *Phys. Chem. Chem. Phys.* **2011**, *13(45)*, 20275–20283.

[162] de Mello, J. C.; Wittmann, H. F.; Friend, R. H. *Adv. Mater.* **1997**, *9*, 230–232.

[163] Sher, P. Carrier dynamics in single semiconductor nanocrystals. D.Phil. thesis, University of Oxford, 2009.

[164] Kuno, M.; Fromm, D. P.; Hamann, H. F.; Gallagher, A.; Nesbitt, D. J. *J. Chem. Phys.* **2001**, *115*, 1028–1040.

[165] EuropeanUnion, Restriction of Hazardous Substances Directive of the European Union. Directive 2011/65/EU, 2011; http://www.rohs.eu/english/index.html.

[166] Jun, Y.-w.; Choi, C.-S.; Cheon, J. *Chem. Commun.* **2001**, 101–102.

[167] Mntungwa, N.; Rajasekhar Pullabhotla, V. S.; Revaprasadu, N. *Mater. Lett.* **2012**, *81*, 108–111.

[168] Xu, S.; Wang, C.; Xu, Q.; Zhang, H.; Li, R.; Shao, H.; Lei, W.; Cui, Y. *Chem. Mater.* **2010**, *22*, 5838–5844.

[169] Wang, C.; Zhang, H.; Xu, S.; Lv, N.; Liu, Y.; Li, M.; Sun, H.; Zhang, J.; Yang, B. *J. Phys. Chem. C* **2008**, *113*, 827–833.

[170] Zhou, D.; Lin, M.; Chen, Z.; Sun, H.; Zhang, H.; Sun, H.; Yang, B. *Chem. Mater.* **2011**, *23*, 4857–4862.

[171] Lee, S. H.; Kim, Y. J.; Park, J. *Chem. Mater.* **2007**, *19*, 4670–4675.

[172] Yu, W. W.; Qu, L.; Guo, W.; Peng, X. *Chem. Mater.* **2003**, *15*, 2854–2860.

[173] Chen, O.; Yang, Y.; Wang, T.; Wu, H.; Niu, C.; Yang, J.; Cao, Y. C. *J. Am. Chem. Soc.* **2011**, *133*, 17504–17512.

[174] Xu, S.; Wang, C.; Cui, Y. *J. Mol. Struc.-Theochem* **2009**, *916*, 168–171.

[175] Rockenberger, J.; Troger, L.; Rogach, A. L.; Tischer, M.; Grundmann, M.; Eychmuller, A.; Weller, H. *J. Chem. Phys.* **1998**, *108*, 7807–7815.

[176] Yordanov, G. G.; Gicheva, G. D.; Bochev, B. H.; Dushkin, C. D.; Adachi, E. *Colloids and Surfaces A: Physicochemical and Engineering Aspects* **2006**, *273*, 10–15.

[177] Suryanarayana, C.; Grant Norton, M. *X-Ray Diffraction: A Practical Approach*; Plenum, 1998.

[178] Pandey, S. C.; Mountziaris, T. J.; Venkataraman, D.; Maroudas, D. *Appl. Phys. Lett.* **2010**, *96*, 201910–3.

[179] Santra, P. K.; Viswanatha, R.; Daniels, S. M.; Pickett, N. L.; Smith, J. M.; O'Brien, P.; Sarma, D. D. *J. Am. Chem. Soc.* **2009**, *131*, 470–477.

[180] Borchert, H.; Haubold, S.; Haase, M.; Weller, H.; McGinley, C.; Riedler, M.; Müller, T. *Nano Lett.* **2002**, *2*, 151–154.

[181] Huang, K.; Demadrille, R.; Silly, M. G.; Sirotti, F.; Reiss, P.; Renault, O. *ACS Nano* **2010**, *4*, 4799–4805.

[182] Fujimori, A.; Minami, F.; Sugano, S. *Phys. Rev. B* **1984**, *9*, 5225–5227.

[183] Martin, J. E.; Herzing, A. A.; Yan, W.; Li, X.-q.; Koel, B. E.; Kiely, C. J.; Zhang, W.-x. *Langmuir* **2008**, *24*, 4329–4334.

[184] Shard, A. G.; J., W.; Spencer, S. J. *Surf. Interface Anal.* **2009**, *41*, 541–548.

[185] Zeng, R.; Zhang, T.; Dai, G.; Zou, B. *J. Phys. Chem. C* **2011**, *115*, 3005–3010.

[186] Zhang, L.; Lin, Z.; Luo, J.-W.; Franceschetti, A. *ACS Nano* **2012**, *6*, 8325–8334.

[187] Efros, A. L.; Rosen, M.; Kuno, M.; Nirmal, M.; Norris, D. J.; Bawendi, M. *Phys. Rev. B* **1996**, *54*, 4843–4856.

[188] Cadirci, M.; Stubbs, S. K.; Fairclough, S. M.; Tyrrell, E. J.; Watt, A. A. R.; Smith, J. M.; Binks, D. J. *Phys. Chem. Chem. Phys.* **2012**, *14*, 13638–13645.

[189] Green, M. *J. Mater. Chem.* **2010**, *20*, 5797–5809.

[190] Willis, S. M.; Cheng, C.; Assender, H. E.; Watt, A. A. R. *Nano Lett.* **2012**, *12*, 1522–1526.

[191] Nikesh, V. V.; Lad, A. D.; Kimura, S.; Nozaki, S.; Mahamuni, S. *J. Appl. Phys.* **2006**, *100*, 113520–6.

[192] Banin, U.; Lee, C. J.; Guzelian, A. A.; Kadavanich, A. V.; Alivisatos, A. P.; Jaskolski, W.; Bryant, G. W.; Efros, A. L.; Rosen, M. *J. Chem. Phys.* **1998**, *109*, 2306–2309.

[193] Bertram, D.; Mićić, O. I.; Nozik, A. J. *Phys. Rev. B* **1998**, *57*, R4265–R4268.

[194] Peterson, J. J.; Huang, L.; Delerue, C.; Allan, G.; Krauss, T. D. *Nano Lett.* **2007**, *7*, 3827–3831.

[195] Trinh, M. T.; Houtepen, A. J.; Schins, J. M.; Piris, J.; Siebbeles, L. D. A. *Nano Lett.* **2008**, *8*, 2112–2117.

[196] Schmidt, M. E.; Blanton, S. A.; Hines, M. A.; Guyot-Sionnest, P. *J. Chem. Phys.* **1997**, *106*, 5254–5259.

[197] Huong, N. Q.; Birman, J. L. *J. Chem. Phys.* **1998**, *108*, 1769–1772.

[198] Shim, M.; Guyot-Sionnest, P. *J. Chem. Phys.* **1999**, *111*, 6955–6964.

[199] Norris, D. J.; Bawendi, M. G. *Phys. Rev. B* **1996**, *53*, 16338–16346.

[200] Guyot-Sionnest, P.; Hines, M. A. *Appl. Phys. Lett.* **1998**, *72*, 686–688.

[201] Tomczak, N.; Jaczewski, D.; Dorokhin, D.; Han, M.-Y.; Vancso, G. In *Methods in Molecular Biology*; Navarro, M., Planell, J. A., Eds.; Humana Press, 2012; Vol. 811.

[202] Empedocles, S. A.; Bawendi, M. G. *Science* **1997**, *278*, 2114–2117.

[203] Empedocles, S. A.; Bawendi, M. G. *J. Phys. Chem. B* **1999**, *103*, 1826–1830.

[204] van Sark, W. G. J. H. M.; Frederix, P. L. T. M.; Bol, A. A.; Gerritsen, H. C.; Meijerink, A. *ChemPhysChem* **2002**, *3*, 871–879.

[205] Ratchford, D.; Dziatkowski, K.; Hartsfield, T.; Li, X.; Gao, Y.; Tang, Z. *J. Appl. Phys.* **2011**, *109*, 103509–6.

[206] Garrett, M. D.; Dukes III, A. D.; McBride, J. R.; Smith, N. J.; Pennycook, S. J.; Rosenthal, S. J. *J. Phys. Chem. C* **2008**, *112*, 12736–12746.

[207] Qin, W.; Shah, R. A.; Guyot-Sionnest, P. *ACS Nano* **2011**, *6*, 912–918.

[208] Presland, K. Synthesis, properties and applications of cadmium based nanoparticles emitting from 400-750 nm. Ph.D. thesis, University of Manchester, 2010.

[209] Nag, A.; Chakraborty, S.; Sarma, D. D. *J. Am. Chem. Soc.* **2008**, *130*, 10605–10611.

[210] Messin, G.; Hermier, J. P.; Giacobino, E.; Desbiolles, P.; Dahan, M. *Opt. Lett.* **2001**, *26*, 1891–1893.

[211] eBioscience, 2012. www.ebioscience.com/.

[212] Peng, A. (Evident Technologies). Semiconductor nanocrystal complexes comprising a metal coating and methods. US Patent 7,482,059, 2009.

[213] Klimov, V. I. *J. Phys. Chem. B* **2000**, *104*, 6112.

[214] Zhao, J.; Chen, O.; Strasfeld, D. B.; Bawendi, M. G. *Nano Lett.* **2012**, *12*, 4477–4483.

[215] Pelton, M.; Smith, G.; Scherer, N.; Marcus, R. *Proc. Natl. Acad. Sci. U. S. A.* **2007**, *104*, 14249–14254.

[216] Cho, J. W.; Kim, H. S.; Kim, Y. J.; Jang, S. Y.; Park, J.; Kim, J.-G.; Kim, Y.-J.; Cha, E. H. *Chem. Mater.* **2008**, *20*, 5600–5609.

[217] Pandey, S. C.; Wang, J.; Mountziaris, T. J.; Maroudas, D. *J. Appl. Phys.* **2012**, *111*, 113526–8.

[218] Han, X.; Pandey, S. C.; Maroudas, D. *Appl. Phys. Lett.* **2012**, *101*, 141906–5.

[219] Bussian, D. A.; Crooker, S. A.; Yin, M.; Brynda, M.; Efros, A. L.; Klimov, V. I. *Nat. Mater.* **2009**, *8*, 35–40.

[220] Korozlu, N.; Colakoglu, K.; Deligoz, E. *J. Phys.: Condens. Matter* **2009**, *21*, 175406.

[221] Landolt-Bornstein, In *Numerical Data and Functional Relationships in Science and Technology*; Madelung, O., M., S., Weiss, H., Eds.; Springer, 1982; Vol. vol. III/17b.

[222] Buschert, J. R.; Peiris, F. C.; Samarth, N.; Luo, H.; Furdyna, J. K. *Phys. Rev. B* **1994**, *49*, 4619–4622.

[223] Surucu, G.; Colakoglu, K.; Deligoz, E.; Ciftci, Y.; Korozlu, N. *J. Mater. Sci.* **2011**, *46*, 1007–1014.

[224] Mnasri, S.; Nasrallah, S. A.-B.; Sfina, N.; Bouarissa, N.; Said, M. *Semicond. Sci. Technol.* **2009**, *24*, 095008.

[225] Ganguli, T.; Mazher, J.; Polian, A.; Deb, S. K.; Pages, O.; Firszt, F. *J. Phys. Conf. Ser.* **2009**, *190*, 012064.

[226] Takeuchi, S.; Suzuki, K.; Maeda, K.; Iwanaga, H. *Philos. Mag. A* **1985**, *50*, 171–178.

[227] Kamran, S.; Chen, K.; Chen, L. *Phys. Rev. B* **2008**, *77*, 094109.

[228] Harris, D. C.; Baronowski, M.; Henneman, L.; LaCroix, L.; Wilson, C.; Kurzius, S.; Burns, B.; Kitagawa, K.; Gembarovic, J.; Goodrich, S. M.; Staats, C.; Mecholsky, J. J., Jr. *Opt. Eng.* **2008**, *47*, 114001.

[229] Bellakhder, H.; Outzourhit, A.; Ameziane, E. *Thin Solid Films* **2001**, *382*, 30–33.

[230] Wang, Y. Q.; Philipose, U.; Xu, T.; Ruda, H. E.; Kavanagh, K. L. *Semicond. Sci. Technol.* **2007**, *22*, 175.

[231] Rajakarunanayake, Y.; Miles, R. H.; Wu, G. Y.; McGill, T. C. *Phys. Rev. B* **1998**, *37*, 10212–10215.

[232] Vaněček, M.; Klier, E. *Phys. Status Solidi (a)* **1975**, *30*, 441–448.

[233] Shokhovets, S.; Ambacher, O.; Gobsch, G. *Phys. Rev. B* **2007**, *76*, 125203.

[234] Neumann, C.; Nöthe, A.; Lipari, N. O. *Phys. Rev. B* **1988**, *37*, 922–932.

[235] J. Sörgel,; Scherz, U. *Eur. Phys. J. B* **1998**, *5*, 45–52.

[236] Harrison, W. A. *J. Vac. Sci. Technol.* **1977**, *14*, 1016–1021.

[237] Wei, S.-H.; Zunger, A. *Appl. Phys. Lett.* **1998**, *72*, 2011–2013.

[238] Li, Y.-H.; Walsh, A.; Chen, S.; Yin, W.-J.; Yang, J.-H.; Li, J.; Da Silva, J. L. F.; Gong, X. G.; Wei, S.-H. *Appl. Phys. Lett.* **2009**, *94*, 212109–3.

[239] Bolcatto, P. G.; Proetto, C. R. *J. Phys. Condens. Matter* **2001**, *13*, 319.

[240] Kootstra, F.; de Boeij, P. L.; Snijders, J. G. *Phys. Rev. B* **2000**, *62*, 7071–7083.

[241] Bransden, B. H.; Joachain, C. J. *Introduction to Quantum Mechanics*, 1st ed.; Longman Scientific and Technical: New York, p 360.

[242] Piryatinski, A.; Ivanov, S. A.; Tretiak, S.; Klimov, V. I. *Nano Lett.* **2007**, *7*, 108–115.

[243] de Mello Donegaà, C.; Koole, R. *J. Phys. Chem. C* **2009**, *113*, 6511–6520.

[244] Guinier, A. *X-Ray Diffraction*; Freeman, San Francisco, 1963.

[245] Hÿtch, M. J.; Potez, L. *Philos. Mag. A* **1997**, *76*, 1119–1138.

[246] Hüe, F.; Hÿtch, M.; Bender, H.; Houdellier, F.; Claverie, A. *Phys. Rev. Lett.* **2008**, *100*, 156602.

[247] Johnson, C. L.; Snoeck, E.; Ezcurdia, M.; Rodriguez-Gonzalez, B.; Pastoriza-Santos, I.; Liz-Marzan, L. M.; Hytch, M. J. *Nat. Mater.* **2008**, *7*, 120–124.

[248] Hÿtch, M.; Plamann, T. *Ultramicroscopy* **2001**, *87*, 199–212.